Bloch oscillations of magnetic solitons as an example of dynamical localization of quasiparticles in a uniform external field (Review)

A. M. Kosevich*

B. Verkin Institute for Low Temperature Physics and Engineering, National Academy of Sciences of Ukraine, pr. Lenina 47, 61103 Kharkov, Ukraine

(Submitted February 6, 2001)
Fiz. Nizk. Temp. **27**, 699–737 (July 2001)

The theory of the oscillatory motion of a band particle or particlelike excitation in a uniform field—the so-called Bloch oscillations—is reviewed. It is explained that this unusual motion is contingent on two circumstances: the time dependence of the motion of the particle under the influence of the external fields is governed by a classical equation of motion ($dp/dt=F$), and the energy spectrum of the particle is of a band nature, which presupposes a periodic dependence of the energy of the particle on its momentum (quasimomentum) $\varepsilon=\varepsilon(p)=\varepsilon(p+p_0)$, where p_0, the period in p space, arises in a natural way in the description of the motion in a spatially periodic structure (lattice). Quasiclassical and quantum descriptions of the Bloch oscillations are given. Since a systematic exposition of the theory of this phenomenon has not been set forth in any monographs, the first part of this review gives a rather detailed presentation (with all the basic calculations) of the results on the oscillatory dynamics of an elementary excitation of a one-dimensional discrete chain, including the theory of the motion both in a uniform static field and in a uniform field with a harmonic time dependence. An interpretation is offered for the relationship of the frequency of quasiclassical Bloch oscillations and the equidistant spectrum of energy levels in the so-called Wannier–Stark ladder. An explanation of the physical nature of the phenomenon of dynamical localization of a band particle in a spatially uniform alternating field is given. It is shown that the basic results of such a dynamics carry over to the motion of a dynamical soliton of the discrete nonlinear Schrödinger equation. The second part of this review describes the Bloch oscillations of topological and dynamical magnetic solitons. It is shown that the phenomenological Landau–Lifshitz equations for the magnetization field in a magnetically ordered medium have surprising soliton solutions. The energy of a soliton is a periodic function of its momentum, even though its motion occurs in a continuous medium. The presence of this periodicity is sufficient to explain the Bloch oscillations of magnetic solitons. The quantum oscillatory dynamics of a soliton in a discrete spin chain is described. The review concludes with a discussion of the conditions for this oscillatory motion and the possibilities for its experimental observation. [DOI: 10.1063/1.1388415]

INTRODUCTION

The term ''Bloch oscillations'' in electronic theory refers to the oscillatory motion of a band electron in a uniform static electric field, with an amplitude inversely proportional to the value of the applied field. This unusual behavior of a quasiparticle in a crystal was predicted by Bloch in 1928[1] and for that reason bears his name. The cause of this unusual (from the standpoint of the mechanics of a charged particle in vacuum) behavior of an electron in a crystal (a so-called Bloch or band electron) is a certain peculiarity of its dynamics in external fields. The particular property of the band motion of an electron which is mainly responsible for this peculiarity is that the energy of a Bloch electron, like that of any quasiparticle in a crystal, is a periodic function of its momentum or, more precisely, its quasimomentum (see any book on electronic theory, e.g., Refs. 2 and 3). In turn, the periodic dependence of the energy of an electron on its quasimomentum (the periodicity of its dispersion relation in k space, with the period of the reciprocal lattice) is due to the translational spatial periodicity of the crystal lattice. If the period of the crystal lattice (the lattice constant) is equal to a, then the curve of the reciprocal lattice is equal to $2\pi\hbar/a$. Assuming the existence of periodicity of the dispersion relation and the possibility of using the classical equation of motion, according to which the time derivative of the momentum of an electron is equal to the electric field acting on it, one can easily estimate the period of the Bloch oscillations. Let $\Delta p=2\pi\hbar/a$ be the period of the electron energy $\varepsilon(p)$ as a function of quasimomentum. The velocity of the electron is equal to the derivative of ε with respect to π, and therefore by virtue of the periodicity of ε it is also a periodic function of p with the same period. In an electric field the evolution of the momentum is governed by the usual equation

$$\frac{dp}{dt}=eE, \tag{1}$$

and therefore $p=eEt$. Consequently, the electron velocity indeed oscillates in time with a frequency $\omega_B=eEa/\hbar$. This

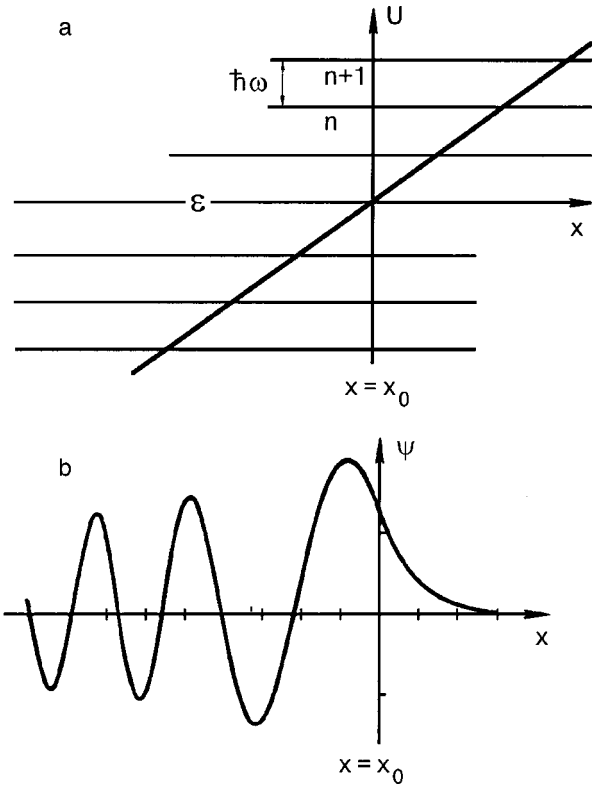

FIG. 1. Energy levels of a band particle in a uniform field (the Wannier–Stark ladder) (a). The wave function of a band particle with energy ε (b).

is the Bloch oscillation frequency. Importantly, the Bloch frequency is proportional to the period of the crystal lattice and to the force acting on the electron.

The proposed quasiclassical explanation of the nature of the Bloch oscillations can be associated to a simple quantum scheme. Let a quantum particle be found in a stationary state with energy ε in a potential field $U=-Fx=-eEx$. We denote by $x=x_0$ the coordinate of the point where $\mathcal{E}=-Fx_0$ (Fig. 1a). Then on the semiaxis $x>x_0$ the kinetic energy of the particle is negative, and its wave function $\psi(x)$ decays exponentially with increasing x (Fig. 1b). On the semiaxis $x<x_0$ the particle has a certain effective negative quasimomentum that depends on the coordinate x, and it is in a state of motion leftward. However, when the quasimomentum reaches the boundary of the Brillouin zone, the velocity of the electron goes to zero, i.e., the particle is, as it were, reflected from the Brillouin zone boundary. Consequently, although the function $\psi(x)$ has an oscillatory character, its amplitude falls off with increasing x_0-x (Fig. 1b). As a result, the wave vector is nonzero only in the region near $x=x_0$. Therefore, the stationary state of the particle is localized around this point. This physical phenomenon is sometimes called *dynamical localization* of a particle in a uniform external field. However, it is known that a localized stationary state must have a discrete energy level. What distinguishes this value of ε in a uniform field? By virtue of the uniformity of the field there is no preferred value of ε. Therefore, the requisite discreteness can only be due to an equidistant discrete spectrum of the type

$$\varepsilon=\varepsilon_0+n\hbar\omega, \quad n=0,\pm1,\pm2,..., \tag{2}$$

where different n correspond to the same wave functions but which are localized around different centers $x_n=x_0+(\hbar\omega/F)n$.

The equidistant spectrum (2), particularly its manifestation in optical experiments, is called a Wannier–Stark ladder. It turns out that the distances between the ''steps'' of this ladder in the case of an electron in a uniform electric field determine the Bloch oscillation frequency: $\omega=\omega_B$.

At reasonable values of the electric field the frequency of the Bloch oscillations of an electron in a metal is many orders of magnitude lower than the collision frequency of the electron even in extremely pure metals (in other words, the oscillation period is much greater than the relaxation time τ in the metal, and the amplitude of the Bloch oscillations is much greater than the electron mean free path). Therefore, in calculating the resistivity of conductors and in other similar cases the periodic character of the electron motion need not be taken into account, and the electron motion over short path lengths can be assumed translational. It was long assumed that the Bloch oscillations are an extremely curious physical phenomenon but are of interest only from a theoretical standpoint.

The situation was fundamentally altered by the development of technology for fabricating extremely perfect semiconductor superlattices with structural periods much greater than the lattice constant. In such structures the period of the reciprocal lattice is greatly diminished, and the electron energy spectrum separates into narrow subbands, with the result that the Bloch oscillations corresponding to them have rather high frequencies (the obvious condition $\omega\tau\gg1$ becomes attainable); thus it becomes realistic to produce such oscillations and observe them experimentally. This possibility was first pointed out by Esaki and Tsu,[4] prompting an experimental search for these oscillations. It is clear that because of the finite value of the relaxation time τ, measurements should be made over very brief time intervals $\Delta t\ll\tau$, but that becomes a problem of experimental technique.

Experiments along this line confirmed, first of all, that a Wannier–Stark ladder is manifested in optical studies.[6] Later the Bloch oscillations of the electron current in the bulk of semiconductor superlattices were observed directly (the first direct experiments of this type were apparently done in Refs. 7 and 8).

It should be noted that what was observed experimentally were oscillations of the macroscopic electric current. Since the actual phenomenon under study consists in the translational electron oscillations, it can be manifested only in the case of coherent motion of all the electrons participating in it. In the experiment a macroscopic group of coherent electrons was produced by acting on the semiconductor superlattice with a laser pulse (interestingly, the laser pulse itself was produced by the collective coherent transition of a large group of electrons from an energy-converted atomic state to some ground state).

The need for macroscopic coherent motion of the electron system for realization of Bloch oscillations places this phenomenon in with a group of other peculiar oscillation effects caused by the periodic dependence of the current on the phase of a system of a large number of current carriers (recall that the quasimomentum of the electron determines

the phase of its wave function). A clear and obvious example is the Josephson effect, in which the current I depends harmonically on the phase Φ:

$$I = I_0 \sin \Phi, \quad I_0 = \text{const}, \tag{3}$$

and the rate of change of the phase Φ with time is given by an expression analogous to (1):

$$d\Phi/dt = eV/h, \quad V = \text{const}, \tag{4}$$

where V is the electrical potential difference across the Josephson junction. As a result, a dc voltage gives rise to an oscillatory current.

A physical system of the kind that should exhibit Bloch oscillations is a superconducting condensate in a periodic superconducting structure (superconducting superlattice). Indeed, a superconducting condensate is a macroscopic system of coherently moving electrons (Cooper pairs) and, when placed in a spatially periodic potential, should execute Bloch oscillations under to influence of, say, an external electric field directed along an axis along which there is periodicity of the order parameter. This circumstance was pointed out long ago,[9] but the author is unaware of any corresponding experiments.

Peculiar electron oscillations of the Bloch type can arise in a layered superlattice in a high magnetic field parallel to the layers (the layers are arranged periodically with period d in the direction perpendicular to the x axis, and the magnetic field H is directed along the z axis). For a suitable choice of gauge of the vector potential the electron momentum component p_y is conserved and determines the x coordinate of the center of the classical orbit of the electron, x_0. For this geometry the electron energy, as was shown in Ref. 10, is a periodic function of x_0 and, hence, a periodic function of p_y. If in such a superlattice an electric field E that does not destroy its energy structure is applied along the y axis, then, in accordance with what we have said, oscillations arise with a frequency $\omega = 2\pi Ec/(Hd)$. Interestingly, in this case the oscillations are observed in the direction perpendicular to the direction of periodicity of the superlattice but are governed by the time required for an electron to traverse the period d at the Hall drift velocity Ec/H.

The fundamental commonality of the phenomena is obvious, as are the conclusions as to the possibility of similar oscillations of the macroscopic electric current or the particle flux, if one is talking about the coherent motion of uncharged particles or quasiparticles. Although the examples given above pertain to the Bloch oscillations of electrons under the influence of an electric field, the electrical properties of the systems mentioned came in through the fact that the external force acting on the quasiparticle was determined by the value of the electric field. If the electric field on the right-hand side of Eq. (1) is replaced by a constant force of any nature, then all of the above discussion will still apply, and therefore:

a) the coherent particle flux (or current) should depend on the phase of the system in a periodic manner (in the case of electrons and Bloch oscillations this phase is the identical momentum of the electrons);

b) a rate of change of the phase should arise under the influence of a uniformly distributed external force;

c) when condition a) holds, another type of oscillations can occur, namely: if the transverse uniform external force creates a phase gradient, then purely spatial longitudinal oscillations of the dc current density can arise (the role of time is assumed by one of the spatial coordinates).

The situation described in this last conclusion has been used in the description and experimental observation of Bloch oscillations in optics.[11,12] Optical Bloch oscillations reduce to spatial oscillations of a narrow laser beam propagating along a periodic system of parallel optical waveguides under the influence of a uniform gradient of the refractive index of the waveguide material. The individual optical waveguides are weakly coupled optically with one another and form a sort of optical periodic medium, and in the experiments of Refs. 11 and 12 the external force (the refractive index gradient) acting on the laser beam was produced by a nonuniform heating of the system of optical waveguides.

A discussion and experimental observation of optical Bloch oscillations confirms the common physical nature of this phenomenon and the possibility that it can arise when any object moves under the influence of a constant force if its kinetic energy is a periodic function of momentum. Such an object may be, for example, a particlelike formation in the nonlinear classical or quantum dynamics of discrete systems, where the presence of a periodic structure is provided by the aforementioned periodicity of the excitation energy. A typical particlelike object of this type is a dynamical soliton. The Bloch oscillations of a soliton in a discrete molecular chain described by a nonlinear Schrödinger equation are analyzed in Ref. 13.

A special class of systems in which the coherent effect under discussion exists is that of magnetic systems, the consideration of which brings us to the main subject of this paper. Low-current magnetic dynamical solitons are described by a nonlinear Schrödinger equation. Therefore, our analysis of the Bloch oscillations of solitons begins with the dynamics of a soliton of this equation.

The oscillatory motion of the simplest magnetic soliton—a domain wall—in a realistic model, namely, in a ferromagnet with biaxial anisotropy, was first predicted in Ref. 14. The specifics of the dynamical equations for the magnetization of ferromagnets are such that even in the continuum approximation a domain wall executes Bloch oscillations in a uniform magnetic field. Comparatively recent theoretical studies have confirmed that Bloch oscillations of domain walls with solitonlike behavior can exist[15] and have calculated them both at the level of quasiclassical dynamics of domain walls moving in a periodic potential[16] and with the use of the quantum dynamics of spin solitons.[17] Bloch oscillations of a dynamical magnetic soliton in a one-dimensional (1D) uniaxial ferromagnet under the influence of a magnetic field gradient were predicted in Ref. 18 and investigated in detail (including numerical calculations based on the Landau–Lifshitz equations) in Ref. 19. The influence of dissipative processes on the damping of Bloch oscillations of a magnetic soliton were analyzed in Ref. 20.

The papers listed, which deal with to oscillations of magnetic solitons under the influence of a constant force, are only a few of the papers on which this review is based.

Nevertheless, they demonstrate that interest in the problem arose long ago in the nonlinear dynamics of the magnetization of magnetically ordered systems and has been rising in recent years.

1. BLOCH OSCILLATIONS AND DYNAMICAL LOCALIZATION

1.1. Quantum theory of the Wannier–Stark ladder and the oscillation of a particle in a uniform external field

Let us consider a 1D discrete system in which the motion of a particle reduces to hops between adjacent sites of the chain. In the tight-binding model the equation for the dynamics of a free particle in the site representation has the form

$$i\frac{\partial\Psi_n}{\partial t}=\alpha(2\Psi_n-\Psi_{n+1}-\Psi_{n-1})+\Omega_0\Psi_n, \tag{5}$$

where n is the number of the site, α is the frequency of transition of the particle between nearest-neighbor sites and determines the kinetic energy of the quantum particle, and Ω_0 is the potential energy of the particle at rest and is independent of the site number (Planck's constant is set equal to 1).

The wave function satisfying Eq. (5) has the obvious form

$$\Psi_n=\Psi_0\exp(ikn-i\omega t), \tag{6}$$

where k is the wave number (the distance between sites is taken equal to 1) and is related to the energy (frequency ω) by the dispersion relation

$$\omega=\Omega_0+\varepsilon(k)\equiv\Omega_0+2\alpha(1-\cos k). \tag{7}$$

The spectrum of steadily moving states of a particle is continuous and has a single band of finite width ($\Omega_0<\omega<\Omega_0+4\alpha$).

From now on we will restrict the analysis to single-band models only. Of course, in using only single-band models we will be unable to discuss many features of the Bloch oscillations, in particular, all those connected with interband transitions. Some effects that go beyond the single-band model have been considered in Ref. 21. However, in the cases of interest to us the spectrum of elementary excitations has a single band, and so we may restrict the analysis to single-band models.

Consider a wave packet whose harmonic components (6) are localized in k space near a certain value of k:

$$\Psi(n,t)=\frac{1}{2\pi}\int_{-\pi}^{\pi}\Phi(k,t)\exp(ikn)dk. \tag{8}$$

As we know, the translational velocity of the envelope of the wave packet (8) is equal to the group velocity of the particle/wave:

$$v=\frac{d\omega}{dk}=2\alpha\sin k. \tag{9}$$

A remarkable property of relation (9) is the periodic dependence of the velocity on the wave number (or wave vector in the 3D case). This property has an interesting manifestation in the motion of a particle under the influence of external forces.

Let us consider the dynamics of the same particle in an external field. It is known from electronic theory[2–4] that in the quasiclassical approximation a potential field producing a uniformly distributed force F on a particle causes a change in wave number (quasimomentum) of the particle/packet:

$$\frac{dk}{dt}=F. \tag{10}$$

Consequently, in a uniform and static field the wave number k varies monotonically with time:

$$k=Ft. \tag{11}$$

Substituting (11) into (9), we see that the velocity of the particle oscillates in time with a frequency

$$\omega_B=F. \tag{12}$$

In dimensional units this frequency is equal to $\omega_B=Fa/\hbar$, where a is the period of the chain (the distance between nearest-neighbor sites). This is the frequency of the Bloch oscillations.

A uniform force field of strength F in a continuous medium corresponds to a potential $U=-Fx$, which in the site representation can be written as

$$\Omega_n=-Fn. \tag{13}$$

One naturally wonders what will happen when the potential (13) is included directly in Eq. (5). Replacing Ω_0 in (5) by (13), we get

$$i\frac{\partial\Psi_n}{\partial t}=\alpha(2\Psi_n-\Psi_{n+1}-\Psi_{n-1})-Fn\Psi_n. \tag{14}$$

We note that the stationary solutions of equation (14), of the type $\Psi_n(t)=\Psi_n^{\omega}\exp(-i\omega t)$, have a certain property which is typical for the dynamics of a particle in a uniform field. It is clear that the solution of the equation of steady-state oscillations,

$$(\omega+Fn)\Psi_n=\alpha(2\Psi_n-\Psi_{n+1}-\Psi_{n-1}) \tag{15}$$

is a function of the variable $z=n+\omega/F$, and it will therefore be the same for different pairs of numbers n and frequencies ω connected by the relation $z=\text{const}$:

$$\Psi_{u-\nu/F}^{\omega+\nu}=\Psi_n^{\omega}. \tag{16}$$

However, since the site number n is an integer, the above property is valid only for wave parameters ν satisfying the requirement

$$\nu=mF, m=0,\pm1,\pm2,... \tag{17}$$

Thus, without using the explicit form of the stationary solutions of equation (15), one can reach the conclusion that the spectrum of this equation has an infinite series of equidistant preferred frequencies (energies) with a distance between levels

$$\Delta\omega=F=\omega_B. \tag{18}$$

It is this series of frequencies that is associated with the Wannier–Stark ladder.

The agreement between the frequency difference (18) determining the height of a step in the Wannier–Stark ladder and the Bloch oscillation frequency (12) is not accidental,

since they reflect two sides of the same physical phenomenon. The relationship between the Wannier–Stark ladder and the Bloch oscillations has been discussed repeatedly in the literature, in particular in the more recent paper by Luban.[22]

But let us return to a systematic analysis of Eq. (10), which we rewrite in k space:

$$\Phi(k)=\sum_n \Psi_n \exp(-ikn). \tag{19}$$

We note that

$$\frac{\partial\Phi}{\partial k}=-i\sum_n n\Psi_n \exp(-ikn), \tag{20}$$

and therefore equation (14) can be rewritten in the form

$$i\frac{\partial\Phi}{\partial t}=\varepsilon(k)\Phi-iF\frac{\partial\Phi}{\partial k}. \tag{21}$$

We turn our attention to the fact that the last term in (21) arose from relation (20), where the sum on the right-hand side contains a factor n that increases at infinity. Therefore, the representation (20) has meaning (the infinite sum on the right-hand side converges) only under the condition that the wave function Ψ_n vanishes sufficiently rapidly as $|n|\to\infty$. Is that possible? We noted above that in the system under study there exists a series of discrete preferred frequencies. It is known that discrete levels correspond to localized states having the obvious property that $\Psi_n\to 0$ as $|n|\to\infty$. Since relation (20) has meaning only for such states, our further analysis of the solutions of equation (20) will pertain to the study of a set of solutions of the preferred set of frequencies (energies).

Turning to an analysis of these solutions, we make two remarks. First, since the wave vector $\Phi(k)$ in dimensionless units is periodic with period 2π, the quasiwave number k is equivalent to the angle variable φ $(0<\varphi<2\pi)$ specifying the state of a ''plane rotator.'' Therefore, the Schrödinger equation (5) studied here is equivalent to the equation of motion of a plane rotator, the dynamical features of which have relevance to the theory of Bloch oscillations.[23]

Second, the term $n\Psi_n$ in Eq. (14), which takes into account the presence of a uniform force field, corresponds to the term $i(\partial\Phi/\partial k)$ in Eq. (21), and this corresponds to the idea that the operator $n=i\partial/\partial k$ has the meaning of the number operator of the site (discrete coordinate) in a single-band model. Using the number operators for site n and the quasiwave number k in the k representation, it is easy to formulate the problem on a rigorous quantum level.

We write the Schrödinger equation (5) in the standard form

$$i\frac{\partial\Psi}{\partial t}=\mathcal{H}\Psi, \tag{22}$$

where the Hamiltonian operator in the k representation is written

$$\mathcal{H}=\varepsilon(k)-iF\frac{\partial}{\partial k}. \tag{23}$$

The role of the boundary conditions or quantization conditions in k space is played by the condition that the wave function $\Phi(k)$ be periodic with period 2π (in dimensional units, with the reciprocal lattice period $2\pi/\alpha$). This periodicity follows directly from definition (19).

According to the usual rules we obtain equations for the time derivatives of the operators k and n:

$$\frac{dk}{dt}=i[\mathcal{H},k]=F,\quad v=\frac{dn}{dt}=i[\mathcal{H},n]=\frac{d\varepsilon}{dk}, \tag{24}$$

where we have used the usual definition of the commutator: $[A,B]=AB-BA$.

Naturally the quantum relations (24) agree with the quasiclassical results of electronic theory (9) and (10), and it remains only to give these relations problem-specific content in the coordinate representation. It is clear that the general solution of equations (21) or (22) can be written as

$$\Phi(k,t)=Q(k-Ft)\exp\left\{-i\frac{E(k)}{F}\right\}, \tag{25}$$

where $Q(k)$ is an arbitrary differentiable function, and the following notation has been introduced for brevity:

$$E(k)=\int_0^k \varepsilon(q)dq=2\alpha k-W(k),\quad W(k)=2\alpha\sin k. \tag{26}$$

Formula (25) allows us to describe the evolution of an arbitrary initial distribution of the Fourier component, $\Phi_0(k)$ (at $t=0$):

$$\Phi(k,t)=\Phi_0(k-Ft)\exp\left\{\frac{i}{F}[E(k-Ft)-E(k)]\right\}. \tag{27}$$

We note that for $F=0$ formula (27) goes over to the obvious relation

$$\Phi(k,t)=\Phi_0(k)\exp(-i\omega t),$$

where the frequency ω is related to the wave number k by the dispersion relation (7) for $\Omega_0=0$ $(\omega=\varepsilon(k))$.

We see that the centroid of the packet (27) moves in k space with a velocity $dk/dt=F$, in agreement with the quasiclassical result (10).

Let us confirm the features of the discrete spectrum of eigenvalues of the stationary dynamical states. We write the Fourier time transform of solution (25):

$$\Phi^{\omega}(k)=\int \Phi(k,t)\exp(i\omega t)dt=\exp\left\{\frac{i}{F}[(\omega-2\alpha)k+W(k)]\right\}\int Q(z)\exp\left\{-i\frac{\omega z}{F}\right\}\frac{dz}{F}. \tag{28}$$

Since, as we have said, $\Phi(k)=\Phi(k+2\pi)$, the eigenvalue ω has the following spectrum:

$$\omega=2\alpha+mF,\quad m=0,\pm 1,\pm 2,... \tag{29}$$

We see that the spectrum of stationary states of the equation under study is discrete and infinite $(-\infty<m<\infty)$. This is the Wannier–Stark ladder. The distance between energy levels (29), equal to $\Delta\omega=F=\omega_B$, coincides with the Bloch oscillation frequency (12), thus confirming prediction (18).

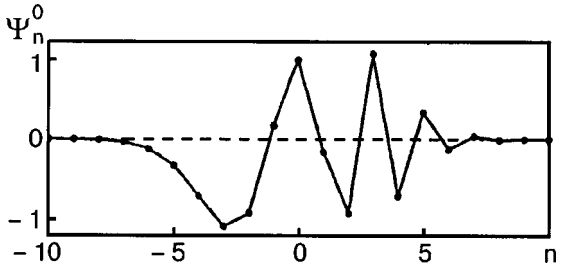

FIG. 2. Amplitude of the wave function of a stationary state localized near the site $m=0$ ($F=0.5\alpha$).

We write expressions for the eigenfunctions of the Wannier–Stark ladder:

$$\Phi^m(k)=A\exp\left\{i\frac{W(k)}{F}\right\}\exp(imk), \tag{30}$$

where the normalization coefficient A is conveniently chosen equal to 1.

In the site representation these states have the form

$$\Psi_n^m=\frac{1}{2\pi}\int\Phi^m(k)\exp(ikn)dk$$

$$=\frac{1}{2\pi}\int_{-\pi}^{\pi}\exp\left(i\frac{W(k)}{F}\right)\exp[i(m+n)k]dk. \tag{31}$$

It follows that the different states of the Wannier–Stark ladder have identical profiles shifted by an amount m along the chain: $\Psi_n^m=\Psi_{n+m}^0$. For an explicit description of the profile of these states we set $m=0$. Then

$$\Psi_n^0=\frac{1}{2\pi}\int_{-\pi}^{\pi}\exp\left(\frac{2\alpha i}{F}\sin k+ikn\right)dk=J_{-n}\frac{2\alpha}{F}, \tag{32}$$

where J_n is a zero-order Bessel function. The function J_{-n} describes the amplitude of a stationary state localized in the neighborhood of the site $m=0$. Figure 2 shows a plot of this function for $F=0.5\alpha$ in arbitrary scale. Since, according to (13), the potential falls linearly with increasing n, the left-hand side of the figure illustrates the total internal reflection of a particle due to the impossibility of penetrating into the region $n=-\infty$, and the right-hand side shows the effect of Bragg reflection from the Brillouin zone boundary, upon reaching which the velocity of the particle changes sign.

In the study of Bloch oscillations of wave packets the width of the packet turns out to be important. For this reason it is necessary to do a detailed treatment of the evolution of wave packets of different types in external fields. Let us first consider a wave packet with a rather narrow Fourier spectrum localized (for $t=0$) near $k=0$. Making use of this circumstance, we write $k-Ft=\xi$ and expand the argument of the exponential function in (27) in a series in powers of ξ, keeping only the first nonvanishing term:

$$E(k-Ft)-E(k)=-E(Ft)-\varepsilon(Ft)\xi. \tag{33}$$

Using this expansion, we rewrite (27) as

$$\Phi(k,t)=\Phi_0(\xi)\exp\left\{-i\frac{\varepsilon(F)}{F}\xi\right\}\exp\left\{-i\frac{E(Ft)}{F}\right\}. \tag{34}$$

We now return to the site representation. We treat the site index n as a continuous variable (this is admissible for a packet that is narrow in k space, since such a packet spans a large interval of sites in the coordinate representation). Then it follows from Eq. (8) that

$$\Psi_n(t)=\exp(iFnt)\Psi_{n-\delta n}(0)\exp\left\{-i\frac{E(Ft)}{F}\right\}, \tag{35}$$

where the shift δn in the site index corresponding to the maximum amplitude of the wave packet is given by the expression

$$\delta n=\frac{\varepsilon(Ft)}{F}. \tag{36}$$

It is this relation that describes the Bloch oscillations of the coordinate of the center of the wave packet:

$$n(t)=n(0)+\varepsilon(Ft)/F. \tag{37}$$

Let us examine the density distribution in the wave packet:

$$\rho_n(t)=|\Psi_n(t)|^2. \tag{38}$$

According to (28), the evolution of $\rho_n(t)$ reduces to a displacement of the center of the density distribution,

$$\rho_n(t)=\rho_{n-\delta n}(0). \tag{39}$$

At short times ($Ft\ll 1$) the particle/packet moves with a constant acceleration:

$$\delta n=\alpha Ft^2.$$

At long times the translational velocity of the packet is given by

$$v=\frac{dn}{dt}=2\alpha\sin(Ft). \tag{40}$$

Naturally expression (40) agrees with the quasiclassical formula (9) for $k=Ft$.

The density distribution $\rho_n(t)$ found numerically in Ref. 23 for the steady-state motion of the packet explicitly demonstrates its Bloch oscillations unaccompanied by any radiation (Fig. 3).

Obviously the given results are based on expansion (33) in which all powers of ξ except the first have been dropped. Consequently, they are the more accurate the narrower the k spectrum of the packet, i.e., the closer the state of the particle to a pure state corresponding to a definite k.

In the other limiting case, when the particle is initially localized at one site ($n=0$) and the Fourier spectrum is a plane wave ($\Phi_0(k)=1$), the dynamics of the Bloch oscillations is different.

Let us use expression (27) and, employing (8), return to the site representation:

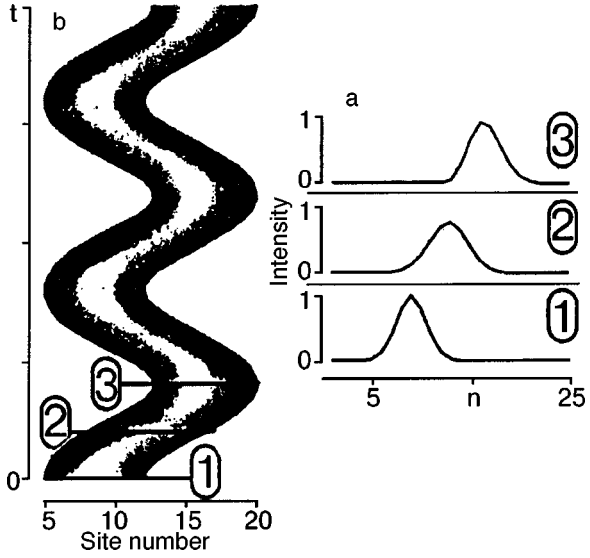

FIG. 3. Bloch oscillations of a rather wide wave packet in a uniform field (a). The distribution of intensities in the packet at three different times (b).

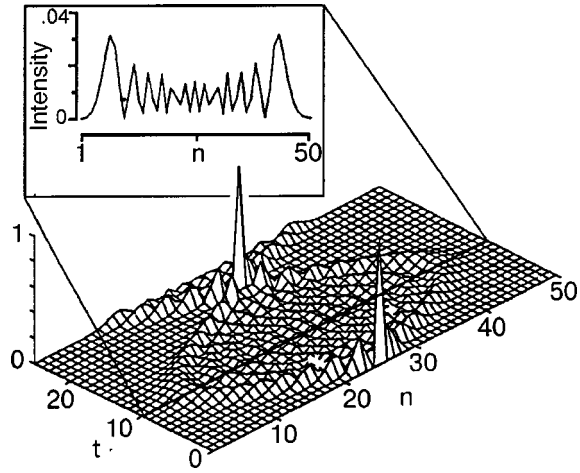

FIG. 4. Evolution of a narrow wave packet, demonstrating the alternating spreading and focusing of the packet. The inset shows the distribution of the field intensity at the time of its stopping and turning.

$$\Psi(n,t)=\frac{1}{2\pi}\exp(-2i\alpha t)\int_{-\pi}^{\pi}\exp\left\{\frac{2\alpha i}{F}[\sin k-\sin \times(k-Ft)]\right\}\exp(ikn)dk$$
$$=\exp(-2i\alpha t)J_{-n}\left[\frac{4\alpha}{F}\sin\frac{Ft}{2}\right]\exp\left\{i\frac{n}{2}(Ft-\pi)\right\}. \tag{41}$$

Using the properties of the Bessel functions, one can easily see that if the function $\Psi(n)$ is a solution of equation (14), then the function $(-1)^n\Psi^*(-n)$ is also a solution with the same profile (envelope) but describing an excitation that differs at neighboring sites by a phase jump equal to π. Consequently, the density produced by the solution (41) is an even function of the site index n counted from the center of localization:

$$\rho_n(t)=J_n^2\left(\frac{4\alpha}{F}\sin\frac{Ft}{2}\right). \tag{42}$$

This means that the excitation propagates symmetrically in the directions of increasing $(n>0)$ and decreasing $(n<0)$ potential. We recall that at small arguments the Bessel function has the form: $J_n(z)=(1/n!)(z/2)^n$ for $z\ll n$ $(n>0)$. The modulus of the function increases monotonically with increasing argument z and reaches a maximum at $z\approx n$, provided that $n\gg 1$. For $z\gg n$ the Bessel function is oscillatory and falls off in proportion to $z^{-1/2}$. In formula (41) the argument $z=(4\alpha/F)\sin(Ft/2)$ depends harmonically on time, reaching a maximum value $z_m=4\alpha/F$ at $t=t_m=\pi/F$. Therefore the evolution of the wave packet occurs as follows: at $t=0$ the particle is localized $(\Psi_n(0)=\delta_{n0})$, and as time goes on, the excitation propagates to the nearest-neighbor sites of the chain (to the left and right), and the maximum actually reaches a remote site $n\gg 1$ at $z\approx n$ (by which time the excitation in the central part of the chain will have fallen off, in an oscillatory manner, as $z^{-1/2}$). However, since $z\leqslant z_m$, the wave can propagate only to a distance $n\approx z_m$, reaching a maximum distance at $t=t_m$; at this time the argument z stops growing (a stopping point), and then the wave "falls back," gathering itself into the original pulse at the site $n=0$ at the time $t=2\pi/F$.

An order-of-magnitude estimate of the peak-to-peak amplitude of the oscillations can be made by calculating the mean-square deviation of the number of the site from the center in the course of the oscillations. It is sufficient to do the calculation for $m=0$, using formula (41) and the identity[24]

$$\sum_n n^2J_n^2(z)=\frac{1}{2}z^2, \tag{43}$$

after which trivial manipulations lead to the result

$$\langle n^2\rangle=\sum_n n^2\rho_n(t)=8\left(\frac{\alpha}{F}\right)^2\sin^2\left(\frac{1}{2}Ft\right). \tag{43a}$$

Averaging over time gives $\langle n^2\rangle=(2\alpha/F)^2$. Thus one indeed has $\langle n^2\rangle^{1/2}=z_m/2$. Figure 4 shows the results of a numerical integration of Eq. (14), which illustrate the oscillatory evolution of the wave packet.[1]

We conclude this Section by remarking that formulas (42) and (43a) admit passing the limit $F\to 0$, which corresponds to treating a quantum particle in the absence of external field. By taking this limit, one can write the several equations:

$$\rho_n=J_n^2(2\alpha t),\quad \langle n^2\rangle=2\alpha^2t^2. \tag{44}$$

We see that a free particle initially localized at the site $n=0$ moves away to infinity as time goes on. Using the aforementioned properties of the Bessel functions, we find that the maximum density ρ_n is observed at the site n $(n\gg 1)$ at the time $t_n\approx n/(2\alpha)$. This means that the translational velocity of the maximum of the distribution $n/t_n=2\alpha$ coincides with the maximum of the group velocity of the particle [see formula (9)].

1.2. Dynamical localization of a particle in an alternating field

The presence of a series of discrete Wannier–Stark frequencies in the spectrum of a particle in a uniform force field should be manifested in resonance phenomena when the particle is acted on by a force which is periodic in time. We assume that the uniform external force F includes a harmonic time-dependent component:

$$F \to F(t) = F_0 + F_1 g(t), \quad F_0, F_1 = \text{const}, \tag{45}$$

where in the simplest case

$$g(t) = \cos(\omega t + \theta). \tag{46}$$

It is clear that Eq. (21) remains valid in this case,

$$\frac{\partial \Phi(k)}{\partial t} + i\varepsilon(k)\Phi(k) = F(t)\frac{\partial \Phi(k)}{\partial k} \tag{47}$$

and the wave number k as before obeys the quasiclassical equation of motion (11). Consequently,

$$k(t) = k_0 + \int_0^t F(s)ds = k_0 + F_0 t + F_1 \int_0^1 g(s)ds.$$

Embarking on a quasiclassical analysis of the particle dynamics, we note that the velocity of the wave packet is determined by the expression $v = 2\alpha \sin k$. Having the simplest case in mind, we relate the constants of integration k_0 and θ by the condition $\omega k_0 = F_1 \sin\theta$. Then

$$v = 2\alpha \sin[F_0 t + (F_1/\omega)\sin(\omega t + \theta)]. \tag{48}$$

Using the properties of series of Bessel functions, we write

$$\begin{aligned} v = 2\alpha \Bigg\{ & \sin F_0 t \cos\left[\frac{F_1}{\omega}\sin(\omega t + \theta)\right] \\ & + \cos F_0 t \sin\left[\frac{F_1}{\omega}\sin(\omega t + \theta)\right]\Bigg\} = 2\alpha \Bigg\{ J_0\left(\frac{F_1}{\omega}\right)\sin F_0 t \\ & + 2\sum_{p=1}^{\infty} J_{2p}\left(\frac{F_1}{\omega}\right)\cos[2p(\omega t + \theta)]\sin(F_0 t) \\ & + 2\sum_{p=1}^{\infty} J_{2p-1}\left(\frac{F_1}{\omega}\right)\sin[(2p-1)(\omega t + \theta)]\cos(F_0 t)\Bigg\}. \end{aligned} \tag{49}$$

Since

$$\cos\theta_1 \sin\theta_2 = \frac{1}{2}[\sin(\theta_1 + \theta_2) - \sin(\theta_1 - \theta_2)],$$

for all $\omega \neq F_0$ the particle executes periodic Bloch oscillations at the fundamental Bloch frequency $\omega_B = F_0$, which is accompanied by an infinite series of satellites with frequencies $\omega_B \pm m\omega$, with $m = 1,2,3....$

A curious resonance arises at the frequency $\omega = \omega_B$, equal to the distance between steps of the Wannier–Stark ladder: a constant component of the particle velocity appears (the term with $m = 1$), the value of which is determined by the initial conditions:

$$v_0 = \alpha J_1(F_1/F_0)\sin\theta, \tag{50}$$

and the oscillatory component acquires a set of higher harmonics with frequencies $m\omega_B$.

If $F_1 \ll F_0$, then the velocity of the particle at resonance $(\omega = \omega_B = F_0)$ is

$$v = \alpha(F_1/F_0)\sin\theta + 2\alpha \sin(\omega_B t) + \alpha(F_1/F_0)\sin(2\omega_B t + \theta). \tag{51}$$

An analogous phenomenon in the physics of Josephson superconducting systems is called the Shapiro effect.[3]

The effect described above means that when a particle executing Bloch oscillations is acted on by a force with a sinusoidal time dependence, under resonance conditions $\omega = \omega_B$ the particle will drift with a certain constant velocity v_0. Consequently, the Bloch oscillations occur in a reference frame moving with a certain constant velocity v_0.

Let us now consider the effect of a purely sinusoidal alternating force (46) on the particle, setting $F_0 = 0$. For convenience in the calculation we choose $\theta = 0$ and $k_0 = \pi/2$. Then in place of Eqs. (48) and (49) we have

$$\begin{aligned} v = & 2\alpha \cos\left[\frac{F_1}{\omega}\sin(\omega t + \theta)\right] = 2\alpha J_0\left(\frac{F_1}{\omega}\right) \\ & + 4\alpha \sum_p J_{2p}\left(\frac{F_1}{\omega}\right)\cos(2p\omega t). \end{aligned} \tag{52}$$

Relations (52) pertain to a situation which is in a certain sense the reverse of that described by formula (51), namely: for an arbitrary ratio F_1/ω the particle velocity has a constant component equal to $2\alpha J_0(F_1/\omega)$. However, if the ratio F_1/ω coincides with a zero of the function $J_0(z)$, then the constant component vanishes. It is said that a *dynamical localization* of the particle by the alternating field occurs.[26] This resonance phenomenon is unusual in that the condition for it is the coincidence of the frequency and amplitude of a force that is alternating in time (but uniform in space).

The time dependence of the mean-square displacement of the center of the packet (Fig. 5) and of the probability of finding the excitation at the initial site of localization (Fig. 6) beautifully illustrates the dependence of the dynamics of the packet on the ratio F_1/ω and shows that the coincidence of F_1/ω with a root of the function $J_0(z)$ is indeed a special condition.

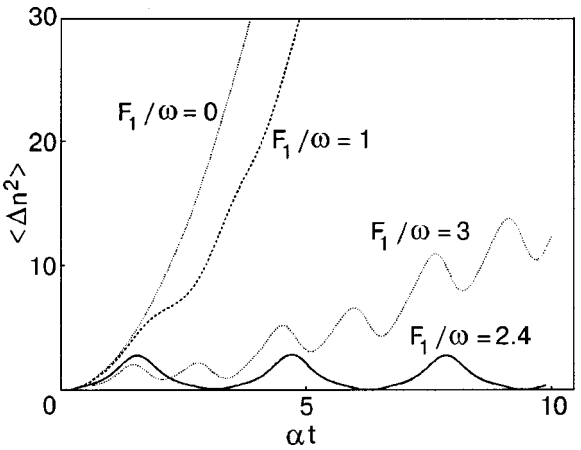

FIG. 5. Time dependence of the mean-square displacement of the center of a packet for different ratios F_1/ω.

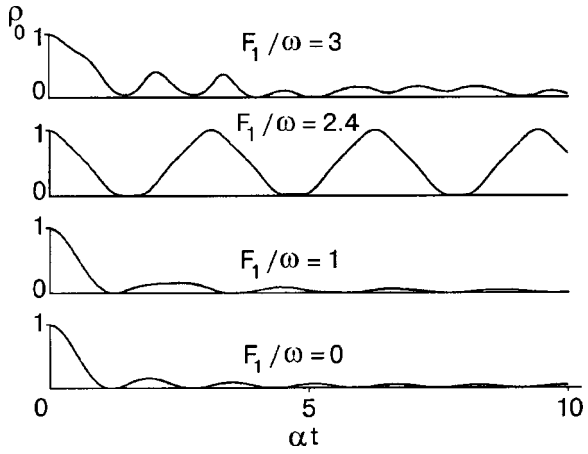

FIG. 6. Probability of finding an excitation at the initial site of localization as a function of time for different F_1/ω.

Naturally, the dynamical localization effect can be described rigorously by analyzing the distribution of the density ρ_n and the mean-square deviation $\langle u^2\rangle$ of the particle from the initial position at the site $n=0$. For this it is convenient to write the solution of equation (47) like (27) but in different independent variables. Together with t we introduce the variable

$$q=k+\int_0^t F(s)ds,$$

having defined a new function $C(q,t)=\Phi(k,t)$. Then Eq. (47) is transformed to

$$i\frac{\partial C}{\partial t}=\varepsilon[q-\eta(t)]C, \tag{53}$$

$$\eta(t)=\int F(s)ds. \tag{54}$$

The solution of equation (53) has a form analogous to (25), viz.,

$$C(q,t)=Q(q)\exp\left\{-i\int_0^t \varepsilon[q-\eta(s)]ds\right\}. \tag{55}$$

Returning to the original variables, we obtain an analog of formula (27):

$$\Phi\left(k,t\right)=\Phi_0\left[k+\eta\left(t\right)\right]\times\exp\left\{-i\int_0^t\varepsilon\left[k+\eta\left(t\right)-\eta\left(s\right)ds\right\}\right\}, \tag{56}$$

where $\Phi_0(k)$ is the initial Fourier component (at $t=0$).

We write (56) in explicit form, using the definition of ε in (7):

$$\Phi(k,t)=\Phi_0[k+\eta(t)]\exp(-2i\alpha t)\times\exp\left\{-2i\alpha\int_0^t\cos[k+\eta(t)-\eta(s)]ds\right\}. \tag{57}$$

We must now pass to the site representation and construct the density $\rho_n(t)$. This procedure is extremely awkward and requires the use of several theorems concerning the properties of series of Bessel functions. It is set forth in the appendix of Ref. 27, and here we just give the results:

$$\rho_n(t)=J_m^2\{2\alpha[u^2(t)+w^2(t)]^{1/2}\}, \tag{58}$$

where $u(t)$ and $w(t)$ are given by the relations

$$u(t)=\int_0^t\cos[\eta(s)]ds,\quad w(t)=\int_0^t\sin[\eta(s)]ds. \tag{59}$$

Using Eq. (43), we obtain the mean-square displacement of the particle in the course of the oscillations:

$$\langle n^2\rangle=2\alpha^2[u^2(t)+w^2(t)]. \tag{60}$$

Formula (59) is valid for any time dependence of the external force. However, we are primarily interested in the simplest case of a sinusoidal force (46). For $F=0$ relation (59) gives

$$u(t)=\frac{1}{\omega}\int_0^{\omega t}\cos\left[\left(\frac{F_1}{\omega}\right)\sin\tau\right]d\tau;$$

$$w(t)=\frac{1}{\omega}\int_0^{\omega t}\sin\left[\left(\frac{F_1}{\omega}\right)\sin\tau\right]d\tau. \tag{61}$$

Let us examine the behavior of the functions $u(t)$ and $w(t)$. Whenever $\omega t=2\pi m$, where m is an integer, we have

$$u_m=(2\pi m/\omega)J_0(F_1/\omega)=t_mJ_0(F_1/\omega),\quad \omega(t_m)=0.$$

Thus the oscillatory function $w(t)$ is bounded for all t, while the function $u(t)$, on average, increases with time for $t\gg 2\pi/\omega$, executing oscillations of finite amplitude $\delta u=u-\langle u\rangle$ about the mean value. At long times one can leave out all but the monotonically increasing function $u(t)\approx tJ_0(F_1/\omega)$ in formulas (58) and (60), in which case it turns out that

$$\rho_n(t)=J_n^2[2\alpha tJ_0(F_1/\omega)],\langle n^2\rangle=2[\alpha tJ_0(F_1/\omega)]^2,\quad t\gg 2\pi/\omega. \tag{62}$$

We note that expression (62) is analogous to formulas (43a), which describe the evolution of the state of a free particle (in the absence of external field). If we introduce the effective intersite transition parameter for a particle in a sinusoidal alternating field, $\alpha_{\text{eff}}=\alpha J_0(F_1/\omega)$, then formula (62) can be rewritten like (43a):

$$\rho_n=J_n^2(2\alpha_{\text{eff}}t),\ \langle n^2\rangle=2\alpha_{\text{eff}}{}^2t^2,\ t\gg 2\pi/\omega. \tag{63}$$

As a result, we have arrived at the conclusion that a sinusoidal external field does not affect the free-particle delocalization process but only renormalizes the rate of delocalization. However, this conclusion is valid only in a general situation, i.e., for some undistinguished value of F_1/ω. If this ratio coincides with a zero of the function $J_0(z)$, then formulas (62) and (63) lose meaning. The functions $u(t)$ and $w(t)$ are now bounded periodic functions, and the finite value of $\langle n^2\rangle$ signifies dynamical localization of the particle.

1.3. The Hamiltonian dynamics of a soliton of the nonlinear Schrödinger equation on a lattice

In the context of our discussion it is natural to turn to a study of the dynamics of particlelike solutions (solitons) of

nonlinear discrete equations. Among the simplest of those which have been well studied from the standpoint of soliton dynamics is the nonlinear Schrödinger partial differential equation. It is a completely integrable equation, and the soliton dynamics of the nonlinear Schrödinger equation (NSE) has been described in detail both for the free motion of the soliton (see, e.g., Ref. 28) and for its motion in an external field.[29] The transition from the continuous to the discrete form of the nonlinear Schrödinger equation is nonunique. If one starts from a model of the tight-binding type, then a nonlinear term $g|\Psi_n|^2\Psi_n$ should be added to Eq. (5). Then, setting $\alpha=1$, one would have the following equation:

$$i\frac{\partial\Psi_n}{\partial t}=2\Psi_n-\Psi_{n+1}-\Psi_{n-1}-2g|\Psi_n|^2\Psi_n. \tag{64}$$

It is an analog of this form that is used in the nonlinear optics of a system of parallel optical waveguides.[30] Unfortunately, Eq. (64) is not completely integrable and does not have exact soliton solutions like the soliton of the continuous NSE. However, there is an exactly integrable version of the nonlinear Schrödinger equation on a lattice:[31,32]

$$i\frac{\partial\Psi_n}{\partial t}=(\Psi_{n+1}+\Psi_{n-1})(1+|\Psi_n|^2)+\Omega\Psi_n. \tag{65}$$

The frequency shift $\Omega=\Omega_0+2$ used in (65) is unimportant, and we write it for consistency with Ref. 33, where this equation is discussed from the point of view of interest to us here.

If $\Omega=\text{const}$, then the linearized equation is characterized by a dispersion relation of the type (8):

$$w=\Omega+\varepsilon(k),\quad \varepsilon(k)=-2\cos k. \tag{66}$$

Equation (65) has two additive integrals of motion:

$$N=\sum_n \ln(1+|\Psi_n|^2), \tag{67}$$

which plays the role of the norm of the wave function, and

$$\mathcal{H}=E+\Omega N,\quad E=-\sum_n(\Psi_n\Psi^*_{n+1}+\Psi^*_n\Psi_{n+1}). \tag{68}$$

The latter can be regarded as the energy, or Hamiltonian, of the system. However, the Hamiltonian (68) generates equation (65) according to the usual definition

$$\frac{\partial\Psi_n}{\partial t}=\{\mathcal{H},\Psi_n\}$$

with the Poisson brackets defined in a nonstandard way:

$$\{\Psi_m,\Psi^*_n\}=i(1+|\Psi_n|^2)\delta_{mn},$$

$$\{\Psi_m,\Psi_n\}=\{\Psi^*_m,\Psi^*_n\}=0. \tag{69}$$

Naturally, in a uniform chain, owing to the translational periodicity, there exists an obvious symmetry connected with displacement by a lattice period, i.e., with the transition $n\to n+1$. We denote the corresponding translation operator by T:

$$T\Psi_n=\Psi_{n+1}.$$

Its eigenfunctions $\exp(ikn)$ correspond to the eigenvalues $\exp(ik)$ ($-\pi<k<\pi$, where k is the quasiwave number).

The operator T generates an additional additive integral of motion $\Sigma_n\Psi^*_nT\Psi_n$, which is conveniently represented in the form

$$S=-i\sum_n[\Psi^*_n(\Psi_{n+1}-\Psi_n)-\Psi_n(\Psi^*_{n+1}-\Psi^*_n)]$$

$$=-i\sum_n\Psi^*_n\Psi_{n+1}-\Psi_n\Psi^*_{n+1}$$

$$=-i\sum_n\Psi^*_n(\Psi_{n+1}-\Psi_{n-1}). \tag{70}$$

The quantity $j_n=-i[\Psi^*_n(\Psi_{n+1}-\Psi_n)-\Psi_n(\Psi^*_{n-1}-\Psi^*_n)]$ in a discrete chain is an analog of the flux density of particles in a continuous medium. Therefore S has the meaning of the total momentum in the excited chain. Let us consider a stationary solution of equation (65) of the type $\Psi_n(t)=\Phi^\omega_n(t)\exp(ikn-i\omega t-i\theta)$, where $\Phi^\omega_n(t)$ is a real function and θ is an arbitrary constant phase. The function Φ_n and the relation between ω and k are determined by two real equations:

$$(\Omega_0-\omega)\Phi_n=\cos k(\Phi_{n+1}+\Phi_{n-1})(1+\Phi^2_n), \tag{71}$$

$$\frac{\partial}{\partial t}\ln(1+\Phi^2_n)=-2\sin k\,\Phi_n(\Phi_{n+1}-\Phi_{n-1}). \tag{72}$$

Soliton solutions correspond to a function Φ_n that vanishes at infinity: $\Phi_n=0$ for $n\to\pm\infty$.

The integrals of motion N, E, and S depend on both the function Φ_n and on k:

$$N=\sum_n\ln[1+\Phi^2_n], \tag{73}$$

$$E=-2\cos k\sum_n\Phi_n\Phi_{n+1}, \tag{74}$$

$$S=2\sin k\sum_n\Phi_n\Phi_{n+1}. \tag{75}$$

Let us consider small variations of the integrals of motion due to small variations of the wave vector Ψ, i.e., to small variations of Φ_n and small variations of the wave number k. It follows from (71) and (73) that

$$(\Omega-\omega)\delta N=\cos k\sum_n(\Phi_{n+1}+\Phi_{n-1})\delta\Phi_n. \tag{76}$$

Similarly, from (74)–(76) and (68) we obtain

$$\delta\mathcal{H}=\omega\delta N+S\delta k. \tag{77}$$

We see that the parameters ω and k of the solution are related by the Hamilton's dynamical equations:

$$\omega=\frac{\partial\mathcal{H}}{\partial N}=\Omega+\frac{\partial E}{\partial N},\quad S=\frac{\partial\mathcal{H}}{\partial k}=\frac{\partial E}{\partial k}, \tag{78}$$

if the Hamiltonian is considered as a function of the independent variables N and k: $\mathcal{H}=\mathcal{H}(N,k)$.

If Eq. (65) has a stationary localized solution that moves along the chain at a velocity V, one would expect that, in analogy to the situation for the continuous nonlinear Schrödinger equation, its real amplitude will have the form

$$\Phi_n(t)=\Phi(n-Vt). \tag{79}$$

On this basis the following solution was proposed in Ref. 33:

$$\Phi(x)=A\ \ \mathrm{cn}[\beta(x-x_0,\kappa)], \tag{80}$$

where $A=\mathrm{const}$ and $\mathrm{cn}(z,\kappa)$ is the Jacobi elliptic cosine, the parameter κ of which lies in the interval $(0<\kappa<1)$. For $\kappa\ll 1$ the elliptic cosine goes over to the trigonometric cosine and Eq. (80) goes over to the solution of the linear equation. In the opposite limiting case $(\kappa\to 0)$ the transition is $\mathrm{cn}(z,\kappa)\to 1/\cosh(z)=\mathrm{sech}(z)$, and we have the solution

$$\Psi_n(t)=\sinh(\beta)\mathrm{sech}[\beta(n-Vt-x_0)]\exp(ikn-i\omega t+i\theta), \tag{81}$$

where $\chi_0,\theta=\mathrm{const}$, and the parameters β, V, ω, and k are related by the formulas

$$\omega=\Omega-2\cosh(\beta)\cos k \tag{82}$$

and

$$V=(2/\beta)\sinh(\beta)\sin k. \tag{83}$$

If the soliton solution in fact has the form (81), then the integrals of motion are invariant with respect to continuous translations, and they can therefore be calculated by replacing the sums in (73)–(75) by integrals: $\Sigma_n\ldots=\int dn\ldots$. Then it turns out that

$$N=2\beta,\ \ E=-4\sinh(\beta)\cos k,\ \ S=4\sinh(\beta)\sin k. \tag{84}$$

Consequently, three of the four parameters β, V, ω, and k are determined by fixed integrals of the motion, and the fourth (the quasiwave number k) remains free. We see that the soliton width $\lambda=1/\beta$ is determined solely by N, while the soliton energy and velocity are periodic functions of k (as in a uniform periodic structure).

It is clear that relation (42) follows from the first of the Hamilton's equations (78), while the second of the Hamilton's equations, together with (83), leads to the conclusion that

$$S=NV. \tag{85}$$

The result (85) agrees completely with the representation of S as the total momentum.

The presence of relation (85) makes it possible to put the Hamiltonian formulas (77) and (78) into a more customary form. We introduce in place of k the new independent variable $P=Nk$ (the total quasimomentum of the excited chain) and assume that the new Hamiltonian ε is a function of the independent variables P and N $[\varepsilon(N,P)=\mathcal{H}(N,P/N)]$. Then formulas (77) and (78) become

$$\delta\varepsilon=(\omega-kV)\delta N+V\delta P,$$

$$\omega-kV=\frac{\partial\varepsilon}{\partial N},\quad V=\frac{\partial\varepsilon}{\partial P}, \tag{86}$$

where $\omega-kV$ is the soliton frequency in a coordinate system moving with velocity V.

Let us return to the periodic dependence of the soliton velocity on k, which can cause Bloch oscillations of the soliton in a nonuniform chain, where the quasiwave number k is not conserved. We assume that the lower boundary of the spectrum of small oscillations, i.e., the quantity Ω, varies weakly along the chain: $\Omega=\Omega_n$. At small intervals of chain length this dependence can be assumed linear:

$$\Omega=\Omega_n\equiv\Omega_0+\eta n, \tag{87}$$

where we have introduced a small gradient η of the function Ω_n. The Hamiltonian generating an equation of the type (65) with $\Omega=\Omega_n$ has the form[33]

$$\mathcal{H}=E+\sum_n\ \Omega_n\ln(1+|\Psi_n|^2)=E+\Omega_0 N$$

$$+\eta\sum_n\ n\ln(1+|\Psi_n|^2), \tag{88}$$

where the last term describes the nonuniform potential in the field of which the soliton is moving.

Using the representation $\Psi_n=\Phi_n^\omega\exp[i(kn-\omega t-\Omega_0 t)]$, we write an equation that generalizes (71):

$$(\eta n-\omega)\Phi_n^\omega=\cos k(\Phi_{n+1}^\omega+\Phi_{n-1}^\omega)[1+(\Phi_n^\omega)^2]. \tag{89}$$

As regards the solution of equation (89), we can repeat what we said in the case of Eq. (11): the solution of equation (89) is a function of the single variable $z=n-\omega/\eta$, and it therefore will be the same for different pairs n,ω satisfying the requirement $z=\mathrm{const}$. This can occur under the following condition, analogous to (13):

$$\omega=m\eta,\ \ m=0,\pm 1,\pm 2. \tag{90}$$

Consequently, among the solutions of equations (72) and (89) is a system of oscillatory stationary solitons—a series of solutions corresponding to the Wannier–Stark ladder (90). These solutions can be represented as

$$\Psi_n^m=\Phi_{n-m}\exp[ik(n-m)-i(\Omega_0+m\eta)t]. \tag{91}$$

The solitons of this series with different numbers m have the same profiles with centers shifted by m sites.

Further analytic calculations require knowledge of the explicit solution of equations (72) and (89). In Ref. 33 exact solutions are given for the particular case (87). However, we would like to set forth an approximate method of analysis that might also be used for more complicated potentials Ω_n.

If the gradient η is small, then such a solution can be found in the so-called adiabatic approximation, which is well proven in the case of continuous systems. If $\eta\ll\Omega_0$, then the soliton is sensitive only to the constant local value of Ω_n at the point where its center is located. We can therefore assume that the shape of the soliton is, as before, described by a solution of the type (81) in which the parameters k and V are weakly time dependent. Setting $m=0$ in (91), we write

$$\Psi_n^0=\Phi(n-X(t))\exp[i(kn-\varphi(t)-\Omega_0 t)], \tag{92}$$

where $X(t)$ is the coordinate of the center of the soliton, and the soliton velocity V and frequency ω are obviously given by

$$V=dX/dt,\ \ \omega=d\varphi/dt.$$

Let us first convince ourselves that the nonuniform potential [the last term in (88)] leads to nonconservation of the total momentum S and determines the equation of motion of the quasiwave number k. Starting from (75), we calculate the time derivative of S:

$$\frac{dS}{dt}=|\mathcal{H},S|=\eta\sum_n n[\Psi_n^*(\Psi_{n+1}+\Psi_{n-1})+\Psi_n(\Psi_{n+1}^*+\Psi_{n-1}^*)].$$

Substituting (91) into this equation and changing from a sum to an integral, we obtain

$$\frac{dS}{dt}=2\eta\cos k\int_{-\infty}^{+\infty}n\Phi(n)[\Phi(n+1)-\Phi(n-1)]dn. \tag{93}$$

Keeping only the leading terms in the expansion in η, we can use on the right-hand side of (93) the solution of equations (72) and (89), where $\Omega=\Omega_0=\text{const}$. Taking (72) into account and noting that $\partial\Phi/\partial t=-V(d\Phi/dn)$, we obtain

$$\frac{dS}{dt}=\eta\cot(kV)\int_{-\infty}^{+\infty}n\frac{d}{dn}\ln(1+\Phi_n^2)dn=-\eta\cot(kVN). \tag{94}$$

On the right-hand side of (94) in accordance with (85) we have $VN=S$. In addition, it is clear that the nonuniformity of Ω_n does not affect the conservation of N as an integral of motion, and therefore equation (94) simplifies to

$$\frac{dV}{dt}=-\eta\cot(kV).$$

Finally, we use the relation of the velocity and wave number (83) and arrive at the final equation

$$\frac{dk}{dt}=-\eta. \tag{95}$$

Consequently, as in the previous Sections, the quasiwave number of the soliton in a uniform external field depends linearly on time, while the soliton velocity oscillates with a frequency $\omega_B=\eta$.

The amplitude of the oscillations is determined directly from the energy conservation law (88) in the adiabatic approximation. We transform the nonuniform potential in (88) as

$$U(X)=\eta\int n\ln[1+\Phi^2(n-X)]dn, \tag{96}$$

where the function $\Phi(n)$ in the given approximation is determined by formula (80) or (81). If we take into account that in this approximation $\Phi(\xi)=\Phi(-\xi)$, then

$$U(X)=\eta NX(t). \tag{97}$$

Thus it turns out that the total energy (88) can be represented in the form

$$\varepsilon=E(N,P/N)+\Omega_0N+\eta N \tag{98}$$

and can be treated as a function of the three independent variables N, P, and X. Since in the sum (98) only $P=Nk$ and X are time-dependent, the time derivative of the wave number (95) plays the role of one of the Hamilton's canonical equations:

$$\frac{dP}{dt}=-\frac{\partial\varepsilon}{\partial X},\quad \frac{dX}{dt}=\frac{\partial\varepsilon}{\partial P}. \tag{99}$$

Later we shall see that dynamical equations of the Hamilton type (99) also arise in the theory of magnetic solitons.[18,19]

Using the explicit expression (84) for $E(N,k)$ and Eq. (97), we obtain from the condition $\mathcal{H}=\text{const}$ the following time dependence of the soliton coordinate:

$$X(t)=X(0)+\frac{4\sinh(N/2)}{\eta N}[\cos k(t)-\cos k(0)], \tag{100}$$

where the time dependence of k is given by Eq. (90):

$$k(t)=k(0)-\omega_Ht,\omega_H=\eta. \tag{101}$$

The amplitude of the spatial oscillations of the soliton is

$$\Delta X=4\sinh(N/2)/(\eta N). \tag{102}$$

It is inversely proportional to η and increases sharply with increasing N. The oscillations of the soliton velocity can be determined directly using (99) or by differentiating (100) with respect to time:

$$V=\frac{dX}{dt}=\frac{4\sinh(N/2)}{N}\sin k(t). \tag{103}$$

The amplitude of the soliton velocity (103) is independent of η.

It is of interest to examine the following formula in the linear limit $N\to 0$. In the case $k(0)=0$ formula (99) reduces to

$$X(t)=X(0)+(2/\eta)\cos\eta t=X(0)-\varepsilon(\eta t)/\eta, \tag{104}$$

where the function $\varepsilon(k)$ is determined by formula (66). It is easy to see that Eq. (104) is analogous to (37) (we note that F and η, by definition, have different signs).

For $\alpha=1$ formula (103) goes over to $V=-2\sin(\eta t)$, an expression analogous to (40).

Equations (98) and (86) could be used to find the oscillations of the soliton frequency ω. However, it is simpler to adopt the expression given in Ref. 33 for the phase $\varphi(t)$, which determines the explicit form of the oscillatory soliton under discussion:

$$\Psi_n^0=\sinh\beta\,\text{sech}[\beta(n-x(t))]\exp(-i\varphi(t)-\Omega_nt), \tag{105}$$

$$\varphi(t)=-(4/\eta)\cosh(N/2)\sin k(t). \tag{106}$$

Naturally, there exists an infinite series of oscillatory solitons, corresponding to the Wannier–Stark ladder ($m\neq 0$). In fact, by substituting (106) into (91), we obtain in place of (92) the general expression

$$\Psi_n^M=\Phi[n-m-X(t)]\exp\{i[kn-\varphi(t)-\Omega_0t]\}, \tag{107}$$

which demonstrates the presence of a series of identical solutions with displaced centers.

The numerical integration of Eq. (64) in the case of a uniform field (87) which was done in Ref. 33 beautifully illustrates the Bloch oscillations of the soliton. Figure 7 shows the oscillations of the soliton for arbitrary signs of the initial velocities. For comparison we present calculations of the evolution of a soliton of the standard discrete NSE (64) in a uniform field (Fig. 8). Although one can speak of oscillatory motion of the soliton, one can readily see that it decays rather rapidly as a consequence of the absence of complete integrability of Eq. (64).

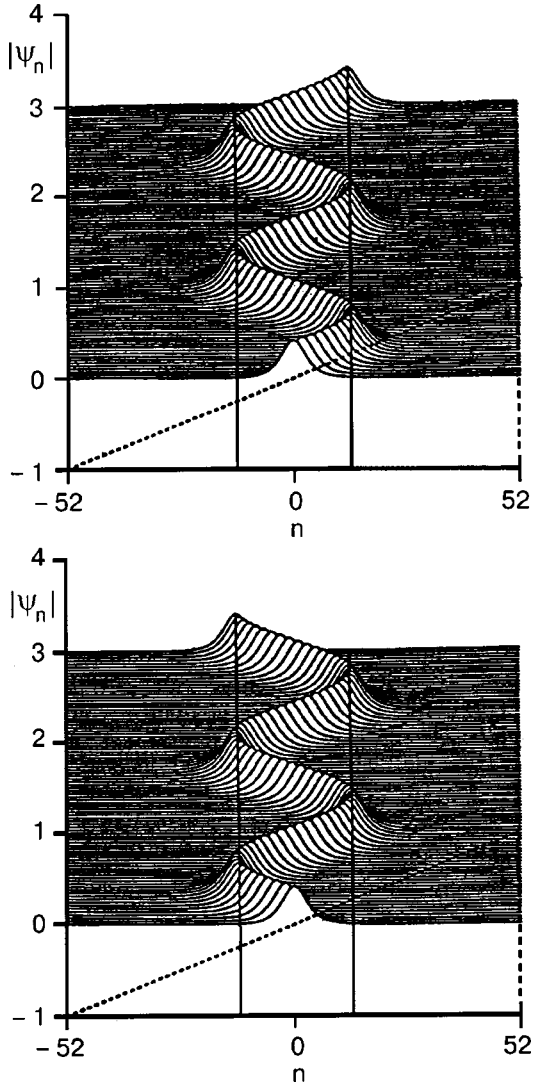

FIG. 7. Bloch oscillations of a soliton in a uniform field for initial velocities of opposite sign (the dotted line is a graph of the potential). The vertical lines indicate the positions of the turning points.

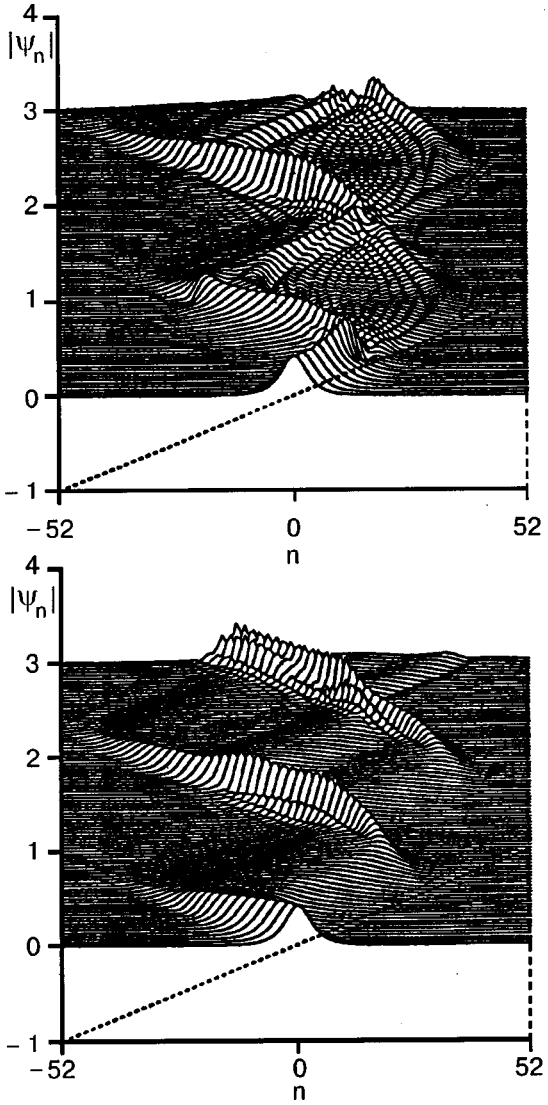

FIG. 8. Stage of decay of a localized (solitonlike) excitation in the case of nonintegrable dynamics in a uniform field; the dotted line shows a graph of the potential.

Finally, that same paper[33] investigated the evolution of the two-soliton dynamics (Fig. 9), which is reminiscent of the process of periodic splitting and subsequent collapse of the wave packet of the linear discrete equation (see Fig. 4).

The peculiar behavior of the soliton under the influence of an external force is manifested particularly in a highly nonuniform field. Its motion in a wide potential well is reminiscent of the oscillatory motion of an ordinary particle in a potential well: a natural bounded motion with two turning points. The soliton dynamics is unusual in that the soliton has this same kind of motion on a potential hump, from which an ordinary particle slides off in an accelerated manner, while a soliton executes oscillatory motion about its crest (Fig. 10). This is a manifestation of the unusual properties of a particle with a periodic dispersion relation (in k space) moving in a highly nonuniform external field (see Appendix).

The theory of Bloch oscillations of a soliton of the discrete NSE in a static uniform field (87) can be generalized to the case of a uniform field with harmonic time dependence of the type (46), when the time dependence of the gradient η in formula (87) has the form

$$\eta = \eta_1 \cos \omega t, \quad \eta_1 = \text{const}. \tag{108}$$

The results of a generalization of the theory set forth above to the case of a uniform field with harmonic time dependence turned out to be analogous to our generalization to dynamical localization of the wave packet of the linear Schrödinger equation. Of course the corresponding formulas for the Bloch oscillations in this case will be more complicated, but nevertheless the situation is qualitatively similar to the linear theory. Here we give only a summary of that study, referring the reader to Ref. 13 for the details.

The dynamical characteristics of a soliton, including the coordinate of its center, are expressed as before in the form of series of Bessel functions of the type (52), with F_1 replaced by η_1. If the ratio η_1/ω coincides with a zero of the Bessel function $J_0(z)$, which is in a certain sense a condition of parametric resonance, then the dynamical localization of the soliton is exactly the same as in the previously considered case of localization of a wave packet in a discrete linear chain.

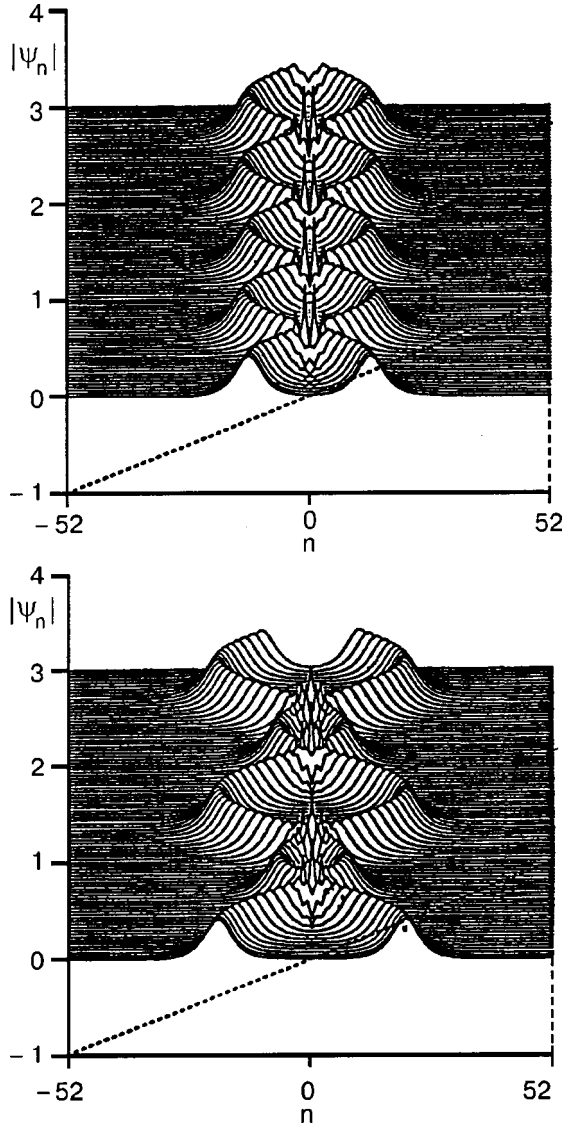

FIG. 9. Reciprocating motion of a pair of solitons in a uniform field (the dashed line is a graph of the potential), reminiscent of the motion of a packet of waves of the linear equation (see Fig. 4).

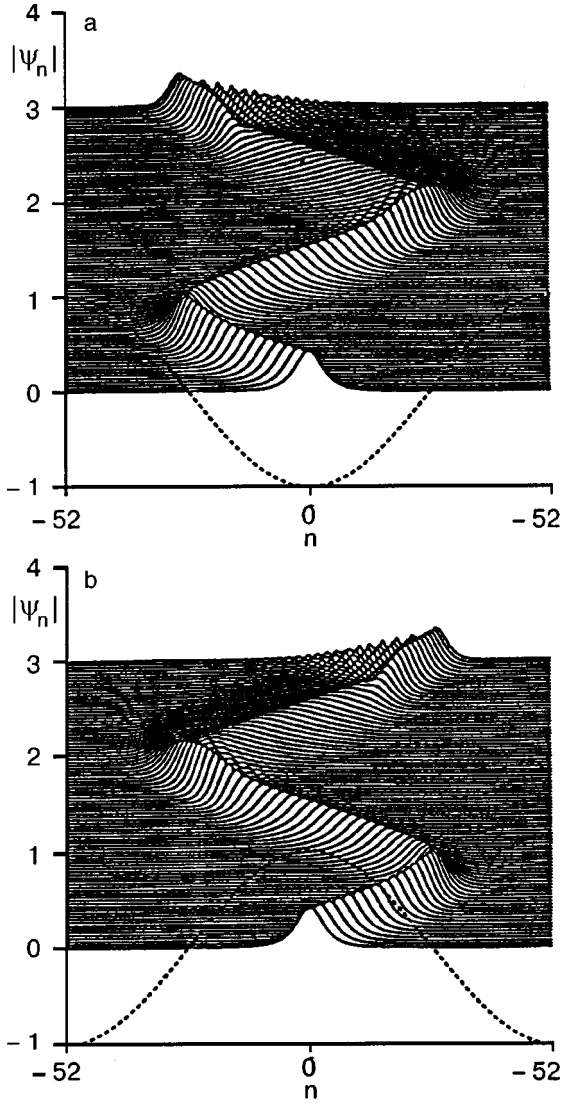

FIG. 10. Oscillatory motion of a soliton: in a potential well (dashed curve) (a), near a potential hump (dashed curve) (b).

An example of the evolution of the investigated system under resonance conditions is shown in Fig. 11, which is taken from Ref. 13. The wave function at the initial time ($t=0$) is taken in the form of a combination of an infinitesimally narrow wave packet, proportional to the Kronecker delta δ_{n0}, and a soliton packet localized near the site $n=n_0=50$, the soliton width Δn being taken small in comparison with the distance to the δ-function packet ($\Delta \ll n_0$). As time goes on, the narrow packet, as in the linear problem, splits into two packets which move in opposite directions at the beginning of the cycle and generate tails of low-amplitude radiation. Having reached a certain maximum peak-to-peak amplitude of oscillation the pair of narrow wave packets "falls back," collecting into a δ function by the end of the period. The soliton interacts noticeably with radiation in the region where radiation is present, but it recovers its form completely upon leaving this region, and it executes regular periodic oscillations.

If the resonance conditions are not satisfied ($\eta_0 \neq \omega$) then one observes a deviation from the strictly cyclical regime which increases linearly with time (as should be the case as one departs from a condition of parametric resonance) (Fig. 12). The deviation from the resonance picture is manifested in the fact that the pair of narrow wave packets

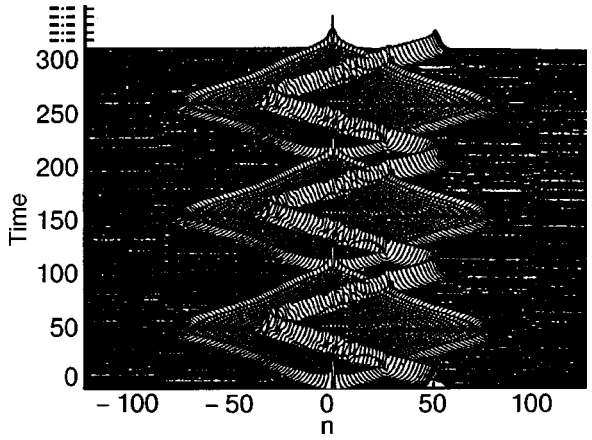

FIG. 11. Interaction of an extremely narrow packet located at the site $n=0$ at $t=0$, and the soliton in a uniform field under resonance conditions.

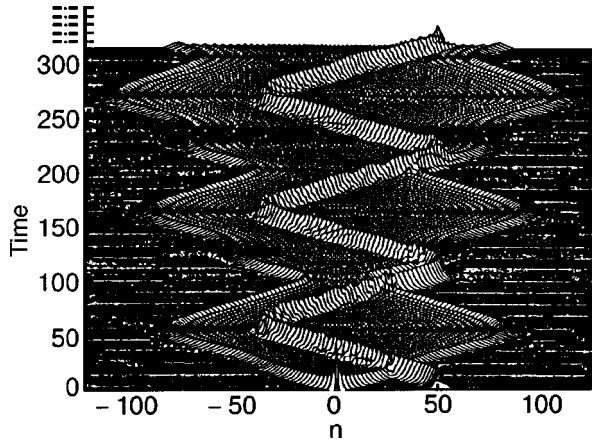

FIG. 12. Growth of the amplitude of oscillations of a narrow packet in a uniform field if the resonance condition is not satisfied ($\eta_0 \neq 0$). The soliton executes Bloch oscillations.

moves apart with time and the packets are damped, generating ripples of low-amplitude oscillations. However, the soliton survives and executes Bloch oscillations as a particle.

2. BLOCH OSCILLATION OF MAGNETIC SOLITONS

2.1. Basic principles of the theory of ferromagnetism and the quasiclassical quantization of magnetic solitons

The main idea of the macroscopic theory of ferromagnetism is that the state of a magnet is uniquely characterized by the magnetization vector **M**. Thus the dynamics and kinetics of a ferromagnet are dictated by changes in its magnetization. The magnetization as a function of the coordinates and time, $\mathbf{M}(\mathbf{x},t)$ is a solution of the phenomenological Landau–Lifshitz equation:[34,35]

$$\frac{\partial \mathbf{M}}{\partial t} = -\frac{2\mu_0}{\hbar}\mathbf{M}\times\mathbf{H}_{\text{eff}} - \gamma\mathbf{M}\times(\mathbf{M}\times\mathbf{H}_{\text{eff}}), \tag{109}$$

where μ_0 is the Bohr magneton and γ is the relaxation constant, which governs the precessional damping of the vector **M**. The effective magnetic field $\mathbf{H}_{\text{eff}}$ is defined as the variational derivative of the energy of the ferromagnet with respect to the vector **M**:

$$\mathbf{H}_{\text{eff}} = -\delta E/\delta \mathbf{M}. \tag{110}$$

It is assumed that the energy of the magnet is a functional of the magnetization **M** and its spatial derivatives:

$$E = \int w\{\mathbf{M}, \partial\mathbf{M}/\partial x_k\} d^3x, \tag{111}$$

where i and k are coordinate indices ($i,k=1,2,3$).

Taking the energy dissipation into account as proposed in (109) is entirely sufficient in the case of a uniform or slightly nonuniform distribution of the magnetization. For describing the energy loss of highly nonuniform dynamical states it is necessary to take into account effects which are analogous to the viscosity in hydrodynamics and depend on the gradients of the magnetization. In the simplest case one should add to the right-hand side of Eq. (109) a term due to a dissipative function of the form[36,37]

$$F = \frac{1}{2}\gamma_e \int \frac{\partial \mathbf{H}_{\text{eff}}}{\partial x_k}\frac{\partial \mathbf{H}_{\text{eff}}}{\partial x_k} d^3x, \tag{112}$$

if the dissipative force is calculated as the variational derivative of F with respect to the argument $\partial\mathbf{H}_{\text{eff}}/\partial x_k$. Here γ_e is a relaxation constant of exchange origin.

In the case of long wavelengths the dissipation at low temperatures is small, and so in the leading approximation we shall neglect it, limiting consideration to a Landau–Lifshitz equation of the form

$$\frac{\partial \mathbf{M}}{\partial t} = \frac{2\mu_0}{\hbar}\mathbf{M}\times\mathbf{H}_{\text{eff}}. \tag{113}$$

Equation (113) has the integral of motion $M^2 = \text{const}$, which is consistent with the idea of **M** being an equilibrium characteristic of the ferromagnet. In the ground state the magnitude of **M** is equal to the so-called spontaneous magnetization $M = 2\mu_0 s/a^3$, where s is the spin of an atom and a is the interatomic distance.

The expression for the energy density w depends on the value of the magnetic anisotropy. We start from the following model for taking into account the anisotropy of a ferromagnet:

$$w = \frac{\alpha}{2}\frac{\partial \mathbf{M}}{\partial x_k}\cdot\frac{\partial \mathbf{M}}{\partial x_k} + w_{\text{an}} - \mathbf{M}\cdot\mathbf{H}, \tag{114}$$

where the first term is the energy density of the inhomogeneous exchange, and **H** is the external magnetic field; the anisotropy energy w_{an} has the form

$$w_{\text{an}} = -\frac{1}{2}\beta_1\mathbf{M}_x^2 - \frac{1}{2}\beta_3\mathbf{M}_z^2. \tag{115}$$

If the anisotropy energy is given by (115), the ferromagnet is called *biaxial*. The case $\beta_1 = 0$ corresponds to a uniaxial ferromagnet with anisotropy axis along z. Anisotropy of the *easy-axis* type occurs when $\beta_1 = 0$ and $\beta_3 > 0$. In the ground state of an easy-axis ferromagnet its magnetization vector is directed along the z axis.

In the quantum theory of ferromagnetism, when one is considering magnetic systems of the given class one starts with an expression for the spin Hamiltonian. As a quantum model we can take a system of localized electron spins with an exchange interaction given by the Heisenberg model with only a nearest-neighbor interaction:[34]

$$\mathcal{H} = -\frac{1}{2}\sum_{n,n_0}(J_1 S_n^x S_{n+n_0}^x + J_2 S_n^y S_{n+n_0}^y + J_3 S_n^z S_{n+n_0}^z), \tag{116}$$

where $\mathbf{S}_n$ is the spin operator for the nth site, J_i ($i=1,2,3$) are the so-called *exchange integrals*, and the index n_0 enumerates the nearest neighbors of each lattice site.

Turning to a continuum description of the magnetization, we define the magnetic moment per unit volume, **M**, in terms of the average spin of a lattice site:

$$\mathbf{M} = -\frac{2\mu_0}{a^3}\langle \mathbf{S}_n\rangle = -\frac{2\mu_0}{a^3}\mathbf{S}(x_n),$$

$$\mathbf{S}_n \to -\frac{a^3}{2\mu_0}\mathbf{M}(x_n). \tag{117}$$

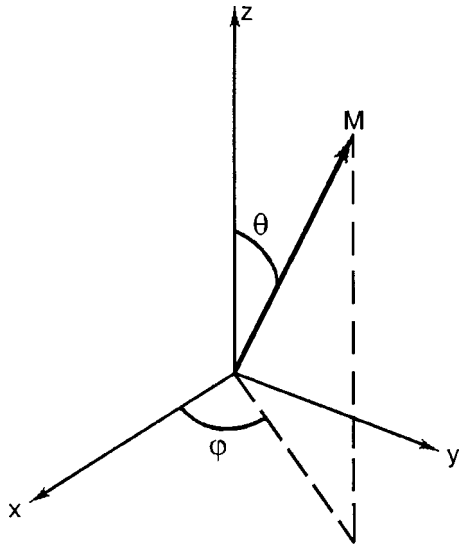

FIG. 13. Angle variables φ and θ, which specify the orientation of the magnetization vector, **M**.

In the long-wavelength approximation

$$\mathbf{M}_{n+n_0}=\mathbf{M}(x_n)+x_i(n_0)\frac{\partial \mathbf{M}}{\partial x_i}+\frac{1}{2}x_i(n_0)x_k(n_0)\times\frac{\partial^2\mathbf{M}}{\partial x_i\partial x_k}+\ldots \tag{118}$$

In writing the energy density it should be remembered that the exchange interaction is isotropic by nature, and the exchange integrals J_1, J_2, and J_3 are close in value. One can put

$$J_k=J_0+a^2j_k, \quad k=1,2,3, \tag{119}$$

where a^2j_k are small corrections. Then to accuracy a^2 we obtain equations (114) and (115), where

$$\alpha=J_0a^5/(2\mu_0)^2, \tag{120}$$

and the anisotropy constants β_1 and β_3, which for a cubic lattice have the form

$$\beta_1=z\left(\frac{a^3}{2\mu_0}\right)^2\frac{j_1-j_2}{a}, \quad \beta_3=z\left(\frac{a^3}{2\mu_0}\right)^2\frac{j_3-j_2}{a}, \tag{121}$$

where z is the number of nearest neighbors.

We change to the angle variables θ and φ (Fig. 13):

$$M_x+iM_y=M_0\sin\theta e^{i\varphi}, \quad M_z=M_0\cos\theta. \tag{122}$$

The dynamical equations for the magnetization in the variables θ and φ are

$$\sin\theta\frac{\partial\theta}{\partial t}=-\frac{2\mu_0}{\hbar M_0}\frac{\delta E}{\delta\varphi},$$

$$\sin\theta\frac{\partial\varphi}{\partial t}=\frac{2\mu_0}{\hbar M_0}\frac{\delta E}{\delta\theta}, \tag{123}$$

where the variational derivatives of the energy (111) appear on the right-hand sides.

We write the energy density of a biaxial ferromagnet in the same variables:

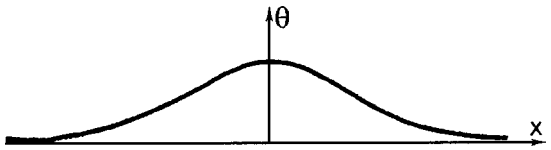

FIG. 14. Distribution of the angle θ in a dynamical magnetic soliton.

$$w=\frac{1}{2}\alpha M_0^2[(\nabla\theta)^2+\sin^2\theta(\nabla\varphi)^2]-\frac{1}{2}\beta_1M_0^2\sin^2\theta\cos^2\varphi+\frac{1}{2}\beta_3M_0^2\sin^2\theta. \tag{124}$$

Treating Eq. (123) as an equation for the field (θ,φ), we define for it a Lagrangian function, the density of which is[38–40]

$$L=\frac{\hbar M_0}{2\mu_0}(1-\cos\theta)\frac{\partial\varphi}{\partial t}-w. \tag{125}$$

In discussing the properties of dynamical solitons we shall use Eq. (123) to study the dynamics of localized magnetic excitations, for which $\theta=0$ and $|\nabla\varphi|<\infty$ at infinity (Fig. 14).

Let a uniform external magnetic field **H** be directed along the z axis. Then equations (123) clearly have two integrals of motion: the total energy (111), and the total momentum of the magnetization field

$$\mathbf{P}=-\int\frac{\partial L}{\partial(\partial\varphi/\partial t)}\nabla\varphi d^3x=-\frac{\hbar M_0}{2\mu_0}\times\int(1-\cos\theta)\nabla\varphi d^3x. \tag{126}$$

In describing the dynamics of domain walls, where it can turn out that $\nabla\varphi=0$, it is convenient to use a somewhat different definition of the field momentum:

$$\mathbf{P}=-\frac{\hbar M_0}{2\mu_0}\int\varphi\sin\theta\nabla\theta d^3x. \tag{127}$$

In an easy-axis ferromagnet ($\beta_1\equiv0$) the energy density of which is independent of the angle variable φ, there exists an additional integral of motion—the z projection of the total magnetic moment

$$N=\frac{\hbar M_0}{2\mu_0}\int(1-\cos\theta)d^3x, \tag{128}$$

which has the meaning of the average number of spin deviations from the ground state $\theta=0$ in a localized magnetic excitation. If $N\gg1$, then it can be set equal to an integer. The requirement of integer N in the classical relation (128) is equivalent to a semiclassical quantization of the corresponding solution of the dynamical equations under discussion. Here N will be referred to as the number of magnons in an excited state of a magnet.[41] One can introduce the density of magnons $n=(M_0/2\mu_0)(1-\cos\theta)$.

Let us begin with an analysis of the dynamics of a magnetic soliton in an easy-axis ferromagnet. First we note that the uniform magnetic field **H** can be eliminated from the Landau–Lifshitz equations by introducing a new angle variable $\varphi=\varphi-\omega_{\mathbf{H}}t$, where $\omega_{\mathbf{H}}=2\mu_0H/\hbar$. Since the energy density of an easy-plane ferromagnet is independent of φ,

this substitution indeed eliminates the magnetic field from the equations. This lets us start by considering the case $H=0$.

We assume that the magnetization depends on a single spatial coordinate x. Then the Landau–Lifshitz equations have a solution describing an excitation propagating along the x axis with a constant velocity:

$$\theta=\theta(r-Vt),\quad \varphi=\Omega t+\psi(r-Vt), \tag{129}$$

where $\mathbf{V}$ is the soliton velocity and Ω is the precession frequency in a reference frame tied to the moving soliton. If the function $\theta(x)$ is like that shown in Fig. 14, then this solution describes a two-parameter dynamical soliton. Since in that case the equations under consideration have the additional integrals of motion P and N, one can find the exact solution of these equations in the one-dimensional situation and calculate the energy of the magnetic soliton:[41,43]

$$E=4a^2M_0^2\sqrt{\alpha\beta}\tanh\frac{N}{N_1}\left\{1+\frac{\sin^2(\pi P/2P_0)}{\sinh^2(N/N_1)}\right\}, \tag{130}$$

where $P_0=\pi\hbar a^2M_0/\mu_0$; $N_1=2a^2l_0M_0/\mu_0$.

Considering the change in energy (111) upon small variations of the functions θ and φ, we can relate this change to the variations of the integrals of motion $\mathbf{P}$ and N:[41]

$$\delta E=\hbar\Omega\,\delta N+\mathbf{V}\cdot\delta\mathbf{P}, \tag{131}$$

$$\mathbf{V}=(\partial E/\partial\mathbf{P})_N,\quad \hbar\Omega=(\partial E/\partial N)_{\mathbf{P}}. \tag{132}$$

The first relation in (132) is the canonical equation of motion, and the second shows that $\hbar\Omega$ is the energy of excitation of a single flipped spin in a bound state of the magnons.

The most unexpected consequence of (130) is the periodic dependence of the soliton energy on the total momentum $\mathbf{P}$. In solid-state theory such a dependence is usually attributed to the discreteness of the crystal lattice and to the existence of quasimomentum instead of momentum in a continuous medium. However, since we have formulated the dynamical equations for a continuous medium, this is an unexpected result.[2]

Assuming a periodic dependence of the energy on momentum, one expects the onset of Bloch oscillations in the motion of a magnetic soliton under the influence of an driving force.

2.2. Oscillatory motion of a magnetic soliton in an easy-axis ferromagnet

Conservation of the total momentum $\mathbf{P}$ is linked to the assumption that the magnetic field is uniform. Let us now analyze the situation in which a one-dimensional dynamical soliton moves in a magnetic field having a small gradient. If the magnetic field has a weak dependence on the coordinate, we can write

$$H(x)=H_0+\eta x,\quad \eta=(dH/dx)_0. \tag{133}$$

Then the time derivative of equation (126) gives

$$\frac{dP}{dt}=-\frac{\hbar M_0}{2\mu_0}\int\left[\sin\theta\frac{\partial\varphi}{\partial t}\frac{\partial\theta}{\partial x}-\sin\theta\frac{\partial\theta}{\partial t}\frac{\partial\varphi}{\partial x}\right]dx. \tag{134}$$

After simple manipulations with the use of the equations of motion (123), we arrive at the equation

$$\frac{dP}{dt}=-2\mu_0\frac{dH}{dx}\int n(x)dx=-2\mu_0\eta N, \tag{135}$$

where N is an integral of motion equal to the number of magnons in the bound state. Thus the quasimomentum depends linearly on time:

$$P(t)=P(0)-2\eta\mu_0Nt,\quad P(0)=\text{const}. \tag{136}$$

Let us now find the total energy of a soliton moving in a magnetic field having a small gradient η. The presence of the small gradient can be taken into account as a weak perturbation of the initial system in a uniform magnetic field. In the adiabatic approximation one can assume that the soliton maintains its shape:

$$\theta=\theta[x-X(t)],\quad \varphi=\varphi_0(t)+\psi[x-X(t)], \tag{137}$$

where the main dynamical parameters V and Ω of the soliton have the form

$$V=dX/dt,\quad \Omega=d\varphi_0/dt. \tag{138}$$

In this case we write the total energy in the following way:

$$E=E_0(P,N)+2\mu_0\left(NH_0+\eta\int n(x)xdx\right), \tag{139}$$

where $E_0(P,N)$ is determined by formula (130), and

$$\int n(x)x\,dx=\frac{M_0}{2\mu_0}\int\{1-\cos\theta[x-x(t)]\}Xdx$$
$$=\frac{M_0X}{2\mu_0}\int[1-\cos\theta(\xi)]d\xi=NX. \tag{140}$$

In the last transformation, as in our analysis of the case of a uniform magnetic field, one has $\theta(\xi)=\theta(-\xi)$, where $\xi\equiv x-Vt$. Combining (139) and (140), we obtain

$$E=E_0(P,N)+2\mu_0NH_0+2\mu_0\eta NX. \tag{141}$$

The energy E can now be treated as a function of three dynamical variables: P, X, and N. The relation for the time derivative of the momentum plays the role of one of the Hamilton's canonical equations[18,19]

$$\frac{dP}{dt}=-\frac{\partial E}{\partial X}\ \text{ and }\ \frac{dX}{dt}\equiv V=\frac{\partial E}{\partial P}. \tag{142}$$

We write an expression for the soliton frequency:

$$\hbar\Omega=\frac{\partial E}{\partial N}=\frac{\partial E_0}{\partial N}+2\mu_0H_0+2\mu_0\eta X, \tag{143}$$

where the first term on the right-hand side is given by the relation

$$\frac{\partial E_0(P,N)}{\partial N}=\hbar\omega\left\{\frac{\cos^2(\pi P(t)/2P_0)}{\cosh^2(N/N_1)}\right.$$
$$\left.-\frac{\sin^2(\pi P(t)/2P_0)}{\sinh^2(N/N_1)}\right\}, \tag{144}$$

and $\omega_0=2\mu_0\beta M_0/\hbar$ is the frequency of the homogeneous ferromagnetic resonance.

On the other hand, by suitably choosing the initial coordinate of the soliton, we can use the constancy of the total

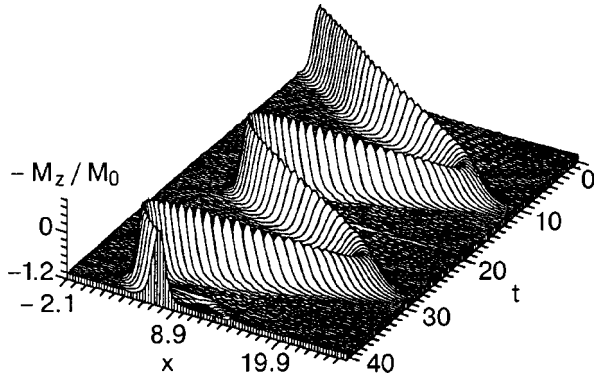

FIG. 15. Bloch oscillations of a magnetic soliton in the field of a magnetic field gradient.

energy of a conservative system together with formula (136) to find the explicit time dependence of the coordinate of the centroid of the soliton:

$$X(t)=X(0)+\frac{W_0[\cos(\pi P(t)/P_0)-\cos(\pi P(0)/P_0)]}{\eta\mu_0 N\sinh(2N/N_1)}, \tag{145}$$

where the time dependence of $P(t)$ is specified by Eq. (136). If $P(0)\neq 0$, then at short times, when $\eta\mu_0 Nt\ll P_0$, we have uniform motion of the soliton:

$$X(t)=X(0)+\frac{2\pi W_0\sin(\pi P(0)/P_0)}{P_0\sinh(2N/N_1)}t. \tag{146}$$

At long times ($\eta\mu_0 Nt>P_0$) one observes oscillatory motion of the soliton. The amplitude of the spatial oscillations, as follows from (145), is

$$\Delta X=W_0/[\eta\mu_0 N\sinh(2N/N_1)] \tag{147}$$

and, naturally, is inversely proportional to the magnetic field gradient and decreases sharply with increasing N, i.e., with the size of the soliton. The soliton velocity

$$V(t)\equiv\frac{dX(0)}{dt}=V_m\frac{\sin(\pi P(t)/P_0)}{\sinh(2N/N_1)}, \tag{148}$$

where $V_m=2gM_0\sqrt{\alpha\beta}$ is the minimum spin-wave phase velocity ($g=2\mu_0/\hbar$).

Since the total momentum of a soliton is a linear function of time (136), under the influence of a constant magnetic field gradient one should observe harmonic oscillations of the soliton, with a frequency $\omega_B=4\mu_0\eta l_0 N/(\hbar N_1)$.

The periodic time dependence of the soliton velocity and frequency is a special type of Bloch oscillation in the dynamics of the magnetization.

A numerical simulation of soliton motion by means of the Landau–Lifshitz equations in the presence of a small magnetic field gradient,[19] the results of which are presented in Fig. 15, demonstrates rather good agreement with the calculations done using the formulas of the adiabatic approximation. However, the more exact calculations show that near the right-hand turning point the soliton emits a low-amplitude spin wave with a frequency corresponding to the precession frequency of the magnetization in the soliton. This phenomenon is due to the breakdown of adiabaticity and is described by corrections of higher order in the magnetic field gradient.

We have analyzed the oscillatory motion of a magnetic soliton under the condition that the magnetic field gradient η is small. The motion of a magnetic soliton remains oscillatory for arbitrary η as well. Studies of the quasiclassical motion of a soliton in a nonuniform external field show[19] that the situation with the soliton dynamics is analogous to that in an analysis of the quasiclassical motion of an ordinary particle in a nonuniform potential field.

When dissipation is taken into account, the picture of the Bloch oscillations will undoubtedly differ from that discussed above. If the presence of both a magnetic field gradient and dissipation is simultaneously taken into account, then, as we shall see below, it becomes possible for the magnetic soliton to undergo translational motion at a constant velocity.

2.3. Influence of dissipation on the Bloch oscillations of a magnetic soliton

In embarking on a description of the relaxation of Bloch oscillations of a magnetic soliton in a slightly nonuniform magnetic field, it should be noted that the braking of a two-parameter soliton in a uniform magnetic field was successfully studied in Ref. 37 on the basis of the Landau–Lifshitz equations with dissipation.

Assuming that the relaxation is weak and, accordingly, that the relaxation constants are small, one can describe the evolution of a soliton in the presence of damping with the aid of adiabatic perturbation theory. To simplify the exposition, we will take into account only relaxation processes of relativistic origin, i.e., we will start from Eq. (109). Dissipative processes of both relativistic and exchange nature are taken into account completely in Ref. 20, and a description of the details of the problem is given. In that case not only P but also E and N cease to be integrals of motion. Writing their time derivatives with allowance for their definitions and for dissipation, one can calculate the rate of change with time for all of these quantities.

From the form of formula (130) and also from the basic relations governing the oscillatory dynamics of a soliton it follows that the energy and momentum of a soliton and also the number of magnons enter only in the form of the dimensionless ratios E/E_0, $\pi P/2P_0$, and N/N_1, where $E_0=4a^2M_0^2(\alpha\beta)^{1/2}$, $P_0=\pi\hbar a^2M_0/\mu_0$, and $N_1=2a^2l_0M_0/\mu_0$. In what follows, we denote these ratios simply by the letters E, P, and N. Moreover, we use dimensionless variables: the coordinate measured in units of the magnetic length l_0, and the time measured in units of $1/\omega_0$. Finally, the dimensionless magnetic field gradient η will be taken as $2\mu_0 l_0\eta/\hbar\omega_0$.

Using the definitions (111), (114), (126), and (128) and the main equation (109), we straightforwardly obtain the following time derivatives:

$$\frac{dP}{dt}=-\eta N-2\gamma(VQ_{\rm ex}-\tilde{\omega}R), \tag{149}$$

$$\frac{dN}{dt}=-2\gamma(\tilde{\omega}Q_{\rm an}-VR), \tag{150}$$

$$\frac{dE}{dt}=-2\gamma(V^2Q_{\rm ex}-2V\tilde{\omega}R+\tilde{\omega}^2Q_{\rm an}), \tag{151}$$

where $\tilde{\omega}$ is the soliton frequency shifted because of the uniform magnetic field, $\tilde{\omega}=\omega+H_0/(\beta M_0)$, and we have introduced the following functions:

$$R=\frac{1}{8}\int \sin^2\theta\frac{\partial\psi}{\partial x}dx, \tag{152}$$

$$Q_{\rm an}=\frac{1}{8}\int \sin^2\theta\,dx, \tag{153}$$

$$Q_{\rm ex}=\frac{1}{8}\int\left[\left(\frac{\partial\theta}{\partial x}\right)^2+\sin^2\theta\left(\frac{\partial\psi}{\partial x}\right)^2\right]dx. \tag{154}$$

Definitions (153) and (154) agree with the expressions for the anisotropy energy and exchange energy:

$$E_{\rm an}=\beta Q_{\rm an},\quad E_{\rm ex}=\beta Q_{\rm ex}.$$

Since in the adiabatic approximation the soliton solution maintains its functional form, one should substitute into these expressions the exact soliton solution of the Landau–Lifshitz equations for $\eta=0$ and $\gamma=0$, assuming its parameters to be smooth functions of time. The corresponding two-parameter solution of equations (109) has the form[41]

$$\varphi=\tilde{\omega}t+\psi(x-Vt);\quad \frac{d\psi}{dx}=-\frac{C}{\cos^2(\theta/2)};$$

$$\tan^2\frac{\theta}{2}=\frac{A+B}{\cosh^2[\kappa(x-V)]-B}. \tag{155}$$

The parameters of the solution are ω and V, which in the adiabatic approximation can be expressed in terms of the integrals of motion P and N:

$$\omega=\frac{\cos^2 P}{\cosh^2 N}-\frac{\sin^2 P}{\sinh^2 N};\quad V=2\frac{\sin 2P}{\sinh 2N}. \tag{156}$$

The constants A, D, C and the parameters κ are functions of ω and V. However, it will be convenient below to express them in terms of the conserved (for $\eta=0$ and $\gamma=0$) quantities N and P:

$$A=\sinh^2 N,\quad B=\sin^2 P,\quad C=\frac{\sin 2P}{\sinh 2N}, \tag{157}$$

$$\kappa=\left(1+\frac{B}{A}\right)\tanh N. \tag{158}$$

The form in which Eqs. (149)–(154) are written is extremely convenient for studying the dynamics of a soliton of large extent ($N\gg 1$) with vanishingly small V and ω. In that case one can describe the relaxation of such a soliton even without having the explicit solution in the general case. Assuming that the isolated factors of V and $\tilde{\omega}$ in Eqs. (149)–(151) give the main dependence on these parameters, one can calculate (152)–(154) for $V\to 0$ and $\omega\to 0$, i.e., essentially in the static regime. But then, as we know,[41] $\psi=0$ and the function $\theta=\theta(x)$ describe the profile of a wide one-dimensional domain with the reversed magnetization direction at infinity ($\theta\approx\pi$ inside the domain, and $\theta=0$ at infinity). The width of the domain $\Delta x\approx 2N$, and its edges are two domain walls in which

$$\theta(x)=\theta_0(x)\equiv 2\tan^{-1}\{\exp[\pm(x\mp x_0)]\}, \tag{159}$$

where $\pm x_0$ are the coordinates of the centers of the two domain walls: $2x_0=\Delta x$. Since the width l_0 of the domain wall is finite and $l_0\ll\Delta x$, it is trivial to calculate the parameters R, $Q_{\rm an}$, and $Q_{\rm ex}$ in the leading approximation:

$$R=0,\quad Q_{\rm an}=\frac{1}{4}\int^{\infty}\sin^2\theta_0(x)dx,$$

$$Q_{\rm ex}=\frac{1}{4}\int_{-\infty}^{\infty}\left(\frac{\partial\theta_0}{\partial x}\right)^2dx. \tag{160}$$

Substituting (159) into (160), we find $Q_{\rm ex}=Q_{\rm an}=1/2$.

In the case of small ω and V the form of Eq. (151) corresponds to the usual definition of the energy change in a dissipative medium,

$$\frac{dE}{dt}=-2F, \tag{161}$$

where the relativistic term of the dissipative function has the standard form:

$$F=\gamma(\tilde{\omega}^2+V^2),$$

which agrees with the equations of motion (149), (150):

$$\frac{dP}{dt}=-\frac{\partial E}{\partial X}-\frac{\partial F}{\partial V}, \tag{162}$$

$$\frac{dN}{dt}=-\frac{\partial F}{\partial\tilde{\omega}}. \tag{163}$$

Here E is the expression (corresponding to formula (141) in dimensional units) for the soliton energy in a nonuniform magnetic field,[18,19]

$$E=\kappa+hN+\tilde{\eta}XN, \tag{164}$$

where X is the coordinate of the center of the soliton, and $h=H_0/(\beta M_0)$.

If the conditions that V and ω be small are not satisfied in the calculation of R, $Q_{\rm ex}$, and $Q_{\rm an}$, then it is necessary to use the explicit form of the solution (155). After integration we obtain

$$R=-VN/2, \tag{165}$$

$$Q_{\rm an}=\frac{1}{2}\left(\frac{1}{2}\Omega\sinh 2N+N\omega\right), \tag{166}$$

$$Q_{\rm ex}=\frac{1}{2}\left(\frac{1}{2}\Omega\sinh 2N-N\omega\right), \tag{167}$$

where $\Omega^2=\omega^2+V^2$, and ω and V are expressed in terms of the integrals of motion by formulas (156). Equations (149) and (150) with these values of R, $Q_{\rm an}$, and $Q_{\rm ex}$ give smooth changes of the soliton parameters P and N with time, and formula (164) can be used to obtain the equation for the coordinate of the center of the soliton, $X(t)$.

To find $X(t)$ we differentiate relation (164) with respect to time and use Eqs. (149)–(151). After some straightforward manipulations we ultimately find

$$\frac{1}{N}\frac{d(NX)}{dt}=2\frac{\sin(2P)}{\sinh(2N)}, \tag{168}$$

where the right-hand side is the same as in Eq. (156) for V, but now P and N are functions of time. We note that if we set $\gamma=0$ (and, hence, $N=\text{const}$) in Eqs. (149), (150), and (164), then we arrive at the same description of the Bloch oscillations of a magnetic soliton as was obtained in Refs. 18 and 19. In the case $\gamma=0$ and $\eta=0$, Eqs. (149)–(151) and (165)–(167) agree with the analogous equations in Ref. 37.

In the general case of arbitrary values of the parameters ω and V (or N and P) the system of equations (149)–(151) describing the relaxation of a soliton can be investigated only numerically.

However, for $N\gg 1$ and $H_0=0$ (which is equivalent to $V,\omega\ll 1$) one can advance further with the analytical studies. In this case equations (149), (150), and (168) in the leading approximation take the form

$$\frac{dP}{dt}=-\tilde{\eta}N-4\gamma e^{-2N}\sin(2P), \tag{169}$$

$$\frac{dN}{dt}=-4\gamma e^{-2N}\cos(2P), \tag{170}$$

$$\frac{dX}{dt}=4e^{-2N}\sin(2P)+4\Gamma\frac{1}{N}e^{-2N}\cos(2P)X. \tag{171}$$

We are most interested in considering the case of weak relaxation, where one expects to see only slightly modified Bloch oscillations. To keep the notation brief, we introduce the parameter $\eta_c=4\gamma\exp(-2N_0)/N_0$, where N_0 is the initial value of the number N, and our use of the term weak relaxation refers to the case $\eta_c\ll\eta$. Here one can find solutions of equations (169) and (170) by interaction, and they can be represented as power series in the parameter η_c/η:

$$P=P(0)-\frac{1}{2}\nu_0 t-\frac{2\gamma}{\eta N_0}\exp(-2N_0)[\cos(\nu_0 t)-1], \tag{172}$$

$$N=N_0-\frac{2\gamma}{\eta N_0}\sin(\nu_0 t),$$

where $\eta_0=2\eta N_0$ is the Bloch oscillation frequency of the soliton. Of course, the dimensionless frequency ν_0 precisely corresponds to the soliton Bloch oscillation frequency ω_B introduced in the previous Section. The terms of higher orders in powers of the parameter η_c/η are proportional to higher harmonics with respect to the frequency ν_0.

We note that on average over the period of the Bloch oscillations of the soliton ($T=2\pi/\nu_0$) the parameter N remains constant and practically equal to its initial value N_0. Using the results obtained for P and N and Eq. (171), one can also straightforwardly find the first two terms of the expansion of $X(t)$ in the parameter ($\gamma\exp(-2N_0)/N_0$):

$$X(t)=\frac{4}{\nu_0}e^{-2N_0}\cos(\nu_0 t)-\frac{4\gamma}{\eta\nu_0 N_0}\times\exp(-4N_0)\sin(2\nu_{0t})-\frac{8\gamma}{\eta N_0}\exp(-4N_0)t, \tag{173}$$

where in the last term we have again omitted the contribution of higher order in the small parameter $1/N_0$. The first term in this expression agrees with the result obtained in Refs. 18 and 19 and describes Bloch oscillations of the magnetic soliton.

Taking the damping into account leads to two effects, as can be seen from formula (173). First, the oscillations of the center of the soliton, while remaining periodic with frequency $2\nu_0$, cease to be harmonic: higher harmonics appear in $X(t)$. Second, the center of the soliton begins to drift at a constant velocity proportional to the damping:

$$V_{\text{dr}}=-\frac{8\gamma}{\eta N_0}e^{-N_0}. \tag{174}$$

The soliton behavior just described is reminiscent of the above-mentioned Shapiro effect in the theory of Josephson junctions.[3]

Since all of the soliton characteristics are periodic functions of P, while N, as we have said, is a periodic function of time, in the case under discussion, viz., $\eta\gg\eta_c$, soliton damping does not occur at all. According to formula (161), the decrease of the soliton energy is proportional only to the square of Ω and is exactly equal to the change in energy due to the drift of the center of the soliton to the region of lower magnetic fields. It must be remembered, however, that as the soliton drifts, the value of the field H gradually changes. The approximation $H_0=0$ is valid only while $h<\Omega$. This leads to the following estimate of the soliton drift time, which agrees in order of magnitude with its lifetime τ: $\tau\sim N_0/(\lambda\Omega)$. Here the change in h on a scale comparable to the Bloch oscillation amplitude Ω/ν_0 is relatively small: $\Delta h\sim\Omega/N_0\ll\Omega$, and consequently, formulas (172)–(174) and, hence, the qualitative conclusions as to the character of the Bloch oscillation of the soliton, remain valid.

Let us now indicate the conditions under which the weak damping regime under study is realized. For adiabatic perturbation theory to be applicable, the characteristic frequency Ω in the soliton must be much higher than the Bloch oscillation frequency $2\nu_0$, i.e., the following inequalities must hold:

$$1\gg 4e^{-2N_0}\gg 2\nu_0.$$

This places a restriction on the maximum value of the magnetic field gradient, since $\nu_0=\eta N_0$. The condition $\eta\gg\eta_c$, on the other hand, gives

$$2\nu_0\gg 8\gamma e^{-2N_0}.$$

In other words, if $\gamma\ll 1$, then there is an interval of η values in which one should observe weakly damped Bloch oscillations of the soliton. Interestingly, even if $\eta\gtrsim\eta_c$ the soliton has time to complete many oscillations ($N_0\eta/\eta_c$) before it vanishes. Finally, we note that over its lifetime a soliton drifts a distance of the order of $\exp(-2N_0)/\eta\ll 1$, which is much greater than both the soliton size N_0 and the Bloch oscillation amplitude $2\exp(-2N_0)/(N_0\eta)$.

In the case when $\Omega\ll 1$ but $H_0\neq 0$ ($h>\Omega$), all of the qualitative results presented above remain good. Only certain quantitative characteristics will change. In particular, the

condition of adiabaticity becomes weaker ($\omega \sim h \gg \nu_0$), and a soliton is able to complete only $N_0(\eta/\eta_c)(\Omega/h)$ Bloch oscillations before vanishing.

Thus if the magnetic field gradient is greater than a critical value (but is still small enough for the adiabatic approximation to be applicable), the Bloch oscillations of the soliton exist even in the presence of damping. However, these oscillations cease to be harmonic, and, in addition, the center of the soliton begins to drift at a constant velocity. Over its lifetime, a soliton can complete a large number of Bloch oscillations, and the value of the drift is much larger than the amplitude of these oscillations.

If the magnetic field gradient is less than the critical value, then the Bloch oscillations vanish completely and the soliton has only a gradually damped translational motion.

2.4. Macroscopic theory of Bloch oscillations of a soliton in a biaxial ferromagnet

In a biaxial ferromagnet the energy density depends explicitly on the variable φ, and therefore N is no longer an integral of motion. It is very important that even in the case of a uniaxial ferromagnet the dependence of the energy on φ is manifested when the magnetic dipole interaction is taken into account.

Let us consider a magnet of very large dimensions and restrict consideration to solutions that depend only on a single spatial coordinate, x. We assume that the sample is in the form of a slab perpendicular to the x axis, and outside it ($x=\pm\infty$) the magnetic field vanishes. Then the boundary conditions for the normal component of the magnetic induction vector ($B_x(\pm\infty)=0$) select a single nonzero component of the vector $\mathbf{H}^{(m)}$, which is the solution of the equations of magnetostatics:

$$H_x^{(m)} = -4\pi M_x . \tag{175}$$

Consequently, we obtain

$$W_m = 2\pi M_x^2 . \tag{176}$$

Even in the case of a uniaxial ferromagnet the energy (176) leads to a certain effective anisotropy in the plane perpendicular to the anisotropy axis if the x axis is not along a preferred direction. In particular, if z is the axis of anisotropy, then we have for the total magnetic energy of a uniaxial ferromagnet

$$W = \frac{\alpha}{2}\left(\frac{\partial \mathbf{M}}{\partial x}\right)^2 - \frac{\beta}{2}M_z^2 + 2\pi M_x^2 . \tag{177}$$

Formally the energy (177) pertains to a biaxial ferromagnet with $\beta_1 = -4\pi$.

Another feature of a biaxial ferromagnet stems from the fact that the external magnetic field cannot be eliminated from the equations. Therefore, the system behaves in completely different ways in the presence and absence of magnetic field. We begin with the case when the external magnetic field is equal to zero.

To simplify the writing of the dynamical equations for the magnetization field, we introduce the magnetic length $l_0 = \sqrt{\alpha/\beta_3}$ and the homogeneous ferromagnetic resonance frequency $\omega_0 = 2\mu_0 M_0 \beta_3/\hbar$; the coordinate will be measured in units of l_0 and the time in units of $1/\omega_0$. Then Eq. (123) can be written, with allowance for (124), in the form

$$\frac{\partial^2 \theta}{\partial x^2} - \left\{1 + \left(\frac{\partial \varphi}{\partial x}\right)^2 + \varepsilon \cos^2 \varphi\right\} \sin\theta\cos\theta + \sin\theta \frac{\partial \varphi}{\partial t} = 0,$$

$$\frac{\partial}{\partial x}\left(\sin^2\theta \frac{\partial \varphi}{\partial x}\right) + \varepsilon \sin^2\theta \cos\varphi \sin\varphi - \sin\theta \frac{\partial \theta}{\partial t} = 0, \tag{178}$$

where $\varepsilon = -\beta_1/\beta_3$ is the ratio of the anisotropy constants.

The simplest dynamical soliton in a biaxial ferromagnet is a topological soliton (domain wall). The solution for a domain wall in a biaxial ferromagnet was first found by Walker[40,44] (see also Ref. 45). For a domain wall moving with velocity V, it has the form

$$\theta = 2\tan^{-1}\exp[s(1+Q\cos^2\varphi)^{1/2}(x-Vt)],$$

$$\varphi = \text{const}, \tag{179}$$

where Q is the topological charge of the domain wall ($Q = \pm 1$) and

$$V = -\frac{Q\cos\varphi\sin\varphi}{\sqrt{1+Q\cos^2\varphi}}. \tag{180}$$

If the anisotropy energy (176) comes from taking into account the magnetic dipole interaction in an easy-plane ferromagnet ($\varepsilon = 4\pi/\beta_3$), then the domain wall with $\varphi = \pi/2$ is called a Bloch wall, and the immobile domain wall with $\varphi = 0$ is a Néel wall.

It is easy to calculate the energy E and field momentum P per unit cell of the crystal in the plane of the domain wall. The result is

$$E = E(P) \equiv E_B\sqrt{1+Q\cos^2(\pi P/2P_B)}, \tag{181}$$

where $E_B = 2\beta_3 M_0^2 a^2\sqrt{\alpha\beta_3}$ is the energy, and $P_B = \pi\hbar M_0 a^2/(2\mu_0)$ is the momentum of an immobile (sessile) Bloch wall.

We have obtained the periodic dependence of the energy of a topological soliton on its momentum, the presence of this periodicity being is a necessary condition for the onset of Bloch oscillations of a soliton in a uniform external force field.

After proving the periodicity of the energy and velocity of a topological soliton as functions of the field momentum in the absence of magnetic field, we need to satisfy ourselves that when a magnetic field is turned on, the field momentum P ceases to be an integral of motion.

The first of equations (178) in the presence of a magnetic field parallel to the $0z$ axis is slightly modified:

$$\frac{\partial^2 \theta}{\partial x^2} - \left\{1 + \left(\frac{\partial \varphi}{\partial x}\right)^2 + \varepsilon \cos^2 \varphi\right\} \sin\theta\cos\theta + \sin\theta \frac{\partial \varphi}{\partial t} = h\sin\theta, \tag{182}$$

where $h = H/(\beta_3 M_0)$, and the second equation remains unchanged.

If the magnetic field is small ($H \ll \beta_3 M_0$), then it can be treated as a small perturbation. In the adiabatic approximation the solution for a domain wall as before is of the type (179), i.e., the solutions of the first equation of (178) for $\partial\varphi/\partial t = 0$ or of Eq. (182) for $\partial\varphi/\partial t = h = 0$:

$$\theta = 2\tan^{-1}\exp[(1+\varepsilon\cos^2\varphi)^{1/2}(x-X)] \tag{183}$$

(for definiteness we take $Q=1$). Now, however, the coordinate X of the center of the soliton and the angle φ depend on time. However, the functional dependence of the total momentum on φ can be taken to be the same as in the absence of magnetic field (when $\varphi=\text{const}$). Therefore, in using expression (127), we shall assume that the following formula is valid:

$$P=(\hbar M_0 a^2/\mu_0)\varphi=(2P_B/\pi)\varphi. \tag{184}$$

This means that the time dependence of P is determined by the time dependence of the angle φ.

In the leading approximation it follows from (182) that

$$\frac{d\varphi}{dt}=h. \tag{185}$$

Consequently, $\varphi=ht$, and in accordance with formula (180) the soliton velocity $V=dX/dt$ executes oscillations at the Bloch frequency $2h$, where in dimensional units $h=2\mu_0 H/\hbar$. The kinetic energy of the soliton (181) will oscillate at this frequency, which is twice the precession frequency of the magnetization vector.

Indeed, the pair of equations (180) and (185) is trivially integrated and gives the following law for the oscillations of the center of the domain wall:

$$X=\frac{1}{h}\sqrt{1+\varepsilon\cos^2 ht}, \quad \varphi=ht. \tag{186}$$

The amplitude of the oscillations $\Delta X=(1/h)(\sqrt{1+\varepsilon}-1)$. At one of the stopping points the domain wall is purely Bloch, and at the other it is purely Néel. The energy difference between these two domain walls, $\Delta E=E_B(\sqrt{1+\varepsilon}-\varepsilon)$, is precisely equal to the work done by the external force $2HM_0a^2$ acting over a length equal to the oscillation amplitude $l_0\Delta X$.

Thus the energy of the magnet averaged over the oscillation period of the wall is conserved. The above analysis of the domain wall motion was given in Refs. 40 and 46. The problem of domain wall motion in a magnetic field was first considered by Slonczewski,[14] who restricted his analysis to the case $\varepsilon\ll 1$ but for arbitrary H. In that limit the solution of the Landau–Lifshitz dynamical equations simplifies to

$$\theta=2\tan^{-1}\exp(x-X), \tag{187}$$

where

$$\frac{dX}{dt}=-\varepsilon\cos\varphi\sin\varphi, \quad \frac{d\varphi}{dt}=h. \tag{188}$$

Thus the oscillatory character of the domain wall motion in a uniform magnetic field is preserved.

The oscillatory character of the motion of a domain wall in a static magnetic field is entirely due to the periodic dependence of the energy (181) on the momentum of the domain wall. However, in studying the oscillations of a dynamical soliton in an easy-axis ferromagnet, we have already seen that the inclusion of dissipative processes in the analysis disrupts this oscillatory motion and makes it possible to have uniform, on average, motion of an electron in a static electric field. Such a situation is also observed in the dynamics of a domain wall. In Slonczewski's paper[14] it was confirmed that taking into account the braking of the domain walls moving under the influence of an external magnetic field below a certain critical value will make it possible to have steady motion of the domain wall at a constant velocity, i.e., the motion first described by Walker.[44] At high fields either oscillatory motion[14] or an increase in the complexity of the domain wall structure[47] can occur.

2.5. Dynamics of solitons of a discrete spin system (quantum description)

The results of the above-described theory of Bloch oscillations of magnetic solitons are applicable to the analysis of dynamic magnetic phenomena in ferromagnets, where the characteristic magnetic length is much greater than the interatomic distance ($l_0=\sqrt{\alpha/\beta}\gg a$). The presence of this inequality allows us to use the long-wavelength (continuum) approximation for describing the effects under study, since a magnetic soliton in such a theory spans a large number of sites of the 1D lattice. However, there exist highly anisotropic magnetic materials in which the distribution of the nonuniform magnetization due to an isolated soliton propagates only a few interatomic distances. For example, in magnets with an extremely strong uniaxial exchange anisotropy, so-called Ising magnets, the simplest topological soliton (domain wall) is realized over a single interatomic distance. To describe solitons in such systems one must explicitly take into account the discreteness of the structure and the quantum character of the dynamics of the magnetization.

In order to present the results in a more or less closed form, let us consider a model obtained by a certain continuous complication of the Ising model. If one starts from the Heisenberg Hamiltonian (116), then the Ising model corresponds to taking into account only nearest-neighbor interactions and setting $J^x=J^y=0$, i.e., it corresponds to the Hamiltonian

$$\mathcal{H}_I=-J^z\sum_n S_n^z S_{n+1}^z. \tag{189}$$

A positive exchange integral ($J^z>0$) corresponds to a ferromagnet (FM), and a negative exchange integral ($J^z<0$) to an antiferromagnet (AFM). The ground state is one of ferromagnetic ordering for the FM and Néel ordering for the AFM.

An excitation of an Ising chain is an immobile domain wall. It is known that two types of domain walls, differentiating in the effective charge Q ($Q=\pm 1$), can exist. In a ferromagnet the wave functions $|m,Q\rangle$ in the basis of eigenfunctions of the operator S^z are

$$\psi_n(m,1)\equiv|m,1\rangle=|\ldots\uparrow\overset{m}{\uparrow}\downarrow\downarrow\ldots\rangle \tag{190}$$

and

$$\psi_n(m,-1)\equiv|,-1\rangle=|\ldots\downarrow\overset{m}{\downarrow}\uparrow\uparrow\ldots\rangle,$$

where the site $n=m$ is the left side of the domain wall, i.e., the domain wall lies between the sites $n=m$ and $n=m+1$.

In the absence of magnetic field the excitation spectrum consists of discrete energy levels, with each level corre-

sponding to a fixed number of domain walls and the degree of its degeneracy being equal to the number of possible distributions of this number of domain walls in the chain.

If an additional small exchange interaction of the transverse components of the spin ($J^x \neq 0$ or $J^y \neq 0$) is taken into account, then the degeneracy of the levels is lifted. The spectrum becomes a series of bands with continuous energy distribution separated by significant gaps. Each band, as before, corresponds to a fixed number of mobile (!) domain walls. The lowest-lying energy band corresponds to single-soliton excitation.

Since in the previous Sections we made use of the single-band approximation, ruling out or neglecting interband transitions, in the present situation we must restrict consideration to single-soliton excitations of the spin system.

The single-soliton model was first discussed seriously by Villain[48] in a study of soliton dynamics in a spin-1/2 Ising-like AFM chain. He described the dispersion of the soliton mode (sometimes called the Villain mode) lying below the continuous spectrum of two-soliton excitations. The validity of the results of Ref. 48 has been confirmed both by theoretical studies (a review of these can be found in Ref. 49) and numerical calculations.[50] It has also been shown that such a mode exists in a spin-1/2 Ising-like FM chain.[51]

Thus we are interested in a 1D magnet model which, on the one hand, is close to purely Ising, having a strong easy-axis anisotropy of the exchange interaction and, on the other hand, admits domain wall dynamics, i.e., it must differ from purely Ising (it must have nonzero J^x and J^y).

We propose a convenient model for our purposes, writing the Hamiltonian of the system in the form

$$\mathcal{H}=\mathcal{H}_I+\mathcal{H}_{xy}-2\mu_0 H\sum_n S_n^z, \tag{191}$$

$$\mathcal{H}_{xy}=-\sum_n (J^x S_n^x S_{n+1}^x + J^y S_n^y S_{n+1}^y). \tag{192}$$

In the basis of eigenfunctions of the operator S^z the matrices appearing in $\mathcal{H}_{xy}$ have only off-diagonal elements. Therefore, the term (192) in the Hamiltonian, in acting on the soliton wave function (190), inevitably leads to the creation of two-soliton states, and only the terms $S_{m-1}S_m$ and S_{m+1} S_{m+2} lead to displacement of the soliton from the position $n=m$ to the position $n=m\pm 2$ while preserving the single-soliton character of the excitations. Desiring to remain only in the single-soliton sector, we must take into account only these terms in (192) and neglect the rest. This operation may be justified by the large value of the energy gap separating the single-soliton band from the bands above it. Without going into the conditions for applicability of this description of the dynamics of an individual soliton, we state our agreement with the authors of Ref. 17 and define the effective Hamiltonian as the projection of (191) onto the subspace of single-soliton states. Then the effective Hamiltonian of the single-soliton excitation in an external magnetic field H can be written as

$$\mathcal{H}_{\text{eff}}=\frac{1}{2}J^2+\Delta(T^2+T^{-2})-FQ\hat{m}, \tag{193}$$

where $F=2\mu_0 H$, T is the translation operator for displacement by one intersite distance, $\hat{m}$ is the operator of the site number specifying the position of the soliton. The intensity of "hopping" between next-nearest-neighbor sites is governed by the quantity[17]

$$\Delta=-\frac{1}{4}(J^y-J^x). \tag{194}$$

It follows from (194) that soliton (domain wall) motion is possible only under the condition $J^x \neq J^y$, i.e., only in a ferromagnet with biaxial exchange anisotropy. This conclusion agrees with the results of the phenomenological theory of magnetic solitons.

An analogous effective model can also be proposed for a uniaxial ferromagnet ($J^x=J^y$) in an external magnetic field having H_x and H_z components:[17]

$$\mathcal{H}_{\text{eff}}=\frac{1}{2}J^z-\mu_0 H_x[T+T^{-1}]-2\mu_0 HQm.$$

However, in such a model jumps between nearest-neighbor sites of the chain are important.

Let us turn back to Eq. (193). Since the soliton charge Q enters this equation as a parameter, it is sufficient to consider the dynamics of a soliton of just one sign (e.g., $Q=-1$). Then (193) becomes formally equivalent to the Hamiltonian of the single-band tight-binding model for a particle in an external uniform field and leads to an equation for the stationary states, analogous to equation (14):

$$i\hbar\frac{\partial\psi_n}{\partial t}=\frac{1}{2}J^z\psi_n+\Delta(\psi_{n-2}+\psi_{n+2})-FQ_n\psi_n. \tag{195}$$

The specifics of the spin problem are manifested in an effective interaction of only the next-nearest neighbors, which leads to the obvious difference of Eq. (195) from (14).

In the absence of an external magnetic field the Hamiltonian (193) or Eq. (195) give the dispersion relation

$$\varepsilon(k)=\frac{1}{2}J^z+2\Delta\cos(2k), \tag{196}$$

which differs from (66) mainly in that the period in k space is one-half as large.

A periodic dependence of the soliton energy $\varepsilon(k)$ on the quasiwave vector arises naturally, causing Bloch oscillations in the presence of a magnetic field. Since the site number operator in k space is $n=i\partial/\partial k$, the field term in (193) leads to the obvious equation of motion

$$\frac{dk}{dt}=FQ=-F. \tag{197}$$

It follows that in the quasiclassical approximation the soliton velocity depends harmonically on time:

$$v=\frac{\partial\varepsilon}{\partial k}=4\Delta\sin(2Ft) \tag{198}$$

with the Bloch frequency $\omega_B=2F=(4\mu_0 H)/\hbar$. Integrating (198) with respect to time and determining the position of the soliton at every point in time, it is easy to find the amplitude of the Bloch oscillations:

$$m(t)=\text{const}-\left(\frac{2\Delta}{F}\right)\cos(\omega_B t). \tag{199}$$

Curiously, the frequency of the Bloch oscillations is equal to twice the precession frequency of the magnetization vector in a magnetic field, $2\mu_0 H/\hbar$. This frequency naturally agrees with the frequency of Bloch oscillations of the domain walls in a biaxial FM, which were described in the previous Section on the basis of the Landau–Lifshitz equations.

It is easy to confirm the results of the quasiclassical analysis by a rigorous quantum calculation based on Hamiltonian (193).

First we can state on the basis of arguments analogous to (29) that there exists a preferred discrete spectrum of domain wall energies[3]

$$E=2\Delta-mF,\ \ m=0,\ \ \pm1,\ \ \pm2,..., \tag{200}$$

which corresponds to the Wannier–Stark ladder. It is a characteristic property that the distance between steps on the ladder, $\delta E=F$, is independent of Δ. In the present case, however, δE differs from the Bloch oscillation frequency $\omega_B=2F$.

Repeating the discussion of Sec. 1.1, we can write the eigenfunctions of the Wannier–Stark ladder, by analogy with (30), in the form

$$\Phi_m(k)=\exp\left(i\frac{\Delta}{F}\sin 2k\right)\exp(-imk). \tag{201}$$

In the site representation

$$\Psi_n^m=\frac{1}{2\pi}\int_{-\pi}^{\pi}\exp\left(i\frac{\Delta}{F}\sin k\right)\exp\left(i\frac{(n-m)}{2}k\right)dk. \tag{202}$$

If the difference $n-m$ is an even number, then Ψ_n^m has the form of a Bessel function of the first kind:

$$\Psi_n^m=J_{(m-n)/2}\left(\frac{\Delta}{F}\right) \tag{203}$$

and describes the amplitude of a stationary state localized in the neighborhood of the site $n=m$. It is these solutions that were obtained and analyzed in Ref. 17.

Let us now satisfy ourselves that the evolution of the soliton in an external field under the condition that it initially occupied a definite site reduces to oscillations at the Bloch frequency $\omega_B=2F$. We write the analog of solution (41) for the case when the soliton at $t=0$ is found at the site $n=m$:

$$\Psi(n-m,t)=\frac{1}{2\pi}e^{-2i\Delta t}\int_{-\pi}^{\pi}\exp\left\{\frac{2\Delta i}{2F}[\sin k-\sin \times(k-2Ft)]\right\}e^{ikn-m/2}dk. \tag{204}$$

For even $n-m$ we obtain a result analogous to that given in Eq. (41):

$$\Psi(n-m,t)=iJ_{(n-m)/2}\left(\frac{2\Delta}{F}\sin 2Ft\right)e^{i(n-m)Ft}. \tag{205}$$

To ascertain the period of the oscillations described by formula (205), we can calculate the mean-square deviation of the site number n from the initial value. Setting $n-m=2p$ and doing the calculation, we arrive at an expression analogous to Eq. (41):

$$\langle(n-m)^2\rangle=4\sum\ p^2J_p^2\left(\frac{2\Delta}{F}\sin Ft\right)=8\left(\frac{2\Delta}{F}\right)^2\sin^2 Ft. \tag{206}$$

Indeed, the Bloch oscillations of a soliton initially localized at a certain site have the character of ''breathing'' at a frequency $\omega_B=2F$. The difference of the frequency ω_B from the energy difference in the Wannier–Stark ladder is due to the specific selection rule $\Delta m=\pm2$, which arises because the dynamics effectively operates by jumps of two intersite distances.

In finishing the exposition of the basic material, we note that we have analyzed Bloch oscillations of dynamical and topological solitons in 1D ferromagnets. Undoubtedly the dynamics of solitons in antiferromagnets is also worthy of attention. This is not without justification, since the equations of motion of the magnetization in antiferromagnets are well studied. However, the macroscopic (phenomenological) dynamics in antiferromagnets is more complicated than in ferromagnets, and the author is unaware of any consistent description of the equations of motion, based on the Landau–Lifshitz equations, for individual solitons in antiferromagnets.

At the same time, the quantum description of the motion of solitonlike excitations in a spin chain with an antiferromagnetic interaction of neighbors can be achieved in a scheme analogous to that set forth above, i.e., in an effective model that takes into account only the single-soliton sector of excitations. Indeed, for an antiferromagnetic spin chain in a longitudinal external magnetic field that increases linearly along the chain (with a constant magnetic field gradient) one can propose the following effective Hamiltonian[17]

$$\mathcal{H}^{AFM}=\frac{|J^z|}{2}+\Delta^{AFM}(T^2+T^{-2})-\mu_0 HQ(-1)^m\left(m+\frac{1}{2}\right),$$

where

$$\Delta^{AFM}=(J^x+J^y)/4.$$

This Hamiltonian is similar to Eq. (193) discussed above. Consequently, much of what we described previously can be used with suitable modifications for analysis of the oscillatory dynamics of solitons in an antiferromagnetic spin chain.

This remark about soliton dynamics in antiferromagnetic chains is particularly topical in view of the fact that the existence of so-called ''dispersion solitons'' (the Villain mode) has been confirmed experimentally in Ising antiferromagnets.[52–57]

2.6. Discussion of the possibilities of observing manifestations of Bloch oscillations of a magnetic soliton

A theoretical analysis of Bloch oscillations of magnetic solitons should be accompanied by an assessment of the conditions and possibilities for observing Bloch oscillations in magnetic systems. In speaking of the general conditions, it should be noted that they are similar to those which exist for the study of mesoscopic effects in electronics (see, e.g., Ref. 58).

We should first recall that the Bloch oscillations are a single-band effect. Therefore, in physical systems for which the energy spectrum of the soliton is multiband, conditions should be provided by which interband transitions can be eliminated (the effect under discussion is a consequence of the reflection of a soliton from the band boundary, which leads to reciprocating motion). The external force acting on the soliton should in a certain sense be not too large, so that the soliton, upon reaching the band boundary, cannot tunnel into the higher band. Transitions of that kind can be neglected if the frequency of the Bloch oscillations is considerably higher than the frequency of tunneling interband transitions. In the context of the previous Section, this means that the exchange integral along the easy axis, J^z, must be considerably greater than the magnetic field ($J^z \gg \mu_0 H$).

Further, inelastic scattering of the soliton should be practically absent. Inelastic scattering disrupts the phase coherence of the motion, without which the Bloch oscillations cannot occur. This scattering is due primarily to the interaction of the soliton with phonons and also to the soliton–soliton interaction. It is clear that this scattering is minimum at low temperatures, when the phonons are ''frozen out'' and the soliton density is small. This situation obtains in Ising spin chains at temperatures much less than J^z.

Of lesser but still considerable importance is that elastic scattering on impurities should not give rise to so-called Anderson localization of the soliton in a disordered chain, which would mask its Bloch oscillations. For this reason one must create conditions in which the amplitude of the Bloch oscillations will be smaller than the Anderson localization length. Since the Bloch oscillation amplitude is inversely proportional to the magnetic field strength, this imposes a restriction on the minimum magnetic field.

The last two arguments lead to the conclusion that the most suitable 1D and quasi-1D magnetic systems for observing Bloch oscillations are those in which solitons of small dimensions exist and the Bloch oscillations have small amplitude. But first we must be convinced of the existence of systems in which magnetic solitons could in principle be observed. Substances whose crystal structure consists of systems of 1D chains that are weakly interacting with one another and which admit excitations of the topological or dynamical soliton type are listed and described in the review by Mikeska and Steiner.[49] Since such excitations create dynamic distortions of the magnetic structure, they may possibly be amenable to observation in inelastic neutron scattering experiments. The values measured in the neutron experiments are expressed in terms of the structure factor of the material under study.

Before turning to the calculation of the structure factor, let us reiterate that attention should be devoted mainly to considering the situation with solitons of small dimensions executing Bloch oscillations of small amplitude. Such situations are typical for the dynamical domain walls analyzed in Sec. 2.5. Therefore, let us give the expression for the structure factor of a ferromagnetic spin chain with a domain wall whose dynamics is described by the Hamiltonian (193). We start from the following definition of the structure factor:

$$S^{zz}(q,\omega)=\frac{1}{2\pi}\int_{-\infty}^{\infty} dt\, e^{-i\omega t}\langle \delta S^{z'}_{-q}(0)\,\delta S^{z'}_{q}(t)\rangle, \qquad (207)$$

where $\delta S^z_q = S^z_q - \langle S^z_q\rangle$, and the Fourier transformation of the spin operators is done in the standard way: $S_q = \Sigma_n \exp(iqn) S_n$ (the period of the chain is taken equal to unity). The calculation in Ref. 17 leads to a final general expression:

$$S^{zz}(q,\omega)=\frac{1}{2}\sum_n G_n(q)\,\delta(\omega - n\omega_B), \qquad (208)$$

$$G_0=\frac{J_0^2(\zeta)}{\cosh(\beta\omega_B/2)-\cos q}, \qquad (209)$$

$$G_n=\frac{J_n^2(\zeta)}{2\sin^2(q/2)}\begin{cases} 1, & n>0,\\ e^{n\beta\omega_B}, & n<0,\end{cases} \qquad (210)$$

where ω_B is the Bloch oscillation frequency, β, as usual, is the inverse absolute temperature, and the parameter $\zeta = (\Delta/\mu_0 H)|\sin q|$. We note that relation (208) is a direct indication of the possibility of ''imaging'' the Wannier–Stark ladder. A soliton originally found in a state with a fixed value of n may be transferred to another state. The intensity of excitation of the nth level is proportional to J_n^2 and is controlled by the value of the parameter ζ.

It is of interest to analyze relation (208) in the limit of vanishingly small wave number q:[17]

$$S_b^{zz}(q\to 0,\omega)\to \frac{\partial(\omega)}{4\sinh(\beta\mu_0 H)}+\left(\frac{\Delta}{2\mu_0 H}\right)^2 \times[\,\delta(\omega-\omega_B)+e^{\beta\omega}\delta(\omega+\omega_B)]. \qquad (211)$$

Expression (211) enables one to calculate rather simply the imaginary part of the uniform magnetic susceptibility of the system under study:[17]

$$\chi''(\omega)=\frac{1}{2}\left(\frac{\Delta}{\mu_0 H}\right)^2(1-e^{-\beta\omega_B})[\,\delta(\omega-\omega_B) - \delta(\omega+\omega_B)]. \qquad (212)$$

Formulas (211) and (212) describe the response of a single chain containing an isolated soliton. In a sample with a large number of chains, each of which may contain many uncorrelated solitons, the total result is obtained by multiplying the given expressions by the integer number of solitons. As a result, the signal becomes fully measurable.

As we want to obtain some quantitative estimates, let us give the characteristics of magnetic materials which are now considered to be genuine candidates as subjects for the measurements under discussion. A rather complete set of experimentally obtained magnetic parameters (those described in Ref. 59) is available for the substance $CoCl_2\cdot 2H_2O$ (see Ref. 17 for the magnetic properties of this salt and the corresponding parameters). $CoCl_2\cdot 2H_2O$ is a ferromagnet of the Ising type with spin 1/2, and its magnetic structure consists of chains formed by the magnetic ions Co with a ferromagnetic interaction along the chains and an antiferromagnetic interaction between chains. The parameters of the exchange interaction along the chains are as follows: exchange integral of the Ising interaction $J^z = 18.3$ K, and biaxial exchange interaction characterized by the quantities $J^y - J^x = 3.7$ K and

$J^x + J^y = 5.6$ K. The presence of a weak antiferromagnetic interaction between chains leads to the circumstance that 3D ordering occurs at 17 K, with the result that at lower temperatures and in weaker longitudinal magnetic fields, half of the chains are polarized along the field and half are polarized against it. As the field strength increases, the system first undergoes a transition to a ferrimagnetic state and then to a 3D ferromagnetic state (the chains themselves are ferromagnetically ordered in any magnetic field).

We neglect the interchain interaction and consider an isolated chain in a static and uniform external magnetic field $H^z_{\rm ext}$. We have mentioned that a single-soliton description can be used if the condition $\mu_0 H < J^z$ holds. For the parameters indicated above this means that the magnetic field should not exceed 4 T. For estimates the authors of Ref. 17 propose to take the magnetic field as 1.8 T. Then on the basis of formula (206) it is easy to find that the amplitude of the oscillations is of the order of the interatomic distance, and the frequency of the Bloch oscillations is approximately 150 GHz. The first estimate holds forth the hope that various types of scattering can be avoided, and the second estimate falls in the range of possibilities for neutron experiments. To determine the interchain effects it is sufficient to use the mean field approximation, as was done in Ref. 60. The effective field acting on an individual chain in such a treatment is made up of the external field and a self-consistent internal field. Therefore the magnetic field required for excitation of Bloch oscillations with an amplitude of the order of the interatomic distance is renormalized in all phases: a magnetic field of 2.8 T is required in the 3D antiferromagnetic phase, a field of 3.6 T in the ferrimagnetic phase, and a field of 5.2 T in the ferromagnetic phase. These estimates show that the compound in question is entirely suitable for use as a material in which to observe Bloch oscillations of magnetic solitons.

Materials which have structures close to that of the salt described above include the following complex compounds: $[(CH_3)_3NH]CoCl_3\cdot 2H_2O$, $CoCl_2\cdot 2NC_5H_5$, and $[(CH_3)_3NH]FeCl_3\cdot 2H_2O$. These substances are described in Refs. 60 and 62, respectively; they are ferromagnets of the Ising type, with a more pronounced one-dimensionality of the magnetic structure than in $CoCl_2\cdot 2H_2O$. The latter circumstance is because the spin magnetic chains in these materials are separated by larger molecules, and one therefore expects that the interchain interaction in them is weaker. However, their magnetic parameters have so far been studied in less detail (for example, it is unclear whether the degree of biaxiality of the magnetic anisotropy in them is sufficient to avoid the need of a more complicated combination of magnetic fields for observation of Bloch oscillations).

In addition to the quasi-1D ferromagnets of the Ising type with extremely anisotropic exchange, there exist 1D ferromagnets with an isotropic exchange interaction but with strong single-ion anisotropy.[63,64] They belong to a family of isostructural orthorhombic quasi-1D compounds of the type mentioned above, with the general formula $[(CH_3)_3NH]MCl_3\cdot 2H_2O$, where the magnetic ion M is Ni, with spin $S=1$. These are crystals in which the Ni magnetic chains are separated by organic molecules. A typical member of this class of magnets is the compound TMANC. In this compound the magnetic anisotropy is substantially biaxial, having an anisotropy constant along the easiest axis which is of the same order as the exchange interaction constant. The quasi-1D ferromagnet TMANC can be described by a discrete quantum Heisenberg model with a Hamiltonian

$$\mathcal{H} = J\sum_n S_n S_{n+1} - D_1\sum_n (S^z_n)^2 - D_2\sum_n (S^x_n)^2.$$

Estimatory data for the parameters J, D_1, and D_2 can be found in Ref. 64. Importantly, the parameter ratios $D_1/J = 0.7$ and $D_2/D_1 = 0.3$ confirm the large value of the single-ion anisotropy energy. Using the magnetic length in the Landau–Lifshitz equations ($l_0 = \sqrt{\alpha/\beta}$) as a rough guide, one can estimate the width of a domain wall in the magnets under discussion as $l_0 = a\sqrt{J/D_1}$, where a is the lattice constant. It follows from the above estimates that these magnetic chains can have ''discrete'' domain walls with a width of the order of the lattice constant. Therefore such materials can be considered as suitable candidates on which to study the dynamics of domain walls and Bloch oscillations in a uniform magnetic field.

I am profoundly grateful to my coauthors on the papers used in writing this review. I thank Mikhail Bogdan for helpful discussions of the possibilities for observation of Bloch oscillations, and I express my heartfelt gratitude to Marina Mamalui for enormous assistance in the preparation of the manuscript. This study was supported in part by an INTAS grant from 1999.

APPENDIX

Features of the quasiclassical motion of a particle with a periodic dispersion relation in a highly nonuniform potential field

Consider the 1D dynamics of a quasiparticle with a dispersion relation of the type $\varepsilon = \varepsilon(p) = \varepsilon(p + p_0)$, where p_0 is the period in p space; it is assumed that $\varepsilon_{\min} = 0$. For example, one can take $\varepsilon = \varepsilon_0 \sin^2(\pi p/p_0)$, where ε_0 is the width of the energy band. We assume that the particle is moving in the field of a highly nonuniform potential $U(x)$, which does not affect its ''kinetic energy'' $\varepsilon(p)$. We assume that the particle obeys the classical equation of motion mentioned repeatedly in the main text:

$$\frac{dp}{dt} = -\frac{\partial U}{\partial x}, \quad v = \frac{\partial \varepsilon}{\partial p}.$$

For definiteness we shall use a dependence $\varepsilon = \varepsilon_0 \sin^2(\pi p/p_0)$ and assume that over a half period $0 < p < p_0/2$ the function $\varepsilon(p)$ is monotonic and, hence, the velocity $v = \partial\varepsilon/\partial p$ goes to zero at $p = 0$ and $p = p_0/2$. It is also convenient to assume that $\varepsilon_{\min} = \varepsilon(0)$. Then on the basis of the energy conservation equation

$$\varepsilon(p) + U(x) = E = \text{const},$$

one can give a rather complete qualitative analysis of the dynamics of such a particle. Without setting forth the perfectly obvious arguments by which the dynamics of 1D motion can be understood, we note the most interesting (and sometimes unusual) properties of the motion of the particle under study.

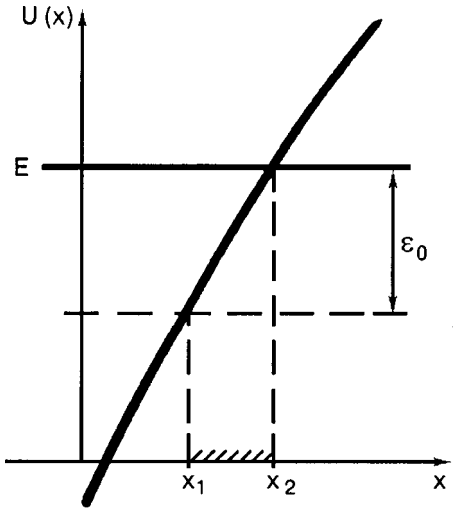

FIG. 16. Region of allowed motion (x_1, x_2) of a band quasiparticle in a potential with a large gradient.

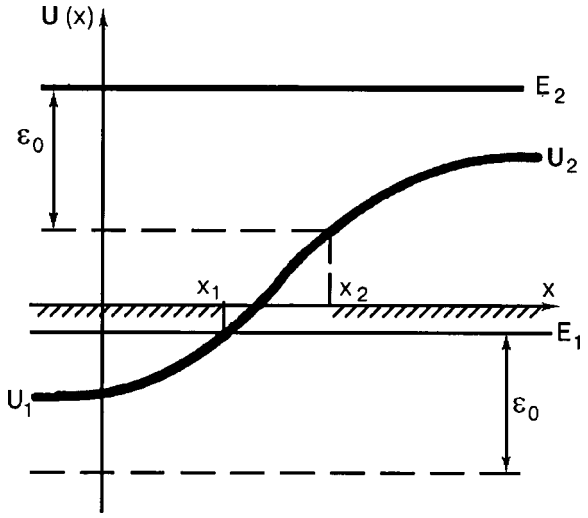

FIG. 18. "Superbarrier" repulsion of a quasiparticle by a nonuniform potential.

1. If the "fall" of the potential relief at distances Δx of the order of the amplitude of the Bloch oscillations is greater than the width of the energy band of the particle, then it will execute oscillatory motion at an arbitrary steepness of the potential relief and any sign of U. In Fig. 16 the region of reciprocating motion of the particle corresponds to the interval (x_1, x_2).

2. At the bottom of the potential well the particle executes oscillations reminiscent of the vibrational motion of an ordinary particle in such a well [in Fig. 17a the region of vibrations is the interval $(x_1, x_2]$. However, if it happens that $E-\varepsilon_0 > U_{\min}$, as is shown in Fig. 17b, then the vibrational motion takes on the character of Bloch oscillations in a uniform field and will occur either in the interval (x_1, x_2) or in (x_3, x_4), depending on the initial conditions.

3. A step of the potential relief can lead to infinite motion of the particle on one semiaxis on each side of the step. For the step in Fig. 18 this is possible both at an energy $U_1 < E_1 < U_2$, in which case the motion occurs on the semiaxis $-\infty < x < x_1$, and at an energy $E_2 > U_2$, in which case the region of infinite motion is $x_2 < x < \infty$. If the step is sufficiently high $(U_2 - U_1 > \varepsilon_0)$, then it can cause localization of the particle, constraining it to execute Bloch oscillations in the inflection region.

4. An analogous treatment leads to the conclusion that a potential well of finite depth can be an insurmountable obstacle for a particle, like a potential barrier for an ordinary particle (Fig. 19). It follows from this figure that if $E-\varepsilon_0 < U(\infty)$, then the potential well reflects the particle, constraining it to move either in the interval $-\infty < x < x_1$ or in the interval $x_2 < x < \infty$.

5. Finally, in regard to the "superbarrier motion" of the particle in the case of a potential barrier of finite height (Fig. 20), if $E-\varepsilon_0 < U_{\max}$ the particle is "trapped" by the potential hump and executes oscillatory motion about its apex.

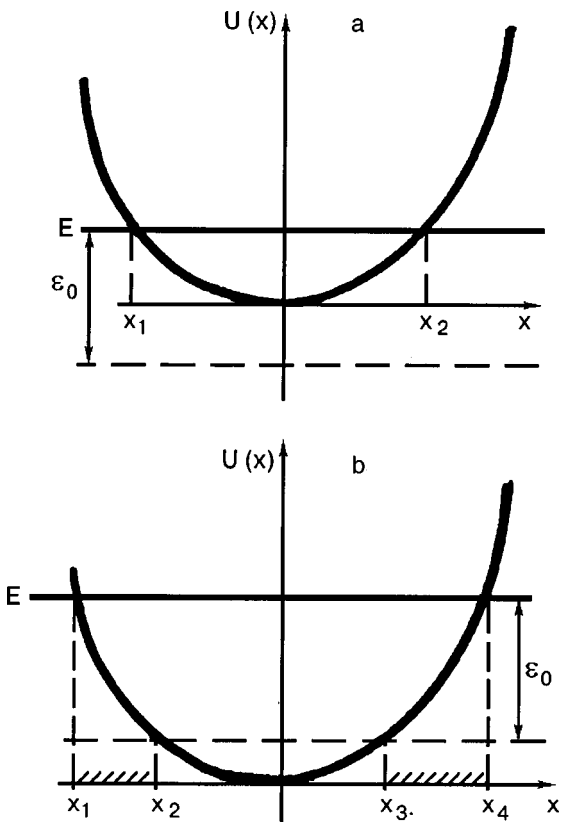

FIG. 17. Vibrational motion of a quasiparticle near the bottom of a potential well at small energy E (a); near the walls of the potential well at large energy E (b).

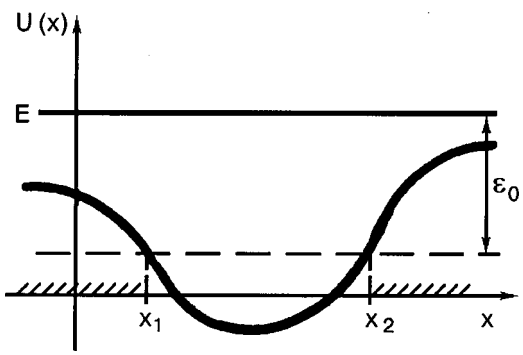

FIG. 19. A potential well repulses a particle whose energy is initially higher than the potential at infinity.

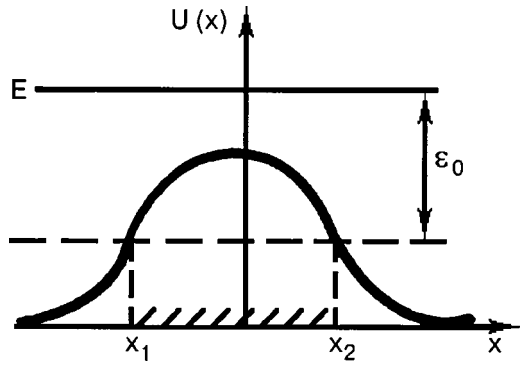

FIG. 20. Trapping of a quasiparticle by a potential hump.

The change in the role of the potential well and potential barrier in the situations described can easily be understood by introducing in place of the particle with energy $\varepsilon(p)$ an analog of the ''hole'' in electronic theory, i.e., a quasiparticle with energy $\varepsilon(p)=\varepsilon_0-\varepsilon(p)$, and reckoning the energy from the top edge of the energy band. Here the effective potential changes sign, as it were, and therefore the potential well and potential barrier ''change places.''

*)E-mail: kosevich@ilt.kharkov.ua

[1]The results of the numerical calculations shown in Figs. 3 and 4 agree with the recent results[25] obtained from a complete analytical description of the analogous dynamics of a Gaussian wave packet in a semiconductor superlattice.

[2]In Ref. 42 it was shown that this periodicity of the soliton dispersion relation is of a topological nature.

[3]For the chosen sign of the soliton charge Q the ''force'' F in Eq. (200) differs in sign from F in (29).

[1] F. Bloch, Z. Phys. **52**, 555 (1928); C. Zener, Proc. R. Soc. London, Ser. A **145**, 523 (1934).
[2] I. M. Lifshits, M. Ya. Azbel', and M. I. Kaganov, *Electronic Theory of Metals* [in Russian], Nauka, Moscow (1971).
[3] A. A. Abrikosov, *Fundamentals of the Theory of Metals* [in Russian], Nauka, Moscow (1987).
[4] C. Kittel, *Quantum Theory of Solids* [Wiley, New York (1963); Nauka, Moscow (1967)].
[5] L. Esaki and R. Tsu, IBM J. Res. Dev. **14**, 61 (1970).
[6] C. Wannier, Phys. Rev. **117**, 432 (1960); T. Mendes, F. Agullo-Rueda, and J. Hong, Phys. Rev. Lett. **60**, 2426 (1988); P. Voisin, J. Bleuse, C. Bouche, S. Gaillard, C. Albert, and A. Regreny, Phys. Rev. Lett. **61**, 1639 (1988).
[7] J. Feldman, K. Leo, J. Shah, D. A. Miller, J. E. Conningham, T. Meier, G. von Plessen, A. Shulze, P. Thomas, and S. Schmitt-Rink, Phys. Rev. B **46**, 7952 (1992); K. Leo, P. H. Bolivar, F. Brueggemann, R. Schwedler, and K. Koehler, Solid State Commun. **84**, 943 (1992).
[8] C. Waschke, H. Roskos, R. Schwedler, K. Leo, H. Kurz, and K. Koehler, Phys. Rev. Lett. **70**, 3319 (1993).
[9] A. N. Omel'yanchuk, G. A. Gogadze, and I. O. Kulik, Fiz. Nizk. Temp. **6**, 40 (1980) [Sov. J. Low Temp. Phys. **6**, 19 (1980)].
[10] A. M. Kosevich and I. D. Wagner, Fiz. Nizk. Temp. **25**, 868 (1999) [Low Temp. Phys. **25**, 650 (1999)].
[11] N. Pertsch, P. Dannberg, W. Elflein, and A. Braeuer, Phys. Rev. Lett. **83**, 4752 (1999).
[12] R. Morandotti, U. Perschel, and J. S. Aitchison, Phys. Rev. Lett. **83**, 4756 (1999).
[13] D. Cai, A. R. Bishop, N. Cronbech-Jensen, and M. Salerno, Phys. Rev. Lett. **74**, 1186 (1995).
[14] J. C. Slonczewski, Int. J. Magn. **2**, 85 (1972).
[15] D. Loss, ''Quantum dynamics in mesoscopic magnetism,'' in *Quantum Tunneling in Magnetism. Proc. NATO*, Conathtyce, Kluwer, Dordrecht (1995).
[16] H.-B. Braun and D. Loss, J. Appl. Phys. **76**, 6177 (1994).
[17] J. Kyriakidis and D. Loss, Phys. Rev. B **58**, 5568 (1998).
[18] A. M. Kosevich, Physica D **119**, 134 (1998).
[19] A. M. Kosevich, V. V. Gann, F. D. Zhukov, and V. P. Voronov, Zh. Éksp. Teor. Fiz. **114**, 735 (1998) [JETP **87**, 401 (1998)].
[20] I. M. Babich and A. M. Kosevich, Fiz. Nizk. Temp. **27**, 46 (2001) [Low Temp. Phys. **27**, 35 (2001)].
[21] M. Gluck, A. R. Kolovski, and H. J. Korsch, Phys. Lett. A **249**, 483 (1998); *ibid.* **82**, 1534 (1999).
[22] M. Luban, J. Math. Phys. **26**, 2386 (1985).
[23] U. Peschel, T. Pertsch, and F. Lederer, Opt. Lett. **23**, 1701 (1998).
[24] I. S. Gradshteyn and I. M. Ryzhik, *Tables of Integrals, Series, and Products* [Academic Press, New York (1980); Gostekhizdat, Moscow (1963)].
[25] W. I. Puller, N. J. M. Horing, L. G. Mourokh, and A. Yu. Smirnov, Phys. Lett. A **281**, 70 (2001).
[26] D. H. Dunlap and V. M. Kenkre, Phys. Rev. B **34**, 3625 (1986).
[27] D. H. Dunlap and V. M. Kenkre, Phys. Lett. A **127**, 438 (1988).
[28] V. E. Zakharov, S. V. Manakov, S. P. Novikov, and L. P. Pitaevskiĭ, *Theory of Solitons. Method of the Inverse Problem* [in Russian], Nauka, Moscow (1980).
[29] A. M. Kosevich, Physica D **41**, 253 (1990).
[30] A. Hasegawa, *Optical Solitons in Fibers*, Springer-Verlag, Berlin (1989).
[31] M. A. Ablowitz and J. F. Ladik, J. Math. Phys. **17**, 1011 (1976).
[32] L. D. Faddeev and L. A. Takhtajan, *Hamiltonian Methods in the Theory of Solitons*, Springer, Berlin (1987).
[33] R. Schart and A. Bishop, Phys. Rev. A **43**, 6535 (1991).
[34] L. D. Landau and E. M. Lifshitz, Phys. Z. Sowjetunion **8**, 153 (1935); L. D. Landau and E. M. Lifshitz, ''Contribution to the theory of the magnetic susceptibility of ferromagnetic objects,'' in *Collected Works of L. D. Landau* [in Russian], Nauka, Moscow (1989), Vol. 1, p. 128.
[35] L. D. Landau and E. M. Lifshits, *Statistical Physics*, 3rd ed. (with L. P. Pitaevskiĭ), Part 2, Pergamon Press, Oxford (1980); Nauka, Moscow (1978).
[36] V. G. Bar'yakhtar, Zh. Éksp. Teor. Fiz. **87**, 1501 (1984) [Sov. Phys. JETP **60**, 863 (1984)].
[37] V. G. Bar'yakhtar, B. A. Ivanov, T. K. Soboleva, and A. L. Sukstanskiĭ, Zh. Éksp. Teor. Fiz. **91**, 1454 (1986) [Sov. Phys. JETP **64**, 857 (1986)].
[38] K. B. Vlasov and L. G. Onoprienko, Fiz. Met. Metalloved. **15**, 47 (1963).
[39] V. M. Tsukernik, Fiz. Tverd. Tela (Leningrad), **10**, 1006 (1968) [Sov. Phys. Solid State **10**, 795 (1968)].
[40] A. Hubert, *Theorie der Domänenwände in Geordneten Medien*, Springer-Verlag, Berlin (1974); Mir, Moscow (1977).
[41] A. M. Kosevich, B. A. Ivanov, and A. S. Kovalev, *Nonlinear Magnetization Waves. Dynamical and Topological Solitons* [in Russian], Naukova Dumka, Kiev (1983); A. M. Kosevich, B. A. Ivanov, and A. S. Kovalev, Phys. Rep. **194**, 117 (1990).
[42] E. A. Galkina and B. A. Ivanov, JETP Lett. **71**, 259 (2000).
[43] A. M. Kosevich, ''Dynamical and topological solitons in ferromagnets and antiferromagnets,'' in *Solitons*, edited by S. E. Trullinger, V. E. Zakharov, and V. L. Pokrovsky, Elsevier, Amsterdam (1986).
[44] L. R. Walker, quoted by F. Dillon, ''Dynamics of domain walls,'' in *Magnetism*, edited by G. T. Rado and H. Suhl, Plenum Press, New York (1963), Vol. 3, p. 321.
[45] I. A. Akhiezer and A. E. Borovik, Zh. Éksp. Teor. Fiz. **52**, 508 (1967) [Sov. Phys. JETP **25**, 332 (1967)]; **52**, 1332 (1967); **25**, 885 (1967).
[46] A. P. Malozemoff and J. C. Slonczewski, *Magnetic Domain Walls in Bubble Materials* [Academic Press, New York (1979); Mir, Moscow (1982)].
[47] V. N. Eleonskiĭ, N. N. Kirova, and E. H. Kulagin, Zh. Éksp. Teor. Fiz. **76**, 705 (1979) [Sov. Phys. JETP **49**, 352 (1979)].
[48] J. Villain, Physica B **79**, 1 (1985).
[49] H.-J. Mikeska and M. Steiner, Adv. Phys. **40**, 191 (1991).
[50] N. Ishimura and H. Shiba, Prog. Theor. Phys. **63**, 743 (1980).
[51] N.-B. Braun and D. Loss, Int. J. Mod. Phys. B **10**, 219 (1996).
[52] H. Yoshizawa, K. Hirakawa, S. K. Satija, and G. Shirane, Phys. Rev. B **23**, 2298 (1981).
[53] J. P. Boucher, L. P. Regnault, J. Rossat-Mignot, and B. Briat, Phys. Rev. Lett. **49**, 590 (1992).
[54] S. E. Nagler, W. J. L. Buyers, R. L. Armstrong, and B. Briat, Phys. Rev. B **28**, 3873 (1983).
[55] K. Adachi, J. Phys. Soc. Jpn. **50**, 3904 (1981); J. P. Boucher, G. Rius, and Y. Henry, Europhys. Lett. **4**, 1073 (1987); H. Kikuchi and Y. Ajiro, J. Phys. Soc. Jpn. **58**, 2531 (1989).
[56] I. Mogi, N. Kojima, Y. Ajiro, H. Kikuchi, T. Ban, and I. Tsijikawa, J. Phys. Soc. Jpn. **56**, 4592 (1987).
[57] Y. Ajiro, H. Kikuchi, T. Okita, M. Chiba, K. Adachi, M. Mekata, and

T. Goto, J. Phys. Soc. Jpn. **58**, 390 (1989); T. Kohmoto, T. Goto, S. Maegawa, N. Judjiwara, Y. Fukuda, M. Kunitomo, and M. Mekata, Phys. Rev. B **57**, 2936 (1998).
[58] Y. Imry, *Introduction to Mesoscopic Physics*, Oxford University Press (1997).
[59] J. B. Torrance Jr. and M. Tinkham, Phys. Rev. **187**, 595 (1969); D. F. Nicoli and M. Tinkham, Phys. Rev. B **9**, 3126 (1974).
[60] K. Takeda, S.-I. Matukawa, and T. Haseda, J. Phys. Soc. Jpn. **30**, 1330 (1971).
[61] K. Takeda and M. Wada, J. Phys. Soc. Jpn. **50**, 3603 (1981).
[62] R. E. Greeney, C. P. Landee, J. H. Zang, and W. M. Reiff, Phys. Rev. B **39**, 12200 (1989).
[63] R. Hoogerbeets, S. A. J. Wiegers, A. I. van Duyneveldt, R. D. Willet, and V. Geiser, Physica B & C **125**, 135 (1984).
[64] A. G. Anders, V. G. Borisenko, S. V. Volotzkii, and Yu. V. Pereverzev, Fiz. Nizk. Temp. **15**, 39 (1989) [Sov. J. Low Temp. Phys. **15**, 21 (1989)].

Translated by Steve Torstveit

SUPERCONDUCTIVITY, INCLUDING HIGH-TEMPERATURE SUPERCONDUCTIVITY

$2\sqrt{2}\times 2\sqrt{2}$ superstructures and charge transfer in $YBa_2Cu_3O_{6+x}$

A. A. Mamalui[a] and I. N. Sablin

Kharkov Polytechnical Institute National Engineering University, ul. Frunze 21, 61002, Kharkov, Ukraine
(Submitted January 25, 2001)
Fiz. Nizk. Temp. **27**, 738–742 (July 2001)

Anomalies of the kinetic and thermodynamic properties of $YBa_2Cu_3O_{6+x}$ ($x\sim 0.9$) in the normal state are interpreted as originating from the ordering of oxygen in the (001) CuO_x basal planes. A sequence of structural phase transitions is proposed, and the phases are analyzed by the method of static concentration waves. It is shown that the anomalous behavior of the resistivity and the relative elongation of the sample may be due to a charge transfer effect.
 [DOI: 10.1063/1.1388416]

INTRODUCTION

The study of the ordering of oxygen in the CuO_x planes of $YBa_2Cu_3O_{6+x}$ and the electronic structure interrelated with it has been the subject of many papers.[1–4] In Ref. 5 the Cu–O chains served as a reservoir of charge carriers. Together with a change in the oxygen index the carrier concentration in the CuO_2 conducting planes also changed by means of the charge transfer out of the chains, and, hence, the system can exhibit both insulator and metallic superconducting properties. In addition, it has been found that the resistivity in the normal state and the critical parameters in the superconducting state depend not only on the oxygen content but also on its degree of ordering.[6] In the Cu–O chains the copper can be found in two valence states: Cu^+ and Cu^{2+}, as is confirmed by ellipsometric measurements[7] and nuclear quadrupole resonance experiments.[8] In the first case, only two apical oxygen atoms O4 are found in the nearest-neighbor environment of the copper, while in the second case the copper is three- or fourfold coordinated. The improvement of the superconducting characteristics of $YBa_2Cu_3O_{6+x}$ for $x\sim 0.5$ (Ref. 6) is due to the formation of chains consisting of alternating Cu and O atoms, corresponding to a structural phase transition OI→OII accompanied by the addition of new holes in the CuO_2 layers. To calculate the contribution to the atom–vacancy ordering energy from the transfer of charge to the CuO_x basal planes as a system of highly correlated electrons, the widely used Hubbard model was employed. In the framework of this approach one can describe a number of properties specific to high-T_c superconductors, e.g., the metal–insulator transition. In the three-band Hubbard model used in Ref. 4, the mixed ionic–covalent character of the bonding was also taken into account. It is also advisable to consider other factors influencing the ordering of the oxygen. For example, increasing the oxygen concentration leads to a decrease in the volume of the unit cell, which, in turn, promotes the formation of a heterophase structure.[9] The participation of the long-range elastic forces plays a decisive role in the formation of the domain structure.[2]

Two types of vacancy superstructures are distinguished: chain and hexagonal or nearly hexagonal ''herringbone'' superstructures. In $YBa_2Cu_3O_{6+x}$ with a high oxygen concentration ($x\sim 1$) the stable superstructures at low temperatures are of the second type, viz., $2\sqrt{2}\times 2\sqrt{2}$, as has been confirmed both experimentally[10] and theoretically.[11] However, effects due to charge transfer can also be manifested in these phases.

In the present study we consider the sequence of structural phase transitions in $YBa_2Cu_3O_{6+x}$ with $x=0.9$ and the charge transfer related to them with the goal of explaining the anomalies observed in the temperature dependence of the resistivity[12] and the relative elongation of the samples.[13]

MODEL OF STRUCTURAL TRANSITION

In connection with the study of atom–vacancy ordering in the oxygen subsystem of $YBa_2Cu_3O_{6+x}$ a model with an asymmetric interaction in the second coordination sphere has been developed.[1] For the Cu–O chains the long-range Coulomb and elastic forces are important. As in Ref. 2, we shall consider the ordering in the basal plane, i.e., the effectively two-dimensional case. We initially have a square lattice of copper atoms with lattice parameter a. The oxygen occupies interstitial positions, which we denote as $(p,\mathbf{r})$, where the index p refers to the particular sublattice (the O(1) or O(5) positions), and $\mathbf{r}$ is the translation vector of the initial square lattice. The distribution of the oxygen atoms among the interstitial positions is characterized by a function $n(p,\mathbf{r})$, which is the probability that an oxygen atom will occupy the interstitial position $(p,\mathbf{r})$. The O–O interaction takes place by the long-range Coulomb and elastic forces, and this provides justification for restricting consideration to the mean field approximation. In that approximation the free energy has the form

$$F=\frac{1}{2}\sum_{p,\mathbf{r}}\sum_{q,\mathbf{r}'}W_{p,q}(\mathbf{r}-\mathbf{r}')n(p,\mathbf{r})n(q,\mathbf{r}')$$
$$+k_BT\sum_{p,\mathbf{r}}(n(p,\mathbf{r})\ln n(p,\mathbf{r})$$
$$+(1-n(p,\mathbf{r}))\ln(1-n(p,\mathbf{r})))-\mu\sum_{p,\mathbf{r}}n(p,\mathbf{r}), \quad (1)$$

where $W_{p,q}$ is the interaction energy of oxygen atoms found in the positions $(p,\mathbf{r})$ and $(q,\mathbf{r}')$, k_B is Boltzmann's constant, and μ is a Lagrange undetermined multiplier, which plays the role of the chemical potential. The equation of the self-consistent field can be obtained by equating to zero the first variation of the free energy (1) with respect to $n(p,\mathbf{r})$:

$$n(p,\mathbf{r})=\left\{\exp\left[-\frac{\mu}{k_BT}+\frac{1}{k_BT}\sum_{q,\mathbf{r}'}W_{p,q}(\mathbf{r}-\mathbf{r}')n(q,\mathbf{r}')\right]+1\right\}^{-1}. \tag{2}$$

It is convenient to use Khachaturyan's method, in which the solution of equation (2) is sought in the form a superposition of the static concentration waves.[2,14]

As in Ref. 15, we shall use a model of the O–O interaction that corresponds to an anisotropic screened Coulomb repulsion:

$$W_{p,q}(\mathbf{r}-\mathbf{r}')=\left\{\begin{array}{ll}\dfrac{z^2}{r_i}\exp\left(\dfrac{r_i}{r_d}\right)+\delta W_i, & i\neq 2\\ (1\pm f)\dfrac{z^2}{a}\exp\left(-\dfrac{a}{r_d}\right)+\delta W_2, & i=2\end{array}\right\}, \tag{3}$$

where r_i is the radius of the ith O–O coordination sphere, z is the effective charge of the oxygen, f is the anisotropy factor for the second coordination sphere (the minus sign being used if there is a copper atom between the oxygen atoms), and δW_i is the correlation to the screened Coulomb interaction in the ith coordination sphere due to spatial dispersion of the dielectric constant.[16]

RESULTS AND DISCUSSION

For studying the ordering that occurs in the $YBa_2Cu_3O_{6+x}$ system with $x=0.9$ we use the results of Refs. 12 and 13, where the resistivity[12] and the relative elongation[13] of the sample were measured in the temperature interval 450–650 K with isothermal holds. Figure 1 shows the curves of the temperature dependence of the ratio of the resistivity ρ_t, which depends on the time of the isothermal hold, to ρ_0, determined for $t=0$; the curves were obtained as isochronal sections of the experimental isotherms. The presence of a temperature region in which $\Delta\rho_t/\rho_0$ is negative is a characteristic feature. An analogous dependence was observed for the relative elongation $\Delta l/l$ of the sample.[13]

The studies of Refs. 12 and 13 supplement the experimental data of Refs. 17–19, which were used in Ref. 16 as a basis for choosing the model of the O–O interaction and the sequence of phase transitions OI→OII→$(2\sqrt{2}\times 2\sqrt{2})_1$ →OIII(3×1) for $YBa_2Cu_3O_{6+x}$ with $x=0.75$. The temperatures of the structural transitions were estimated over a wide range of concentrations $0.5<x<0.8$ by studying the relaxation behavior of the superconducting transition temperature after various heat treatments[17] and also on the basis of the neutron-diffraction studies.[18,19]

To achieve the best agreement with the experiments,[12,13] we proposed the following sequence of structural transitions

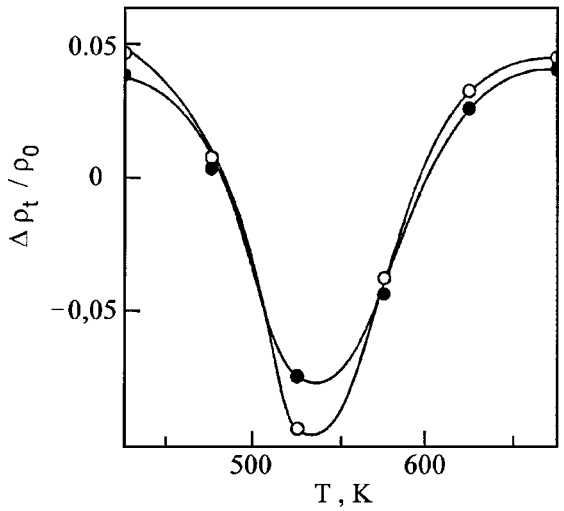

FIG. 1. Temperature dependence of the ratio of the resistivity ρ_t, which depends on the time of the isothermal hold, to ρ_0, determined for $t=0$, in a $YBa_2Cu_3O_{6.9}$ sample; $t=5$ h (●), $t=7$ h (○).

for $x=0.9$: OI→OII→$(2\sqrt{2}\times 2\sqrt{2})_1$→$(2\sqrt{2}\times 2\sqrt{2})_2$. At low temperatures in $YBa_2Cu_3O_{6+x}$ with $x\sim 0$ and $x\sim 1$ the superstructure $(2\sqrt{2}\times 2\sqrt{2})$ is more stable, in agreement with the results of Refs. 10 and 11. The superstructures $(2\sqrt{2}\times 2\sqrt{2})_1$ and $(2\sqrt{2}\times 2\sqrt{2})_2$ are illustrated in Fig. 2.

To simplify the calculations it is assumed that at the point of the OI→OII transition the orthorhombic phase OI is almost completely ordered, i.e., the oxygen atoms occupy only one of the sublattices. For this reason, when the symmetry of the OI phase is taken into account, the model described above can be reduced to one of ordering in a simple lattice under the influence of an interaction potential W_{22}. The OII, $(2\sqrt{2}\times 2\sqrt{2})_1$, and $(2\sqrt{2}\times 2\sqrt{2})_2$ phases are then described by the functions

$$\begin{aligned}n_1&=x+\eta_1\cos(\mathbf{k}_1'\mathbf{r}),\\ n_2&=x+\eta_1\cos(\mathbf{k}_1'\mathbf{r})+\eta_2[\cos(\mathbf{k}_2'\mathbf{r})+\sin(\mathbf{k}_2'\mathbf{r})\\ &\quad+\cos(\mathbf{k}_2''\mathbf{r})+\sin(\mathbf{k}_2''\mathbf{r})],\\ n_3&=x+\eta_1[\cos(\mathbf{k}_1'\mathbf{r})+\cos(\mathbf{k}_1''\mathbf{r})]+\eta_2[\cos(\mathbf{k}_2'\mathbf{r})\\ &\quad+\cos(\mathbf{k}_2''\mathbf{r})]+\eta_3\cos(\mathbf{k}_3'\mathbf{r}),\end{aligned} \tag{4}$$

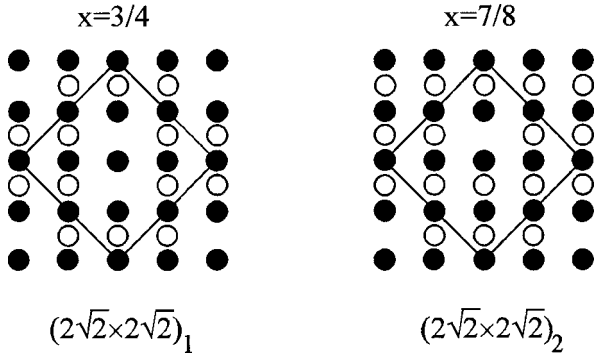

FIG. 2. Superstructures $(2\sqrt{2}\times 2\sqrt{2})_1$ and $(2\sqrt{2}\times 2\sqrt{2})_2$; oxygen atom (○), copper atom (●).

where η_1, η_2, and η_3 are order parameters with the following wave vectors:

$$\mathbf{k}_1' = \frac{2\pi}{a}\left(\frac{1}{2}0\right), \quad \mathbf{k}_1'' = \frac{2\pi}{a}\left(0\,\frac{1}{2}\right),$$

$$\mathbf{k}_2' = \frac{2\pi}{a}\left(\frac{1}{4}\,\frac{1}{4}\right), \quad \mathbf{k}_2'' = \frac{2\pi}{a}\left(\frac{\overline{1}}{4}\,\frac{1}{4}\right),$$

$$\mathbf{k}_3 = \frac{2\pi}{a}\left(\frac{1}{2}\,\frac{1}{2}\right).$$

Stoichiometry is attained for the corresponding phases at $x_1 = \eta_1 = 1/2$; $x_2 = 3/4$, $\eta_1 = \eta_2 = -1/4$; $x_2 = 7/8$, $\eta_1 = \eta_3 = -1/8$, $\eta_2 = -1/4$. Substituting (4) into the equation of the self-consistent field (2), we obtain a system of transcendental equations for the order parameters, enabling us to consider their temperature dependence. The temperatures of the structural transitions were determined from the condition of equality of the free energies of the successive phases. The choice of parameters of the O–O interaction was restricted by requiring that the exact sequence of transitions be followed, that the transitions OI→OII and $(2\sqrt{2}\times 2\sqrt{2})_1 \rightarrow (2\sqrt{2}\times 2\sqrt{2})_2$ occur at the temperatures 500 and 600 K, and that phases which order according to other superstructure vectors do not appear. Only four coordination spheres were considered, and the redistribution of oxygen between sublattices, as we have said, was neglected; the following values were used for the parameters of the O–O potential:

$$\frac{z^2}{a} = 5015\,\mathrm{K}; \quad r_d = \sqrt{5}a; \quad \delta W_2 = 0;$$

$$\delta W_3 = -281\,\mathrm{K}, \quad \delta W_4 = 98\,\mathrm{K}. \tag{5}$$

The fraction f of twofold coordinated copper is a characteristic that can serve as a quantitative measure of the effect of charge transfer. Knowing the function $n(\mathbf{r})$ for each superstructure, we can easily calculate the parameter f, which is a characteristic of the short-range order,[20] by employing the mean field approximation adopted here and neglecting correlations. The temperature dependence of f is given in Fig. 3. From a comparison of Figs. 1 and 3 we can conclude that the behavior of the resistivity and the variation of the parameter f are interrelated.

In the temperature interval 500–600 K the number of holes in the CuO_2 layers increases upon the ordering under study, and that leads to the observed decrease of the resistivity. The appearance of new current carriers is accompanied by a decrease in the charge of the copper atoms in the CuO_x layers upon the transition $Cu^{2+} \rightarrow Cu^{+}$. For this reason, in $YBa_2Cu_3O_{6+x}$, as occurs upon an increase in the oxygen index x, the Ba ions can be more strongly attracted by the CuO_x planes; as a result, the lattice parameter c decreases, as is reflected in the dilatometric measurements.[13]

Thus $YBa_2Cu_3O_{6+x}$ undergoes a sequence of structural phase transitions OI→OII→$(2\sqrt{2}\times 2\sqrt{2})_1$→$(2\sqrt{2}\times 2\sqrt{2})_2$ in the temperature interval 500–600 K. In this temperature interval the stable phases are OII and $(2\sqrt{2}\times 2\sqrt{2})_1$, in which charge transfer to the conducting planes occurs, causing anomalous behavior of the physical properties of $YBa_2Cu_3O_{6+x}$.

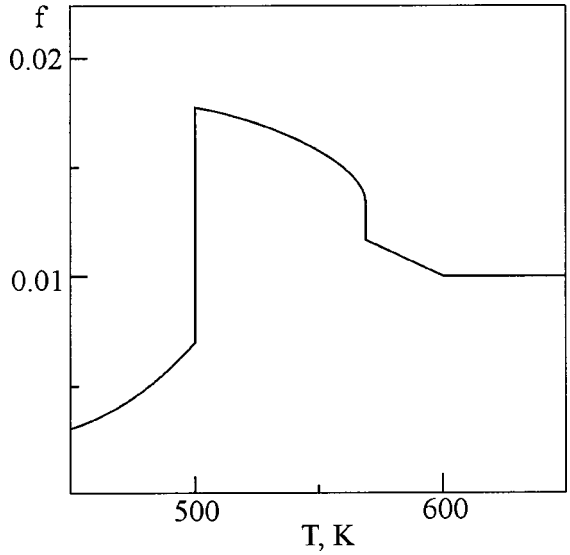

FIG. 3. Temperature dependence of the fraction f comprised of twofold coordinated copper in the CuO_x layers of $YBa_2Cu_3O_{6.9}$.

[a)]E-mail: mamalui@kpi.kharkov.ua

[1] L. T. Wille, A. Berera, and D. de Fontaine, Phys. Rev. Lett. **60**, 1065 (1988).
[2] S. Semenovskaya and A. G. Khachaturyan, Phys. Rev. B **46**, 6511 (1992).
[3] G. V. Uimin and J. Rossat-Mignod, Physica C **199**, 6251 (1992).
[4] A. A. Aligia and J. Garces, Phys. Rev. B **49**, 524 (1994).
[5] R. J. Cava, Physica C **195**, 419 (1990); R. J. Cava, Science **247**, 656 (1990).
[6] B. W. Veal, A. P. Paulicas, Hoydoo You, Hao Shi, Y. Fang, and J. W. Downey, Phys. Rev. B **42**, 6305 (1990).
[7] J. Kircher, E. Brücher, E. Schönherr, R. K. Kremer, and M. Gardona, Phys. Rev. B **46**, 588 (1992).
[8] W. W. Warren, Jr., R. E. Walstedt, G. F. Brennert, R. J. Cava, B. Batlogg, and L. W. Rupp, Phys. Rev. B **39**, 831 (1989).
[9] A. A. Aligia, J. Garces, and J. P. Abriata, Physica C **221**, 109 (1994).
[10] M. A. Alario-Franco, C. Chaillout, J. J. Capponi, J. Chenavas, and M. Marezio, Physica C **156**, 455 (1988).
[11] A. A. Aligia, S. Koval, and R. Migoni, Phys. Rev. B **57**, 1241 (1998).
[12] A. A. Mamalui and K. V. Bednov, Functional Materials **3**, 198 (1996).
[13] K. V. Bednov, A. A. Mamalui, N. B. Fatyanova, and I. N. Sablin, Functional Materials **7**, 256 (2000).
[14] A. G. Khachaturyan and G. A. Shatalov, Acta Metall. **23**, 1089 (1975).
[15] A. A. Aligia, J. Garces, and H. Bonadeo, Phys. Rev. B **42**, 10226 (1990).
[16] S. Semenovskaya and A. G. Khachaturyan, Phys. Rev. B **54**, 7545 (1996).
[17] S. Yang, H. Claus, B. V. Veal, R. Wheeler, A. P. Paulicas, and J. W. Downey, Physica C **193**, 243 (1992).
[18] W. Swartz, O. Blaschko, G. Collin, and F. Marucco, Phys. Rev. B **48**, 6513 (1993).
[19] Th. Zeiske, R. Sonntag, D. Hohlwein, N. H. Andersen, and T. Wolf, Nature (London) **353**, 542 (1991).
[20] L. A. Girifalco, *Statistical Physics of Materials* [Wiley, New York (1973); Mir, Moscow (1985)].

Translated by Steve Torstveit

Effect of multiplicative noise on the nonequilibrium properties of vortices in layered superconductors

T. S. Shaposhnikova[a)]

Kazan Science Center, E. K. Zavoĭskiĭ Kazan Physico-Technical Institute, Russian Academy of Sciences, ul. Sibirskiĭ trakt 10/7, 420029 Kazan, Russia

(Submitted March 5, 2001)
Fiz. Nizk. Temp. **27**, 743–751 (July 2001)

The conditions for the appearance of multiplicative noise in the vortex system of superconductors with pronounced layering are considered. A stochastic differential equation of motion is constructed for a pinned 2D vortex, and its stationary solution is found. The region of parameters of this equation in which a stochastic phase transition can occur in the vortex system is determined. An experimental scheme is proposed for observing such a transition by the method of power absorption from an alternating magnetic field. © *2001 American Institute of Physics.* [DOI: 10.1063/1.1388417]

INTRODUCTION

The two-dimensional (2D) character of vortices in high-T_c superconductors having a pronounced layered structure[1] leads to the appearance of many new states on the temperature–magnetic field phase diagram.[2,3] Studies of the dynamics of vortices in different regions of the phase diagram of high-T_c superconductors (HTSCs) have shown that in a large range of fields and temperatures there is an effective bulk pinning governed by the interaction of vortices with inhomogeneities of the material, such as oxygen vacancies, impurity atoms, twin boundaries in single crystals, and grain boundaries in ceramics. These ''internal'' pinning centers, like the pinning centers created artificially (e.g., pinning centers in the form of columns), have various characteristic sizes and energies, and the number of these centers can vary over wide limits.

One of the most important characteristics of a superconductor is the critical current, the value of which is determined, as a rule, by the averaged pinning potential,[4] while the distribution of currents over the volume is determined by the shape of the sample. The value of the critical current is substantially temperature-dependent, since a rise in temperature leads to an increase in the thermal fluctuations of the position of the vortices and to thermally activated depinning.[2,5,6] The studies of Refs. 7–10 are devoted to the influence of these thermal fluctuations of the position of the vortices on the value of the critical current,[8] the position of the line of depinning of the vortex lattice,[7,8] the dimensional transition in the vortex system,[9] and hysteresis of the modulated microwave absorption.[10]

Thermal fluctuations are treated by introducing a temperature-dependent random force in the equation of motion (see, e.g., Refs. 8 and 11). This force has the form of additive white noise, and when it is taken into account the position of the vortex becomes a random quantity characterized by a steady-state probability density $\rho_s(x)$ of the vortex position near the point x of the potential well. In the case of additive noise the positions of the extrema x_m of the probability density always coincide with the determinate steady-state equilibrium positions of the vortex,[12] and increasing the intensity of such noise leads only to a smearing of the probability density in the neighborhood of the determinate equilibrium position. In a superconductor through which a current is passed a low-frequency additive noise also appears,[13] which is due to hops of the flux bundles or to the formation of vortex avalanches in samples of $YBa_2Cu_3O_7$ (Refs. 14–18) and $Bi_2Sr_2CaCu_2O_8$ (Ref. 19).

We wish to call attention to the fact that in superconductors there also arises a multiplicative noise, which, unlike the additive noise, may be due to fluctuations of the parameters of the pinning potential itself or can have an external source. It is known[12] that if the intensity of the multiplicative noise exceeds a certain theoretical value, then the functional dependence $\rho_s(x)$ can change sharply, i.e., a stochastic phase transition can occur, at which new extrema appear in the stationary probability density $\rho_s(x)$. This means that, besides the disorganizing effect on the system which is also present in the case of additive noise, the multiplicative noise can give rise to new states and induce new nonequilibrium phase transitions, i.e., it can lead to situations in which the system no longer accommodates to the averaged characteristics of the medium but reacts to changes of the medium in a more active way. For example, some systems with multiplicative noise possess supersensitivity to weak alternating signals.[20]

In this paper we consider the conditions under which multiplicative noise appears in a system of 2D vortices in layered superconductors, leading to a stochastic phase transition, and discuss the features of the absorption of high-frequency power due to the onset of this stochastic phase transition. This article is arranged as follows. In Sec. 1 we introduce and discuss the stochastic equation of motion of a 2D vortex pinning at a point pinning center. In Sec. 2 we obtain the stationary solution of the stochastic equation (i.e., an expression for $\rho_s(x)$) and show that in certain cases a stochastic phase transition can arise in a system of pinned vortices. In Sec. 3 we discuss the main results and propose an experimental scheme for observing the phase transition. The main findings of this study are summarized in the Conclusion.

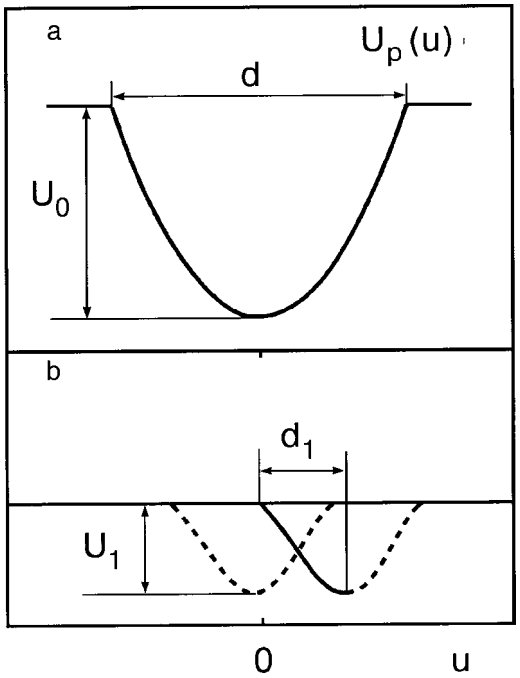

FIG. 1. Potentials in which a pinned 2D vortex oscillates: $U_p(\mathbf{u})$ is the pinning potential (a); the potential describing the interaction of a pinned and an unpinned 2D vortex (b). (Its position varies randomly with respect to $U_p(\mathbf{u})$. Two of a set of possible positions of the vortex are shown.)

1. STATEMENT OF THE PROBLEM. MODEL

We consider a type-II superconductor with pronounced layering and which is found in the mixed state. It is known that at high temperatures and high magnetic fields the system of vortices in layered superconductors decomposes into a system of 2D vortices (see, e.g., Refs. 2 and 3). We propose that in superconductors there exist effective pinning centers which confine around themselves only individual 2D vortices or their bundles, while the rest of the vortices remain free. Such a situation is apparently realized in layered HTSCs in the region of the temperature–magnetic field phase diagram where the critical current is either equal to zero or very small. We shall show that under certain conditions the interaction of a pinned 2D vortex with freely fluctuating 2D vortices can be described by multiplicative noise.

Let us consider such a 2D vortex, pinned at a point pinning center. Suppose that this center is described by a simple parabolic potential $U_p(\mathbf{u})$ (see Fig. 1a),[21]

$$U_p(u)=\begin{cases}\dfrac{4U_0}{d^2}u^2, & |u|\leqslant\dfrac{d}{2},\\[2ex] U_0, & |u|>\dfrac{d}{2},\end{cases} \tag{1}$$

where U_0 is the depth of the potential well and d is its spatial extent. It is known[22] that U_0 depends on the magnitude of the external static magnetic field H: the depth of the potential well increases as the magnetic field is lowered. For example, in $Bi_2Sr_2CaCu_2O_{8+x}$, where the pinning centers are oxygen vacancies, U_0 varies from 0.01 to 0.2 eV.[22] The width d of the well is of the order of several coherence lengths and is independent of the magnitude of the external field.

If a transport current J is passed through a superconductor, the equation of motion of a 2D vortex in the potential U_p under the influence of the Lorentz force $\mathbf{F}_L=[\mathbf{\Phi}_0\times\mathbf{J}]$ will have the form

$$\eta\dot{\mathbf{u}}=-\frac{\partial U_p(\mathbf{u})}{\partial\mathbf{u}}+\mathbf{F}_L, \tag{2}$$

where $\mathbf{u}$ is the displacement of the vortex from the equilibrium position, η is the viscosity of a 2D vortex,[23,24] and Φ_0 is the magnetic flux quantum.

It follows from the structure of highly layered superconductors that the superconducting layers in them alternate with nonsuperconducting interlayers (spacers),[1] and therefore a vortex line, even in the region of low fields and low temperatures, consists of 2D vortices interconnected by Josephson contacts. As the magnetic field is increased, the interaction of the vortices located on the same superconducting plane increases, and under the influence of various fluctuations the linear vortex decays into individual 2D vortices. Suppose that a pinned 2D vortex is found in the nth conducting plane. If at some point in time a free vortex of the $(n-1)$th or $(n+1)$th plane accidentally happens to come near the pinned vortex, an attractive force will arise between the free and pinned vortices. The attractive force arises because the potential energy of two 2D vortices arranged one above the other is less than the sum of the potential energies of two isolated vortices. The pair interaction potential $U_{\text{int}}(u)$ due to the mobile vortex can be represented as a segment of a cubic parabola, with parameters chosen in such a way that the force of interaction between the vortices is equal to zero for $u=0$ and $u=d_1$ (at the center of the well and at its boundary) and the depth of the well is $U_1=kT_D$, where T_D is the temperature at which a linear vortex decays into individual 2D vortices.[3] Then if the mobile vortex is centered at a distance d_1 from the pinned vortex, the left half of the potential well can be represented in the following form (the solid line in Fig. 1b):

$$U_{\text{int}}(u)=\frac{U_1}{d_1^3}u^2(2u-3d_1)\quad\text{for}\quad 0\leqslant u\leqslant d_1. \tag{3}$$

The right half of the potential well is symmetric with respect to the center of the mobile 2D vortex (see Fig. 1b). The half-width of the mobile potential well d_1 is of the order of the extent of the vortex in the ab plane ($d_1\sim\xi_{ab}$, where ξ_{ab} is the coherence length),[25] and the lower temperature boundary T_D can be estimated as 30 K.[3]

Since the position of the free 2D vortex fluctuates, the position of the potential well U_{int} relative to the pinning center varies in a random manner. In what follows we shall consider a simplified model in which it is assumed that a "free" 2D vortex can occupy only two positions relative to a pinned vortex: above the center of the vortex (point 0) and at a distance d_1 from it, and the times at which the free vortex appears at points 0 and d_1 are determined at random. Then the force exerted on the pinned vortex by the mobile vortex will have the form of a random force: $(-\partial U_{\text{int}}/\partial u)\zeta(t)$, where $\zeta(t)$ is noise. We assume that the noise $\zeta(t)$ is Gaussian white noise ξ_t with the properties $\langle\xi_t\rangle=0$ and $\langle\xi_t\xi_{t+\tau}\rangle=\delta(\tau)$.

Then the equation of motion (2) takes the form

$$\eta|\dot{\mathbf{u}}| = |[\mathbf{\Phi}_0 \times \mathbf{J}]| - \frac{8U_0}{d^2}u - \frac{6U_1}{d_1^3}u(u-d_1)\xi_t. \tag{4}$$

It should be noted that in the investigated model of the interaction of a pinned and a fluctuating 2D vortex the relative motion of the potential wells $U_p(u)$ and $U_{\text{int}}(u)$ is important. The additive noise, which is manifested in a random walk of equilibrium points in the well $U_p(u)$, is already taken into account in this model, at least for walks at distances of the order of the size d_1 of the "mobile" potential well. The probability of walks of a pinned 2D vortex at distances greater than d_1 is exponentially small and can be neglected.

Let us estimate the characteristic time scales for variations of $u(t)$ and $\xi(t)$. The time t_{macro} required for macroscopic evolution of the system to a steady state can be estimated as

$$t_{\text{macro}} = \frac{d^2\eta}{8U_0}. \tag{5}$$

For an estimate let us take, e.g., the usual parameters for HTSC materials: $U_0 \approx 0.1$ eV, $\eta(T=0) = 10^{-6}$ N·s/m^2, and $d \approx 200$Å, i.e., $t_{\text{macro}} \approx 10^{-10}$ s.[26,27] A measure of the rapidity of the random fluctuations of the free vortices is the correlation time t_{corr}, i.e., the inverse of the frequency of natural oscillations of the free 2D vortex:[12]

$$t_{\text{corr}} = \frac{a^2\eta}{8U_a}\left(\frac{\xi_{ab}}{a}\right)^2, \tag{6}$$

where a is the average distance between vortices in the same CuO_2 plane ($a \propto 1/\sqrt{B}$, where B is the magnetic induction), U_a is the average potential, which determines the equilibrium position of a free vortex in an environment of other vortices ($U_a \approx U_0(H_{\text{irr}})$, where H_{irr} is the field of irreversibility); $(\xi_{ab}/a)^2$ gives the fraction of the total time that the mobile vortex is found near the pinned vortex and can interact with it (with allowance for the two-dimensional character of the motion of the mobile 2D vortex). For our case $t_{\text{corr}} < t_{\text{macro}}$ for $U_0(H)/U_a < (d/\xi_{ab})^2$, i.e., for $a < 500$ Å or $H > 1$ kOe. Under these conditions the medium can be regarded as rapidly fluctuating.

Let us put Eq. (4) in dimensionless form:

$$\frac{\partial x}{\partial \tau} = j - x + \sigma\left(\frac{1}{\alpha} - x\right)x\xi_\tau, \tag{7}$$

where

$$x = \frac{u}{d};\quad \tau = \frac{t}{t_{\text{macro}}};\quad j = \frac{t_{\text{macro}}F_L}{\eta d} = \frac{dF_L}{8U_0};$$

$$\alpha = \frac{d}{d_1};\quad \beta = \frac{U_0}{U_1};\quad \sigma = \frac{3\alpha^3}{4\beta} = \frac{3d^3U_1}{4d_1^3U_0};$$

the amplitude σ of the multiplicative noise ξ_τ is determined by the ratio of the parameters of the pinning potential well and the mobile well that describes the interaction of the pinned 2D vortex with free vortices. With increasing magnetic field the parameters of the mobile well U_1 and d_1 and the size d of the pinning well remain unchanged, while the depth U_0 of the pinning well decreases,[22] and so the noise amplitude increases. Equation (7) has the form of a stochastic differential equation (SDE) with multiplicative white noise.

2. SOLUTION OF THE EQUATION

We note first of all that Eq. (7) is valid for $0 \leqslant j < 1/\alpha$, and the random process develops in the region $(0,1/\alpha)$. For $-1/\alpha < j \leqslant 0$ the random process develops in the region $(-1/\alpha,0)$, and a SDE analogous to (7) can be constructed for this case also; it is sufficient to replace j by $-j$ and $1/\alpha$ by $-1/\alpha$ in (7). This is confirmed by the character of the boundaries of the random process $b1=0$ and $b2=1/\alpha$ (see Appendix).

The standard method of solving a SDE is to use the Fokker–Planck equation.[12] The Fokker–Planck equation for the SDE (7), understood in the Stratonovich sense, for the probability density $\rho(x,\tau|x_0,0)$ for the transition of a random process x from the state $(x_0,\tau=0)$ to the state (x,τ) has the form

$$\frac{\partial}{\partial\tau}\rho(x,\tau|x_0,0) = -\frac{\partial}{\partial x}\left[\left(f(x) + \frac{\sigma^2}{2}g'(x)g(x)\right)\rho(x,\tau|x_0,0)\right] + \frac{\sigma^2}{2}\frac{\partial^2}{\partial x^2}(g^2(x)\rho(x,\tau|x_0,0)), \tag{8}$$

where

$$f(x) = j - x \quad \text{and} \quad g(x) = \left(\frac{1}{\alpha} - x\right)x.$$

In finding the stationary solution of equation (8) it is important to investigate the behavior of the function $\rho(x,\tau|x_0,0)$ at the boundaries of the random process. As is shown in the Appendix, the point $x = b2 = 1/\alpha$ is a natural boundary for $j < 1/\alpha$ and an absorbing boundary for $j > 1/\alpha$. As to the left-hand boundary of the interval, $x = b1 = 0$, its character varies substantially depending on the parameter j. For $j = 0$ the stationary probability density is not normalized and has a singularity at the point $x = 0$ (see, e.g., Ref. 12). For $j \neq 0$ ($j \geqslant 0$) the boundary $x = 0$ becomes a natural boundary. This means that at the transition from $j > 0$ to $j < 0$ the probability density around the point $x = 0$ over a time $t_{\text{macro}} = 10^{-10}$ s shifts from the region $x > 0$ to the region $x < 0$. Thus it is necessary to find the solution for the stationary probability density $\rho_s(x)$ at the boundaries of the intervals $0 < x \leqslant 1/\alpha$ and $0 < j \leqslant 1/\alpha$ with zero boundary conditions. This solution has the form[12]

$$\rho_s(x) = \frac{N}{g(x)}\exp\left(\frac{2}{\sigma^2}\int^x \frac{f(u)}{g(u)^2}du\right) = \frac{N}{\left(\frac{1}{\alpha} - x\right)^{1-(2/\sigma^2)\alpha^3[(1/\alpha)-2j]_x 1+(2/\sigma^2)\alpha^3[(1/\alpha)-2j]}} \times \exp\left\{\frac{2}{\sigma^2}\left[\frac{\alpha^2\left(2x - \frac{1}{\alpha}\right)}{x\left(\frac{1}{\alpha - x}\right)}j - \frac{\alpha}{\left(\frac{1}{\alpha} - x\right)}\right]\right\}, \tag{9}$$

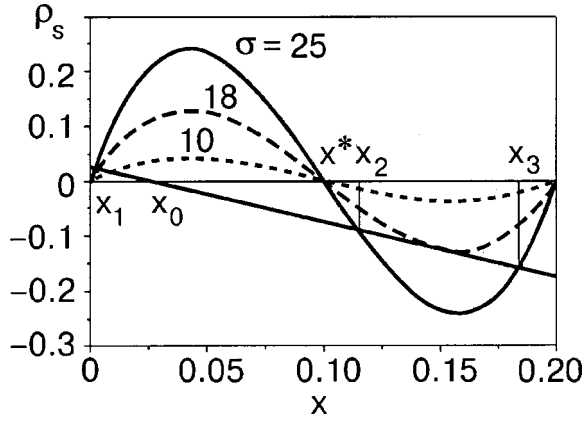

FIG. 2. Extrema of the stationary probability density $\rho_s(x)$ for three values of the noise intensity σ—the points of intersection of the curves and the straight line $(j-x)$ for $j=0.025$ and $\alpha=5$, $x_0=j$ is the sole equilibrium position of the vortex (maximum of $\rho_s(x)$) in the absence of noise, x_1, x_2, and x_3 are the extrema of $\rho_s(x)$ in the case when the noise intensity $\sigma=25$ is greater than the critical value ($\sigma>\sigma_{cr}=18$); x^* is the point at which $g'(x)=0$.

where N is a normalizing factor.

The points x_m at which extrema of the stationary probability density $\rho_s(x)$ are obseved are solutions of the following equation:[12]

$$f(x)=\frac{\sigma^2}{2}g(x)g'(x)$$

or

$$j-x=\frac{\sigma^2}{2}\left(\frac{1}{\alpha}-x\right)\left(\frac{1}{\alpha}-2x\right)x. \tag{10}$$

We recall that in Eq. (10) the left-hand side is determined by the dynamical part of Eq. (7), while the right-hand side, which is proportional to σ^2, is determined by the stochastic part. The roots in (10) are conveniently found by means of a graphical solution of this equation. Figure 2 shows the solutions of equation (10) determined from the points of intersection of the lines described by the expressions on the right- and left-hand sides of Eq. (10), for $j=0.025$ and three different values of σ, viz., $\sigma=10$, 18, and 25. It is seen in the figure that for $\sigma>\sigma_{cr}(j)=18$ there are three extrema of $\rho_s(x)$, and thus growth of the multiplicative noise will lead to a stochastic phase transition. Figure 3 shows the change observed in the stationary probability density $\rho_s(x)$ when the intensity of the multiplicative noise changes from $\sigma=1$ to $\sigma=85$ for $\alpha=5$ and $j=0.025$. We see that as the noise increases for $\sigma>\sigma_{cr}$, the maxima of the function $\rho_s(x)$ shift toward the edges of the interval $[0,1/\alpha]$ and a redistribution of the probability density between these maxima occurs (the equilibrium position x_3 becomes more probable with increasing noise).

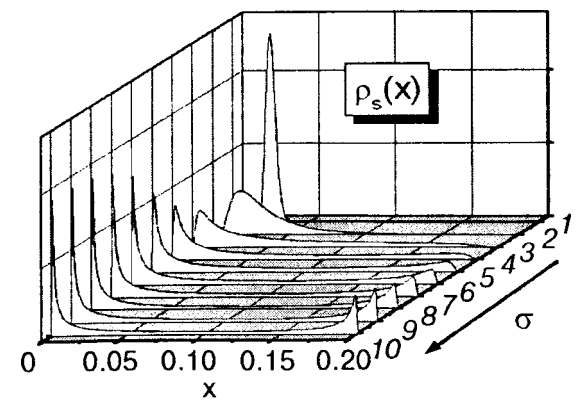

FIG. 3. Stationary probability density $\rho_s(x)$ for $j=0.025$, $\alpha=5$ and various values of the multiplicative noise intensity σ: 1 (*1*), 5 (*2*), 15 (*3*), 25 (*4*), 35 (*5*), 45 (*6*), 55 (*7*), 65 (*8*), 75 (*9*), and 85 (*10*).

Figure 4 shows the regions of values of the parameters appearing in Eq. (7) for which the stationary probability density has three extrema. These parameters are $\alpha=d/d_1$—the ratio of spatial extents of the two wells, $\beta=U_0/U_1$—the ratio of energies of the large immobile (U_0) and small mobile (U_1) wells, and j—the external current density (a dimensionless quantity measured in units of j_0).

3. DISCUSSION OF THE RESULTS

In Sec. 2 it is shown that a stochastic phase transition is observed under the influence of multiplicative noise, i.e., in addition to the one equilibrium state that exists in the absence of noise, another equilibrium state appears near the interval boundary $b2$. As the multiplicative noise increases, this new equilibrium state becomes more probable. Thus the multiplicative noise causes an appreciable change in the probability density distribution $\rho_s(x)$ of the vortex in the potential well.

As we said in Sec. 2, the characteristic time for system changes is $t_{macro}\approx 10^{-10}$ s, while the correlation time of thermal oscillations of the 2D vortices t_{corr} is 1–2 orders of magnitude smaller. Therefore, any external currents that induce an external magnetic field with frequency ω smaller than $1/t_{macro}$ can be considered constant (dc) in this case. This means that for every value of the alternating magnetic field $h(t)=h_0\exp(i\omega t)$ with $\omega\ll 1/t_{macro}$ the system has time to relax toward the equilibrium state determined by the stationary probability density distribution function $\rho_s(x)$.

Let us consider the dynamics of vortices in a layered superconductor placed in an alternating magnetic field with a frequency of the order of 10 MHz. This field induces on the surface of the superconductor an alternating current which causes oscillations of the vortices. In the region of the normal core of the oscillating vortex a scattering of Cooper pairs occurs, and the vortex therefore absorbs energy from the alternating magnetic field, the absorbed power being proportional to the mean-square displacement $\langle\Delta u^2\rangle$ of the vortex from its position of local equilibrium (for free vortices) or from the pinning center (for pinned vortices).[22] The inset in Fig. 5 shows how the quantity $I=\langle\Delta u^2\rangle_\sigma/\langle\Delta u^2\rangle_0$ depends on the multiplicative noise intensity σ for $j=0.025$, where $\langle\Delta u^2\rangle_\sigma$ is the mean-square displacement of a pinned vortex in the presence of multiplicative noise, and $\langle\Delta u^2\rangle_0$ is the displacement in the case $\sigma=0$. The arrow indicates the value of the noise intensity σ_{cr} at which a stochastic phase transition is observed. According to the general theory of stochastic phase transitions,[12] $\langle\Delta u^2\rangle_\sigma$ does not have features at the phase transition point. From the inset in Fig. 5 one can see that the function $I(\sigma)$ indeed does not have any features at this point, but when the noise intensity is increased from a

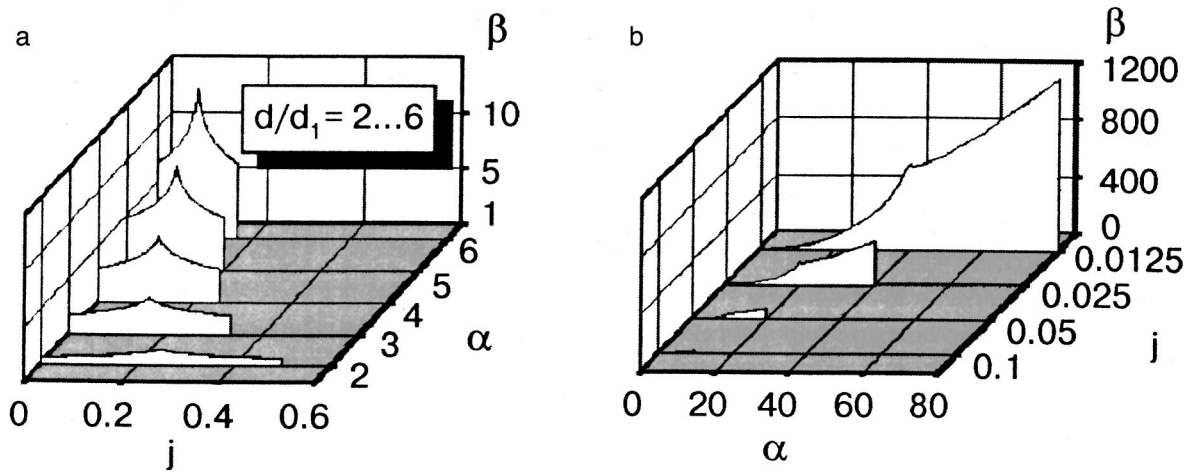

FIG. 4. Regions of values (unshaded) of the parameters $j=(d/8)(F_L/U_0)$, $\alpha=d/d_1$, and $\beta=U_0/U_1$ for which the stationary probability density $\rho_s(x)$ has three extrema, i.e., for which there exists two equilibrium positions of the vortex: in the $j-\beta$ plane for $\alpha=2$, 3, 4, 5, 6 (a); in the $\alpha-\beta$ plane for $j=0.0125$, 0.025, 0.05, and 0.1 (b).

value $\sigma\to 0$ to $\sigma\gg\sigma_{\rm cr}$, the mean-square displacement of the vortex and, hence, the power absorbed by the vortex, increases by approximately a factor of 20.

For observation of this effect we propose the following experimental scheme. A single-crystal sample of a highly layered high-T_c superconductor is cooled to a temperature $T<T_c$ at which the bulk pinning is operative (e.g., $T<35\,$K for $Bi_2Sr_2CaCu_2O_8$) and is placed in crossed magnetic fields: a static magnetic field $H>H_{2D}\gg H_{c1}$ (H_{2D} is the field at which a linear vortex decays into 2D vortices) parallel to the c axis, and an alternating magnetic field perpendicular to the c axis, with a low amplitude $h\ll H_{c1}$ and a velocity $\nu=10\,$MHz. Then, as the static field is slowly increased to $H>H_{\rm irr}$, the power $P(H)$ absorbed by the vortices from the alternating field is measured. Figure 5 shows $\partial P/\partial H$, the derivative of the power absorbed by the vortices with respect to the field, as a function of this field H, according to a calculation for the superconductor $Bi_2Sr_2CaCu_2O_8$ with the following values of the parameters: $d=200\,$Å, $d_1=40\,$Å, and $U_1=30\,$K$=2.6\times10^{-3}\,$eV.[3] The parameters d, d_1, and U_1 do not depend on the field H. The depth of the pinning well has a weak field dependence: $U_0\approx 1/\sqrt{H}$ (Ref. 28). Then $U_0/U_1=A/\sqrt{H}$, where $A=630$ and H is measured in oersteds. It is seen in Fig. 5 that the curve of $\partial P/\partial H(H)$ is nonmonotonic. The field in which $\partial P/\partial H$ has a maximum is lower than the field at which the sochastic phase transition takes place, $H(\sigma_{\rm cr})$. The dashed lines in the figure indicate the interval of magnetic fields ($1\,$kOe$<H<17\,$kOe) in which this theory is applicable. In fields below 1 kOe (the left-hand dashed line) the correlation time $t_{\rm corr}$ of the random fluctuations of the vortices becomes comparable to the characteristic time $t_{\rm macro}$ for the evolution of a vortex toward the steady state in the pinning potential, and the medium cannot be considered to be rapidly fluctuating. In fields above 17 kOe (the right-hand dashed line) there is evidently a thermally activated depinning of vortices, i.e., the frequency at which the 2D vortices "jump out" of the pinning well will be comparable to 10 MHz. The extent of the region in which the given theory is applicable depends on the frequency of the alternating field: the lower the frequency, the narrower the magnetic field region in which the existence of the stochastic phase transition can be detected from its influence on the absorption of power from the alternating field. Thus it can be assumed that a nonmonotonic dependence of $\partial P/\partial H$ will be observed in the region of the stochastic phase transition described here (Fig. 5).

Here it is important to note that the absorption of power from the alternating magnetic field occurs both at the pinned and at the free 2D vortices, the absorption at the free vortices being proportional to the number of such vortices, i.e., proportional to H, so that the nonmonotonic dependence of $\partial P/\partial H$ will be observed against a rather high background $\partial P/\partial H=$const from the free 2D vortices. However, as the frequency ν of the alternating field increases and its power decreases, the contributions to the $\partial P/\partial H$ signal from the free and bound vortices change sharply: as can be seen in Fig. 2, under conditions of a developed stochastic phase transition, when the probability of finding a 2D vortex in the neighborhood of the point x_3 increases substantially, the po-

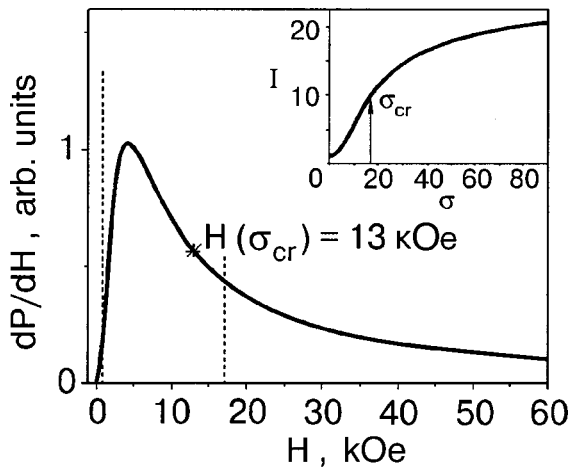

FIG. 5. Predicted field dependence of $\partial P/\partial H$, where P is the power absorbed from an alternating magnetic field by a system of 2D vortices acted on by multiplicative noise; H is the static magnetic field. The inset shows the quantity $I=\langle\Delta u^2\rangle_\sigma/\langle\Delta u^2\rangle_0$ as a function of the multiplicative noise intensity σ for $j=0.025$ and $\alpha=5$.

sition of this point depends weakly on the amplitude of the alternating current j and is independent of frequency. Calculations show that for $\nu = 500$ MHz and $h \approx 0.01$ Oe (h is the amplitude of the alternating field) under the condition that the number of pinned 2D vortices is approximately 10%, the power absorbed by the pinned 2D vortices can turn out to be even greater than the power absorbed by the mobile vortices.

Finally, we note that the shape of the potential $U_p(u)$ in this model is not important, since for $d_1 \ll d$ the anharmonic admixtures to the potential (1) are unimportant. As to the shape of the potential U_{int}, it is also not very important. As can be seen in Fig. 2, the position of the roots x_1, x_2, and x_3 varies somewhat upon changes in the shape of the potential, but it is clear that extrema x_2 and x_3 will always be to the right of the point $x = x^*$ (at which $g'(x^*) = 0$), so that the main characteristics of the mobile well are its depth and spatial extent.

CONCLUSION

We have shown theoretically that in type-II superconductors with pronounced layering there can exist a multiplicative noise due to the interaction of 2D vortices, and the growth in intensity of this noise will lead to a stochastic phase transition. We have determined the parameters at which a noise-induced phase transition is possible. We have also shown that the onset of multiplicative noise will lead to nonmonotonic dependence of $\partial P/\partial H$ on the magnetic field H.

The author thanks G. B. Teitelbaum for suggesting the subject of this study and showing interest in it and for a discussion of the results. The author is grateful to Yu. I. Talanov for helpful discussions of the results.

This study was done with the financial support of the fund NIOKR AN RT (Project No. 14-64) and the Ministry of Industry and Science of Russia under government contract No. 107-1(00)-P.

APPENDIX

Character of the boundaries

As was shown in Ref. 12, the character of the boundaries of the stochastic process is determined by the behavior of the transport $f(x)$ and diffusion $g(x)$ near these boundaries. A classification of the boundaries is based on the integrability of certain functions $L1(x)$ and $L2(x)$ composed of $g(x)$ and $f(x)$. Boundary b is a natural boundary if

$$L1(b) = \int_\beta^b \varphi(x)\,dx = \infty, \tag{A1}$$

where

$$\varphi(x) = \exp\left(-\int_\beta^x \frac{2[f(z) + (\sigma^2/2)g'(z)g(z)]}{\sigma^2 g(z)^2}\,dz \right).$$

For the left-hand boundary $b1 = 0$ we have

$$\varphi(x) \approx C \exp\left(\frac{2j\alpha^2}{\sigma^2 x} \right) |x|^{2\alpha^3/\sigma^2(1/\alpha - 2j) - 1}, \quad x \to 0$$

where

$$C = \text{const}. \tag{A2}$$

It is seen from formula (A.2) that the functional dependence of $\varphi(x)$ has a different form for $j = 0$ and $j > 0$, and therefore the character of a given boundary will depend on j:

1. $j = 0$, $\varphi(x) \approx C|x|^{2\alpha^2/\sigma^2 - 1}$, $L1(b1) < \infty$, and $L2(b1) = \infty$ (Ref. 12), i.e., the boundary is attractive; because the transport and diffusion go to zero at this boundary, the entire ''mass'' of the probability density is concentrated at this point. Therefore, independently of the noise intensity σ, the stationary probability density $\rho_s(x) = \delta(x)$, where $\delta(x)$ is the Dirac delta function.

2. $j > 0$, $L1(b1) \to \infty$; therefore the boundary $b1$ is natural, i.e., unreachable.

In order to estimate the character of the right-hand boundary $b2 = 1/\alpha$, we expand the functions $f(x)$ and $g(x)$ in series in the small parameter y, where $y = 1/\alpha - x$ and $y \to 0$. Then

$$\varphi(x) \approx \frac{C}{\left(\frac{1}{\alpha} - x\right)^{2\alpha^2/\sigma^2(1-2j\alpha)+1}} \exp\left(\frac{2\alpha^2}{\sigma^2} \frac{1 - j\alpha}{1 - x\alpha} \right), \quad x \to 1/\alpha \tag{A3}$$

We see from expression (A3) that for $j < j_{\text{cr}} = 1/\alpha$ one has $L1(b2) = \infty$, i.e., the boundary is natural. For $j > j_{\text{cr}}$ one has $L1(b2) < \infty$ and $L2(b2) = \infty$, i.e., the boundary becomes attractive. This means that a 2D vortex leaves the interval $(b1, b2)$ in a finite time, and always through the right-hand boundary.[12]

[a)]E-mail: t_shap@dionis.kfti.kcn.ru

[1] J. R. Clem, Phys. Rev. B **43**, 7837 (1991); M. W. Coffey, *ibid.* **51**, 15600 (1995).
[2] G. Blatter, M. V. Feigel'man, V. B. Geshkenbein, A. I. Larkin, and V. M. Vinokur, Rev. Mod. Phys. **66**, 1147 (1994).
[3] B. Horovitz and T. R. Goldin, Phys. Rev. Lett. **80**, 1734 (1998).
[4] B. Khaykovich, M. Konczykowski, E. Zeldov, R. A. Doyle, D. Mayer, P. H. Kes, and T. W. Zi, Phys. Rev. B **56**, R517 (1997).
[5] E. H. Brandt, Phys. Rev. Lett. **63**, 1106 (1989).
[6] L. I. Glazman and A. E. Koshelev, Phys. Rev. B **43**, 2835 (1991).
[7] L. L. Daeman, L. N. Bulaevskii, M. P. Maley, and J. Y. Coulter, Phys. Rev. Lett. **70**, 1167 (1993).
[8] K. Yamafuji, T. Fujiyoshi, K. Toko, T. Matsuno, K. Kahio, and T. Matsushita, Physica C **212**, 424 (1993).
[9] Y. Ando, S. Koniya, Y. Kotaka, and K. Kishio, Phys. Rev. B **52**, 3765 (1995).
[10] T. Shaposhnikov, Yu. Vashakidze, R. Khasanov, and Yu. Talanov, Physica C **300**, 239 (1998).
[11] B. Chen and J. Dong, Phys. Rev. B **44**, 10206 (1991).
[12] W. Horsthemke and R. Lefever, *Noise-Induced Transitions* [Springer-Verlag, Berlin (1984); Mir, Moscow (1987)].
[13] J. R. Clem, Phys. Rev. B **1**, 2140 (1970).
[14] G. Jung, S. Vitale, J. Konopka, and M. Bonaldi, J. Appl. Phys. **70**, 5440 (1991).
[15] H. Safar, P. L. Gammel, D. A. Huse, G. V. Alers, D. J. Bishop, W. C. Lee, J. Giapintzakis, and D. M. Ginsberg, Phys. Rev. B **52**, 6211 (1995).
[16] G. D'Anna, P. L. Gammel, H. Safar, G. B. Alers, D. J. Bishop, J. Giapintzakis, and D. M. Ginsberg, Phys. Rev. Lett. **75**, 3521 (1995).
[17] R. Prozorov and D. Giller, Phys. Rev. B **59**, 14687 (1999).
[18] K. E. Gray, Phys. Rev. B **57**, 5524 (1998); D. H. Kim, K. E. Gray, N. Jukam, D. J. Miller, Y. H. Kim, J. M. Lee, J. H. Park, and T. S. Hahn, *ibid.* **60**, 3551 (1999).
[19] T. Tsuboi, T. Hanaguri, and A. Maeda, Phys. Rev. Lett. **80**, 4550 (1998).
[20] S. L. Ginzburg and M. A. Pustovoĭt, JETP Lett. **64**, 592 (1998).

[21] N.-C. Yeh, Phys. Rev. B **43**, 523 (1991).
[22] M. J. Ferrari, M. Johnson, F. C. Wellstood, J. Clarke, D. Mitzi, P. A. Rosenthal, C. B. Eom, T. H. Geballe, A. Kapitulnik, and M. R. Beasley, Phys. Rev. Lett. **64**, 72 (1990).
[23] M. Golosovsky, M. Tsindelkht, and D. Davidov, Supercond. Sci. Technol. **9**, 1 (1996).
[24] A. S. Mel'nkov, Phys. Rev. B **53**, 449 (1996); Phys. Rev. Lett. **77**, 2786 (1996).
[25] T. Pe, M. Benkraouda, and J. R. Clem, Phys. Rev. B **55**, 6636 (1997).
[26] M. J. Ferrari, M. Johnson, F. C. Wellstood, J. Clarke, D. Mitzi, P. A. Rosenthal, C. B. Eom, T. H. Geballe, A. Kapitulnik, and M. R. Beasley, Phys. Rev. Lett. **64**, 72 (1990).
[27] S. L. Lee, M. Warden, H. Keller, J. W. Schneider, D. Zech, P. Zimmermann, R. Cubitt, E. M. Forgan, M. T. Wylie, P. H. Kes, T. W. Li, A. A. Menovsky, and Z. Tarnawski, Phys. Rev. Lett. **75**, 922 (1995).
[28] J. T. Kucera, T. P. Orlando, G. Virshup, and J. N. Eckstein, Phys. Rev. B **46**, 11004 (1992).

Translated by Steve Torstveit

LOW-TEMPERATURE MAGNETISM

Nonlinear oscillations of the magnetization in small cylindrical ferromagnetic particles

B. A. Ivanov*

Institute of Magnetism, National Academy of Sciences of Ukraine, rp. Vernadskogo 36-b, 03142 Kiev, Ukraine; Taras Shevchenko Kiev National University, pr. Glushkova 2, 03127 Kiev, Ukraine

I. A. Yastremskiĭ

Taras Shevchenko Kiev National University, pr. Glushkova 2, 03127 Kiev, Ukraine

(Submitted February 5, 2001)
Fiz. Nizk. Temp. **27**, 752–760 (July 2001)

The radially symmetric nonlinear oscillations of the magnetization in small cylindrical particles of a ferromagnet are considered in the cases of free and fixed boundary conditions at the lateral surface of the particles. It is found that even for nonlinear oscillations of small amplitude the dependence of the frequency on the amplitude of the oscillations is rather complicated and can include a series of bifurcations. The character of the oscillations depends substantially on the boundary conditions; for example, for free boundary conditions the solutions exhibit bifurcations that are not present in the case of fixed boundary conditions. We discuss the possibilities for generalizing the results to the case of oscillations in a cylinder with a more complicated angular dependence and to the case of radially symmetric oscillations in a spherical particle. © *2001 American Institute of Physics.* [DOI: 10.1063/1.1388418]

INTRODUCTION

In recent decades the technology of deposition and lithography has made it possible to produce nanometer periodic magnetic superlattices of various types, both one-dimensional (e.g., multilayer magnetic films) and two-dimensional, among which the so-called magnetic dot lattices are especially popular.[1,2] Magnetic dots are particles in the shape of circular[1] or elliptical[2] cylinders or rectangular prisms, made of magnetically soft ferromagnets such as Co, Fe, FeNi, etc. on a nonmagnetic substrate. Magnetic dot lattices are important from a practical standpoint (high-density magnetic storage) and are interesting as fundamentally new objects in the basic physics of magnetism. Indeed, although the physical properties of the material within an individual particle (magnetic dot) with dimensions of the order of hundreds of nanometers are close to those of the bulk ferromagnet, the behavior of a superlattice of such dots, because of the weakness of their interaction,[3] is substantially different from that of both bulk ferromagnets and standard continuous magnetic thin films.

The special properties of such materials should be manifested in resonance experiments. Studies done on long, axially magnetized ferromagnetic wires[4] and on magnetic dot lattices[5,6] have shown that the spin-wave (SW) spectrum in such systems is discrete, which is a direct consequence of the boundary conditions on the lateral surface of the particles. This same effect has been discussed for nanometer ferromagnetic particles of cylindrical shape.[3]

All of the studies mentioned above dealt with linear SWs. It is known that taking nonlinearity into account leads to a number of effects, such as the parametric excitation of magnons,[7,8] frequency dependence of the oscillation amplitude, possible bifurcations, various instabilities, etc. It is clear that these effects can be very different in superlattices than in massive samples or continuous magnetic thin films. Knowledge of the properties of a single particle is fundamental to the study of the dynamics of the magnetization in such an ensemble, since if the interparticle distance is somewhat greater than the size of the particles, one can neglect the magnetostatic interaction between them.[3]

This paper is devoted to a study of nonlinear spin waves (NLSWs) in a cylindrical particle of an easy-axis ferromagnetic material. We show that even in the approximation of low-amplitude nonlinear waves the picture of the nonlinear modes is extremely complex and can include a series of bifurcations. The NLSW picture depends substantially on the character of the boundary conditions. We discuss generalizations of the problem to the case of spherical particles.

1. MODEL AND STATEMENT OF THE PROBLEM

We consider nonlinear spin waves in an easy-axis ferromagnet in the form a cylindrical particle of radius L_0 and height h, assuming that $L_0 \gg h$. This is a typical situation in real superlattices. The easy axis of the ferromagnet is perpendicular to the base of the cylinder. The macroscopic dynamics of the ferromagnet is described by a classical vector order parameter, in the capacity of which one can choose the unit vector $\mathbf{m}=\mathbf{M}/M_0$, where $\mathbf{M}$ is the magnetization of the ferromagnet, and M_0 is the saturation magnetization. The vector $\mathbf{m}$ is conveniently written in angular variables: $\mathbf{m}=(\sin\theta\cos\varphi;\sin\theta\sin\varphi;\cos\theta)$. The energy density of the ferromagnet is written in the form[9,10]

$$W=\frac{A}{2}\{(\nabla\theta)^2+\sin^2\theta(\nabla\varphi)^2\}$$

$$-\frac{1}{2}K\cos^2\theta-\frac{1}{2}(\mathbf{M}\cdot\mathbf{H}^{(m)}), \tag{1}$$

where A is the exchange constant, K is the anisotropy constant, and $\mathbf{H}^{(m)}$ is the magnetostatic field. We have used a cylindrical coordinate system (r,χ,z), where r and χ are the polar coordinates in the plane of the base of the cylinder, and the $0z$ axis is parallel to the axis of the cylinder. It is known that for nonelliptical samples the ground state of the magnetization is inhomogeneous. The cause of the inhomogeneity is that the magnetostatic field $\mathbf{H}^{(m)}$ is a complicated functional of $\mathbf{M}$. However, two substantial simplifications can be made in the case $L_0\gg h$. First, when this inequality holds, one can go over to a local dependence of the magnetostatic field on $\mathbf{M}$, viz., $\mathbf{H}^{(m)}=-4\pi M_z\mathbf{e}_z$, and the dipole–dipole interaction can be taken into account by a simple redefinition of the anisotropy constants: $K\to K^{(m)}=K-2\pi M_0^2$ (for $K<2\pi M_0^2$ the ferromagnet becomes easy-plane, but we will restrict discussion to ferromagnets with perpendicular anisotropy). Second, although $\mathbf{H}^{(m)}$ is still nonuniform near the lateral surface, this nonuniformity is concentrated in a region of the order of h, and the corresponding effects are negligible. Therefore, we can assume that the magnetization in the ground state is homogeneous and directed along the easy axis of the ferromagnet. In a cylindrical geometry there can exist, against the background of the uniform ground state, both eigenmodes with nonuniformity along the $0z$ axis and modes characterized by nonuniformity in the plane of the cylinder. In the first case $(\mathbf{m}=\mathbf{m}(z))$ the situation is the same as for nonlinear modes in thin ferromagnetic slabs, and there are no specific effects of two-dimensionality. Therefore, we consider eigenmodes for which $\mathbf{m}$ is independent of z. The approximations made above do not alter qualitatively the character of the nonlinear modes but do simplify the analysis considerably and make the results more transparent and clear.

The dynamics of a ferromagnet is described by the Landau–Lifshitz equation, which for an energy of the form (1) can be written as

$$r_v^2\nabla^2\theta-[1+r_v^2(\nabla\varphi)^2]\sin\theta\cos\theta=-\frac{\sin\theta}{\omega_0}\frac{\partial\varphi}{\partial t}, \tag{2}$$

$$r_v^2\,\mathrm{div}\,(\sin^2\theta\nabla\varphi)=\frac{\sin\theta}{\omega_0}\frac{\partial\theta}{\partial t}, \tag{3}$$

where $r_v=\sqrt{A/K^{(m)}}\gg a$ is the characteristic magnetic length, a is the lattice constant, $\omega_0=(2\mu_B K^{(m)}/\hbar)M_0$ is the frequency of uniform precession of the magnetization in the linear theory.

The system of equations (2), (3) has a discrete set of classes of solutions, which are characterized by different angular dependence; these classes are defined by the formulas

$$\theta=\theta(x),\quad \varphi=\omega t+q\chi+\varphi_0, \tag{4}$$

where $x=r/r_v$, φ_0 is an arbitrary phase, $q=0,\pm1,\pm2,...$ (see Ref. 10). For the choice of a solution in the form (4), equation (3) is satisfied identically, and we obtain an ordinary differential equation for the function $\theta(x)$. We shall assume below that for a particle of rather large dimensions the nonlinearity is manifested even at rather small amplitudes of the deviation of the magnetization from the easy axis of the ferromagnet, when $\theta\ll1$ and the frequency ω obeys the condition $|\omega_0-\omega|\ll\omega_0$. We restrict the discussion to such low-amplitude NLSWs. We expand the function in Eq. (2) in a series in powers of θ, keeping terms of order θ^3, $(1-\omega/\omega_0)\theta$, $q^2/x^2\theta$. As a result, we obtain

$$\frac{d^2\theta}{dx^2}+\frac{1}{x}\frac{d\theta}{dx}-\frac{q^2}{x^2}\theta-\left(1-\frac{\omega}{\omega_0}\right)\theta+\frac{1}{2}\theta^3=0. \tag{5}$$

In studying Eq. (5) one should distinguish the cases $\omega>\omega_0$ and $\omega<\omega_0$.

For the case $\omega<\omega_0$ we make the usual substitution

$$\theta(x)=\sqrt{2}\varepsilon f(\xi),\quad \varepsilon=(1-\omega/\omega_0)^{1/2},\quad \xi=\varepsilon x, \tag{6}$$

and obtain for the function $f(\xi)$ an equation with a cubic nonlinearity:

$$\frac{d^2f}{d\xi^2}+\frac{1}{\xi}\frac{df}{d\xi}-\frac{q^2}{\xi^2}f-f+f^3=0, \tag{7}$$

which is widely discussed in various physical applications. In particular, this equation is used for describing self-focusing of optical beams,[11] and for $q=0$ and $q=1$ it describes two-dimensional solitons in FMs.[12,13]

For $\omega>\omega_0$ we make the analogous substitution

$$\theta(x)=\sqrt{2}\varepsilon g(\xi),\ \ \varepsilon=(\omega/\omega_0-1)^{1/2},\ \text{where}\ \ \xi=\varepsilon x. \tag{8}$$

The function $g(\xi)$ satisfies the following differential equation:

$$\frac{d^2g}{d\xi^2}+\frac{1}{\xi}\frac{dg}{d\xi}-\frac{q^2}{\xi^2}g+g+g^3=0. \tag{9}$$

Thus for both cases ($\omega>\omega_0$ and $\omega<\omega_0$) we have obtained universal differential equations that do not depend on ω, and this simplifies the analysis substantially. For $\xi\to0$ the solutions of equations (7) and (9) which are nonsingular at the origin have the same behavior, $g=g_0\xi^q/q!$, $f=f_0\xi^q/q!$, but at the origin distances the character of the solutions is substantially different. This is easily established in an analysis of the corresponding equations on the phase plane.[10]

The equation for $g(\xi)$, independently of the choice of constant g_0, has only oscillatory solutions at large ξ:

$$g(\xi)\to[C_{1,q}\sin\xi+C_{2,q}\cos\xi]/\sqrt{\xi}\ \ \text{as}\ \ \xi\to\infty,$$

where the values of the constants $C_{1,q}$ and $C_{2,q}$ are determined by the behavior of the solution at zero, i.e., by the value of g_0.

The function $f(\xi)$ behaves differently. For all values of f_0 and various q, except for a certain countable set $f_0=F_m^{(q)}$, $m=0,1,2,...,$ the solutions for $\xi\to\infty$ also oscillate, but about two different finite values $f=\pm1$, specifically,

$$f(\xi)\to1+[B_{1,q}\sin\xi+B_{2,q}\cos\xi]/\sqrt{\xi}$$

or

$$f(\xi)\to-1-[D_{1,q}\sin\xi+D_{2,q}\cos\xi]/\sqrt{\xi}.$$

TABLE I. Characteristic values of F_m.

m	1	2	3	4	5	6	7	8
$F_m^{(q=0)}$	2.2	3.33	4.14	4.82	5.42	5.95	6.44	6.9
$F_m^{(q=1)}$	1.25	2.43	3.58	4.72	5.88	7.03	8.19	9.33

The solutions with these two different asymptotic behaviors are separated by a soliton solution with $f(\xi)$ going exponentially to zero as $\xi\to\infty$:

$$f(\xi)\to(\alpha_q/\sqrt{\xi})\exp(-\beta_q\xi).$$

The soliton solutions form a countable set and are obtained when one of the values $f_0=F_m^{(q)}$ is chosen as a condition at $\xi=0$. The characteristic values F_m for eight values of m and $q=0$, 1 are given in Table I. The smallest of these values, $F_1^{(q)}$, corresponds to a soliton without nodes, for which $f(\xi)$ is nonzero at any finite value of ξ. The remaining $F_m^{(q)}$ with $m-1$ give solitons with $(m-1)$ nodes. The soliton solutions for any q and m can be obtained numerically by the shooting method.[10]

2. FORMATION OF NONLINEAR MODES FOR PARTICLES OF FINITE SIZE

In the analysis below we will take into account the finite size of the particles. We construct solutions that satisfy specified boundary conditions at the surface of the particle, i.e., at $r=L_0$. In terms of the dimensionless variables x or ξ the boundary conditions, with allowance for (6) and (8), are taken at $x=L=L_0/r_v$ or $\xi=|(\omega/\omega_0-1)|^{1/2}L_0/r_v$, respectively. The boundary conditions for the magnetization under different conditions on the surface of the cylinder can be written as $a\theta+b(\mathbf{n}\partial\theta/\partial\mathbf{r})=0$, where $\mathbf{n}$ is the vector normal to the surface.[7,9] We consider in detail the two limiting cases $a\neq0$, $b=0$ and $a=0$, $b\neq0$, which correspond to fixed and free magnetic moments at the surface. Generalization to the case of an arbitrary relationship between a and b is not very simple, and we shall discuss it in the concluding Section. Thus the problem is to investigate the dependence of the frequency ω of a nonlinear mode on the amplitude of the magnetization oscillations for different types of angular dependence of the solution (different q) for these two boundary conditions.

For the linear case this problem is simple to solve—the solution of the equation is the Bessel function (of index q) $J_q(kr)$. The eigenvalues of the wave number k are determined by the conditions $k_{n,q}L_0=j_{n,q}$ or $k_{n,q}L_0=j'_{n,q}$, where $j_{n,q}$ is the nth root of the Bessel function and $j'_{n,q}$ is the nth root of its derivative for the fixed or free conditions, respectively. The relation between $\omega_{n,q}$ and $k_{n,q}$ is given by the linear dispersion relation for magnons: $\omega_{n,q}=\omega_0[1+(r_vk_{n,q})^2]$.

For the nonlinear problem this method does not work: the linear dispersion relation is invalid, and the relation of $\omega_{n,q}$ with the size of the particle and the amplitude of the wave must be found from the solution of the equation for $\theta(r)$, the coefficients of which depend on ω. Going to universal equations for $f(\xi)$ and $g(\xi)$ simplifies the analysis, although not as much as in the linear case, since the solutions of the universal equations still depend on the amplitude of the wave. In order to analyze the nonlinear modes for some specific q, it is sufficient to construct two families of solutions for $f(\xi)$ and $g(\xi)$ with different initial conditions:

$$g(\xi\to0)\to g_0\xi^q/q!,\quad f(\xi\to0)\to=f_0\xi^q/q!$$

and to find the behavior of the characteristic points (the zeros of the functions and of their derivatives) as functions of the initial values g_0 or f_0, respectively.

We denote by $\xi_{n,q}(g_0)$ the nth root of the function $g(\xi)$ with the specified initial condition $g(\xi\to0)\to g_0\xi^q/q!$ and by $\xi'_{n,q}(g_0)$ the nth root of the derivative $dg(\xi)/d\xi$. Similarly, for analysis of the solutions with $\omega<\omega_0$ we introduce the notation $\xi_{n,q}(f_0)$ and $\xi'_{n,q}(f_0)$ for the nth roots of f and $df/d\xi$. For the sake of definiteness, we begin with the case of fixed boundary conditions. Then, differentiating relation (8) q times with respect to the variable x and using the relation $L\sqrt{\omega/\omega_0-1}=\xi_n(g_0)$, we obtain a system of algebraic equations for finding $\omega=\omega_n[d^q\theta/dx^q(x=0),L]$ for $\omega>\omega_0$, where $d^0\theta/dx^0(x=0)=\theta(0)$. It is necessary to differentiate because for a given value of q one has

$$g(0)=0,\ d^1g(0)/dx^1=0,\ d^2g(0)/dx^2=0,...$$

$$d^{q-1}g(0)/dx^{q-1}=0.$$

The situation for $f(\xi)$ is analogous. For $\omega<\omega_0$ one must use (7) and the relation $L\sqrt{1-\omega/\omega_0}=\xi_n(f_0)$. For the case $q=0$ considered below it is convenient to rewrite these systems in the form (for brevity in the formulas we shall henceforth omit the index $q=0$)

$$\theta(0)=\frac{\sqrt{2}}{L}g_0\xi_n(g_0),\ \frac{\omega}{\omega_0}=1+\left(\frac{\xi_n(g_0)}{L}\right)^2,\ \omega>\omega_0; \tag{10}$$

$$\theta(0)=\frac{\sqrt{2}}{L}f_0\xi_n(f_0),\ \frac{\omega}{\omega_0}=1-\left(\frac{\xi_n(f_0)}{L}\right)^2,\ \omega<\omega_0. \tag{11}$$

The system of equations for free boundary conditions has the same form but with $\xi_n(g_0)$ and $\xi_n(f_0)$ replaced by $\xi'_n(g_0)$ and $\xi'_n(f_0)$.

Thus the relation $\omega=\omega_n[\theta(0),L]$ is specified parametrically with the aid of Eqs. (10) for $\omega>\omega_0$ and Eqs. (11) for $\omega<\omega_0$, where g_0 and f_0, respectively, play the role of auxiliary parameters. In order to obtain the desired relation $\omega=\omega_n[\theta(0),L]$ it is necessary to solve Eq. (9) in the case $\omega>\omega_0$ and Eq. (7) in the case $\omega<\omega_0$ with various initial values g_0 and f_0 (at $q=0$) and construct the functions $\xi_n(g_0)$ and $\xi_n(f_0)$ for fixed boundary conditions or $\xi'_n(g_0)$ and $\xi'_n(f_0)$ for free boundary conditions.

Using these numerical data, one can find a set of frequencies corresponding to each value of the real amplitude $\theta(0)$ of the magnetization oscillations and size L of the system. Let us apply this approach to some specific examples.

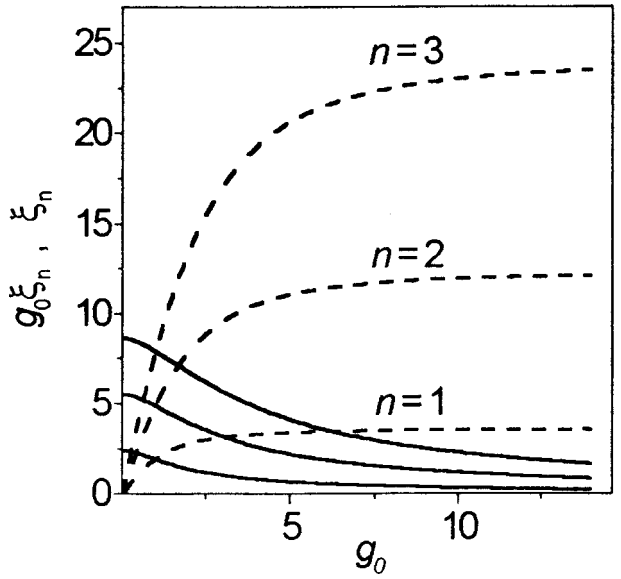

FIG. 1. The functions $\xi_n(g_0)$ (——) and $g_0\xi_n(g_0)$ (— — —) for different values of n.

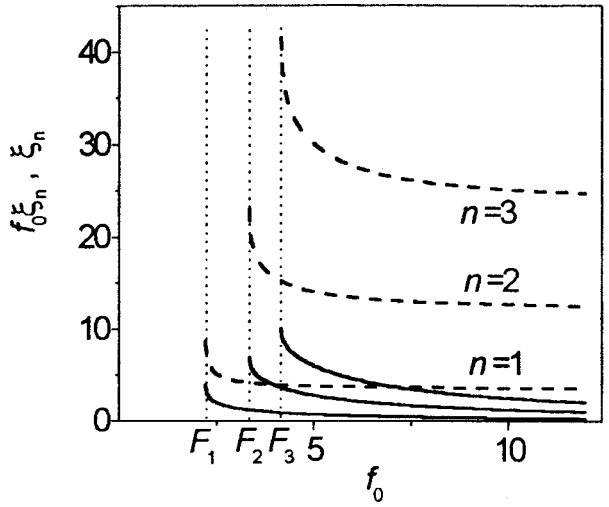

FIG. 2. The functions $\xi_n(f_0)$ (——) and $f_0\xi_n(f_0)$ (— — —) for different values of n.

3. FIXED BOUNDARY CONDITIONS

For fixed boundary conditions ($b=0$) the NLSWs are governed by the behavior of the roots of the function $g(\xi)$ (for $\omega>\omega_0$) and $f(\xi)$ (for $\omega<\omega_0$). A numerical calculation shows that for any g_0 the function $g(\xi)$ oscillates with decreasing amplitude. When the amplitude of the solution is small ($g_0\to 0$), the function $g(\xi)$ is proportional to the zero-order Bessel function $J_0(\xi)$, and its roots $\xi_n(g_0)$ coincide to high accuracy with the roots $j_{0,n}$ of the function $J_0(\xi)$. Figure 1 shows and behavior of the nth root $\xi_n(g_0)$ as a function of g_0 for values of g_0 that are not small. (It should be remembered that, as follows from Eqs. (10) and (11), by choosing a sufficiently large value of L it is possible even for large g_0 to make $\theta(0)$ arbitrarily small and ω/ω_0 arbitrarily close to 1, and our approximation therefore remains valid.)

We see that $\xi_n(g_0)$ is a monotonically decreasing function. Also plotted in Fig. 1 are the functions $g_0\xi_n(g_0)$, which appear in Eq. (10) and are important for calculating the frequencies. For $g_0\to 0$ the function $g_0\xi_n(g_0)\to 0$. On the other hand, if g_0 is large, then $g_0\xi_n(g_0)$ goes to a constant value X_n; the values of X_n for the first eight n are given in Table II.

We see that when $\theta(0)\to 0$ ($g_0\to 0$) we have $\omega/\omega_0=1+(j_{0,n}/L)^2$ and $d\omega/d\theta=0$, in agreement with the conclusions of the linear theory of spin waves. With increasing $\theta(0)$ the oscillation frequency decreases monotonically, and for $\theta(0)=\sqrt{2}X_n/L$ its value becomes equal to ω_0.

Let us turn to the region $\omega<\omega_0$ and consider the function $f(\xi)$. For sufficiently small f_0 ($f_0<F_1$) the function $f(\xi)$ does not have any roots. For $f_0=F_1$ this root appears for $\xi\to\infty$, which corresponds to the soliton solution. For $F_1\leqslant f_0<F_2$ the function $f(\xi)$ has one root, for $F_2\leqslant f_0<F_3$ it has two roots, etc. In the general case $f(\xi)$ has m roots if $F_m\leqslant f_0<F_{m+1}$, where $m=1,2,\ldots,\infty$; here $\xi_n(F_m)=\infty$ if $m\leqslant n$. Graphs of $\xi_n(f_0)$ and $f_0\xi_n(f_0)$ are given in Fig. 2. We see that $f_0\xi_n(f_0)$ is a monotonically decreasing function. When $f_0\to F_m+0$, $F_m\xi_n(F_m)\to\infty$. For large f_0, as in the case of $g_0\xi_n(g_0)$, the function $f_0\xi_n(f_0)$ goes to a constant, the numerical values of which coincide with X_n to a high degree of accuracy. Using (11), for values $f_0\approx F_m$ one can write approximately $\theta(0)=(\sqrt{2}/L)F_n\xi_n(f_0)$. Solving for $\xi_n(f_0)$ and substituting into (11), we can obtain the asymptotic expression for $\omega=\omega_n(\theta(0),L)$, viz., $\omega=\omega_0[1-0.5(\theta(0)/F_n)^2]$. There are two interesting features that should be emphasized here. First, the asymptote does not depend explicitly on the size of the system. In this case the value of L comes into the picture in the following way: the larger L, the smaller the amplitudes $\theta(0)$ at which ω approaches its asymptotes. Second, the asymptote is independent of the specific form of the divergences at the points $f_0=F_m$. The analogous statement is also true for free boundary conditions.

The NLSW frequencies $\omega=\omega_n[\theta(0),L]$ found from these data for $L=100$ are shown in Fig. 3. We see that the oscillation frequency decreases as as $\theta(0)$ increases. For sufficiently large $\theta(0)$ the value of ω_n asymptotically approaches $\omega_0[1-0.5(\theta(0)/F_n)^2]$. Since the values of F_m are rather large (see Table I), this regime is realized for $\theta(0)\ll 1$ and $\omega/\omega_0\approx 1$, and therefore our approximation remains applicable.

4. FREE BOUNDARY CONDITIONS

The case of free boundary conditions is more interesting, since in addition to the dependence of the frequency on the

TABLE II. Characteristic values of X_n for large g_0.

n	1	2	3	4	5	6	7	8
X_n	3.5	12.2	24.1	38.1	54.2	72.1	91.6	112.6
X_n'	7.2	17.6	30.6	45.8	62.8	81.6	101.9	123.6

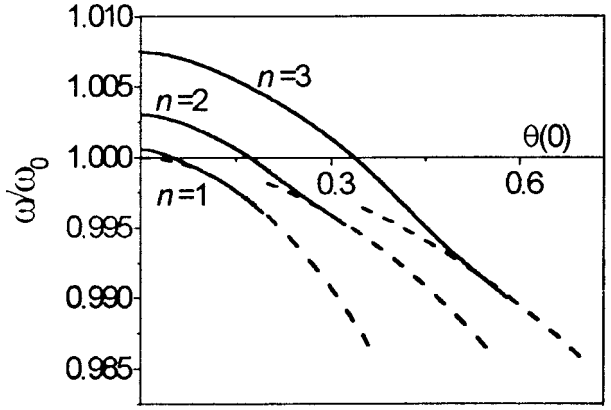

FIG. 3. Curves of $\omega=\omega_n[\theta(0),L]$ for fixed boundary conditions and $L_0=100r_v$—solid curves; the asymptotes $\omega/\omega_0=1-0.5[\theta(0)/F_n]^2$—dashed curves.

amplitude of the oscillations now another property inherent to nonlinear systems appears: bifurcations of the solutions. However, the bifurcations arise only for $\omega<\omega_0$, while for $\omega>\omega_0$ the picture is similar to that observed in the case of fixed boundary conditions. The roots of the derivative of the solution, $\xi_n'(g_0)$, are defined for all g_0, and when $g_0\to 0$, $\xi_n'(g_0)$ coincides with $j_{0,n}'$ (the nth roots of $dJ_0/d\xi$). The curves of $\xi_n'(g_0)$ and $g_0\xi_n'(g_0)$ as functions of g_0 are qualitatively similar to those for $\xi_n(g_0)$ and $g_0\xi_n(g_0)$ shown in Fig. 1. Like $g_0\xi_n(g_0)$, the derivative $g_0\xi_n'(g_0)$ tends toward a constant value X_n' as $g_0\to\infty$; the numerical values of these constants are given in Table II. As in the case of fixed boundary conditions, for $\theta(0)\to 0$ the frequency $\omega/\omega_0=1+(j_{0,n}'/L)^2$ and $d\omega/d\theta=0$. With increasing $\theta(0)$ the frequency ω decreases monotonically, and for $\theta(0)=\sqrt{2}X_n'/L$ is coincides with the boundary of the continuous spectrum $(\omega=\omega_0)$.

If $\omega<\omega_0$, on the other hand, the picture is qualitatively altered. The function $\xi_n'(f_0)$ is plotted in Fig. 4a. We see that $\xi_n'(f_0)$ has $(n+1)$ divergences. The first is observed when $f_0\to 0$. This characteristic feature (nonlinear effect at small f_0) is due to the fact that Eq. (7) is essentially nonlinear. Even if $f_0\to 0$ its solution $f(\xi)$ for small f_0 begins to grow, and it continues to grow until the nonlinear term f^3 becomes substantial. The remaining divergences occur for $f_0=F_m$; the characteristic values of F_m were discussed above and are given in Table I. Graphs of $f_0\xi_n'(f_0)$ are given in Fig. 4b. We see that as $f_0\to 0$ the value of $f_0\xi_n'(f_0)\to 0$. When $f_0\to\infty$, the values of f_0 tend toward the same constants X_n' as in the case $\omega>\omega_0$. The function $f_0\xi_n'(f_0)$ has n divergences.

These features in the behavior of the functions $\xi_n'(f_0)$ and $f_0\xi_n'(f_0)$ for $f_0=0,F_1,F_2$, etc., lead to the onset of bifurcations. Fig. 5 shows graphs of $\omega=\omega_n[\theta(0),L]$. Only for NLSWs with $n=1$ are bifurcations absent. When $\theta(0)<\sqrt{2}X_n'/L$, for $\omega>\omega_0$ we have the upper branch of oscillations, which was discussed above, and for $\omega<\omega_0$ we have the lower branch. The difference between these modes is manifested most clearly as $\theta(0)\to 0$, when the upper branch corresponds to a nearly linear solution $g(\xi)$ while the lower branch corresponds to an essentially nonlinear solution $f(\xi)$ in which $f(\xi\approx 1)\gg f(0)$. If $\theta(0)=\sqrt{2}X_n'/L$, then, as we have said, the upper branch passes through $\omega=\omega_0$. For $\theta(0)>\sqrt{2}X_n'/L$ we have two branches of oscillations with $\omega<\omega_0$. If $\theta(0)$ is sufficiently large, both branches tend toward the asymptote $\omega/\omega_0=1-0.5[\theta(0)/F_1]^2$.

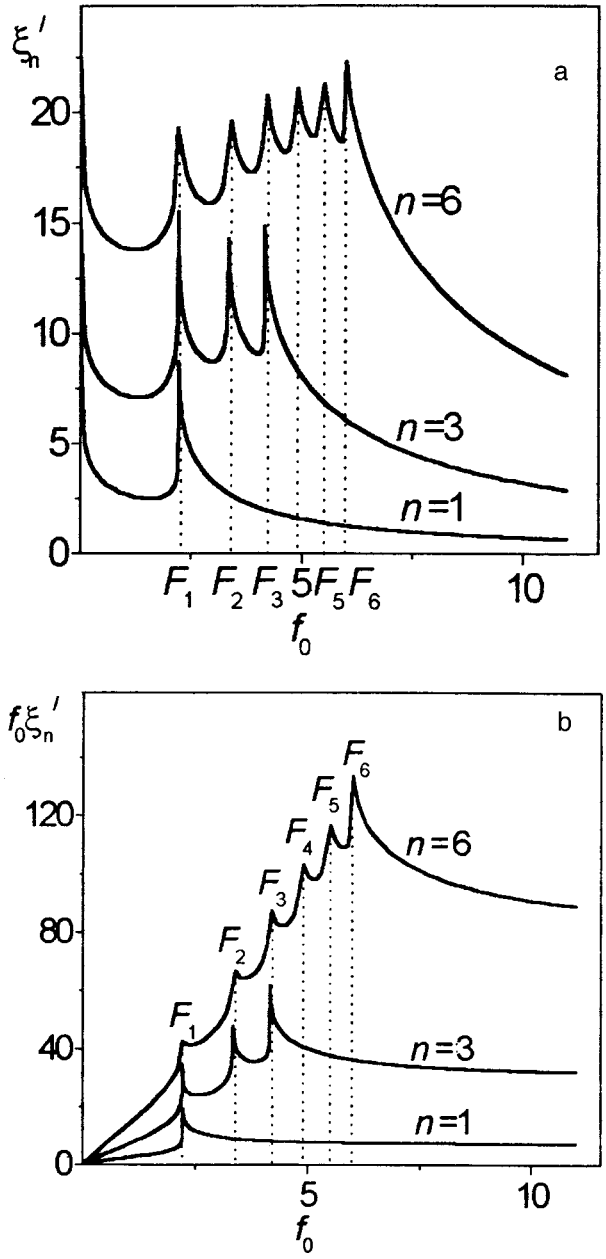

FIG. 4. The functions $\xi_n'(f_0)$ (a) and $f_0\xi_n'(f_0)$ (b) for different values of n.

Let us consider the NLSWs with $n=2$. It can be seen in Fig. 5 that when $\theta(0)<\theta_{2,1}^c$ (expressions for $\theta_{n,k}^c$ will be given below), two branches of oscillations are observed. If $\theta(0)>\theta_{2,1}^c$, two new branches of oscillations appear. When $\theta(0)$ is large, ω tends toward the asymptotes $\omega/\omega_0=1-0.5[\theta(0)/F_i]^2$, where $i=1,2$. In the general case for NLSWs with any n there are $(n-1)$ bifurcation parameters $\theta_{n,k}^c$, where $k=1,2,\ldots n-1$. At each $\theta_{n,k}^c$ two new branches of oscillations appear, with a characteristic amplitude dependence of the frequency: $\omega=\omega_{1,2}=\omega[\theta(0)]\pm P_{n,k}[\theta(0)-\theta_{n,k}^c]^s$, where $P_{n,k}$ and s are numbers, with $s<1$. The values of $\theta_{n,k}^c$ can be determined from the relation $d\omega/d\theta=\infty$ or $d(f_0\xi_n'(f_0))/df_0=0$. This formula leads to the dependence $\theta_{n,k}^c=\sqrt{2}t_{n,k}/L$, in which the parameters $t_{n,k}$ can be determined numerically. The actual values of $t_{n,k}$ for n not

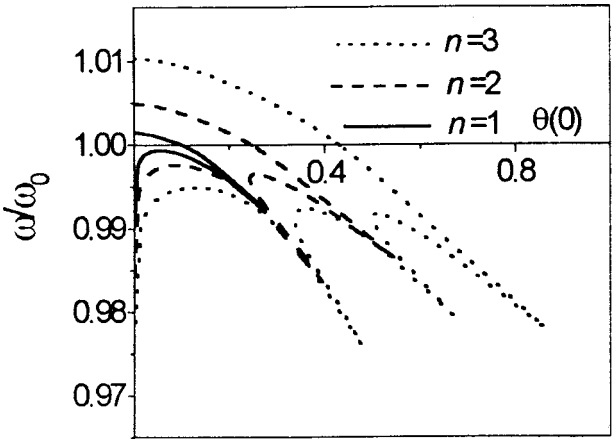

FIG. 5. The functions $\omega=\omega_n[\theta(0),L]$ for free boundary conditions and $L_0=100r_v$.

very large are also not very large, not exceeding 10 for $n<8$; for example:

$t_{2,1}=2.8$; $t_{3,1}=2.6$; $t_{3,2}=3.8$; $t_{4,1}=2.5$;

$t_{4,2}=3.7$; $t_{4,3}=4.6$; $t_{5,1}=2.4$; $t_{5,2}=3.6$;

$t_{5,3}=4.5$; $t_{5,4}=5.2$; $t_{6,1}=2.4$; $t_{6,2}=3.6$;

$t_{6,3}=4.4$; $t_{6,4}=5.1$; $t_{6,5}=5.8$; $t_{7,1}=2.4$;

$t_{7,2}=3.6$; $t_{7,3}=4.4$; $t_{7,4}=5.1$; $t_{7,5}=5.7$;

$t_{7,6}=6.3$.

Therefore, for sufficiently large values of L, the complex picture of bifurcations can be described using the approximation of weakly nonlinear waves employed here. For sufficiently large values of $\theta(0)$ the frequencies ω for the different branches approach their asymptotes $\omega/\omega_0=1-0.5[\theta(0)/F_i]^2$, $i=1,2,\ldots,n$.

CONCLUDING REMARKS AND A DISCUSSION OF POSSIBLE GENERALIZATIONS

We have considered NLSWs with radial symmetry, $\theta=\theta(r)$, $\varphi=\omega t+\varphi_0$, in a cylindrical ferromagnetic particle of radius L_0. We found that, even in the approximation of small-amplitude nonlinear waves, for sufficiently large $L_0 \gg r_v$ the picture of the nonlinear modes is extremely complicated and can include a series of bifurcations.

For fixed boundary conditions the bifurcations do not occur, and the classification of the modes is the same as in the linear case—each branch of oscillations is characterized by an integer (the mode index n). The mode frequency ω_n falls off smoothly with increasing amplitude $\theta(0)$, and for $\theta(0)=\sqrt{2}X_n/L$ it crosses the boundary ω_0 of the continuous spectrum and then approaches the asymptotes $\omega/\omega_0=1-0.5[\theta(0)/F_n]^2$.

The case of free boundary conditions is more interesting, since then bifurcations are also present, and the number of branches is greater than in the linear case or for the nonlinear problem with fixed boundary conditions. For the mode with $n=1$ there are two such branches (see Fig. 5). For $\theta(0)\to 0$ the upper branch describes nonlinear spin waves with the dispersion relation $\omega/\omega_0=1+(j'_{0,n}/L)^2$ and $d\omega/d\theta=0$; the lower mode is essentially nonlinear. For the remaining modes with $n\geqslant 2$ there are $(n-1)$ bifurcation parameters $\theta^c_{n,k}$, $k<n$. If at fixed n the amplitude is smaller than $\theta^c_{n,1}$, then one observes two branches of oscillations. When $\theta(0)$ becomes larger than $\theta^c_{n,1}$, two more branches appear, etc. In general, if $\theta^c_{n,k}<\theta(0)<\theta^c_{n,k+1}$, then there exist $2(k+1)$ different branches of oscillations. When the amplitude $\theta(0)$ becomes sufficiently large, the mode frequencies ω_n corresponding to the different branches fall off smoothly with increasing $\theta(0)$ to the asymptotic values $\omega/\omega_0=1-0.5[\theta(0)/F_i]^2$, $i=1,2,\ldots n$.

For arbitrary boundary conditions, when the parameters a and b are finite, it is necessary to analyze in terms of the functions $f(\xi)$ and $g(\xi)$ the relation $(r_v a)f+b\sqrt{1-\omega/\omega_0}(\partial f/\partial\xi)=0$ for frequencies $\omega<\omega_0$, and $(r_v a)g+b\sqrt{\omega/\omega_0-1}(\partial g/\partial\xi)=0$ for $\omega>\omega_0$. Here the frequency approximates in the condition and the initial universality is to a considerably degree lost, and the analysis becomes more complicated. However, qualitatively the result can be described by noting that for finite values of $r_v a/b$, as the boundary of the continuous spectrum is approached the boundary conditions effectively become fixed. For $r_v a/b\sim 1$, since $|\omega/\omega_0-1|\ll 1$, the behavior of the SW modes is practically the same as for fixed boundary conditions. The transition to a picture effectively corresponding to free conditions is possible only at large values of b, when $(r_v a)^2 \ll b^2|\omega/\omega_0-1|$.

A concrete analysis of the NLSW frequencies has been done only for modes with radial symmetry $(q=0)$ and for the two simplest cases of the boundary conditions. As we have said [see Eq. (4)], for cylindrical particles there can be more-general solutions of the form $\theta=\theta(x)$, $\varphi=\omega t+q\chi+\varphi_0$, where q takes integer values. Let us discuss the general regularities in the formation of nonlinear modes with different angular dependence. It can be said that the possibility of bifurcations and their character for NSWs with $q=0$ are due to the presence of localized solutions ($\theta=0$ or $d\theta/d\xi=0$, when $\xi\to\infty$) for a countable set of values of the initial conditions $\theta(0)$. This property is evidently preserved for modes with various $q\neq 0$ as well. This provides grounds for assuming that bifurcations of the nature described will be observed for all values of q.

For a spherical particle the angle dependence of the magnetization is much more complicated,[10] and a detailed examination of this case is beyond the scope of this paper. However, analysis of the simplest version of radially symmetric oscillations, neglecting their dipole–dipole interaction (as can be done when $K\gg 2\pi M_0^2$), does not present difficulty. For this case one can also simplify the initial Landau–Lifshitz equation to two universal equations of the type (7), (9), which will differ from (7) for $\omega<\omega_0$ or (9) for $\omega>\omega_0$ only by the absence of the term containing q and the replacement of $(1/\xi)(d/d\xi)$ by $(2/\xi)(d/d\xi)$. For these equations all of the regularities, in particular the presence of a countable set of localized solutions, remain the same, and one can expect an analogous picture of the nonlinear modes, including the possibility of bifurcations of the type described above.

We conclude by noting that the modification of the magnetic two-dimensional axially symmetric solitons in a cylindrical region of finite radius is not specific to two-

dimensional systems. The existence of a sequence of bifurcations creating solitons of increasingly complex form in the case of free boundaries and the absence of these bifurcations for fixed boundary conditions is also observed in one-dimensional systems[14–16] and is solely a consequence of the finite size of the system.

The study was supported by the grant INTAS 97-31 311.

*E-mail: bivanov@i.com.ua

[1] B. Hillebrands, C. Mathieu, C. Hartmann, M. Bauer, O. Buettner, S. Riedling, B. Roos, S. O. Demokritov, B. Bartenlian, C. Chappert, D. Decanini, F. Rosseaux, E. Cam, A. Muller, B. Hoffmann, and U. Hartmann, J. Magn. Magn. Mater. **75**, 10 (1997).
[2] M. Grimsditch, Y. Jaccard, and I. K. Shuller, Phys. Rev. B **58**, 11539 (1998).
[3] K. Yu. Guslienko and A. N. Slavin, J. Appl. Phys. **87**, 6337 (2000).
[4] C. Mathieu, J. Jorzick, A. Frank, S. O. Demokritov, A. N. Slavin, B. Hillebrands, B. Bartenlian, C. Chappert, D. Decanini, F. Rosseaux, and E. Cambril, Phys. Rev. Lett. **81**, 3968 (1998).
[5] C. Mathieu, C. Hartmann, M. Bauer, O. Buettner, S. Riedling, B. Roos, S. O. Demokritov, B. Hillebrands, B. Bartenlian, C. Chappert, D. Decanini, F. Rosseaux, E. Cambril, A. Müller, B. Hoffmann, and U. Hartmann, Appl. Phys. Lett. **70**, 2912 (1997).
[6] J. Jorzick, S. O. Demokritov, B. Hillebrands, B. Bartenlian, C. Chappert, D. Decanini, F. Rosseaux, and E. Cambril, Appl. Phys. Lett. **75**, 3859 (1999).
[7] A. G. Gurevich and G. A. Melkov, *Magnetic Oscillations and Waves* [in Russian], Nauka, Moscow (1994).
[8] V. S. L'vov, *Nonlinear Spin Waves* [in Russian], Nauka, Moscow (1987).
[9] A. I. Akhiezer, B. G. Bar'yakhtar, and S. V. Peletminskii, *Spin Waves* [North-Holland, Amsterdam (1968); Nauka, Moscow (1967)].
[10] A. M. Kosevich, B. A. Ivanov, and A. S. Kovalev, *Nonlinear Magnetization Waves. Dynamical and Topological Solitons* [in Russian], Naukova Dumka, Kiev (1983); A. M. Kosevich, B. A. Ivanov, and A. S. Kovalev, Phys. Rep. **194**, 117 (1990).
[11] R. Y. Chiao, E. Garmire, and C. H. Townes, Phys. Rev. Lett. **13**, 479 (1964).
[12] A. S. Kovalev, A. M. Kosevich, and K. V. Maslov, JETP Lett. **30**, 296 (1980).
[13] B. A. Ivanov, C. E. Zaspel, and I. A. Yastremskiĭ, Phys. Rev. B **63**, 134 413 (2001).
[14] A. S. Kovalev, Teor. Mat. Fiz. **37**, 135 (1978).
[15] A. S. Kovalev, Fiz. Tverd. Tela (Leningrad), **21**, 1729 (1979) [Sov. Phys. Solid State **21**, 991 (1979)].
[16] A. S. Kovalev and M. M. Bogdan, Fiz. Mnogochastichnykh Sistem **31**, 20 (1988).

Translated by Steve Torstveit

Influence of pressure, temperature, and magnetic field on the resistivity and magnetoresistive effect of lanthanum manganite ceramics and films with the composition $La_{0.7}Mn_{1.3}O_{3\pm\delta}$

S. S. Kucherenko, V. P. Pashchenko, P. I. Polyakov,[a] V. A. Shtaba, and A. A. Shemyakov

A. A. Galkin Donetsk Physico-Technical Institute, National Academy of Sciences of Ukraine, ul. R. Lyuksemburg 72, 83114 Donetsk, Ukraine

(Submitted February 16, 2001)
Fiz. Nizk. Temp. **27**, 761–766 (July 2001)

The effects of magnetic fields $H=0$–8 kOe and high hydrostatic pressures $P=0$–2.2 GPa on the resistivity ρ, magnetoresistive effect $\Delta R/R_0$, metal–semiconductor phase transition temperature T_{ms}, and peak temperature T_p of the magnetoresistive effect are investigated over a wide range of temperatures $T=77$–350 K in a ceramic target and a laser film of the same cationic compound $La_{0.7}Mn_{1.3}O_{3\pm\delta}$. Increasing H and P leads to a decrease of the resistivity. The observed difference in ρ, T_{ms}, and T_p between the ceramics and film samples is explained by the difference of their oxygen nonstoichiometry. The magnetoresistive effect decreases with increasing H and decreases with increasing P. The temperatures T_{ms} and T_p of the ceramics and film increase with increasing P, but the effect is stronger in the film. The observation of two phase transitions in the ceramics (the main transition at $T_{ms}=250$ K and an additional transition at $T'_{ms}=210$ K) is explained by its mesoscopic inhomogeneity of the cluster type.
 [DOI: 10.1063/1.1388419]

INTRODUCTION

Rare-earth manganites are attracting a heightened interest because of the colossal magnetoresistive (CMR) effect[1–3] observed in these perovskitelike metal oxides when doped with divalent ions: $R_{1-x}Me_x^{2+}Mn_{1-x}^{3+}Mn_x^{4+}O_3^{2-}$ (R is La^{3+}, Pr^{3+}, Nd^{3+}, or Sm^{3+}; Me^{2+} is Ca^{2+}, Sr^{2+}, Ba^{2+}, or Pb^{2+}). In spite of a large number of papers, including review articles,[4–6] the nature of the unusual coupling of the electric and magnetic properties in these materials remains in dispute.

Elucidation of the nature of the CMR effect and the development of new magnetoresistive materials based on rare-earth manganites are topical problems in science and technology. To help solve them it is useful to investigate the influence of temperature, magnetic field, and especially high hydrostatic pressures, about which little information is available.[7,8]

The most promising of the magnetoresistive rare-earth manganites are manganite–lanthanum oxides with the perovskite structure.[9–11] In distinction to conventional rare-earth manganites doped with Me^{2+}, we have investigated autodoped lanthanum manganite perovskites with excess superstoichiometric manganese.[12,13] It is of particular interest to do comparative studies of ceramic (polycrystalline) samples used as targets and thin single-crystal films obtained from these targets by magnetron[14,15] or laser[16,17] sputtering. The usefulness of such studies is suggested by the substantial difference of the magnetic and semiconductor states of powder[18] and thin-film[19] samples of $Sm_{0.6}Sr_{0.4}MnO_3$, which have been studied by various methods. The present study is devoted to a comprehensive investigation of the influence of temperature, magnetic field, and high hydrostatic pressure over wide ranges on the resistivity and magnetoresistive effect (MRE) for a ceramic target and a single-crystal laser film of the same cationic compound $La_{0.7}Mn_{1.3}O_{3\pm\delta}$.

METHODS OF PREPARING AND STUDYING THE SAMPLES

The ceramic samples — targets of manganite–lanthanum oxides of the series $La_{1-x}Mn_{1+x}O_{3\pm\delta}$ (Ref. 12) with $x=0.3$ — were obtained by a synthesizing anneal of a mixture of ChDA-grade powders of La_2O_3 ($Ia3$, $a=11.498$ Å) and Mn_3O_4 ($I4_1/amd$, $a=5.77$ Å, $c=9.38$ Å) at 900 °C (20 h) and sintering the pressings at 1150 °C for 24 h, followed by a slow cooling.

The single-crystal films were deposited by laser sputtering at 800 °C on a $LaSrGaO_4$ single-crystal substrate. For saturation of the film with oxygen it was subjected to additional annealing at 780 °C.

The phase composition and crystal lattice parameters were determined by x-ray diffraction in Cu radiation on a DRON-2 diffractometer.

The resistance R and the value of the magnetoresistive effect $\Delta R/R_0=(R_0-R_H)/R_0$ were determined by a four-probe method over a wide range of temperatures 77–350 K at several different values of the magnetic field ($H=0$, 2, 4, 6, and 8 kOe). High hydrostatic pressures P were obtained in a special two-layer chamber[20] made of nonmagnetic 40Kh-NYu refined steel, with a channel diameter of 6.5 mm and an outer diameter of 31 mm. The pressure was determined from the load on the press and was monitored by measuring the resistance of a manganese pressure sensor.[21] The errors of measurement of the quantities mentioned were within the following limits: phase composition — 3%, lattice parameters — 1%; resistivity — 0.7%, temperature — 0.1%, mag-

netic field — 1.5%, hydrostatic pressure — 3%.

EXPERIMENTAL RESULTS AND DISCUSSION

According to the x-ray data, the ceramic targets had a rhombically distorted ($Pnma$) lanthanum manganite perovskite structure with the parameters $a=5.464$ Å, $b=5.515$ Å, $c=7.728$ Å. The Curie temperature of the target was $T_C=255$ K.

The NMR spectrum of ^{55}Mn is broad, with a frequency at maximum amplitude $F=377$ MHz. In view of the frequencies for Mn^{3+} ($F=420$ MHz)[22,23] and Mn^{4+} ($F=320$ MHz)[24] this is evidence of high-frequency electron exchange between Mn^{3+} and Mn^{4+} found in the B positions, with an averaged valence $\bar{\omega}=3.5$.[25]

With identical base composition $La_{0.7}Mn_{1.4}O_{3\pm\delta}$, the ceramic target ($c$) and the films deposited by magnetron (m) and laser (l) sputtering were characterized by the following properties: resistivity (at $H=0$, $P=0$) at maximum ${}^{c}\rho_m=0.04\ \Omega\cdot$cm, ${}^{m}\rho_m=0.25\ \Omega\cdot$cm, ${}^{l}\rho_m=0.01\ \Omega\cdot$cm; temperature at maximum resistivity, corresponding to the metal–semiconductor transition, ${}^{c}T_{ms}=240$ K, ${}^{m}T_{ms}=220$ K, ${}^{l}T_{ms}=260$ K for the ceramics, magnetron film, and laser film, respectively. The difference of these temperatures, in our opinion, is due to the different oxygen content and the nonstoichiometry of the ceramic and film samples. Comparing the lattice parameters, Curie temperature, and metal–semiconductor transition temperature with those given in Refs. 26 and 27, in which the influence of nonstoichiometry on the listed properties of the lanthanum manganite perovskites $La_{1-y}Mn_{1-y}O_{3\pm\delta}$ was established, one notices that the values of a, b, and c are comparable and that the values of T_{ms} are higher for our samples. The reason for this lies apparently not only in the different nonstoichiometry but also in the mesoscopic inhomogeneity due to the excess manganese, which in the real perovskite structure of $La_{0.7}Mn_{1.3}O_{3\pm\delta}$ is found predominantly in the form of planar clusters of γ-Mn_2O_3 (Ref. 12), or, more precisely, it is due to the mixed-valence manganese ions: $Mn^{2+}_{0.5}Mn^{3+}_{1.0}Mn^{4+}_{0.5}O_3$. The magnetism of such clusters is manifested at temperatures below 45 K both in the ceramics[28] and in the magnetron films at spin-wave resonance.[29]

The temperature dependence of the resistivity of the ceramics and laser-deposited film is shown in Fig. 1 for $H=0$ and 8 kOe and $P=0$ and 1.8 GPa. One notices substantial differences not only in the value of ρ but also in the character of its temperature dependence for the ceramics and film. The higher values of the resistivity of the ceramic samples are possibly due to their porosity and the different degree of nonstoichiometry.

For the ceramic target, but not for the film, at temperatures below the main resistivity peak ($T_{ms}=250$ K) there is an additional smaller, smeared peak ($T'_{ms}=210$ K), which, like the main peak, decreases markedly with increasing pressure, i.e., the ceramics characteristically have two metal–semiconductor transitions. The main transition, depending on the magnetic field and pressure, lies in the interval from $T_{ms}=235$ K ($H=0$, $P=0$) to $T_{ms}=275$ K ($H=8$ kOe, $P=1.8$ GPa). The second transition lies between $T'_{ms}=200$ K ($H=0$, $P=0$) and $T'_{ms}=235$ K ($H=8$ kOe, $P=1.8$ GPa). The two resistive transitions in the ceramic target are apparently due to the intercrystallite zones,[12] to the mesoscopic structural[30] and magnetic[31] inhomogeneities, the nature of which is in dispute and is now being clarified. One notices that the temperature of the main resistivity peak for the ceramics ($T_{ms}=235$–275 K) is substantially lower than for the film ($T_{ms}=275$–300 K). This may be due to the different oxygen content and nonstoichiometry of the ceramic and film samples, or to the difference in the characteristic dimensions of the crystallites of the ceramic ($D\approx10$ μm) and the thickness of the single-crystal film ($d\approx0.1$ μm) and also to the influence of the substrate. These factors may be the cause of the different influence of high hydrostatic pressures ($P=1.8$ GPa) on the resistivity and value of the MRE in the ceramics and film.

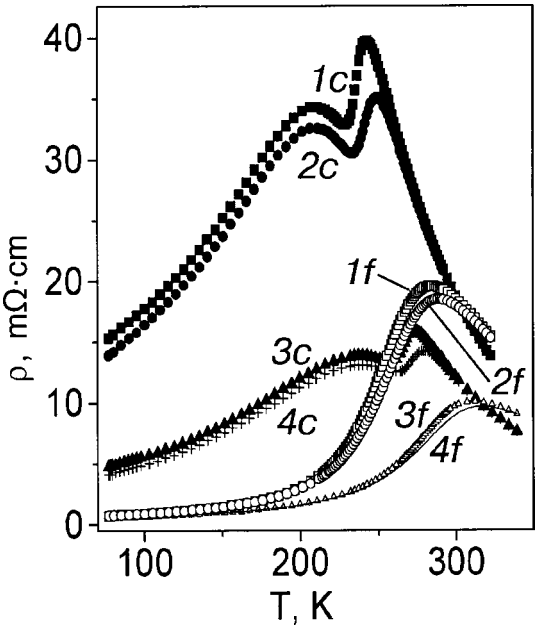

FIG. 1. Temperature dependence of the resistivity of a ceramic target (c) and a single-crystal film (f) of $La_{0.7}Mn_{1.3}O_{3\pm\delta}$ for various pressures and magnetic fields: *1c,1f* — $P=0$, $H=0$; *2c,2f* — $P=0$, $H=8$ kOe; *3c,3f* — $P=1.8$ GPa, $H=0$; *4c,4f* — $P=1.8$ GPa, $H=8$ kOe.

The temperature dependence of the magnetoresistive effect $\Delta R/R_0$ at $P=0$ and various values of the magnetic field ($H=2$, 4, 6, and 8 kOe) for the ceramic and film samples is shown in Fig. 2. One notices first the large values of the MRE in the ceramics and the less smeared $\Delta R/R_0$ peak in comparison with the film. Here the temperature of the peak of the MRE is lower in the ceramics ($T_p=237$ K) than for the film ($T_p=257$ K). As the magnetic field is increased from 2 to 8 kOe for the ceramic target, the MRE increases from 4 to 18.5%, i.e., by a factor of 4.6, while for the single-crystal film it increases from 2 to 13%, i.e., by a factor of 6.5.

The influence of the magnetic field strength on the MRE at $P=1.8$ GPa for the ceramics and film is shown in Fig. 3. At high hydrostatic pressures the value of the MRE decreases and the temperature of its peak increases. $\Delta R/R_0$ increases with increasing H from 2 to 8 kOe: for the ceramics from 3.8 to 16%, i.e., a factor of 4.2, and for the film from 1.8 to 9.8%, i.e., a factor of 5.4. In spite of the lower MRE in the film, it is influenced by the magnetic field to a greater degree.

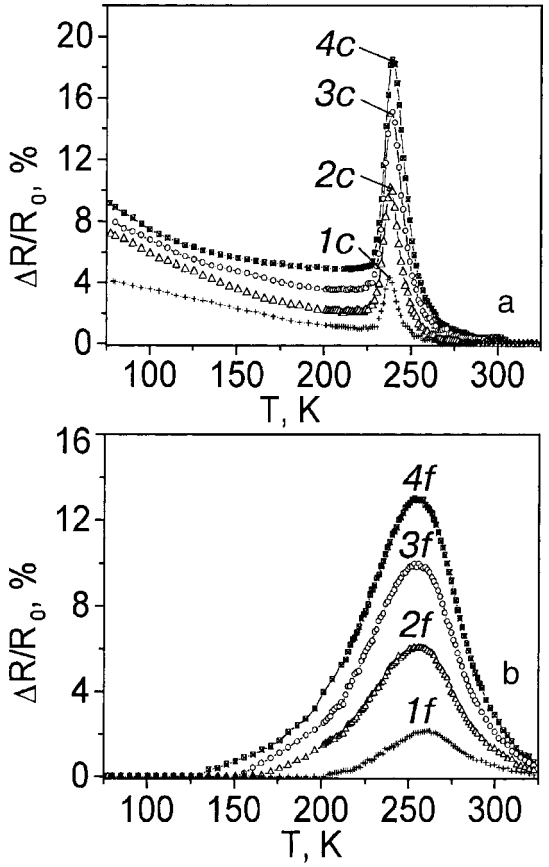

FIG. 2. Temperature dependence of the magnetoresistive effect at $P=0$ and various magnetic fields for the ceramics (a) and film (b): *1c,1f* — $H=2$ kOe; *2c,2f* — $H=4$ kOe; *3c,3f* — $H=6$ kOe; *4c,4f* — $H=8$ kOe.

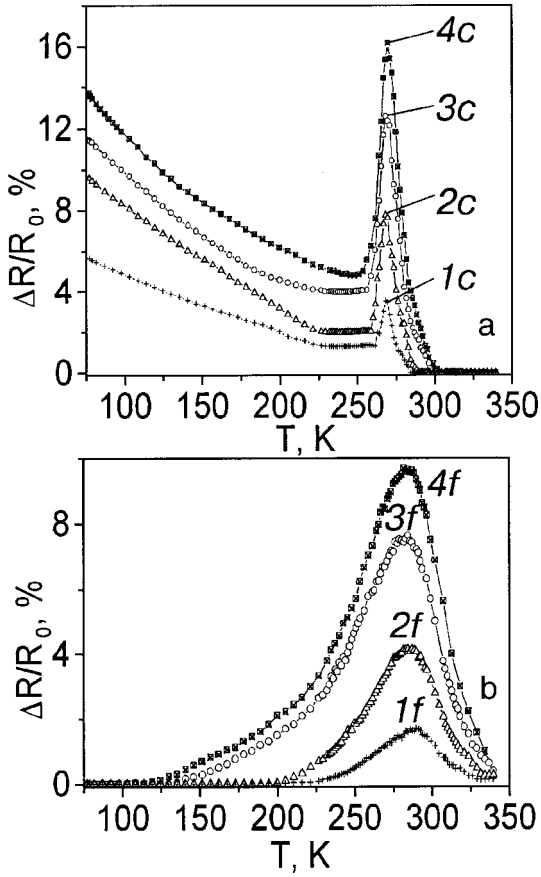

FIG. 3. Temperature dependence of the MRE at $P=1.8$ GPa and various magnetic fields for the ceramics (a) and film (b): *1c,1f* — $H=2$ kOe; *2c,2f* — $H=4$ kOe; *3c,3f* — $H=6$ kOe; *4c,4f* — $H=8$ kOe.

Figure 4 shows the effect of high hydrostatic pressures on the resistivity of the ceramics and film at $H=0$. As the pressure is increased to 2.2 GPa the resistivity decreases: by a factor of 1.75 for the ceramics and 2.5 for the film. It appears as if the resistivities of the ceramics and film should converge somewhere in the region of negative hydrostatic pressures.

The effect of high hydrostatic pressures on the metal–semiconductor transition temperature T_{ms} at $H=0$ and 8 kOe and the temperature of the magnetoresistance peak T_p for the ceramic target (the unfilled symbols) and the single-crystal film (filled symbols) is illustrated in Fig. 5. With increasing P the temperatures T_{ms} and T_p increases practically linearly in the entire pressure interval investigated, and their temperature coefficients are close in value. The reason is apparently the decrease in the inter-ion distances and the change in the exchange interaction, which shifts the region of the "metallic" state to higher temperatures.

CONCLUSIONS

Comprehensive studies of the influence of temperature, magnetic field, and high hydrostatic pressures on the resistivity and magnetoresistive effect of ceramic and film samples of the lanthanum manganite perovskites $La_{0.7}Mn_{1.4}O_{3\pm\delta}$ have established the following:

1) the resistivity of the ceramic target is higher than that of the laser film;

2) the temperature of the metal–semiconductor transition is substantially higher for the film;

3) for the ceramic samples two temperature peaks of the

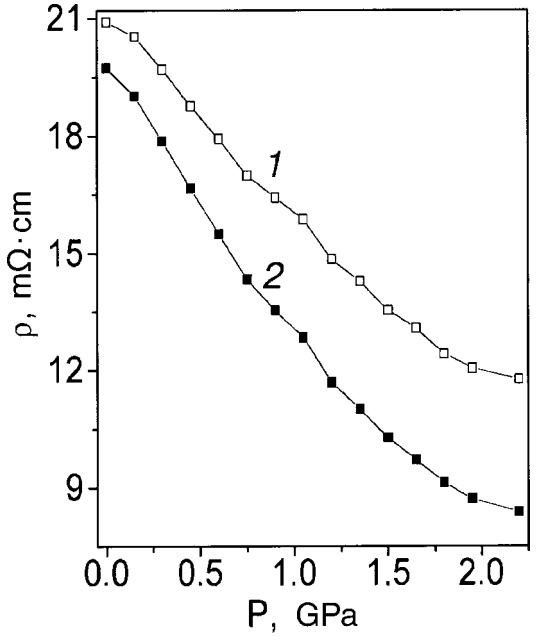

FIG. 4. Effect of high hydrostatic pressures on the resistivity of the ceramic (*1*) and film (*2*) at $H=0$.

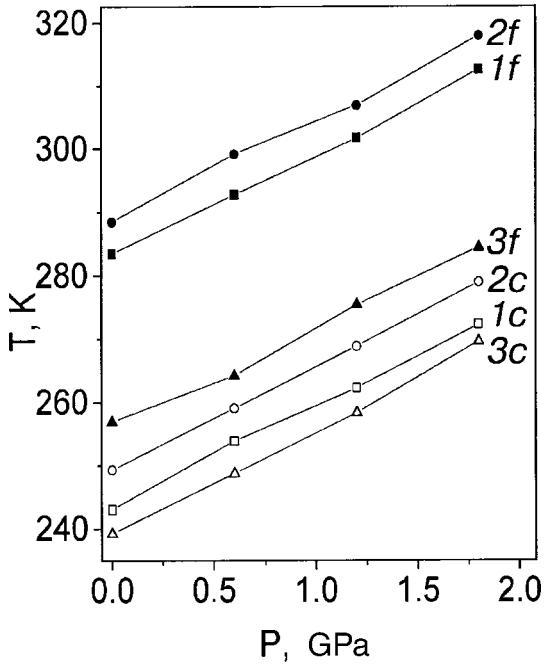

FIG. 5. Effect of high hydrostatic pressures on the metal–semiconductor phase transition temperature T_{ms} at $H=0$ and 8 kOe and the peak temperature T_p of the MRE for the ceramics (c) and film (f): *1c,1f* — T_{ms}, $H=0$; *2c,2f* — T_{ms}, $H=8$ kOe; *3c,3f* — T_p, $H=8$ kOe.

resistivity are observed, which are explained by a cluster type of mesoscopic inhomogeneity;

4) for the ceramics the MRE is larger and its peak temperature is lower than for the film, on account of the different nonstoichiometry;

5) with increasing magnetic field the MRE increases in both the ceramics and film, the effect being stronger in the film;

6) high hydrostatic pressures decrease the resistivity and increases the temperatures of the metal–semiconductor transition and of the peak of the MRE.

The authors thank V. V. Zavrazhin for assistance in doing the experiment.

[a)]E-mail: poljakov@host.dipt.donetsk.ua

[1] A. Urushibara, Y. Moritomo, A. Asamitsu, G. Kido, and Y. Tokura, Phys. Rev. B **51**, 14103 (1995).
[2] H. Y. Hwang, S. W. Cheong, P. G. Radaelli, M. Marezio, and B. Batlogg, Phys. Rev. Lett. **75**, 914 (1995).
[3] Y. Tokura, Y. Tomioka, and H. Kuwahara, J. Appl. Phys. **79**, 5288 (1996).
[4] E. L. Nagaev, Usp. Fiz. Nauk **166**, 833 (1996).
[5] A. P. Ramirez, J. Phys.: Condens. Matter **9**, 871 (1997).
[6] V. M. Loktev and Yu. G. Pogorelov, Fiz. Nizk. Temp. **26**, 231 (2000) [Low Temp. Phys. **26**, 171 (2000)].
[7] V. E. Arkhipov, V. S. Gaviko, and K. M. Demchuk, JETP Lett. **71**, 114 (2000).
[8] J.-S. Zhou and J. B. Goodenough, Phys. Rev. B **62**, 3834 (2000).
[9] N. D. Mathur, G. Burnell, S. P. Isaac, T. J. Jackson, B.-S. Teo, J. L. McManus-Driscoll, L. F. Cohen, J. E. Evetts, and M. G. Blamire, Nature (London) **387**, 266 (1997).
[10] X. Xiong, B. Dabrowski, O. Chmaissem, Z. Bukowski, S. Kolesnik, R. Dybzinski, C. W. Kimball, and J. D. Jorgensen, Phys. Rev. B **60**, 10186 (1999).
[11] N. G. Bebenin, R. I. Zaĭnullina, V. V. Mashkautsan, V. C. Gaviko, V. V. Ustinov, Ya. M. Mukovskiĭ, and D. A. Shulyatev, Zh. Éksp. Teor. Fiz. **117**, 1181 (2000) [JETP **90**, 1027 (2000)].
[12] V. P. Pashchenko, S. I. Khartsev, and O. P. Cherenkov, Neorg. Mater. **35**, 1294 (1999).
[13] G. J. Chen, Y. H. Change, and H. W. Hsu, Neorg. Mater. **219**(3), 317 (2000).
[14] S. I. Khartsev, V. N. Krivoruchko, and V. P. Pashchenko, Fiz. Nizk. Temp. **23**, 840 (1997) [Low Temp. Phys. **23**, 631 (1997)].
[15] V. N. Krivoruchko and S. I. Khartsev, Fiz. Nizk. Temp. **24**, 1070 (1998) [Low Temp. Phys. **24**, 803 (1998)].
[16] R. von Helmolt, J. Wecker, and B. Holzapfel, Phys. Rev. Lett. **71**, 2331 (1984).
[17] V. A. Berezin, V. I. Nikoalaĭchik, V. T. Volkov, Yu. B. Gorbatov, V. I. Levashov, G. L. Klimenko, V. A. Tulin, V. N. Matveev, and I. I. Khodos, JETP Lett. **25**, 398 (1995).
[18] C. Martin, A. Maignar, M. Hervieu, and B. Ravean, Phys. Rev. B **60**, 12199 (1999).
[19] Y. Morimoto, A. Machida, and K. Matsuda, Phys. Rev. B **56**, 5088 (1997).
[20] A. V. Oleĭnik, P. I. Polyakov, and V. G. Synkov, Fiz. Tekh. Vysokikh Davlenii **4**, 88 (1994).
[21] L. Yu. Vereshchagin, *Solid State at High Pressure* [in Russian], Nauka, Moscow (1991).
[22] A. A. Shemyakov and V. A. Klochan, Zh. Éksp. Teor. Fiz. **101**, 1014 (1992) [Sov. Phys. JETP **74**, 544 (1992)].
[23] A. A. Shemyakov, V. P. Pashchenko, and A. D. Loyko, Appl. Magn. Reson. **16**, 403 (1999).
[24] G. J. Tomka, R. S. Riedi, Gz. Kapusta, G. Balakrishnan, D. Mck. Paul, M. R. Lees, and J. Barratt, Appl. Phys. **83**, 7151 (1998).
[25] V. P. Pashchenko, A. A. Shemyakov, V. K. Prokopenko, V. N. Derkachenko, O. P. Cherenkov, V. I. Mihajlov, V. N. Varyukhin, V. P. Dyakonov, and H. Szymczak, J. Magn. Magn. Mater. **220**, 52 (2000).
[26] R. Mahendiran, S. K. Tiwary, A. K. Raychaudhuri, and T. V. Ramakhrishnan, Phys. Rev. B **53**, 3348 (1996).
[27] M. R. Ibarra, J. M. De Teresa, P. A. Algarabele, C. Marguina, J. Blasco J. Garcia, S. Oseroff, and S.-W. Cheong, Phys. Rev. B **56**, 8902 (1997).
[28] VV. P. Pashchenko, V. K. Prokopenko, A. A. Shemyakov, V. N. Varyukhin, V. N. Derkachenko, A. D. Loĭko, V. P. D'yakonov, G. Shimchak, and A. Gladchuk, Metallofizika (Kiev) **22**, No. 12, 18 (2000).
[29] V. Dyakonov, A. Prohorov, and V. Shapovalov, Phys. Lett. A **268**, 202 (2000).
[30] V. P. Pashchenko, E. G. Darovskikh, V. S. Abramov, O. B. Topchienko, G. A. Potapov, L. I. Medvedeva, and S. M. Lisitsyn, Neorg. Mater. **30**, 939 (1994).
[31] V. V. Runov, D. Yu. Chernyshov, A. I. Kurbakov, M. K. Runova, V. A. Trunov, and A. I. Okorokov, Zh. Eksp. Teor. Fiz. **118**, 1174 (2000) [JETP Lett. **91**, 1017 (2000)].

Translated by Steve Torstveit

QUANTUM EFFECTS IN SEMICONDUCTORS AND DIELECTRICS

Polarization of far-IR radiation from *p*-type germanium under uniaxial pressure and strong electric field

V. Bondar* and P. Tomchuk

Institute of Physics of National Academy of Sciences of Ukraine, 46 Pr. Nauki, Kiev, 03028, Ukraine

V. Tulupenko

Donbass State Engineering Academy, 72 Str. Shkadinov, Kramatorsk, 84313, Ukraine

(Submitted February 28, 2001)
Fiz. Nizk. Temp. **27**, 767–768 (July 2001)

Experimental results on the polarization of the far-IR radiation ($\lambda = 80-120\ \mu$m) from *p*-type germanium under strong uniaxial pressure in a heating electric field at liquid-helium temperature are reported. The directions of the polarization and electric field are shown to be mainly coaxial for samples under pressure and perpendicular to each other for unstrained samples. The possible reasons for this phenomenon are discussed. [DOI: 10.1063/1.1388420]

INTRODUCTION

As is well known, a strong electric field disturbs the cubic symmetry of the carrier distribution of a semiconductor in *k* space. This results in anisotropic optical properties connected with free carriers. In particular, the electromagnetic radiation from a semiconductor must be polarized.[1,2] Indeed, polarization of the far-IR radiation ($\lambda = 80-120\ \mu$m) from Ge and Si was observed and studied in Refs. 3–5. It was proposed that in *p*-Ge the polarization is caused by asymmetry of the distribution function of heavy holes (by the second spherical harmonic in the development of the distribution function in a strong electric field). On the other hand, there is a theoretical model of radiation polarization that takes into account the possible intersubband transitions in the *p*-material.[1] Uniaxial pressure splits the light and heavy subbands and must change the intersubband transitions. In view of this, the main goal of the present study was to investigate the influence of uniaxial pressure (up to 8 kbar/cm^2) on the polarization and intensity of the far-IR radiation from *p*-Ge under strong electric fields at liquid-helium temperature.

EXPERIMENTAL DETAILS

Samples of *p*-Ge with a resistivity at room temperature of 5 $\Omega\cdot$cm and $1\times1\times7$ mm dimensions were used in our experiments. The sides were well parallel (to within 20″). The samples were oriented along the ⟨100⟩ axis. To improve the mechanical strength of the samples at liquid-helium temperature, Pb-In contacts were utilized. Injection of minority carriers from the contacts started when the value of the applied field reached 200–250 V/cm. This injection was controlled by the form of the current pulse and did not exceed ~10%. To cut off the short-wavelength part of the IR emission spectrum, black polyethylene was used as a filter. The strong electric field was provided by a pulse generator with a 0.8 μs pulse duration and a repetition rate of 6 Hz. The measurements were carried out at temperatures of 4.2–5 K. A Ge–Ga photodetector with a range of sensitivity of 80–120 μm was employed. The results were reproducible (reliability up to 95%) and corresponded to elastic deformation, as after having been released from the maximal pressure (7–8 kbar/cm^2) the samples gave the same signals as did the original unstrained states.

RESULTS AND DISCUSSION

Figure 1 presents the dependence of the far-IR signal intensity on the angle between the ⟨100⟩ axis and transmission direction of the polarizer when the directions of the electric field and pressure coincide with the ⟨100⟩ axis. In the absence of pressure the radiation is partially polarized, and the degree of polarization reached nearly 10%. The maxi-

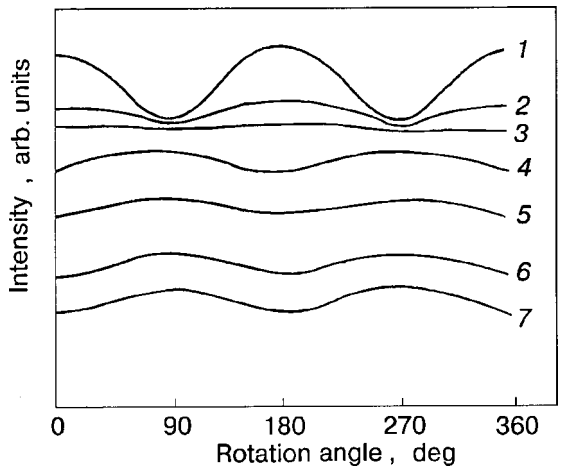

FIG. 1. Dependence of the direction of radiation polarization upon the angle rotation of the polarizer. Uniaxial pressure, kbar/cm^2: 0 (*1*); 0.25 (*2*); 1 (*3*); 2 (*4*); 3 (*5*); 4 (*6*); 6 (*7*). The value of electric field $V = 100$ V/cm.

mum intensity of the radiation is observed for zero angle of rotation of the polarizer. At low pressure (up to around 0.7 kbar/cm^2) the intensity dependence on the angle of rotation of the polarizer is almost a straight line (curve *3*). Increasing the applied pressure causes a change of the polarization direction to 90°, which remains constant up to 6 kbar/cm^2.

We can propose at least two reasonable explanations for this phenomenon. The first one is a significant role of the intersubband transitions, which play the main role in the emission of IR light from *p*-Ge in a heating electric field without applied pressure. It has been shown[1] that in this case the radiation will be partially polarized in the direction perpendicular to the electric field. The degeneracy of the valence band vanishes under uniaxial pressure, and the role of the intersubband transitions decreases. Under strong pressure and not so strong a heating electric field the intersubband transitions do not play any role at all in the light emission. On the other hand, the isoenergetic surfaces under strong pressure are known to be ellipsoids with different hole populations.[6] The effective mass of the holes in a more populated ellipsoid is smaller along the field than in the perpendicular direction. In this case the radiation should be oriented along the electric field.

The second probable explanation derives from the different scattering probability of a hole on an acoustic phonon and an ionized impurity. The effective mass of the majority of the holes along the field direction is considerably less in the strained samples than in the unstrained ones. As a result of the effective mass reduction, the carrier scattering from the ionized impurities is expected to be less efficient in the strained samples than in the unstrained ones. On the other hand, the scattering on acoustic phonons is assumed to be essentially unaffected by the applied pressure. The temperature dependences of the degree of polarization could be helpful to test this hypothesis.

It should be noted that the same change of the polarization with respect to the applied heating electric field and pressure was observed for *n*-Ge samples with different resistivities: for pure samples the polarization is oriented along the field direction, while for heavily doped samples it is perpendicular to the field.

The authors are much obliged to Prof. O. G. Sarbey for fruitful discussion, to A. M. Vasiliev and A. P. Larionov for supplying the experimental setup with liquid helium and nitrogen, and to N. F. Chornomorets and V. V. Bondarenko for active engineering support.

*E-mail: vbondar@iop.kiev.ua

[1] F. T. Vas'ko, Fiz. Tekh. Poluprovodn. **24**, 682 (1990) [Sov. Phys. Semicond. **24**, 428 (1990)].
[2] I. Ferretti, A. Abramo, R. Brunetti, and J. Jacoboni, Phys. Status Solidi B **204**, 538 (1997).
[3] V. M. Bondar, A. V. Kuznetsov, and A. S. Khanenko, Ukr. Fiz. Zh. **36**, 344 (1991).
[4] V. M. Bondar, A. V. Kuznetsov, and P. M. Tomchuk, Ukr. Fiz. Zh. **36**, 517 (1991).
[5] V. M. Bondar, A. V. Kuznetsov, P. M. Tomchuk, and A. S. Khanenko, Ukr. Fiz. Zh. **36**, 824 (1991).
[6] G. L. Bir and G. E. Pikus, *Symmetry and Strain Induced Effects in Semiconductors*, Wiley, New York (1975).

This article was published in English in the original Russian journal. Reproduced here with stylistic changes by AIP.

PHYSICAL PROPERTIES OF CRYOCRYSTALS

Lower limit on the thermal conductivity of krypton–xenon solid solutions

V. A. Konstantinov,* V. P. Revyakin, and M. A. Pokhodenko

B. Verkin Institute for Low Temperature Physics and Engineering, National Academy of Sciences of Ukraine, pr. Lenina 47, 61103 Kharkov, Ukraine

(Submitted February 5, 2001)
Fiz. Nizk. Temp. **27**, 769–772 (July 2001)

The isochoric thermal conductivity of the solid solutions $Kr_{1-\xi}Xe_{\xi}$ ($\xi=0.14$ and 0.37) is investigated in the temperature interval from 80 K to the onset of melting. Its value and temperature dependence are in good agreement with the lower limit of the thermal conductivity of the crystal lattice. © *2001 American Institute of Physics.*
[DOI: 10.1063/1.1388421]

INTRODUCTION

Solid rare gases Ar, Kr, and Xe are among the simplest objects in solid-state physics, and for this reason they are traditionally used for comparison of experimental and theoretical results.[1] In perfect crystals at temperatures of the order of their Debye temperatures and above ($T \geqslant \Theta_D$) the thermal conductivity is almost entirely governed by three-phonon scattering processes and should vary according to the law $\Lambda \propto 1/T$ (Ref. 2). This temperature dependence arises because of the change of the populations of the modes. For it to be realized, the volume of the crystal must remain unchanged, since otherwise the modes will change, and that will lead to a different temperature dependence of the thermal conductivity.

Isochoric studies of the thermal conductivity of solid Ar, Kr, and Xe have shown[3–5] that a dependence $\Lambda \propto 1/T$ holds only roughly for $T \geqslant \Theta_D$. As the temperature is increased, the temperature dependence begins to deviate noticeably in the direction of a weaker dependence, the deviation gradually increasing to 20–25% at temperatures just below where the sample starts to melt.[5] This deviation is due to the fact that the phonon mean free path cannot decrease without limit as the temperature is raised. It follows from simple arguments that it must be bounded by either the interatomic distance[6] or by one-half of the phonon wavelength.[7] This means that the thermal conductivity also tends toward a lower limit $\Lambda_{\min}$, which for the cases mentioned differs by 20% in absolute value.[8]

The thermal conductivity of a number of amorphous solids and highly disordered crystals has been well described[7] under the assumption that all of the excitations are scattered at a distance of one-half the wavelength, $\lambda/2$. Here the lower limit $\Lambda_{\min}$ of the thermal conductivity of the crystal lattice can be written in the form

$$\Lambda_{\min}=\left(\frac{\pi}{6}\right)^{1/3} k_B n^{2/3} \sum_i v_i \left\{ \left(\frac{T}{\Theta_i}\right)^2 \int_0^{\Theta_i/T} \frac{x^3 e^x}{(e^x-1)^2}\, dx \right\}. \quad (1)$$

The summation is taken over three modes with (two transverse and one longitudinal) with sound velocities v_i; Θ_i is the Debye temperature for each polarization, $\Theta_i = v_i(\hbar/k_B)(6\pi^2 n)^{1/3}$, where n is the number of atoms per unit volume; $x = v h/k_B T\lambda$. Table I shows $\Lambda_{\min}$ for the solid rare gases Ne, Ar, Kr, and Xe, calculated at the temperatures of their triple points. The densities and sound velocities needed in the calculation were taken from Refs. 1 and 9–11. Also given are the experimental values of the thermal conductivity Λ_{meas}, measured at the saturated vapor pressure.[1,5] It is seen that at pre-melting temperatures the thermal conductivity of the solid rare gases Ne, Ar, Kr, and Xe is only 1.5–2 times larger than the lower limit of the thermal conductivity of the lattice. This circumstance was first pointed out by Slack.[6] He also proposed that the phonon–phonon scattering at these temperatures is maximal and that further decrease of the thermal conductivity is impossible.

This conjecture is easily checked. The thermal conductivity of a crystal can be lowered by creating defects in it, in particular, by adding impurities. In Ref. 12 the isochoric thermal conductivity of solid krypton containing 3 and 6.3 mol.% methane was investigated in the temperature interval from 50 K to the melting temperature. It was noted that the contribution of point defects to the thermal resistance of the crystal decreases with increasing temperature, but the absolute value of the thermal conductivity was nevertheless 30–40% higher than the lower limit $\Lambda_{\min}$ calculated according to Eq. (1).

TABLE I. Thermal conductivity of solid rare gases Ne, Ar, Kr, and Xe, measured at the saturated vapor pressure[1] at temperatures corresponding to the triple points (Λ_{meas}), and calculated according to Eq. (1) ($\Lambda_{\min}$); the triple-point temperatures T_t and the molar volumes V_m are from Ref. 1, and the longitudinal v_l and transverse v_t sound velocities are from Refs. 9–11.

Gas	T_t, K	V_m, cm^3/mole	v_l km/s	v_t km/s	$\Lambda_{\min}$ mW/(cm·K)	Λ_{meas} mW/(cm·K)	$\frac{\Lambda_{\text{meas}}}{\Lambda_{\min}}$
Ne	24.6	14.0	0.97	0.60	1.35	3.6	2.5
Ar	83.8	24.7	1.3	0.72	1.2	2.1	1.75
Kr	116	30.1	0.98	0.59	0.92	1.45	1.65
Xe	161	38.5	0.98	0.58	0.78	1.25	1.6

In the present study we investigated the isochoric thermal conductivity of the solid solutions $Kr_{1-\xi}Xe_{\xi}$ ($\xi=0.14$ and 0.37) in the temperature interval from 80 K to the start of melting.

EXPERIMENTAL PROCEDURE

Studies can be carried out at constant volume in the case of molecular solids, which are characterized by comparatively low values of the temperature coefficient of the pressure $(dP/dT)_V$. If the high-pressure cell is filled with a solid samples of sufficiently high density, then the sample can subsequently be cooled at a practically constant volume, while the pressure in the sample decreases comparatively slowly. In a certain interval of densities the sample will pull away from the walls of the cell at a certain characteristic temperature T_0, and the condition of isochoricity is violated. The onset of melting is shifted to higher temperatures with increasing density of the sample. The deviations from constant volume due to the thermal and elastic strains of the measurement cell can be easily taken into account.

The present studies were done by the steady-state method on an apparatus with coaxial geometry.[13] The measurement cell of beryllium bronze had an inner diameter of 17.6 mm and a length of 160 mm and was designed for a maximum pressure of 800 MPa. The diameter of the inner measurement cylinder was 10.2 mm. The temperature sensors (platinum resistance thermometers) were placed in special channels of the inner and outer cylinders and were not subject to the influence of high pressure. The samples were grown at a temperature gradient along the measurement cell of around 1 K/cm, and the pressure in the cylinder was varied over the range 50–250 MPa to obtain samples of different density. After the growth the inlet capillary was blocked off by freezing it with liquid nitrogen (hydrogen), and the samples were annealed for 5–6 h at premelting temperatures. After the measurements were completed the samples were evaporated in a thin-walled vessel and their mass was determined by weighing. The molar volume of the samples was determined from the known volume of the measurement cell and the mass of the sample. The total systematic error of the measurements was dominant and did not exceed 5% for the thermal conductivity and 0.2% for the volume. The purity of the initial Kr and Xe gases used in preparing the solution was 99.98% or better. The concentration of the components was determined by a chromatographic method in the gas phase.

DISCUSSION OF THE RESULTS

Two samples of the solid solution $Kr_{1-\xi}Xe_{\xi}$ with $\xi=0.14$ and 0.37 were investigated in the temperature interval from 80 K to the onset of melting. The choice of this system and of the concentrations and temperature interval of the measurements was based on the following considerations:

—the phase diagram of the solid solution $Kr_{1-\xi}Xe_{\xi}$ is well known;[14]

—the liquid and solid phases have a point of equal concentrations at a temperature of 114.1 K and $\xi=0.15$;

—between 75 and 114 K the components form a solid solution with an fcc structure for all $1\geqslant\xi\geqslant 0$.

Scattering on point defects is governed by the factor Γ, which can be written[15]

$$\Gamma=\xi(1-\xi)\left[\frac{\Delta M}{M}+2\gamma\frac{\Delta\Omega_0}{\Omega_0}\right]^2, \tag{2}$$

where γ is the Grüneisen coefficient, $M=(1-\xi)M_{Kr}+\xi M_{Xe}$, and $\Omega_0=(1-\xi)\Omega_{0Kr}+\xi\Omega_{0Xe}$ are, respectively, the averaged atomic weight and the volume per atom of the solid solution ($\Omega_0=6.3\times10^{-23}\,\mathrm{cm}^3$, $M=131$ for pure Xe and $\Omega_0=5.0\times10^{-23}\,\mathrm{cm}^3$, $M=83.8$ for pure Kr), $\Delta M=M-M_{Xe}$ and $\Delta\Omega_0=\Omega_0-\Omega_{0Xe}$ are the difference between the averaged atomic weight of the solid solution and the atomic weight of the impurity and the difference between the volume of the solid solution and the volume of the impurity. Although $\Delta M/M$ for the solution $Kr_{1-\xi}Xe_{\xi}$ is a factor of 1.5 smaller than for $Kr_{1-\xi}(CH_4)_{\xi}$, the relative difference of the volumes per atom, $\Delta\Omega_0/\Omega_0$, is twice as large in the first case, since at equal ξ the coefficient Γ is 1.6 times larger for the solution $Kr_{1-\xi}Xe_{\xi}$ than for $Kr_{1-\xi}(CH_4)_{\xi}$. This means that a Xe impurity in Kr should scatter more strongly than a CH_4 impurity in Kr on account of the larger distortion of the crystal lattice.

The first sample had a ratio of components close to the point of equal concentrations ($\xi=0.15$), for which the possibility of phase separation of the solid solution during growth can be ruled out. This sample has a molar volume of 29.9 cm^3/mole; the temperature T_0 corresponding to the the point at which the constant-volume condition ($V=\mathrm{const}$) began to hold was 84 K, and the temperature T_m at which the sample started to melt was of the order of 170 K. Sample No. 2 had a molar volume of 30.7 cm^3/mole, $T_0=78$ K, and $T_m\approx180$ K.

Since the molar volume of the solid solution varies strongly from Kr to Xe, the comparison of the experimental results is conveniently done for samples that attain constancy of the volume at the same temperature T_0. The two samples were grown under identical conditions (pressure of 80 MPa in the capillary, a temperature gradient of 1 K/cm along the measurement cell), so that the temperatures T_0 for them differed by only 5 K. According to our estimates, the correction to the thermal conductivity from rescaling to densities corresponding to the intermediate temperature 80 K does not exceed 3–4%, which is less than the error of measurement. Therefore, the experimental results are shown in Fig. 1 without rescaling. The thermal conductivity of pure krypton and xenon for samples whose volume was fixed starting at 80 K was calculated using the semiempirical relation proposed in Ref. 5. The Debye temperatures for Kr and Xe are equal to 72 and 64 K, respectively, so that $\Lambda_{\min}$ can be assumed constant in the investigated temperature range.

We see that the thermal conductivity of the solid solutions $Kr_{1-\xi}Xe_{\xi}$ for $\xi=0.14$ and 0.37 is practically equal to the lower limit of the thermal conductivity over the entire temperature range studied. The thermal conductivity is somewhat higher for the solution with $\xi=0.37$ than for that with $\xi=0.14$. This may be due to partial phase separation of the sample. The sample was grown from a dense liquid phase at a temperature gradient along the measurement cell of 1 K/cm. According to the phase diagram,[13] a solution enriched with xenon should have precipitated out in the lower part of

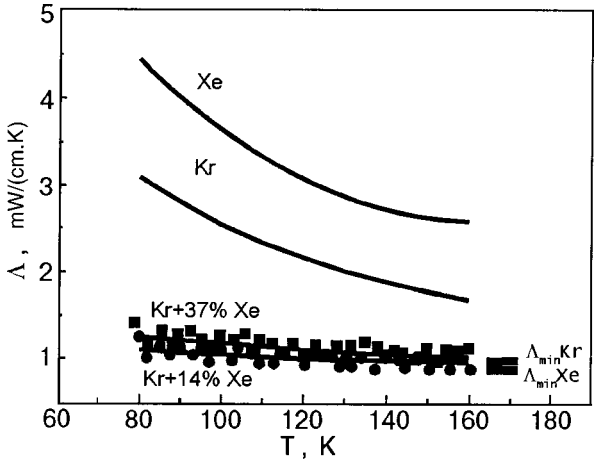

FIG. 1. Isochoric thermal conductivity of $Kr_{1-\xi}Xe_{\xi}$ solid solutions: ●—$\xi=0.14$, $V_m=29.9$ cm^3/mole, ■—$\xi=0.37$, $V_m=30.7$ cm^3/mole. The solid curves show the thermal conductivity of pure Kr and Xe for samples whose volume is fixed starting at 80 K. The lower limits of the thermal conductivity, $\Lambda_{\min}$, for pure Kr and Xe in the isochoric case ($T_0=80$ K) are shown at the lower right of the figure.

the cell, and the subsequent annealing might have been insufficient to equalize the impurity concentration along the cell.

CONCLUSIONS

The isochoric thermal conductivity of the solid solutions $Kr_{1-\xi}Xe_{\xi}$ with $\xi=0.14$ and 0.37 is practically constant in the temperature interval from 80 K to the start of melting. Its absolute value and temperature dependence are in good agreement with the lower limit of the thermal conductivity of the crystal lattice, $\Lambda_{\min}$.

The authors thank Academician V. G. Manzhelii and Prof. R. O. Pohl for a fruitful discussion. This study was supported by the Ministry of Education and Science of Ukraine (contract No. 2m/1862-97).

*E-mail: konstantinov@ilt.kharkov.ua

[1] M. L. Klein and J. A. Venables (Eds.), *Rare Gas Solids, Vols. I–II*, Academic Press, London–New York (1977).
[2] R. Berman, *Thermal Conduction in Solids*, Clarendon Press, Oxford (1976).
[3] F. Clayton and D. N. Batchelder, J. Phys. C **6**, 1213 (1973).
[4] A. I. Bondarenko, V. G. Manzhelii, V. A. Popov, M. A. Strzhemechnyi, and V. G. Gavrilko, Fiz. Nizk. Temp. **8**, 1215 (1982) [Sov. J. Low Temp. Phys. **8**, 617 (1982)].
[5] V. A. Konstantinov, V. G. Manzhelii, M. A. Strzhemechnyi and S. A. Smirnov, Fiz. Nizk. Temp. **14**, 90 (1988) [Sov. J. Low Temp. Phys. **14**, 88 (1988)].
[6] G. A. Slack, in *Solid State Physics*, Vol. 34, edited by H. Ehrenreich, F. Seitz, and D. Turnbull, Academic Press, New York–London (1979), p. 1.
[7] D. G. Cahill, S. K. Watson, and R. O. Pohl, Phys. Rev. B **46**, 6131 (1992).
[8] V. A. Konstantinov, J. Low Temp. Phys. **122**, 459 (2001).
[9] P. A. Bezuglyi, R. O. Plakhotin, and L. M. Tarasenko, Fiz. Tverd. Tela (Leningrad) **12**, 1199 (1970) [Sov. Phys. Solid State **12**, 934 (1970)].
[10] A. G. Peterson, D. N. Batchelder, and R. O. Simmons, Phys. Rev. **150**, 703 (1966).
[11] P. A. Bezuglyi, L. M. Tarasenko, and O. I. Baryshevskii, Fiz. Tverd. Tela (Leningrad) **13**, 2392 (1971) [Sov. Phys. Solid State **13**, 2003 (1971)].
[12] V. A. Konstantinov, V. G. Manzhelii, V. P. Revyakin, and S. A. Smirnov, Physica B **262**, 421 (1999).
[13] V. A. Konstantinov, S. A. Smirnov, and V. P. Revyakin, Prib. Tekh. Éksp. **42** , No. 1, 145 (1999) [Instrum. Exp. Techn. **42**, 133 (1999)].
[14] V. G. Manzhelii, A. I. Prokhvatilov, I. Ya. Minchina, and L. D. Yantsevich, *Handbook of Binary Solutions of Cryocrystals*, Begell House, New York; Wallingford, UK (1996).
[15] L. A. Turk and P. G. Klemens, Phys. Rev. B **9**, 4422 (1974).

Translated by Steve Torstveit

Heat capacity of methane–krypton solid solutions. Conversion effect

I. Ya. Minchina, V. G. Manzhelii, M. I. Bagatskii,* O. V. Sklyar, D. A. Mashchenko, and M. A. Pokhodenko

B. Verkin Institute for Low Temperature Physics and Engineering of the National Academy of Sciences of Ukraine, 47 Lenin Ave., Kharkov 61103, Ukraine

(Submitted February 9, 2001)
Fiz. Nizk. Temp. **27**, 773–779 (July 2001)

The heat capacity of Kr–nCH$_4$ solid solutions with the concentrations $n=1$; 5; 10% and of the solid solution Kr–1% CH$_4$–0.2% O$_2$ is studied at 0.7–8 K. The contributions $C_{\rm rot}$ to the heat capacity of the solutions due to the rotation of the CH$_4$ molecules are estimated. The deviations of the measured $C_{\rm rot}$ from the values corresponding to the equilibrium distribution of the CH$_4$ nuclear spin modifications are dependent on the correlation between the characteristic times of conversion and of the calorimetric experiment. The effects of temperature, O$_2$ impurities, and CH$_4$ clusters upon the conversion rate are studied. It is shown that the hybrid mechanism of conversion proposed by Berlinsky and Nijman, which takes into account both intramolecular and intermolecular interactions of the proton spins, is predominant. © *2001 American Institute of Physics.* [DOI: 10.1063/1.1388422]

INTRODUCTION

This paper reports a calorimetric investigation of the quantum behavior of CH$_4$ rotators in a crystal field of cubic symmetry. The degree of the quantum effect in the rotational motion can be characterized by the parameter $\lambda_\varphi=\hbar/\sqrt{I\varepsilon_\varphi}$, where I is the moment of inertia of the molecule, and ε_φ is the energy barrier that the molecule has to overcome when its orientation changes. The higher λ_φ is, the stronger are the quantum effects in the behavior of the rotator. The moment of inertia I is quite small because the CH$_4$ molecule has light hydrogen atoms at its periphery. In matrices of solidified inert gases, methane molecules are surrounded by spherically symmetric atoms. Under this condition, the magnitude of ε_φ is also quite low (several tens of kelvin[1]). Solutions of methane in matrices of solid inert gases with the fcc structure are therefore most suitable for answering the questions of this study. The spectrum of a quantum rotator in a crystal field is close to that of a free rotator. As a consequence, the spectra of different nuclear spin modifications of a rotator differ considerably,[2] and their mutual transformation (interconversion) should be taken into account. Solid Kr has been chosen as a matrix because, of all the inert gases, only Kr has Lennard-Jones potential parameters very close to those of CH$_4$. As a result, the solubility of CH$_4$ in solid Kr is as high as 80% at low temperatures. This offers an opportunity to investigate not only the behavior of isolated rotators but their interaction as well. Since the low concentration case more readily lends itself to interpretation, we considered it reasonable to use Kr–CH$_4$ solutions with CH$_4$ concentrations of 1–10%. The quantum behavior of rotators shows up at low temperatures. In addition, the relative contribution of the rotator subsystem to the heat capacity of Kr–CH$_4$ solutions decreases as the temperature rises. The temperature interval of this study was therefore bounded from above by 8 K.

We should mention some problems which are much assisted by studies of the heat capacity of solid CH$_4$–Kr solutions at low (helium) temperatures.

1. Mechanism of mutual transformation of nuclear spin CH$_4$ modifications (conversion mechanism)

It is known that CH$_4$ molecules can come in three modifications having different mutual proton spin orientations and rotational energy spectra. These CH$_4$ modifications, specified as *A, T, E,* have the total nuclear spins 2, 1, 0, respectively. Their rotational spectra (the low-energy region) are shown in Fig. 1 for a free rotator and a rotator in a Kr matrix.

The *A* modification has the lowest energy of the ground state. Owing to conversion, the modifications are in equilibrium at different temperatures. The temperature dependence of the equilibrium *A, T,* and *E* concentrations of free CH$_4$ rotators is shown in Fig. 2.[2] In the high temperature limit the concentration ratio $x_A:x_T:x_E$ is 5:9:2.

Two factors are responsible for the rate of conversion—the interaction of the proton spins and the possibility for the phonons to gain energy from the transitions between different rotational states. Since the spacing of the protons is quite small within the molecule, the intramolecular spin interaction is an order of magnitude stronger than the spin interaction between the neighboring molecules. The intramolecular spin interaction is, however, only weakly connected with the translational vibrations of the lattice, and this considerably impedes conversion. According to Nijman and Berlinsky,[6] a hybrid mechanism of conversion predominates in solid CH$_4$ at low temperatures: the intramolecular interaction mixes the nuclear spin states, and the intermolecular interaction induces transitions between the energy levels, which are accompanied by emission of phonons. CH$_4$–Kr solid solutions are very suitable for testing the Nijman and Berlinsky model. The conversion of isolated CH$_4$ molecules can be studied on weak solutions. At increasing concentrations, the number of clusters of CH$_4$ molecules increases rapidly, and they trigger

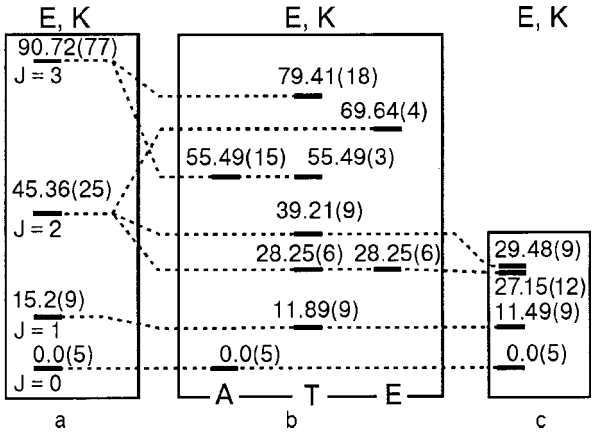

FIG. 1. Rotational energy spectra of the methane molecule: a—free rotator[3]; b,c—hindered CH_4 rotator in the crystal Kr field (b—calculation[4], c—experimental[5]). *J*-rotational quantum number, *R*—energy (degeneracy levels are in brackets to the right).

the hybrid mechanism of conversion. The heat capacity of the CH_4 subsystem is very dependent on the *A*, *T*, and *E* concentrations achieved by the time of measurement and on whether their concentration ratio has a chance to change during a single measurement run. It follows from the above consideration that we can derive information about conversion from the measured heat capacity.

To avoid misunderstanding, it is appropriate to note here that our term ''heat capacity'' has the meaning of the derivative of the heat transferred to the system with respect to temperature, irrespective of whether the system is at equilibrium or not.

It is also interesting to investigate how small amounts of paramagnetic impurities can influence the heat capacity of diluted CH_4–Kr solid solutions. If the hybrid mechanism prevails and no paramagnetic impurity is present in the Kr–CH_4 solution, during the time of experiment the conversion will mainly occur in the clusters. The addition of a paramagnetic impurity will increase strongly the rate of conversion in the isolated CH_4 molecules and hence the heat capacity $C_{\rm rot}$ of the rotational subsystem. This problem can also be tackled in the context of heat capacity studies.

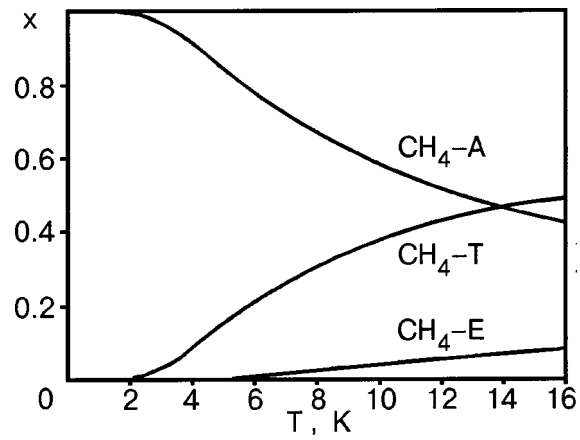

FIG. 2. The temperature dependence of the equilibrium *A*, *T*, and *E* concentrations of free CH_4 rotators.[2]

2. Dynamics of quantum rotators in a crystal field

The heat capacity C_V of the system is determined by its energy levels. Our heat capacities $C_P(P=0)$ estimated at a constant pressure coincide, within the experimental error, with the values C_V obtained at a constant volume. The inverse problem of obtaining the energy spectrum from heat capacity[7] can be solved uniquely only for the low-temperature heat capacity, which is determined by a small number of excited levels in the spectrum. The first excited state of the rotator subsystem estimated from the heat capacity can sometimes surpass the spectroscopic data in accuracy.[8]

The high solubility of CH_4 in solid Kr[9,10] may provide more evidence about how the octupole rotator interaction influences the low-energy part of the spectrum of the rotator subsystems. The multipolar moment of quantum rotators (unlike the classical ones) is dependent on the state of the rotator. In the ground state the CH_4 molecule has the smallest[3] octupole moment. As the temperature of the Kr–CH_4 solution rises, the occupancy of the excited states of the CH_4 rotators increases, and so do the octupole moment of the CH_4 molecules and their interaction. Thus the interaction between the CH_4 molecules changes with temperature, which should manifest itself in the behavior of the heat capacity of the rotator subsystem.

3. Octupole glasses in Kr–*n*CH_4 solutions: existence and features

At sufficiently low temperatures an orientational octupole glass can develop in a Kr–*n*CH_4 solution.[14] In our solutions with low CH_4 concentrations ($n \leqslant 10\%$) we can hardly expect an orientational glass to be formed due to a direct octupole interaction of CH_4 molecules. Such concentrations may, however, allow an octupole glass caused by an indirect interaction. This type of glass can develop due to an indirect interaction of impurity molecules through the strain fields induced by the impurities themselves in the host lattice. The presence and type of glass can be identified from the temperature and concentration dependences of the heat capacity.[12] Quadrupole glasses with an indirect interaction have been detected and studied by several investigators.[12–14]

EXPERIMENT

The heat capacity of solid Kr–*n*CH_4 solutions with the concentrations $n=1$; 5; 10% and the Kr–1% CH_4–0.2% O_2 solution were studied at 0.7–8 K by a pulse-heating method using an adiabatic vacuum calorimeter.[15] The temperature of the sample changed as $\Delta T_i = T_{i+1} - T_i$, where T_i and T_{i+1} are the temperatures before and after heating. The change during one measurement run was about 10% of T_i. The heat capacity corresponded to the temperature $T=(T_i+T_{i+1})/2$. The heating time t_h was usually two or three minutes. The time $t_{\rm exp}$ taken to measure one heat capacity value was 0.5–1.4 hour and depended mainly on the duration (t_e) of temperature equalization over the sample after switching off the heater. The effective (characteristic) time t_m of one measurement run is taken to be $t_m = t_h + t_e$. The mass of the samples was 0.5–0.7 mole.

The purity of the gases was: CH_4–99.94% (0.04% N_2, $<0.01\%$ Ar, O_2); Kr–99.72% (0.08% N_2; 0.2% Xe); O_2–99.99%.

Gas mixtures with a pre-assigned composition were prepared at room temperature. The impurity concentration and the mass of the samples were found from the *PVT* data to within 0.2%. A solid solution was prepared in a calorimeter at $T \approx 70$ K by condensing the gas mixture into the solid phase. The error of the heat capacity measurement was 6% at 0.7 K; 2% at 1 K; 1% at 2 K, and 0.5% above 4 K. To minimize the systematic measurement errors and to improve the accuracy of separation of the heat capacity component $C_{\rm rot}$ contributed by the CH_4 impurity rotation, the heat capacity of pure Kr was measured in the same calorimeter.

The heat capacity of Kr–CH_4 solutions had been measured only once, by A. Euken and H. Veight[9] in 1936 ($T = 12$–25 K; 28–96% CH_4).

DATA PRESENTATION

The heat capacity of the Kr–CH_4 solution can be represented as a sum, $C_{\rm sol} = C_{\rm tr} + C_{\rm rot}$, where $C_{\rm rot}$ is the heat capacity contributed by the rotational motion of the CH_4 molecules, and $C_{\rm tr}$ is the heat capacity due to translational vibrations of the lattice. $C_{\rm tr}$ can in turn be represented as $C_{\rm tr} = C_{\rm Kr} + \Delta C_L$, where $C_{\rm Kr}$ is the heat capacity of pure krypton, and ΔC_L is the change in the translational heat capacity caused by the presence of a lighter impurity (CH_4) in the Kr lattice. ΔC_L was calculated by the Jacobi matrix method[16] for the mass ratio $m_{\rm CH_4}/m_{\rm Kr} = 0.2$, the force constant variation being neglected. The rotational component $C_{\rm rot}$ was found by subtracting $C_{\rm Kr}$ and ΔC_L from the experimental $C_{\rm sol}$ values. The $C_{\rm rot}$ value thus obtained was compared with calculations for three limiting cases:

1. Equilibrium distribution (ED) of the nuclear spin (*A*, *E*, *T*) modifications (fast conversion).

It is assumed that conversion is so fast that the *A*, *E*, and *T* concentrations can be thought of as equilibrium at any instant at the temperature of the experiment. This is possible if conversion occurs during the effective time t_m of a single measurement run. In this case the heat capacity is obtainable from the unified rotational energy spectrum based on all levels.

2. Frozen equilibrium distribution (FED)

The *A*, *E*, and *T* concentrations are equilibrium with respect to the initial temperature T_i and do not change during the effective time t_m when the sample is heated from T_i to T_{i+1}. This is possible when the characteristic conversion time is $\tau \gg t_m$. Prior to measurement, the sample must be kept at T_i during the time $t \gg \tau$. At the mid-heating temperature $T = (T_i + T_{i+1})/2$, the heat capacity is calculated as

$$C_{\rm rot}(T) = x_A(T_i)C_A(T) + x_T(T_i)C_T(T) + x_E(T_i)C_E(T), \quad (1)$$

where x_A, x_T, x_E are the relative equilibrium *A*, *E*, and *T* concentrations at T_i; C_A, C_T, and C_E are the heat capacities of the corresponding modifications at the temperature *T*.

3. Frozen distribution (FD) (no conversion)

The *A*, *E*, and *T* concentrations are constant in the whole range of temperatures and equal to the high-temperature distribution, i.e., $x_A : x_T : x_E = 5:9:2$. This occurs if at all temperatures the conversion is very slow and the *A*, *E*, and *T* concentrations are practically invariable during the whole experiment (several weeks). In this case the heat capacity $C_{\rm rot}$ can be found as

$$C_{\rm rot}(T) = \frac{5}{16}C_A(T) + \frac{9}{16}C_T(T) + \frac{2}{16}C_E(T). \quad (2)$$

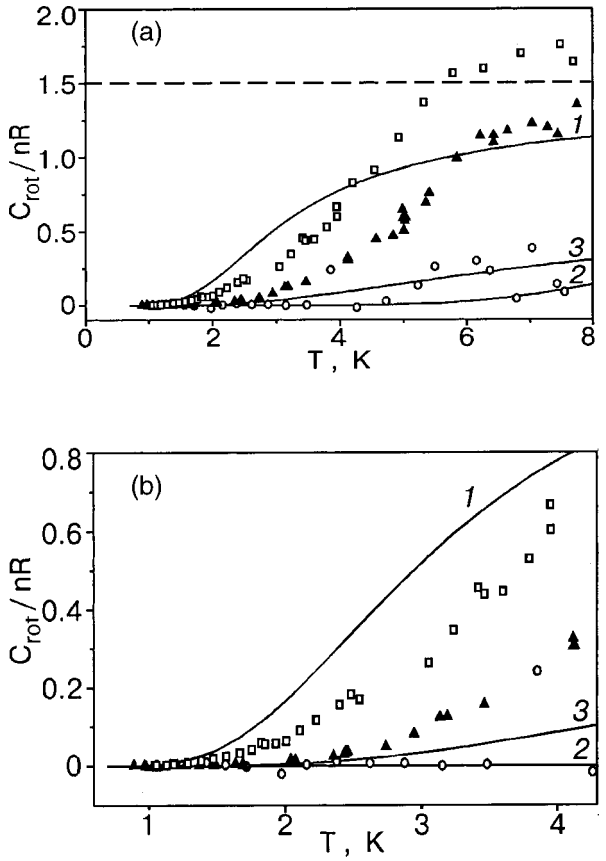

FIG. 3. Temperature dependence of reduced rotational heat capacity of Kr–CH_4 solutions containing 1% CH_4 (○), 5% CH_4 (▲), 10% CH_4 (□) for the whole temperature range (a) and up to 4.3 K (b). The solid lines are the theoretical curves for the three limiting cases mentioned (*1*–ED, *2*–FED, *3*–FD).

To calculate $C_{\rm rot}$ for the above limiting cases, we need to know the rotation spectrum of the CH_4 molecule in the crystal field of krypton. This spectrum has been calculated in Ref. 4 (see Fig. 1b). The energies of four low-lying rotational levels of the CH_4 molecule in a Kr matrix were found experimentally by the method of inelastic neutron scattering.[5,17] It turns out that three of them agree well with theoretical predictions,[4] the discrepancy being within 3% (see Fig. 1c). The fourth level differs by about 30%. We thought it reasonable to use the spectrum of Fig. 1(b) in the subsequent $C_{\rm rot}$ calculation.

RESULTS OF THE MEASUREMENTS. DISCUSSION

The heat capacities $C_{\rm rot}$ measured on the solutions with 1; 5; 10% CH_4 and normalized to the CH_4 concentration *n* and the universal gas constant *R* are shown in Fig. 3a for the whole range of measurement temperatures and in Fig. 3b (enlarged scale) up to 4.3 K. As is seen in Fig. 3a, the data scatter increases with rising temperature, and the accuracy of the $C_{\rm rot}$ component degrades. This is due to the lattice con-

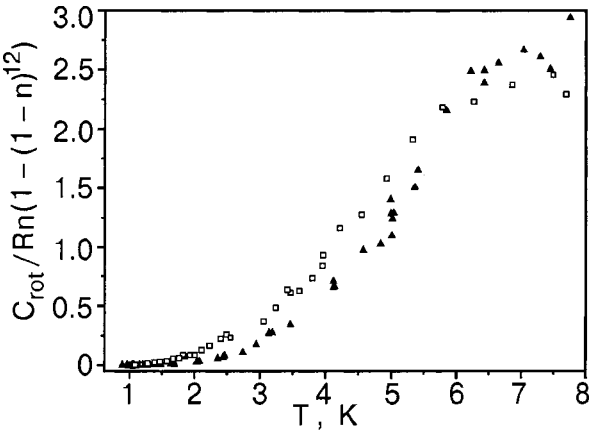

FIG. 4. Temperature dependence of rotational heat capacity of Kr–CH_4 solutions containing 5% CH_4 (▲) and 10% CH_4 (□), in reduced coordinates.

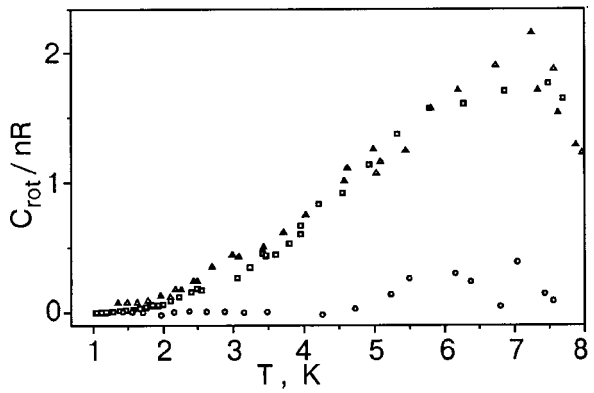

FIG. 5. Temperature dependence of reduced rotational heat capacity of binary Kr–CH_4 solutions containing 1% CH_4 (○), 10% CH_4 (□), and the triple solution Kr–1% CH_4–0.2% O_2 (△).

tribution C_{tr} to the total heat capacity of the solution, which increases as the temperature rises: 47% at $T=4$ K and 78% at $T=8$ K ($n=10\%$). The dotted line in Fig. 3a corresponds to the high-temperature value, $C_{rot}/nR=3/2$, for a mole of isolated CH_4 molecules in a Kr matrix.

Along with experimental results, Fig. 3 show the calculated heat capacities for the above three limiting cases: ED (curve *1*), FED (curve *2*), FD (curve *3*). It is seen that in the whole temperature region, the heat capacity of the Kr–1% CH_4 solution hardly exceeds the experimental error and is much below curves *1* (ED) and *3* (FD) at $T\leqslant 5$ K. Curve *2* (FED) is the best description of the solution at $T\leqslant 5$ K. This suggests that the characteristic conversion times of this solution greatly exceed the effective times t_m of a single measurement run. This conclusion is consistent with Refs. 18 and 19. According to Ref. 18, the characteristic conversion time τ of isolated CH_4 molecules in a Kr matrix is 3.5 hours at $T=2$ K.

It is seen in Fig. 3 that the reduced rotational heat capacity increases rapidly with the concentration n, and above $T\approx 4$ K ($n=10\%$) or $T\approx 6$ K ($n=5\%$) it exceeds the C_{rot}/nR value corresponding to the instantaneous thermodynamic equilibrium of the nuclear spin modifications of isolated CH_4 molecules. This can be explained as follows. As the concentration n grows, the number of CH_4 clusters increases, too. Clusters of two and three CH_4 molecules prevail at $n=5$; 10% CH_4. The hybrid mechanism of conversion operating in the clusters[6] enhances the conversion rate considerably. As a result, the nonequilibrium nuclear spin modifications come into equilibrium, and the entropy S of the solution increases. The higher the conversion rate is in the nonequilibrium system, the more intensively the entropy changes at the initial temperature T_i during the effective time t_m of a single measurement run. Correspondingly, the measured heat capacity $C_V=T(dS/dT)$ appears to be higher. Note that in this case the measured heat capacity can exceed that of the equilibrium system. The higher heat capacity of clustered molecules (as compared to that of isolated ones) can also contribute appreciably to the concentration dependence of the heat capacity. We should therefore not overestimate the quantitative comparison between the C_{rot} of the solutions with $n=5$; 10% CH_4 and the theoretical curve describing the rotational heat capacity of the equilibrium system of isolated impurity molecules (the ED case).

Additional arguments for or against the enhanced conversion in clusters can be furnished by the consequences that follow from this assumption. Let us assume that (i) the contribution of isolated CH_4 molecules (singles) to the heat capacity is negligible, (ii) the conversion rate in a cluster is independent of its size, and (iii) the rotational energy spectrum of the molecules in clusters is also independent of the cluster sizes. If these conditions are realized, the reduced heat capacity $C_{rot}/n'R$, where n' is the molecule concentration in the clusters, will be independent of the methane concentration n. And we remember that the number of CH_4 singles in a solution containing N particles is $Nn(1-n)^{12}$; correspondingly, the number of molecules in clusters is $Nn[1-(1-n)^{12}]$, i.e., $n'=n[1-(1-n)^{12}]$.

In Fig. 4 the heat capacity of the rotational subsystem in the solutions with 5%; 10% CH_4 is shown in the reduced coordinates $C_{rot}/Rn[1-(1-n)^{12}]-T$. It is seen that the reduced heat capacities of these solutions at 5–8 K coincide within the measurement error, i.e., they are independent of the methane concentration. This supports the assumption of considerably enhanced conversion in clusters and suggests that the above three conditions are realized in this temperature interval.

At lower temperatures (see Fig. 4) there are some deviations from the universal dependence which exceed the experimental error. This may occur because conditions (ii) and (iii) (or one of them) are not fulfilled. According to Ref. 3, the first effective excited rotational level ($J=1$) is somewhat lower for three-molecule clusters ($i=3$) than for two-molecule clusters ($i=2$). Correspondingly, at rather low temperatures the heat capacity of the solution with $n=10\%$, which contains more $i=3$ clusters, should be appreciably higher than in the $n=5\%$ case. Another reason may be connected with the conversion rate, which becomes dependent on the cluster size as the temperature is lowered.

To estimate the effect of a paramagnetic impurity on the conversion rate and hence on the heat capacity, we investigated the heat capacity of the Kr–1% CH_4–0.2% O_2 solution. The contributions of the impurities (CH_4, O_2) were assumed to be additive. The contribution of O_2 to the heat capacity of the solution was estimated using the data of Ref. 20. In the

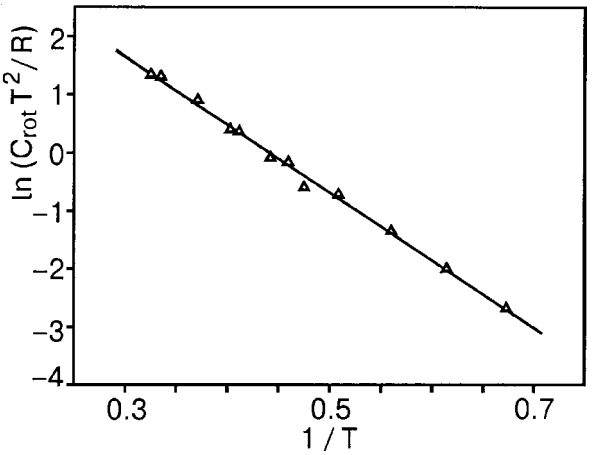

FIG. 6. Temperature dependence of $C_{\rm rot}$ of the Kr–1% CH_4–0.2% O_2 solid solution in $\ln(C_{\rm rot}T^2/R)-1/T$ coordinates.

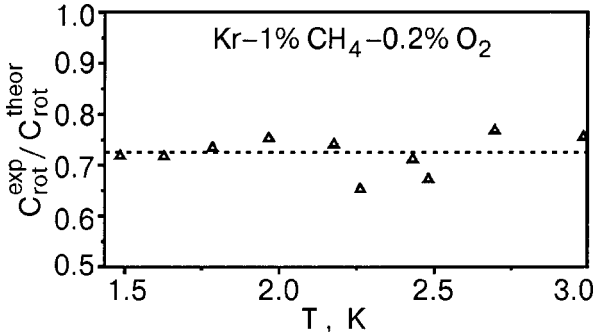

FIG. 7. Temperature dependence of the ratio of $C_{\rm rot}^{\rm exp}$ to $C_{\rm rot}^{\rm theor}$ for $E_1 = 11.7$ K.

presence of O_2 the CH_4 contribution to the heat capacity is an order of magnitude higher than that in the Kr–1% CH_4 solution containing no appreciable paramagnetic impurities (see Fig. 5).

With an equilibrium distribution of the CH_4 modifications, the heat capacity at $T \leqslant 3$ K is determined by the position of the first excited level in the rotational spectrum of the CH_4 molecules (see Fig. 1). We assume that at $T \leqslant 3$ K some part of the CH_4 molecules influenced by the paramagnetic impurities convert so fast that their heat capacity corresponds to the equilibrium distribution (the ED case). Let this fraction of molecules be denoted as n''. The value of n'' also includes a relatively small number of the fast-converting CH_4 molecules from the clusters. We then assume that the contribution of the rest of the CH_4 molecules, whose fraction is $(1-n'')$, to $C_{\rm rot}$ is negligible. When the above three conditions are fulfilled, $C_{\rm rot}$ can be written as

$$C_{\rm rot} = Nk_B \frac{n''}{T^2} E_1^2 \frac{g_1}{g_0} e^{-E_1/T}, \tag{3}$$

where N is the number of CH_4 molecules in the sample; E_1 is the first excited level energy; g_0 and g_1 are the degeneracies of the ground and the first excited levels, respectively; k_B is Boltzmann's constant. In Fig. 6 the measured $C_{\rm rot}$ of the Kr–1% CH_4–0.2% O_2 solution is shown in the coordinates $\ln(C_{\rm rot}T^2/R)-1/T$.

The linear dependence $\ln(C_{\rm rot}T^2/R)-1/T$ is fulfilled within the experimental error, which indicates that our assumptions are realistic. The E_1 value $(11.7 \pm 0.4\,{\rm K})$ was estimated from the slope of the obtained straight line and is in good agreement with the neutron-diffraction magnitude $E_1 = 11.7$ K.[17]

The ratio of the experimental value $C_{\rm rot}^{\rm exp}$ and the value $C_{\rm rot}^{\rm theor}$ calculated for $E_1 = 11.7$ K on the assumption that all the CH_4 molecules convert during the effective time t_m of a single heat capacity measurement (the ED case) is shown in Fig. 7. It is seen that $n'' = 72\%$, which implies that only 72% of CH_4 molecules convert in the Kr–1% CH_4–0.2% O_2 solid solution at $T \leqslant 3$ K during the effective time t_m of a single heat capacity measurement. This suggests that during the time t_m the conversion takes place in the CH_4 molecules which are situated in seven coordination spheres around the O_2 molecule.

Finally, we discuss the possibility of an orientational glass in our Kr–CH_4 solutions. At the CH_4 concentrations used in this study, we can only expect the orientational glass with an indirect interaction.[12] In such glasses the rotators interact through the strain fields which they form in the matrix. Our temperature and concentration dependencies do not display any features typical for the heat capacity of such glasses.[12] This means that the shift of the CH_4 rotation energy levels caused by the indirect interaction of the CH_4 molecules is smaller than the distance E_1 between the ground and the first excited levels of the spectrum. It is quite possible that the glasslike behavior should be sought in the temperature and concentration dependencies of CD_4–Kr solid solutions, because E_1 is smaller in that case.

The authors are indebted to E. S. Syrkin, S. B. Feodosiev, and I. A. Gospodarev for the calculated data on the translational component of the heat capacity of Kr–CH_4 solutions. This study has been supported by the Ministry of Education and Science of Ukraine within the Project ''Optical and Thermal Spectroscopy of Small Molecules in Cryogenic Matrices,'' No. M/1862-97.

*E-mail: bagatskii@ilt.kharkov.ua

[1] *Physics of Cryocrystals*, edited by V. G. Manzhelii and Yu. A. Freiman, AIP press, Woodbury, New York (1997).
[2] G. Herzberg, *Infrared and Raman Spectra of Polyatomic Molecules*, New York (1945), p. 647.
[3] T. Yamamoto, Y. Kataoka, and K. Okada, J. Chem. Phys. **66**, 2701 (1977).
[4] K. Nishiyama and T. Yamamoto, J. Chem. Phys. **58**, 1001 (1973).
[5] B. Asmussen, M. Prager, W. Press, H. Blank, and C. J. Carlile, J. Chem. Phys. **97**, 1332 (1992).
[6] A. J. Nijman and A. J. Berlinsky, Can. J. Phys. **58**, 1049 (1980).
[7] I. M. Lifshits, Zh. Éksp. Teor. Fiz. **26**, 551 (1954).
[8] A. I. Krivchikov, M. I. Bagatskii, V. G. Manzhelii, I. Ya. Minchina, and P. I. Muromtsev, Fiz. Nizk. Temp. **14**, 1208 (1988) [Sov. J. Low Temp. Phys. **14**, 667 (1988)].
[9] A. Euken and H. Veith, Z. Phys. Chem. Abt. B **34**, 275 (1936).
[10] H. Veith and E. Schrouder, Z. Phys. Chem. Abt. A **179**, 16 (1937).
[11] F. de Luca and B. Maraviglia, Phys. Lett. **101**, 300 (1983).
[12] V. G. Manzhelii, M. I. Bagatskii, I. Ya. Minchina, and A. N. Aleksandrovskii, J. Low Temp. Phys. **111**, 290 (1998).
[13] A. I. Burin, Fiz. Nizk. Temp. **17**, 872 (1991) [Sov. J. Low Temp. Phys. **17**, 456 (1991)].

[14] M. I. Bagatskii, V. G. Manzhelii, M. A. Ivanov, P. I. Muromtsev, and I. Ya. Minchina, Fiz. Nizk. Temp. **18**, 1142 (1992) [Sov. J. Low Temp. Phys. **18**, 801 (1992)].
[15] M. I. Bagatskii, I. Ya. Minchina, and V. G. Manzhelii, Fiz. Nizk. Temp. **10**, 1039 (1984) [Sov. J. Low Temp. Phys. **10**, 542 (1984)].
[16] V. I. Peresada and V. P. Tolstoluzhskii, Fiz. Nizk. Temp. **3**, 788 (1977) [Sov. J. Low Temp. Phys. **3**, 378 (1977)].
[17] B. Asmussen, W. Press, N. Prager, and H. Blank, J. Chem. Phys. **98**, 158 (1993).
[18] S. G. Grieger, H. Friedrich, B. Asmussen, K. Guckelsberger, D. Nettling, W. Press, and R. Scherm, Z. Phys. B. Condens. Matter **89**, 203 (1992).
[19] V. V. Dudkin, B. Ya. Gorodilov, A. I. Krivchikov, and V. G. Manzhelii, Fiz. Nizk. Temp. **26**, 1023 (2000) [Low Temp. Phys. **26**, 762 (2000)].
[20] P. I. Muromtsev, M. I. Bagatskii, V. G. Manzhelii, and I. Ya. Minchina, Fiz. Nizk. Temp. **20**, 247 (1994) [Low Temp. Phys. **20**, 195 (1994)].

This article was published in English in the original Russian journal. Reproduced here with stylistic changes by AIP.

LATTICE DYNAMICS

Manifestation of quasi-symmetry of the cation sites of Gd_2SiO_5, Y_2SiO_5, and Lu_2SiO_5 in the spectra of the impurity ion Pr^{3+}

Yu. V. Malyukin,* R. S. Borisov, P. N. Zhmurin, A. N. Lebedenko, and B. V. Grinev

Institute of Single Crystals, National Academy of Sciences of Ukraine, pr. Lenina 60, 61001 Kharkov, Ukraine

N. V. Znamensky, É. A. Manykin, Yu. V. Orlov, E. A. Petrenko, and T. G. Yukina

Kurchatov Institute Russian Research Center, pl. Kurchatova 1, 123182 Moscow, Russia

(Submitted February 6, 2001)
Fiz. Nizk. Temp. **27**, 780–785 (July 2001)

The quasi-symmetry of the inequivalent cation sites in the crystals Gd_2SiO_5, Y_2SiO_5, and Lu_2SiO_5 is established on the basis of an analysis of the features of the low-temperature optical spectra of the impurity ion Pr^{3+}. One type of cation site of the crystals Y_2SiO_5 and Lu_2SiO_5 manifests the quasi-symmetry of a distorted octahedron, and the other type, that of a distorted tetrahedron. The parameters characterizing the energy spectrum of the free Pr^{3+} ion in the crystalline field of the cation sites are determined. [DOI: 10.1063/1.1388423]

INTRODUCTION

Rare-earth-doped crystals of Gd_2SiO_5 (GSO), Y_2SiO_5 (YSO), and Lu_2SiO_5 (LSO), which belong to the family of oxyorthosilicates with the general formula $RE_2(SiO_4)O$ (RE=Gd, Y, Lu) are objects of intensive research. This research is primarily in connection with the search for efficient laser and scintillator materials.[1–5] The high chemical and photochemical stability of oxyorthosilicates makes them promising materials for use in display technologies.[6]

From an applied standpoint, the important optical and luminescence properties of rare-earth ions is to a considerable degree determined by the microstructure of their crystalline environment and to a lesser degree by the macroscopic properties of the crystal. Therefore it is of topical interest to ascertain the microstructure of the substitutional cation sites of the oxyorthosilicates. The narrowness of the spectral lines makes the low-temperature optical spectra of impurity ions highly informative, affording efficient study of the microstructure of the activation centers.

In the present paper, which is a logical continuation of a previously published report,[8] we present a detailed analysis of the low-temperature optical spectra of the impurity ions Pr^{3+} and determine the parameters characterizing the energy spectrum of the free Pr^{3+} ion in the crystalline field of the cation sites in GSO, YSO, and LSO crystals.

EXPERIMENTAL RESULTS AND DISCUSSION

The luminescence spectrum of the Pr^{3+} impurity ions was excited by a tunable narrow-band organic dye laser and was recorded using an MDR-23 grating monochromator and an FÉU-64 photomultiplier operating in the current mode. The signal from the photomultiplier was preamplified and digitized by an ATsP-712 analog-to-digital converter. The scanning of the monochromator and digitizing of the signal were automated with the aid of a computer.

Since the crystalline field has a weak influence on the f electrons of rare-earth ions, their energy spectrum is determined mainly by the Coulomb and spin–orbit interactions. The system of terms of the free ion is described by the quantum numbers L, S, and J (L, S, and $J=L+S$ are the orbital, spin, and total angular momenta, respectively). For the f^2 configuration of the Pr^{3+} ion there are nine triplet terms, $^3H_{4,5,6}$, $^3F_{2,3,4}$, $^3P_{0,1,2}$, and four singlet terms, $^1S_0$, $^1D_2$, $^1G_4$, and $^1I_6$. Since the f^2 configuration does not give degenerate terms, the energy of the thirteen terms of the free Pr^{3+} ion, if higher-order corrections are not taken into account, is given by the expression

$$E(LSJ)=\sum_{k=0}^{2l} f_k(f^2,\ LS)F^k(4l,\ 4l)+\eta(\mathbf{L}\cdot\mathbf{S}), \qquad (1)$$

where $f_k(f^2,LS)$ is an angular coefficient, $F^k(4l,4l)$ is a Slater integral, $l=3$, and η is the spin–orbit interaction constant.

Ordinarily $F^k(4l,4l)$ and η are chosen as variational parameters and are determined from experiment. The angular coefficients are calculated from the known formulas or taken from data tables.[9–12]

In the crystalline field the terms of the impurity ion are split, and therefore relation (1) gives the position of the centroid of the terms. The results of Refs. 7 and 8 enable one to determine uniquely the positions of the centroids of the terms $^3H_4$, $^1D_2$, and $^3P_0$ for the two Pr^{3+} optical centers in YSO and LSO crystals. For the GSO crystal we were unable to give a complete interpretation of the Stark components of the term $^3H_4$. For a more precise determination of the values of

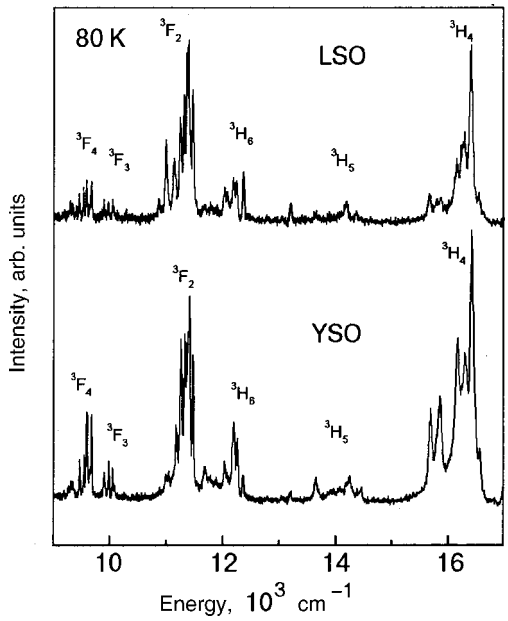

FIG. 1. Fragments of the luminescence spectra of YSO:Pr^{3+} and LSO:Pr^{3+} crystals under selective excitation of the Pr^{3+} impurity centers in the region of the optical transitions $^3H_4 \rightarrow {}^1D_2$ at $T=80$ K.

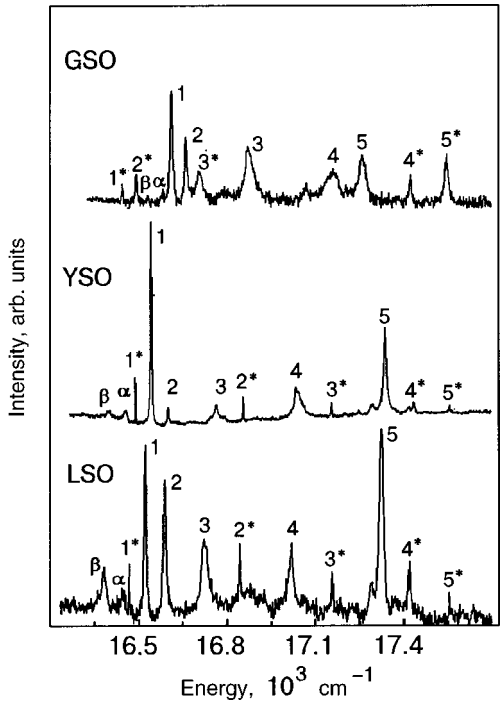

FIG. 2. Fragments of the absorption spectra of LSO, YSO, and GSO crystals in the region of the optical transitions $^3H_4 \rightarrow {}^1D_2$ of Pr^{3+} impurity ions at $T=80$ K.

the four variational parameters $F^k(4l,4l)$ and η it is necessary to know the positions of the centroids of several more terms. For this reason we studied the low-temperature IR luminescence spectra of the two optical centers Pr^{3+} in the YSO and LSO crystals upon their selective excitation (Fig. 1). The use of selective excitation and low temperatures made it possible to simplify the structure of the luminescence spectra considerably and to interpret them without ambiguity. Figure 1 shows groups of spectral lines belonging to the same Pr^{3+} optical center in the YSO and LSO crystals. The spectra correspond to optical transitions from the lowest Stark component of the $^1D_2$ term to the Stark components of the split terms $^3H_{4,5,6}$ and $^3F_{2,3,4}$. From these spectra and the analogous data for the second Pr^{3+} optical center one can find the centroids of five more terms. The values of the variational parameters $F^k(4l,4l)$ and η for the two Pr^{3+} optical centers in YSO and LSO crystals were determined from the condition of minimization of the sum $\Sigma_{i=1}^{7}(E_i^{\exp} - E_i(L,S,J))^2$, where $E_i^{\exp}$ are the centroids of the terms determined experimentally from the optical spectra. As expected,[9–11] the values of the variational parameters $F^k(4l,4l)$ and η (see Table I) are quite similar for the two Pr^{3+} optical centers in the YSO and LSO crystals.

TABLE I. Values of the Slater integrala $F^k(4l,4l)$ and spin-orbit interaction constant η for two types of Pr^{3+} centers in crystals of Y and Lu oxyorthosilicates.

	Y_2Si_5		Lu_2SiO_5	
Parameter	Type I	Type II	Type I	Type II
$F^2(4l,\ 4l)$	293.3	299.2	294.1	298.1
$F^4(4l,\ 4l)$	42.7	41.0	42.4	42.2
$F^6(4l,\ 4l)$	4.5	4.6	4.4	4.5
η	782.1	746	759.8	745.3

Note: The parameter values are given in cm^{-1}.

By virtue of the specific character of the splitting of the $^1D_2$ term by a crystalline field of definite symmetry, it can be used as a probe for studying the microscopic structure of the crystalline field of the ligands. To show this, let us turn to the classification of the states of the free Pr^{3+} ion in the group-theoretic formalism.[9–11] The term $^1D_2$ corresponds to the irreducible representation $D^{(2)}$ of the three-dimensional rotation group. In the case of octahedral or tetrahedral symmetry, $D^{(2)}$ decomposes into a twofold and a threefold irreducible representation. In a crystalline field of octahedral symmetry the energy of the threefold degenerate state t_{2g} is lower than the energy of the twofold degenerate state e_g, while in a field of tetrahedral symmetry the opposite is true. This has been confirmed experimentally in the optical spectra of the Ti^{3+} ion and is analyzed in Refs. 9–11, 14, and 15.

It is known[7,8,13] that the Pr^{3+} ions in the YSO, LSO, and GSO crystals occupy two inequivalent cation sites with the lowest possible, triclinic, local symmetry C_1. Both cation sites are characterized by the crystalline field of the distorted REO_6 octahedra. Consequently, the terms of the Pr^{3+} ion must split completely, and that is observed experimentally.[7,8] However, a detailed analysis of the structure of the absorption spectrum of the Pr^{3+} impurity ion in YSO, LSO, and GSO crystals in the region of the optical transitions $^3H_4 \leftrightarrow {}^1D_2$ (Fig. 2) shows that there is a special grouping of the Stark components of the $^1D_2$ term. For example, in the absorption spectrum of the GSO:Pr^{3+} crystal, the spectral lines 1*, 2*, and 3* are separated from the lines 4* and 5* by an energy interval of $\sim 692\,\mathrm{cm}^{-1}$, which is larger than corresponding splitting between these lines within each group. It can be conjectured that for the two types of Pr^{3+} optical centers in the GSO crystal and for the first type of

Pr^{3+} optical centers in the YSO and LSO crystals the spectral lines 1, 2, and 3 (Fig. 2) appear as a result of the crystal-field splitting of the originally threefold degenerate state t_{2g}, while the spectral lines 4 and 5 appear as a result of the splitting of the e_g state.[9–11] In the YSO and LSO crystals, however, for the second type of Pr^{3+} optical centers (Fig. 2) the grouping of the spectral lines is the opposite: first come the spectral lines 1* and 2* and then 3*, 4*, and 5*. Consequently, it can be supposed that in the cation sites of the second type in the YSO and LSO crystals the Pr^{3+} impurity centers are found in the crystalline field of a distorted tetrahedron. It should be noted that a structural analysis[13] gives a distorted octahedral symmetry for both types of cation sites in the YSO crystal.

The qualitative arguments presented above are based on the analogy with the splitting of the $^1D_2$ term of the d electron in crystalline fields of octahedral and tetrahedral symmetry. Therefore, in the case of two f electrons one should do a detailed analysis with allowance for the fact[9–11] that in the expansion of the crystalline field in spherical harmonics $Y_{l,m}(\theta,\varphi)$ for f electrons it is necessary to take into account terms with $l \leqslant 6$.

For analysis of the features of the splitting of the $^1D_2$ term of the Pr^{3+} ion in a crystalline field of octahedral or tetrahedral symmetry, we construct an orthonormalized basis $\varphi_{2,m}(\theta,\varphi)$ $(m=[-2,2])$ of the representation $D^{(2)}$. The wave functions $\varphi_{2,m}(\theta,\varphi)$ are written in the form of a linear combination of products $Y_{3,k}(\theta_1,\varphi_1)Y_{3,p}(\theta_2,\varphi_2)$ $(\theta_1,\varphi_1$ and θ_2,φ_2 are the coordinates of the first and second electrons) with the use of the Clebsch–Gordan coefficients.[9–11] The combination of spherical harmonics in the expression for the crystal-field potential is chosen from the condition that it be invariant with respect to the symmetry operators of the groups O_h and T_d. The radial integrals of the crystalline field are taken as variational parameters. If the quantization axis is taken along the fourfold axis, the crystal-field potential can be written in the form

$$V_{\rm cr}=\sum_{i=1}^{2}\{\pm B_{4,0}[Y_{4,0}(\theta_i,\varphi_i)+\sqrt{5/14}(Y_{44}(\theta_i,\varphi_i) + Y_{4,-4}(\theta_i,\varphi_i))]+B_{6.0}[Y_{6,0}(\theta_i,\varphi_i) - \sqrt{7/2}(Y_{6,4}(\theta_i,\varphi_i)+Y_{6,-4}(\theta_i,\varphi_i))]\}, \quad (2)$$

$$B_{4,4}=B_{4,0}\sqrt{5/14}, \quad (3)$$

where $B_{4,0}$ and $B_{6,0}$ are variational parameters, and $Y_{l,m}(\theta_i,\varphi_i)$ are spherical harmonics.

In relation (2) the plus sign corresponds to the octahedral symmetry and the minus sign to the tetrahedral. The matrix elements of the crystal-field operator are calculated in the basis of orthonormalized wave functions $\varphi_{2,m}(\theta,\varphi)$. A calculation shows a complete analogy with a single d electron,[9–11,14,15] viz: in a crystalline field of octahedral symmetry the threefold degenerate level of the $^1D_2$ term of the Pr^{3+} impurity ion has a lower energy than the twofold degenerate level (Fig. 3). In a field of tetrahedral symmetry the situation is reversed. For the model crystalline field (2) the splitting of the $^1D_2$ term depends only on the parameter $B_{4,0}$: $\Delta = B_{4,0}\ 20/7\sqrt{\pi}$. An estimate of $B_{4,0}$ can be obtained from experiment. To do this we find the centroids of the spectral lines 1, 2, 3 and 4, 5 (1*, 2* and 3*, 4*, 5*) for the two Pr^{3+} optical centers in the YSO and LSO crystals and also the centroids of the spectral lines 1, 2, 3 and 4, 5 and 1*, 2*, 3* and 4*, 5* in the GSO crystal (Fig. 2). The difference of the positions of the corresponding centroids gives the value of the desired parameter: for the first type of Pr^{3+} optical center $B_{4,0}=350\,\mathrm{cm}^{-1}$ (LSO), $B_{4,0}=343\,\mathrm{cm}^{-1}$ (YSO), and $B_{4,0}=296\,\mathrm{cm}^{-1}$ (GSO), and for the second type of center $B_{4,0}=448\,\mathrm{cm}^{-1}$ (LSO), $B_{4,0}=442\,\mathrm{cm}^{-1}$ (YSO), and $B_{4,0}=560\,\mathrm{cm}^{-1}$ (GSO). It is seen that the second type of Pr^{3+} optical centers are acted upon more strongly by the field of the ligands.

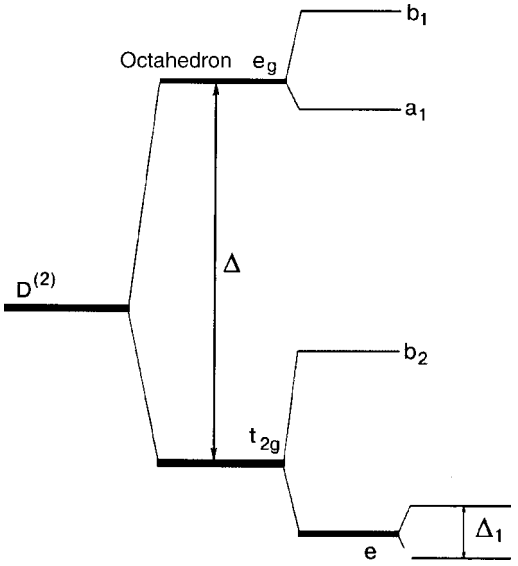

FIG. 3. Simplified scheme of the splitting of the $^1D_2$ term of the Pr^{3+} impurity ion.

Further analysis of the lowering of the symmetry of the cation sites will be confined to the case of octahedral coordination, since there is a chain of distortions (tetragonal, trigonal, and rhombic) of a regular octahedron which lead to successive splitting of the $^1D_2$ term and to complete lifting of the degeneracy. We will not discuss the trigonal distortion of the octahedron in detail, since it is manifested in a manner analogous to the tetragonal. In the case of tetragonal distortion of the octahedron the point symmetry of the cation site is lowered to D_{4h} (Refs. 9–11): the e_g and t_{2g} representations of the O_h group become reducible, and the states e_g and t_{2g} are therefore split. In the splitting of t_{2g} the twofold degenerate level is conserved.

For finding the quantitative characteristics of the crystalline field in the case of tetragonal distortion, a term $A_{2,0}Y_{2,0}(\theta_i,\varphi_i)$ must be added to the crystal-field potential (2). If the tetragonal distortion is treated as a weak perturbation, then relation (3) remains unchanged. Further, in the basis of wave functions $\varphi_{2,m}(\theta,\varphi)$ we find the matrix elements of the modified crystal-field operator, and we obtain and solve the secular equation. The desired roots of the secular equation and, hence, the energies of the Stark components of the $^1D_2$ term relative to the centroid are as follows:

$$E_{1,2}=-\frac{8B_{4,0}}{7\sqrt{\pi}}-\frac{11A_{2,0}}{21\sqrt{5\pi}},$$

$$E_3=-\frac{120B_{4,0}}{105\sqrt{\pi}}+\frac{11\sqrt{5}A_{2,0}}{105\sqrt{\pi}},$$

$$E_4=\frac{12B_{4,0}}{7\sqrt{\pi}}-\frac{11A_{2,0}}{21\sqrt{5\pi}}, \tag{4}$$

$$E_5=\frac{180B_{4,0}}{105\sqrt{\pi}}+\frac{11\sqrt{5}A_{2,0}}{105\sqrt{\pi}}.$$

The system of equations (4) gives a symmetric splitting of the levels e_g and t_{2g} (Fig. 3). However, it follows from the optical absorption spectra (Fig. 2) that for the YSO and LSO crystals the energy interval between the spectral lines 4 and 5 is almost twice as large as the energy interval between line 3 and the centroid of lines 1 and 2. Asymmetric splitting is also observed in the absorption spectrum of the GSO:Pr^{3+} crystal. To describe the asymmetry in the splitting of the $^1D_2$ term it is necessary to consider two independent variational parameters $B_{4,0}$ and $B_{4,4}$. In that case the roots of the secular equation are:

$$E_{1,2}=-\frac{8B_{4,0}}{7\sqrt{\pi}}-\frac{11A_{2,0}}{21\sqrt{5\pi}},$$

$$E_3=\frac{10B_{4,0}-150B_{4,4}+11\sqrt{5}A_{2,0}}{105\sqrt{\pi}},$$

$$E_4=\frac{12B_{4,0}}{7\sqrt{\pi}}-\frac{11A_{2,0}}{21\sqrt{5\pi}}, \tag{5}$$

$$E_5=\frac{30B_{4,0}+150B_{4,4}+11\sqrt{5}A_{2,0}}{105\sqrt{\pi}}.$$

The parameters $B_{4,0}$, $A_{2,0}$, and $B_{4,4}$ can be estimated from the absorption spectra (Fig. 2). For this we find the position of the centroid of the spectral lines 1 and 2 in the YSO and LSO crystals and then compare the corresponding differences (E_i-E_j) according to the scheme in Fig. 3. For the GSO crystal we follow similar procedures for each of the two Pr^{3+} optical centers. The best approximation to the splitting of the $^1D_2$ term is achieved at $A_{2,0}=1040\,\mathrm{cm}^{-1}$, $B_{4,0}=310\,\mathrm{cm}^{-1}$, and $B_{4,4}=380\,\mathrm{cm}^{-1}$ for the LSO crystal and at $A_{2,0}=1103\,\mathrm{cm}^{-1}$, $B_{4,0}=306\,\mathrm{cm}^{-1}$, and $B_{4,4}=357\,\mathrm{cm}^{-1}$ for YSO. Accordingly, for the first type of Pr^{3+} optical centers of the GSO crystal we find $A_{2,0}=746\,\mathrm{cm}^{-1}$, $B_{4,0}=329\,\mathrm{cm}^{-1}$, and $B_{4,4}=232\,\mathrm{cm}^{-1}$, and for the second type $A_{2,0}=838.9\,\mathrm{cm}^{-1}$, $B_{4,0}=585.5\,\mathrm{cm}^{-1}$, and $B_{4,4}=499.7\,\mathrm{cm}^{-1}$.

Further lowering of the symmetry of the octahedron to rhombic (D_{2h}) completely lifts the degeneracy of the $^1D_2$ term. The point group D_{2h} contains only one-dimensional irreducible representations. The model of the crystal-field potential becomes more complicated, and the secular equation becomes too awkward to solve because of the two additional variational parameters $A_{2,2}$ and $B_{4,2}$. We therefore give only the expression for the splitting of the lower, twofold degenerate state (Fig. 3):

$$\Delta_1=\left(\frac{640(B_{4,2})^2}{49\pi}-\frac{352B_{4,2}A_{2,2}}{49\sqrt{3}\pi}+\frac{242(A_{2,2})^2}{735\pi}\right)^{1/2}. \tag{6}$$

If we set $B_{4,2}\approx A_{2,2}$, then we can estimate their value from the experiment. It follows from the splitting of lines 1 and 2 (Fig. 2) that for LSO $B_{4,2}\approx A_{2,2}\approx 45\,\mathrm{cm}^{-1}$ and for YSO $B_{4,2}\approx A_{2,2}\approx 43.6\,\mathrm{cm}^{-1}$. For the first type of optical centers in GSO we find $B_{4,2}\approx A_{2,2}\approx 36.4\,\mathrm{cm}^{-1}$, and for the second type $B_{4,2}\approx A_{2,2}\approx 30.7\,\mathrm{cm}^{-1}$.

Analysis of the numerical values of the variational parameters characterizing the microstructure of the crystalline field of the ligands at the cation sites of the YSO, LSO, and GSO crystals shows that the greatest effect of the crystalline field of the ligands is felt by the second type of Pr^{3+} optical centers in the GSO crystal (the large values of $B_{4,0}$ and $B_{4,4}$). At the same time, however, the octahedral symmetry of the cation sites of the GSO crystal is less distorted than in YSO and LSO. The values of the parameters $A_{2,0}$, $A_{2,2}$, and $B_{4,2}$ for the YSO and LSO crystals are larger than for GSO. In YSO and LSO the values of the variational parameters characterizing the crystalline field are of the same order. It should be noted that the YSO and LSO crystals belong to one crystalline type and the GSO crystal to another.[16]

Thus on the basis of an analysis of the low-temperature optical spectra of the crystals YSO:Pr^{3+}, LSO:Pr^{3+}, and GSO:Pr^{3+} we have obtained the values of the parameters characterizing the Coulomb and spin–orbit interactions in the free Pr^{3+} ion and also of the parameters governing the microstructure of the crystalline field of the ligands at the cation sites of the crystal lattices of YSO, LSO, and GSO. The features of the splitting of the $^1D_2$ term indicate that the quasi-symmetry of the cation sites is conserved. In contrast to the structural data, the features of the splitting of the $^1D_2$ term of the second type of optical centers in YSO and LSO indicate a tetrahedral quasi-symmetry of the cation sites.

*E-mail: malyukin@isc.kharkov.com

[1] H. Suzuki, T. A. Tombrello, C. L. Melcher, and J. S. Schweitzer, Nucl. Instrum. Methods Phys. Res. A **320**, 263 (1992).
[2] C. L. Melcher, R. A. Manente, C. A. Peterson, and J. S. Schweitzer, J. Cryst. Growth **128**, 1001 (1993).
[3] P. Dorenbos, C. W. E. van Eijk, A. J. J. Bos, and C. L. Melcher, J. Lumin. **60&61**, 979 (1994).
[4] A. A. Kaminskiĭ, Dokl. Akad. Nauk SSSR **319**, 870 (1991) [Sov. Phys. Dokl. **36**, 586 (1991)].
[5] K. Holliday, M. Croci, E. Vauthey, and U. P. Wild, Phys. Rev. **47**, 14741 (1993).
[6] Yun Liu, Chao-Nan Xu, H. Matsui, T. Imamura, and T. Watanabe, J. Lumin. **87–89**, 1297 (1994).
[7] Yu. V. Malyukin, B. I. Minkov, R. S. Borisov, V. P. Seminozhenko, N. V. Znamenskii, E. A. Manykin, D. V. Marchenko, and E. A. Petrenko, Fiz. Nizk. Temp. **24**, 571 (1998) [Low Temp. Phys. **24**, 432 (1998)].
[8] Yu. V. Malyukin, R. S. Borisov, P. N. Zhmurin, A. N. Lebedenko, B. V. Grinev, N. V. Znamensky, É. A. Manykin, Yu. V. Orlov, E. A. Petrenko, and T. G. Yukina, Fiz. Nizk. Temp. **26**, 1207 (2000) [Low Temp. Phys. **26**, 894 (2000)].
[9] C. J. Ballhausen, *Introduction to Ligand Field Theory*, McGraw-Hill, New York (1962); Mir, Moscow (1964).
[10] N. A. Kulagin and D. T. Sviridov, *Introduction to the Physics of Activated Crystals* [in Russian], Vyshcha Shkola, Kharkov (1990).
[11] I. B. Bersuker, *Electronic Structure and Properties of Coordination Compounds* [in Russian], Khimiya, Leningrad (1986).

[12] A. P. Yutsis and A. Yu. Savukinas, *Mathematical Principles of Atomic Theory* [in Russian], Minshis, Vilnius (1973).
[13] B. A. Maksimov, Yu. A. Kharitonov, V. V. Ilyukhin, and N. V. Belov, Kristallografiya **15**, 926 (1970) [Sov. Phys. Crystallogr. **15**, 806 (1970)].
[14] M. Grinberg, A. Mandelis, K. Fjeldsted, and A. Othonos, Phys. Rev. B **48**, 5922 (1993).
[15] M. Grinberg, A. Mandelis, K. Fjeldsted, and A. Othonos, Phys. Rev. B **48**, 5935 (1993).
[16] G. V. Anan'eva, A. M. Korovkin, T. I. Merkulyaeva, A. M. Morozov, M. V. Petrov, I. R. Savinova, V. P. Startsev, and P. P. Feofilov, Neorg. Mater. **17**, 1037 (1981).

Translated by Steve Torstveit

Dynamics of nonlinear excitations in the Frenkel–Kontorova model with a double-barrier potential

A. V. Gorbach

V. N. Karazin Kharkov National University, pl. Svobody 4, 61077 Kharkov, Ukraine

A. S. Kovalev*

B. Verkin Institute for Low Temperature Physics and Engineering, National Academy of Sciences of Ukraine, pr. Lenina 47, 61103 Kharkov, Ukraine

O. V. Usatenko

V. N. Karazin Kharkov National University, pl. Svobody 4, 61077 Kharkov, Ukraine; Institute of Radiophysics and Electronics, National Academy of Sciences of Ukraine, ul. Akad. Proskury 12, 61085 Kharkov, Ukraine

(Submitted February 13, 2001)
Fiz. Nizk. Temp. **27**, 786–792 (July 2001)

A nonlinear elastic chain in an external periodic double-barrier potential (a generalized Frenkel–Kontorova model) is considered. Small-amplitude dynamical localized excitations whose parameters lie in and near the gap of the spectrum of linear waves—gap and near-gap solitons—are investigated. [DOI: 10.1063/1.1388424]

INTRODUCTION

The Frenkel–Kontorova model is widely used in solid-state physics for the theoretical description of dislocations in crystals,[1–3] the motion of crowdions in an elastic lattice,[4–6] fluxons in Josephson junctions, domain walls in magnetically ordered media, etc.[3,7] In recent years a great deal of attention has been devoted to generalized Frenkel–Kontorova models in which the chain of interacting atoms is found in a periodic potential of complex form—a so-called double-well or double-barrier potential.[3,5,6,8] Such systems can support the existence of topological soliton excitations with a specific structure: in particular, fractional and split crowdions.[5,6]

Besides the topological soliton excitations (kinks) that have been considered in the majority of studies, the Frenkel–Kontorova model also supports the existence of dynamical small-amplitude soliton excitations (envelope solitons). The study of this type of soliton excitations in the generalized Frenkel–Kontorova model is the subject of the present paper.

We consider a monatomic elastic chain in a double-barrier potential. Such a modulation of the potential causes a gap to appear in the spectrum of linear waves, the width of the gap being proportional to the difference between the two minima of the double-barrier potential. We investigate small-amplitude dynamical soliton solutions with parameters lying in and near the gap in the spectrum of linear waves—the so-called gap and near-gap solitons.

STATEMENT OF THE PROBLEM AND THE BASIC DYNAMICAL EQUATIONS

In the standard Frenkel–Kontorova model one considers a chain atoms interacting harmonically with one another and executing one-dimensional motion in a potential well of the form $U \propto 1-\cos x_n$ created by the immobile periodic substrate, where x_n is the spatial coordinate of the nth atom. Here we use a generalized model[5,6] in which the periodic potential created by the substrate (the ''external'' nonlinearity) is assumed to have the form

$$V(x_n)=\gamma\left[\eta(1-\cos x_n)+\frac{1}{2}(1-\cos 2x_n)\right], \tag{1}$$

where $\gamma>0$, and η is a dimensionless parameter describing the double-barrier potential.

The interaction between atoms along the chain will also be assumed anharmonic (the ''internal'' nonlinearity):

$$U(\xi_n)=\frac{K_2}{2}(\xi_n-\xi_{n-1})^2+\frac{K_4}{2}(\xi_n-\xi_{n-1})^4, \tag{2}$$

where ξ_n is the displacement of the nth atom from its equilibrium position $x_n^0=\pi n$: $\xi_n=x_n-x_n^0$; the constant K_2 is positive, and the interatomic distance is assumed equal to π.

Let us assume that in the ground state the coordinates of the atoms correspond to the minima of the external potential (see Fig. 1). Here the even-numbered atoms lie in the absolute minima of the function (1), which correspond to values of the potential energy $V(\pi n)\equiv 0$, $n=0,\pm 2,\pm 4,,\ldots$, while the odd-numbered atoms lie in relative minima, which correspond to a value of the potential energy $V(\pi n)\equiv 2\eta\gamma$, $n=\pm 1,\pm 3,\ldots$. This corresponds to having an interatomic distance in the monatomic chain equal to one-half the period of the substrate. Thus the parameter η characterizes the energy difference of the two minima.

The equation of motion for the nth atom is

$$m\frac{d^2\xi_n}{dt^2}+K_2(2\xi_n-\xi_{n+1}-\xi_{n-1}) + \gamma[\eta\sin(\pi n+\xi_n)+\sin(2\xi_n)]=0. \tag{3}$$

In the majority of papers employing the Frenkel–Kontorova model it is the topological soliton solutions (kinks) of equa-

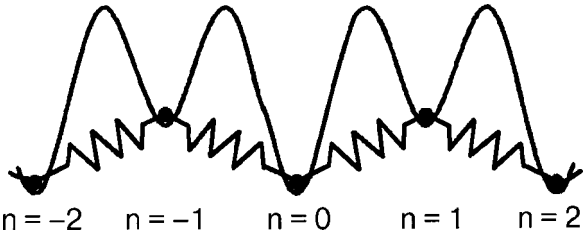

FIG. 1. Schematic illustration of the arrangement of atoms in the chain. The even-numbered atoms lie in the absolute minima of the double-barrier potential of Eq. (1), while the odd-numbered atoms lie at relative minima.

tion (3) that are studied. We will be considering small-amplitude dynamical solitons, in which the position of each atom deviates slightly from its equilibrium position. We can then expand the external potential (1) in small displacements ξ_n to the first nonlinear terms. The expansion will be different for the even- and odd-numbered atoms. As a result, we obtain the following dynamical equation for the nth atom:

$$m\frac{d^2\xi_n}{dt^2}+K_2(2\xi_n-\xi_{n+1}-\xi_{n-1})+\gamma[2+\eta\cos(\pi n)]\xi_n$$

$$+K_4[(\xi_n-\xi_{n+1})^3+(\xi_n-\xi_{n-1})^3]-\frac{8}{3}\gamma\xi_n^3=0,$$

$$n=0,\pm 1,\pm 2... \tag{4}$$

The modulation of the parameters of the system is assumed small ($\eta\ll 1$), and we are neglecting the small terms proportional to $\eta\xi_n^3$. A distinctive feature of this equation is the presence of the term containing $\cos(\pi n)$, which modulates the harmonic part of the external potential of the system. This modulation makes it impossible to seek the general solution of the linearized equations in the standard form $\xi_n \propto \exp(i\omega t-i\beta n)$; it must contain two waves propagating with different phase velocities:[9]

$$\xi_n=A_1\exp i(\omega t-\beta n)+A_2\exp i(\omega t-(\beta-\pi)n)+\text{c.c.} \tag{5}$$

The spectrum of linear waves of the system (see Fig. 2) is determined by the dispersion relation

$$\omega^4-(\omega_1^2+\omega_2^2)\omega^2+\omega_1^2\omega_2^2-\tilde{\omega}_0^4\cos^2\beta=0, \tag{6}$$

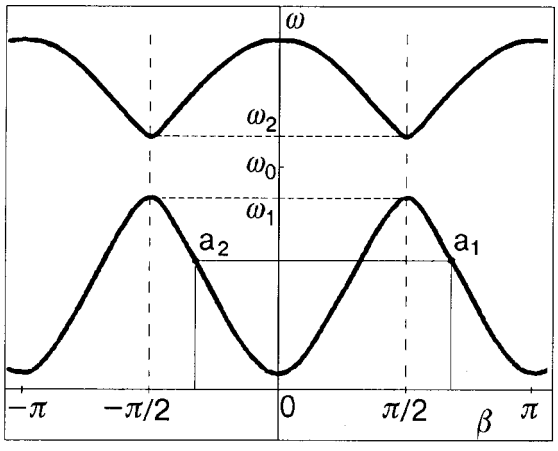

FIG. 2. Spectrum of linear waves of the form in Eq. (5); the spectrum is described by the characteristic equation (6).

where $\omega_1^2=(2K_2+2\gamma-\eta\gamma)/m$; $\omega_2^2=(2K_2+2\gamma+\eta\gamma)/m$; $\tilde{\omega}_0^2=2K_2/m$, and $\omega_0=\sqrt{(\omega_1^2+\omega_2^2)/2}$. At a given frequency ω the two partial waves of the solution (5) correspond to the points a_1 and a_2 in Fig. 2. We see that these two waves have the same group velocity $V=d\omega/d\beta$ but different phase velocities.

For $\beta=\pm\beta_0=\pm\pi/2$ the spectrum of linear waves has a gap with a width proportional to η: $\omega_2^2-\omega_1^2=2\eta\gamma/m$. The formation of this gap is due to the modulation of the parameters of the system. We will be interested in nonlinear excitations whose parameters lie in and near the gap.

The amplitude of a linear wave is arbitrary. In the case of a nonlinear wave the amplitudes A_1 and A_2 in solution (5) can also take on different values, but their ratio is determined by the frequency of the wave:

$$\frac{A_2}{A_1}=\frac{\sqrt{|1-\omega^2/\omega_2^2|}\pm\sqrt{|1-\omega^2/\omega_1^2|}}{\sqrt{|1-\omega^2/\omega_2^2|}\mp\sqrt{|1-\omega^2/\omega_1^2|}}, \tag{7}$$

where the upper (lower) sign corresponds to excitations with frequencies lying on the parts of the spectrum where an increase of the modulus of the wave vector corresponds to an increase (decrease) of the frequency.

We restrict discussion to nonlinear waves with frequencies $\omega\sim\omega_1,\omega_2$ and wave numbers $\beta\approx\beta_0$ (i.e., values $\beta=\beta_0+\kappa$, where $\kappa\ll 1$). In this region of parameters the spectrum of linear waves (6) has a quadratic form.

We seek a solution of the system of nonlinear equations (4) in the form (5), with coefficients A_1 and A_2 that are slowly varying functions of t and n:

$$\xi_n=A_1(n,t)\exp i\left(\omega t-\frac{\pi}{2}n\right)+A_2(n,t)$$

$$\times\exp i\left(\omega t+\frac{\pi}{2}n\right)+\text{c.c.} \tag{8}$$

We will be interested in small-amplitude nonlinear solutions with parameters lying near the gap of the spectrum of linear waves. The condition that the amplitudes of these waves be small is satisfied near the curve $\omega=\omega(k)$, which corresponds to the linear wave dispersion relation (6). From now on we shall assume that the parameter η is small, ensuring that the gap in the spectrum of linear waves is narrow. Thus the condition that the amplitudes be small will hold both inside the gap and in the neighborhood around it.

In the long-wavelength limit, when $A_i(n,t)$ is a slowly varying function of the atom number n, we replace the discrete number n in $A_i(n,t)$ by a continuous coordinate x and use the expansion

$$A_i(x\pm 1,t)=A_i(x,t)\pm\frac{\partial A_i(x,t)}{\partial x}+\mathcal{O}(\eta^2A_i)$$

(as we shall see below, $\partial A_i(x,t)/\partial x\sim\eta A_i$, $\partial A_i(x,t)/\partial t\sim\omega_0\eta A_i$).

In the case of a small difference between the potential energy minima ($\eta\ll 1$), when $\partial A_i/\partial t\ll\omega_1A_i,\omega_2A_i$ and $\partial A_i/\partial x\ll A_i$, for treating the region in and around the gap in the spectrum of linear waves we need to keep only the first derivatives $\partial A_i/\partial t$ and $\partial A_i/\partial x$ in the linear part of the equation obtained by substituting Eq. (8) into (4). In addition,

when the small-amplitude character of the atomic oscillations is taken into account ($|K_4||A_i|^2/K_2 \ll 1$, $|A_i|^2 \ll 1$), in the nonlinear part of that equation we can drop all the derivatives of the amplitudes A_i. The validity of assumptions will be checked for the solutions obtained. For the amplitudes A_1 and A_2 we have the following system of first-order differential equations:

$$
\begin{aligned}
&i\frac{2}{\omega_0}\frac{2(K_2+\gamma)}{\eta\gamma}\frac{\partial A_1}{\partial t}+i\frac{2K_2}{\eta\gamma}\frac{\partial A_1}{\partial x}=\frac{2\delta}{\omega_0}\frac{2(K_2+\gamma)}{\eta\gamma}\\
&\quad\times A_1-A_2-\frac{3K_4}{\eta\gamma}[(3p+1)A_1(|A_1|^2+2|A_2|^2)\\
&\quad+3(p-1)A_2^2A_1^*],\\
&i\frac{2}{\omega_0}\frac{2(K_2+\gamma)}{\eta\gamma}\frac{\partial A_2}{\partial t}-i\frac{2K_2}{\eta\gamma}\frac{\partial A_2}{\partial x}=\frac{2\delta}{\omega_0}\frac{2(K_2+\gamma)}{\eta\gamma}\\
&\quad\times A_2-A_1-\frac{3K_4}{\eta\gamma}[(3p+1)A_2(|A_2|^2+2|A_1|^2)\\
&\quad+3(p-1)A_1^2A_2^*],
\end{aligned}
\tag{9}
$$

where $\omega_0^2=2(K_2+\gamma)/m$ is the frequency corresponding to the midpoint of the gap in the spectrum of linear waves, $\delta=\omega-\omega_0$ is the frequency measured from the midpoint of the gap, and $p=[1-(4\gamma/3K_4)]/3$ is a parameter characterizing the relative strength of the ''internal'' and ''external'' nonlinearities.

As we see from system (9), a spectrum of linear waves of the form (5) will have the following appearance in the neighborhood of wave number $\beta_0=\pi/2$:

$$
\omega=\omega_0\pm\frac{\omega_0\eta\gamma}{4(K_2+\gamma)}\sqrt{1+(2K_2\kappa/\eta\gamma)^2}. \tag{10}
$$

Introducing the renormalized amplitudes $\sqrt{12|K_4|/\eta\gamma}A_i=F_i$, coordinate $(\eta\gamma/(2K_2))x\to x$, and time $[\omega_0\eta\gamma/4(K_2+\gamma)]t\to t$, we obtain the following system of equations in the dimensionless variables:

$$
\begin{aligned}
&i\frac{\partial F_1}{\partial t}+i\frac{\partial F_1}{\partial x}=\Omega F_1-F_2-\frac{\sigma}{4}[(3p+1)F_1(|F_1|^2\\
&\qquad+2|F_2|^2)+3(p-1)F_2^2F_1^*],\\
&i\frac{\partial F_2}{\partial t}-i\frac{\partial F_2}{\partial x}=\Omega F_2-F_1-\frac{\sigma}{4}[(3p+1)F_2(|F_2|^2\\
&\qquad+2|F_1|^2)+3(p-1)F_1^2F_2^*],
\end{aligned}
\tag{11}
$$

where $\Omega=4\delta(K_2+\gamma)/(\omega_0\eta\gamma)$ is the dimensionless deviation of the frequency from the midpoint of the gap in the spectrum of linear waves, and $\sigma=\mathrm{sgn}(K_4)$.

In the new variables the spectrum of linear waves (10) in a coordinate system moving with the group velocity $V=\partial\omega/\partial\kappa$, i.e., for solutions of the form $F_i\propto\exp(-i\kappa(x-Vt))$, takes the form

$$
\Omega_L=\frac{4(K_2+\gamma)}{\eta\gamma}\pm\sqrt{1-V^2}. \tag{12}
$$

The system of differential equations (11) obtained here is analogous to the system describing the dynamics of a diatomic chain.[10]

ANALYSIS OF THE SOLITON SOLUTIONS

A detailed qualitative analysis of a system of equations of the form (11) for arbitrary values of the parameter p is done in Ref. 10. Here we give analytical expressions for the soliton solutions of the system (11) in the particular case $K_4=0$, i.e., when the ''internal'' nonlinearity in the chain is absent. For such a choice of the constant K_4 the system (11) reduces to

$$
\begin{aligned}
&i\frac{\partial F_1}{\partial t}+i\frac{\partial F_1}{\partial x}=\Omega F_1-F_2-\frac{1}{2}\\
&\qquad\times[F_1(|F_1|^2+2|F_2|^2)+F_2^2F_1^*],\\
&i\frac{\partial F_2}{\partial t}-i\frac{\partial F_2}{\partial x}=\Omega F_2-F_1-\frac{1}{2}\\
&\qquad\times[F_2(|F_2|^2+2|F_1|^2)+F_1^2F_2^*],
\end{aligned}
\tag{13}
$$

where $F_i=\sqrt{8/\eta}A_i$.

We shall assume that the coordinate and time dependence of the amplitudes F_i is of the form $F_i(x,t)=F_i(x-Vt)$, which is standard for envelope solitons moving at velocity V. We introduce the new real variables u_1, u_2, q, and s:

$$
\begin{aligned}
&F_1=u_1\exp(iq+is),\\
&F_2=u_2\exp(iq-is),
\end{aligned}
\tag{14}
$$

which satisfy the following system of equations:

$$
\frac{du_1}{dz}=u_1\sin(2s)+\beta(V)u_1^3\sin(4s), \tag{15}
$$

$$
\frac{ds}{dz}=-\nu+\cos(2s)+\alpha(V)u_1^2+\beta(V)u_1^2\cos(4s), \tag{16}
$$

$$
\frac{dq}{dz}=-\nu V+\frac{V}{\sqrt{1-V^2}(1+V)}u_1^2, \tag{17}
$$

$$
u_2=\sqrt{(1-V)/(1+V)}u_1, \tag{18}
$$

where

$$
\alpha(V)=3-V^2/2\sqrt{1-V^2}(1+V);\quad z=x-Vt/\sqrt{1-V^2};
$$

$$
\beta(V)=\sqrt{(1-V)/(1+V)}/2,
$$

and the parameter $\nu(\Omega,V)$ is defined by the relation

$$
\nu(\Omega,V)=\frac{\Omega}{\sqrt{1-V^2}}. \tag{19}
$$

The relation of the form (18) between the amplitudes u_1 and u_2 corresponds to two-parameter solutions of system (11). In general, this system admits a solutions of a more general form with dependence on three parameters, but we will not consider those solutions here. The possibility of existence of three-parameter solitons is discussed in Ref. 11. In

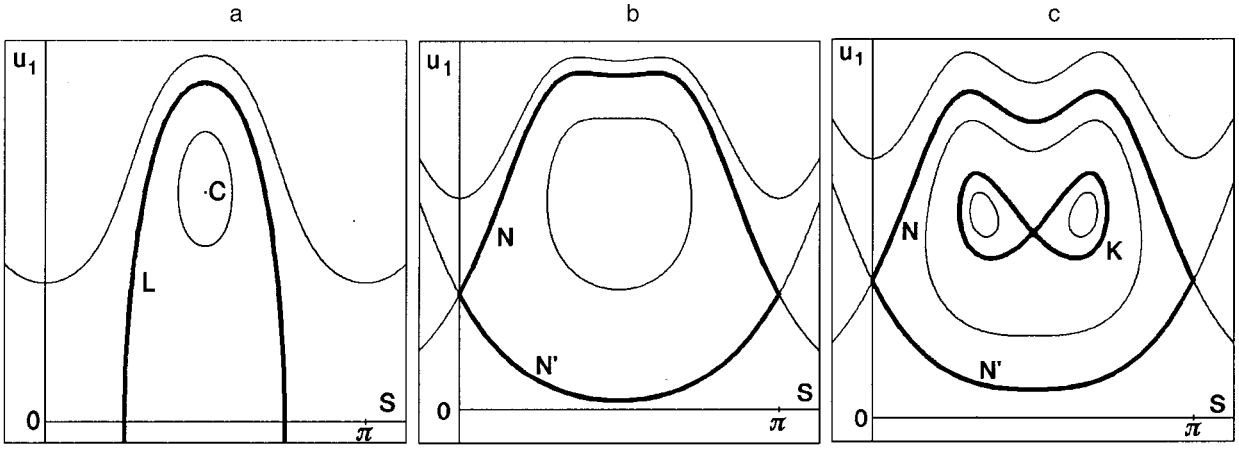

FIG. 3. Phase portraits of the system of equations (15), (16) for different values of the frequency ν: $-1<\nu<1$ (a), $1<\nu<\nu_*$ (b), $\nu>\nu_*$ (c).

the case of the two-parameter solutions it is convenient to choose the shift of the frequency Ω and the velocity V as the parameters of a solution.

Equations (15) and (16) for u_1 and s in the system (15)–(18) separate, forming a system of equations with the following effective Hamiltonian:

$$H=(-\nu+\cos(2s))u_1^2+\frac{\alpha}{2}u_1^4+\frac{\beta}{2}u_1^4\cos(4s), \tag{20}$$

where the variables u_1^2 and $2s$ play the role of canonically conjugate coordinate and momentum, and the coordinate z plays the role of an effective ''time.''

It is convenient to study the possible solutions of system (15), (16) on the phase plane of the variables (u_1,s). In the general case the phase portrait is symmetric about the axis $u_1=0$ and is periodic in the variable s with period π. We shall therefore consider it in the region $u_1>0$, $0<s<\pi$ (see Fig. 3). The form of the phase portrait of the system under study depends on the value of the parameter ν, which is a function of the dimensionless velocity V and frequency shift Ω (19).

For $\nu<-1$, i.e., when the frequency of the nonlinear excitation is less than the frequency of the lower branch of the spectrum of linear waves ($\Omega<-\sqrt{1-V^2}$), there are no singular points on the phase plane (u_1,s), and soliton solutions do not exist in this frequency region. At the frequency $\nu=-1$ ($\Omega=-\sqrt{1-V^2}$) a singular point appears at the coordinates $u_1=0$, $s=\pi/2$, which splits into two saddle points $u_1=0$, $s=\pi/2\pm\cos^{-1}(-\nu)/2$ and a center C with coordinates $u_1=\sqrt{(\nu+1)(\alpha+\beta)}$, $s=\pi/2$ in the frequency region $-1<\nu<1$ (see Fig. 3a). The saddle points are connected by separatrices L, which correspond to moving gap solitons. The phase portraits illustrated in Fig. 3a and 3b are analogous to those for an anharmonic oscillator under conditions of parametric pumping.[12] The similarity of these systems derives from the fact that the coefficient periodic in the coordinate x in the evolution equations plays the role of the coefficient periodic in time in the case of parametric excitation.

The next bifurcation occurs on the upper branch of the spectrum of linear waves, i.e., for $\nu=1$ ($\Omega=\sqrt{1-V^2}$): each saddle point splits into two saddle points situated symmetrically in the regions $u_1>0$ and $u_1<0$. Thus in the frequency region $1<\nu<\nu_*=1/(1-V^2)$ there exist on the phase plane (u_1,s) two saddle points with coordinates $u_1=\pm\sqrt{(\nu-1)(\alpha+\beta)}$, $s=0,\pi$ and two centers with coordinates $u_1=\pm\sqrt{(\nu+1)(\alpha+\beta)}$, $s=\pi/2$ (see Fig. 3b). The saddle points are connected by separatrices N and N', which correspond to moving near-gap solitons in which, unlike the gap solitons L, the asymptotes at infinity ($z\to\pm\infty$) are not equal to zero. The separatrix N corresponds to the so-called ''bright soliton on a pedestal,'' since in it the amplitude of the field at zero is greater than the amplitudes at infinity. The separatrix N' corresponds to a ''dark soliton of the nonzero vacuum'' (see Ref. 12).

Finally, when the parameter ν becomes equal to $\nu_*=1/(1-V^2)$ the last bifurcation occurs: the center $u_1=\sqrt{(\nu-1)(\alpha+\beta)}$, $s=\pi/2$ splits into a saddle point with the same coordinates and two new centers with coordinates $u_1=\sqrt{\nu/(\alpha-\beta)}$, $s=\pi/2\pm\cos^{-1}(\nu_*/\nu)/2$ (see Fig. 3c). Then two new separatrices K appear in addition to N and N'. Thus three types of moving near-gap solitons exist in the region $\nu>\nu_*$: N, N', and K.

The gap solitons L and near-gap solitons N and N' are studied in detail in Ref. 10. Here we consider the near-gap solitons K. The analytical expression for this type of soliton has the form

$$u_1=\left[\frac{(1+V)\sqrt{1-V^2}(1+\nu)}{2-V^2}\right]^{1/2}\times\left\{\frac{(1+\nu)(1-\nu_*)+\nu(\nu_*+1)\cosh^2(\xi)}{(\nu-1)(\nu-\nu_*)+\nu(\nu_*+1)\cosh^2(\xi)\pm4\sqrt{\nu}(\nu-\nu_*)\sinh(\zeta)}\right\}^{1/2},$$

$$s=\pi\pm\tan^{-1}\left[\left(\frac{\nu(\nu_*+1)}{(\nu+1)(\nu-\nu_*)}\right)^{1/2}\cosh(\zeta)\right],$$

$$q=-\frac{V(\nu+1)}{2-V^2}z\pm\frac{2V\sqrt{(\nu-\nu_*)(\nu+1)}}{(2-V^2)\sqrt{\nu_*}}\times\tan^{-1}[c^{(1)}(\exp(-\zeta)\mp\sqrt{\nu_*(\nu+1)/\nu^2(\nu_*+1)}c^{(2)})]\mp\frac{2V\sqrt{(\nu-\nu_*)(\nu+1)}}{(2-V^2)\sqrt{\nu_*}}\times\tan^{-1}[c^{(2)}(\exp(-\zeta)\pm\sqrt{\nu_*(\nu+1)/\nu^2(\nu_*+1)}c^{(1)})], \tag{21}$$

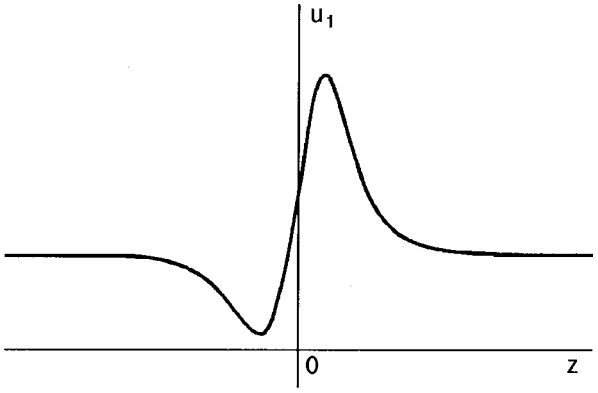

FIG. 4. Dependence of the amplitude u_1 on the coordinate z in a K soliton.

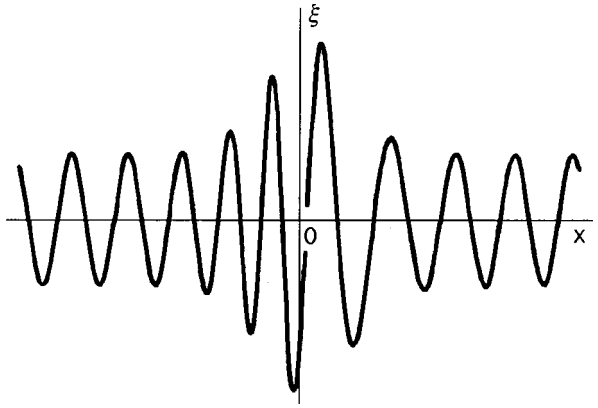

FIG. 5. Dependence of the resultant displacement field ξ of atoms in the chain on the coordinate (the number of the atom in the chain).

where $\zeta=2\sqrt{(\nu+1)(\nu-\nu_*)/(\nu_*+1)}z$, $c^{(n)}=\sqrt{\nu/\nu_*}(1-(-1)^n\sqrt{(\nu-\nu_*)/(\nu+1)})$, and the different signs correspond to the different separatrix loops.

This near-gap soliton is formed by two nonlinear waves with the same frequency, propagating in opposite directions. The frequency ω of the waves and one of the two wave numbers $\beta_{1,2}$ completely determine the parameters of the soliton, viz., the velocity V and frequency shift Ω in the coordinate system moving with the soliton:

$$\omega=\omega_0+\frac{\omega_0\eta\gamma}{4(K_2+\gamma)}\left[\Omega+\frac{V^2}{(2-V^2)(1-V^2)}\times(\Omega+\sqrt{1-V^2})\right],$$

$$\beta_{1,2}=\pm\beta_0+\frac{\eta\gamma}{2K_2}\frac{V}{(2-V^2)(1-V^2)}(\Omega+\sqrt{1-V^2}).$$

Unlike the L, N, and N' solitons, in the K solitons the phase s has the same asymptotes for $z\to\pm\infty$. Thus the phase shift of the nonlinear waves forming the soliton as the coordinate z varies from $-\infty$ to $+\infty$ is determined solely by the asymptotic behavior of the phase q and is given by

$$\Delta=\mp\frac{4V\sqrt{(\nu-\nu_*)(\nu+1)}}{(2-V^2)\sqrt{\nu_*}}\times\tan^{-1}[c^{(1)}c^{(2)}\sqrt{\nu_*(\nu+1)/\nu^2(\nu_*+1)}]. \quad (22)$$

The profiles of the fields u_1 and u_2 in the K soliton differ substantially from those in the L, N, and N' solitons. Figure 4 shows a schematic illustration of the dependence of the amplitude u_1 on the coordinate z, which has an asymmetric shape that is uncharacteristic for a soliton. The positions of the maximum and minimum of the amplitude are determined by the relation

$$\zeta_0=2\sqrt{(\nu+1)(\nu-\nu_*)/(\nu_*+1)}z_0=\sinh^{-1}\left[-\frac{1}{\sqrt{\nu}}\left(1\pm\frac{\nu+1}{\sqrt{\nu_*+1}}\right)\right].$$

The resulting field ξ of atomic displacements (see Eq. (8)) in the K soliton has the form of a localized excitation against the background of nonlinear waves that do not decay at infinity; its dependence on the coordinate (number of the atom) is shown schematically in Fig. 5. The maximum of the amplitude in the soliton is shifted relative to its center on account of the specifics of the profiles of fields u_1 and u_2.

The localization region of the K soliton is inversely proportional to $(1-V^2)$. As the velocity V approaches its maximum value ($|V|\to 1$), the soliton delocalizes and, in the limit, goes over to a periodic nonlinear wave (the so-called ''cnoidal'' wave).

CONCLUSION

We have studied the nonlinear dynamics of a monatomic chain in an external double-barrier potential. We have shown that this system is described by dynamical equations analogous to those for a diatomic chain. We have studied the evolution of the phase portrait of the system upon changes in the frequency of the nonlinear excitation and found explicit expressions for the soliton solutions in the particular case when the interaction between particles is assumed linear.

The analogy that we have drawn between two different modulated elastic systems reconfirms the previous conclusion of the authors[13] that the dynamics of different one-dimensional modulated systems with cubic nonlinearity can be described by analogous differential equations which differ only in the coefficients of the linear and nonlinear terms.

This study was supported in part by the program INTAS-99 (grant No. 167) and the program MNOP (grant USU 082087).

*E-mail: kovalev@ilt.kharkov.ua

[1] Ya. I. Frenkel' and T. A. Kontorova, Zh. Éksp. Teor. Fiz. **8**, 1340 (1938).
[2] J. P. Hirth and J. Lothe, *Theory of Dislocations* [McGraw-Hill, New York (1967); Atomizdat, Moscow (1972)].
[3] O. M. Braun and Yu. S. Kivshar, Phys. Rep. **306**, 1 (1998).
[4] A. M. Kosevich and A. S. Kovalev, ''Theory of dynamical crowdions. Radiation and other effects in solids,'' *Materials of the School on Radiation-Induced and Other Defects in Solids* [in Russian], Tbilisi, October 15–28, 1973; pub. Tbilisi (1974), Vol. 1, p. 186.
[5] V. D. Natsik and E. I. Nazarenko, Fiz. Nizk. Temp. **26**, 283 (2000) [Sov. J. Low Temp. Phys. **26**, 210 (2000)].
[6] V. D. Natsik, S. N. Smirnov, and E. I. Nazarenko, Fiz. Nizk. Temp. **27**, 316 (2001) [Sov. J. Low Temp. Phys. **27**, 233 (2000)].
[7] M. J. Ablowitz and H. Segur, *Solitons and the Inverse Scattering Transform*, SIAM, Philadelphia (1981); Mir, Moscow (1987).
[8] I. F. Lyuksutov, A. G. Naumovets, and V. L. Pokrovskii, *Two-Dimensional Crystals* [in Russian], Naukova Dumka, Kiev (1988).

[9] P. S. Landa and V. F. Marchenko, Usp. Fiz. Nauk **161**, 201 (1991) [Sov. Phys. Usp. **34**, 830 (1991)].
[10] A. S. Kovalev, O. V. Usatenko, and A. V. Gorbach, Fiz. Tekh. Tela (St. Petersburg) [in press].
[11] A. S. Kovalev, O. V. Usatenko, and A. V. Gorbach (submitted to Phys. Rev. E).
[12] A. M. Kosevich and A. S. Kovalev, *Introduction to Nonlinear Physical Mechanics* [in Russian], Naukova Dumka, Kiev (1989).
[13] A. S. Kovalev, O. V. Usatenko, and A. V. Gorbatch, Phys. Rev. E **60**, 2309 (1999)

Translated by Steve Torstveit

Low-temperature control of nanoscale molecular dynamics

P. Hyldgaard*

Department of Applied Physics, Chalmers University of Technology and Göteborg University, S-412 96 Göteborg, Sweden

(Submitted February 23, 2001)
Fiz. Nizk. Temp. **27**, 793–798 (July 2001)

A novel *in situ* probe of the nanoscale molecular dynamics of organic-molecule and fullerene-tube nanostructures is proposed. General and consistent results for the nonlinear-current coupling to the nanostructure excitations are presented to document a frequency-selective electrostatic control of this current stimulation and optimal operation as a local source of current-induced molecular excitations Ω_i. The control is possible for temperatures $T \ll \Omega_i$. Finally, it is explained in detail how Raman measurements of this molecular dynamics would probe the nanoscale excitations within organic and fullerene nanostructures under nonlinear transport conditions. © *2001 American Institute of Physics.* [DOI: 10.1063/1.1388425]

A successful future molecular-electronics technology requires an understanding of the fascinating nanoscale molecular devices themselves, of their nonlinear and interacting transport properties, and of the current-induced molecular dynamics. Fullerene tubes (nanotubes)[1] and organic molecules,[2] which assemble between metal contacts to form organic nanostructures, offer interesting candidates for such a molecular-transport program. These organic nanostructures and the fullerene tubes implement, for example, the molecule resonant-tunneling diode,[3] the single-Bucky-ball (C_{60}) transistor,[4] and the nanotube field-effect transistor,[5] which achieves room-temperature operation and a nanoscale feature size in all but the transport direction. Fullerene-tube heterostructures can be identified by experimentally observed kinks[6] and permit one to create additional nanoscale molecular-electronic devices by combining sections of different local chirality[7] and thus a different nature of electron conduction.[8] The experimental selection of single-kink heterojunctions produce the nanotube equivalent of current-rectifying diodes.[6] A corresponding selection,[6] and/or proposed engineering,[9] of double-kink nanotube samples produces either the nanotube quantum dot[10] or the robust, i.e., temperature- and scattering-insensitive, nanotube resonant-tunneling transistor,[11] which achieves a nanoscale feature size in all dimensions. Nanostructure device robustness is of central importance as, e.g., experiments on single-Bucky-ball transistors[4] and on current-induced atom/molecule manipulation,[12] document significant molecular excitation induced by the nonlinear transport.[13] The coupling to this molecular excitation can even provide novel transport mechanisms as in the electron shuttle.[14] A molecular-electronics program must characterize devices both in terms of the nonlinear molecular current and in terms of the nonlinear-transport coupling to the molecule-structural dynamics—the molecular excitation.

Here I document frequency-selective electrostatic control of the current-induced molecular excitations and propose a probe of this local nanostructure dynamics. The control and suggested molecular probe work for characteristic excitation frequencies $\Omega_i = \Omega_{0,1,\ldots}$ that are larger than the temperatures T and would operate at the relevant nonequilibrium device condition, i.e., with the nonlinear transistor current enabled. For use in the molecular-dynamics probe, I furthermore detail the optimal operation as a strong frequency-selective source of current-induced molecular excitations at the large frequencies $\Omega_i \gg T_{\text{room}}$ that characterize the local fullerene-tube nanostructure dynamics.[15] The suggested nanostructure probe extends an earlier proposal by Narayanamurti[16] that used a burst of incoherent (acoustic) phonons to identify and map defects deep inside semiconductor heterostructures. Here, instead, I propose (1) to exploit the nonlinear nanostructure transport conditions for a direct *in situ* and controlled excitation of the relevant high-energy vibrations $\Omega_i - \Omega_{0,1,\ldots}$ and (2) to use surface-enhanced Raman spectroscopy[15,17] to measure the resulting molecular excitation $\delta N_{\text{vib}}(\Omega_i)$, establish the associated decay $1/\tau_i$, and thus probe the density of material defects,[16] the mutual coupling between such vibrations, and the intrinsic nature of the excitation (phonon) propagation.[18,19]

Figure 1 illustrates a pair of resonant-tunneling systems that could produce a strong source of molecular excitations

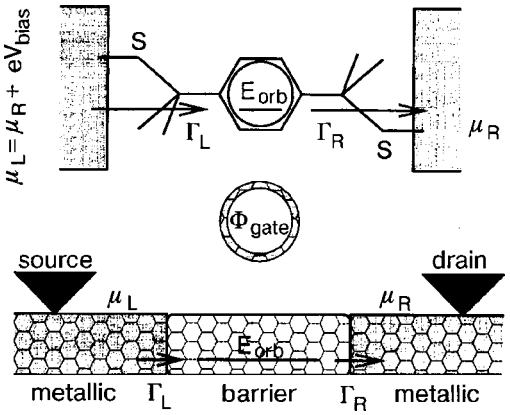

FIG. 1. Schematics of transport and local vibration-source realizations as organic resonant-tunneling nanoparticle (top panel) or as resonant-tunneling nanotube heterostructure (bottom panel). A metal gate (gray ring) at voltage Φ_{gate} controls the current and molecular excitation in either nanostructures by adjusting the resonant-level energy position $E_{\text{orb}}(\Phi_{\text{gate}})$.

and hence the proposed nanostructure-dynamics probe. The upper scheme involves an organic nanostructure[3] (ORTN)—an organic molecule assembled between and connected both mechanically and electrically to the source and drain metal contact through the synthesisized inclusion of sulphur atoms *S*. The lower scheme involves a double-kink nanotube resonant-tunneling heterostructure (NRTH),[11] in which metallic nanotube leads (gray tubes) connect to the metal contacts (wedges), e.g., scanning-tunneling microscope tips. In both schemes the central barrier region traps a single resonant level having energy $E_{\rm orb}$ and connected by tunneling rates $\Gamma_{L/R}$ to the surrounding metal leads or contacts. A close metal gate, e.g., another metallic nanotube (gray ring at potential $\Phi_{\rm gate}$) adjusts $E_{\rm orb}(\Phi_{\rm gate})$ and enables a gate-controlled resonant-tunneling transport.[4,11,20,21]

The proposed nanostructure-dynamics probe exploits this gate control of the nanostructure tunneling transport by a selective optimization of the current-induced molecule stimulation. To document the suggested operation, this paper (i) provides a conserving nonequilibrium Green function calculation[13,22] of the current-induced spontaneous emission (net absorption) rates $R_{\rm sp}(E_{\rm orb};\Omega_i)$ $[R_{\rm ab}(E_{\rm orb};\Omega_i)]$ as a function of $E_{\rm orb}(\Phi_{\rm gate})$ and at a set of characteristic excitation frequencies; (ii) details how phase-space restrictions that rest on the Pauli exclusion principle permit a frequency-selective gate control of $R_{\rm sp,ab}(E_{\rm orb};\Omega_i)$; and (iii) identifies nonequilibrium tunneling conditions that can maximize and/or inhibit the resulting effective current excitation $\delta N_{\rm vib}(\Omega_i)$. At a given gate voltage and thus resonant-energy position $E_{\rm orb}(\Phi_{\rm gate})$, they determine an excess nanostructure vibrational population:[23]

$$\frac{1}{\tau_i}\,\delta N_{\rm vib}(E_{\rm orb}(\Phi_{\rm gate});\Omega_i) = [R_{\rm sp}(E_{\rm orb};\Omega_i) - R_{\rm ab}(E_{\rm orb};\Omega_i)\,\delta N_{\rm vib}(E_{\rm orb}(\Phi_{\rm gate});\Omega_i)]. \tag{1}$$

The local electrostatic-field control $E_{\rm orb}(\Phi_{\rm gate})$ (Refs. 4, 11, and 20) can, for example, produce a strong (frequency-selective) burst of nanostructure excitations $\delta N_{\rm vib}(\Omega_0)$. Simultaneous Raman measurements[15] of the strength of the anti-Stokes Raman signal at nanostructure-vibration frequency Ω_0 can thus determine the decay $1/\tau_0$ of this excess population[17] $\delta N_{\rm vib}(\Omega_0)$ and probe intrinsic mechanisms[16,18,19] affecting the nanoscale molecular dynamics.

Electrostatic control of resonant-tunneling transport

A theoretical description of the electrostatic gate control $E_{\rm orb}(\Phi_{\rm gate})$ exists for both the organic nanostructure[20] and the fullerene heterostructure[11] scheme (Fig. 1, upper and lower schemes). In both transport schemes this local electrostatic control permits current-switch and transistor effects[4,11,20] in which transport is focused onto a single molecular level. Such nanostructure transistors improve the semiconductor resonant-tunneling transistor design[21] through a dramatic miniaturization to nanoscale dimensions. For a calculation of the noninteracting resonant-tunneling transport in an organic-nanostructure transistor, refer to the analysis in Ref. 20. For a nonequilibrium Green function[13,22] calculation of the interacting transport in the nanotube heterostructure transistor (Fig. 1, lower scheme) refer to Ref. 11. Before reporting calculations of gate control in the current-induced molecular excitation, however, I summarize the description of the important tunneling-transport mechanisms.[11,20]

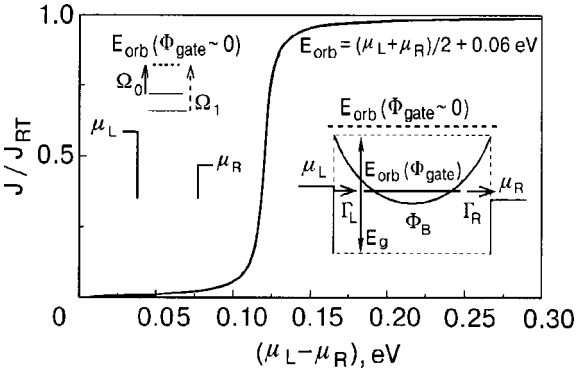

FIG. 2. Gate control of nonequilibrium resonant-tunneling current $J < J_{RT}$. The inset panels contrast transport conditions at (i) $\Phi_{\rm gate}\sim 0$, when the molecular gap E_g forces a resonance-level energy position $E_{\rm orb}(\Phi_{\rm gate}\sim 0)$ (dashed line in right inset) and vibration satellites $E_{\rm orb}(\Phi_{\rm gate}\sim 0) - \Omega_{0,1}$ (left inset) far above the lead chemical potentials $\mu_{L/R}$; and at (ii) $\Phi_{\rm gate}\sim 2$ V, when the adjusted electron potential Φ_B (solid curve in right inset) positions $E_{\rm orb}(\Phi_{\rm gate})\approx(\mu_L+\mu_R)/2$ (solid line). The main panel assumes such a fixed $E_{\rm orb}(\Phi_{\rm gate})$; a moderate bias $\mu_L-\mu_R\approx 0.3$ eV then saturates the current $J\approx J_{RT}$.

Figure 2 illustrates the electrostatic-gate effects on the nonlinear resonant-tunneling current. A finite applied bias $eV_{\rm bias}$ maintains the left and the right metallic-nanotube leads at the different chemical potentials μ_L and $\mu_R=\mu_L - eV_{\rm bias}$, respectively. The main panel in Fig. 2 assumes that a finite gate voltage $\Phi_{\rm gate}$ maintains a fixed resonant-level position $E_{\rm orb}(\Phi_{\rm gate})=(\mu_L+\mu_R)/2+0.06$ eV, and it documents how the application of a moderate bias can then saturate a significant resonant-tunneling current

$$eJ < eJ_{RT} = e\left(\frac{4\Gamma_L\Gamma_R}{\Gamma_L+\Gamma_R}\right) - \begin{cases} 1 \text{ nA for ORTN,} \\ 5\ \mu\text{A for NRTH.} \end{cases} \tag{2}$$

The current is characterized by the resonance width $\Gamma = \Gamma_L+\Gamma_R$. At low temperatures this tunneling current[13,22,24]

$$J[E_{\rm orb}(\Phi_{\rm gate});\mu_{L/R}] - J_{RT}[P_{\rm occ}^{\mu_L}(E_{\rm orb}) - P_{\rm occ}^{\mu_R}(E_{\rm orb})] \tag{3}$$

results as a difference between contributions

$$P_{\rm occ}^{\mu}(E_{\rm orb}) = \left[\frac{1}{2} + \frac{1}{\pi}\arctan\left(\frac{\mu - E_{\rm orb}}{\Gamma}\right)\right] \tag{4}$$

evaluated at $\mu=\mu_L$ and μ_R, respectively. I focus on the NRTH transport realizations where it is possible to achieve $\Gamma\sim 10$ meV.[11]

The pair of inset diagrams illustrate the gate operation and contrast the transport conditions in the absence and presence of a finite voltage $\Phi_{\rm gate}$ applied to the metal gate. At $\Phi_{\rm gate}\sim 0$ (left inset) the molecular gap E_g ($\gtrsim 1$ eV for the previously investigated NRTH transistor[11]) forces a resonance-level energy position $E_{\rm orb}(\Phi_{\rm gate}\sim 0)\approx \mu_L + E_g/2$ (dashed line in right inset). No current results, since both $E_{\rm orb}$ and the vibration satellites[13] $E_{\rm orb}(\Phi_{\rm gate}\sim 0)-\Omega_{i=0,1,\ldots}$ remain far above the chemical potentials of the leads. However, a voltage $\Phi_{\rm gate}\sim 2$ V suppresses the electron potential

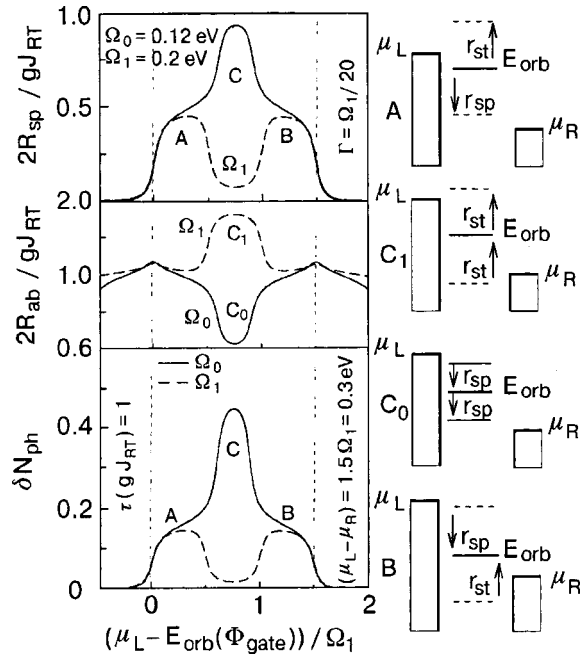

FIG. 3. Frequency selective current stimulation of molecular vibrations. The left-most top and middle panels contrast the gate variation of the spontaneous phonon emission rate R_{sp} and net absorption rate R_{ab} at two frequencies $\Omega_{0,1}$. Both rates are proportional to J_{RT} and the electron–vibration coupling constant g. The gate variation is implicit and defined through $E_{orb}(\Phi_{gate})$. The set of four right-most schematics illustrates the Pauli exclusion mechanism responsible for the frequency-selective control. The set of downward (upward) arrows labeled by $r_{sp}(r_{ab})$ identify inelastic tunneling events that contribute to the spontaneous emission (to the net stimulated absorption). Finally, the left-most bottom panel contrasts the current-induced increase in excitation level $\delta N_{vib}(\Omega_0)$ (solid curve) and $\delta N_{vib}(\Omega_0)$ (dashed curve) for a given intrinsic vibration decay time τ.

Φ_B (solid curve, right inset) within the fullerene barrier and adjusts the resonance-level position $E_{orb}(\Phi_{gate}) \approx (\mu_L + \mu_R)/2$ (solid line) to enable the tunneling processes (arrows). Below, I assume a fixed bias $eV_{bias} = 300$ meV and use the resonant-level gate control $E_{orb}(\Phi_{gate})$ also to optimize the current stimulation of molecular excitations.

The molecular excitations

For the NRTH it is relevant to consider current-induced excitation at energies $\Omega_i = 100-200$ meV (800–1600 cm^{-1}).[15] I concentrate on a pair of high-energy modes, at assumed frequencies $\Omega_{1(0)} = 200$ meV (120 meV) $\gg \Gamma$ and describe the current stimulation at zero temperature to illustrate my results and predictions.

The top and middle panels in Fig. 3 contrast the independent gate-voltage control of the electron-vibration interaction effects in R_{sp} and R_{ab} for a pair of vibration energies Ω_0 (solid curve) and Ω_1 (dashed curve). The gate control is implicit as the gate voltage Φ_{gate} adjusts the resonant level energy position $E_{orb}(\Phi_{gate}) - \mu_L$. The fixed applied bias satisfies $2\Omega_1 > eV_{bias} > 2\Omega_0$ and $eV_{bias} > \Omega_1$. The documented current-excitation gate control arises within the region $\mu_L > E_{orb} > \mu_R$ (identified by vertical lines), where the electrostatic gate enables a strong resonant-tunneling current, Eq. (3). The excitation transition rates are illustrated for equal electron tunneling rates $\Gamma_L = \Gamma_R$.

I determine the magnitude and gate dependence of the current-induced molecular-excitation transition rates R_{sp} and R_{ab} through a separate nonequilibrium Green function calculation similar to that for the nonequilibrium defluctuations (shot noise).[25] The calculation involves a determination of the nonequilibrium density-correlation components:

$$\Pi_r^0(\omega) = -i\int_0^\infty dt' \exp(i\omega t')\langle[n(t+t')n(t)]\rangle, \tag{5}$$

$$\Pi_<^0(\omega) = -\int_{-\infty}^\infty dt' \exp(i\omega t')\langle n(t+t')n(t)\rangle, \tag{6}$$

where n denotes the electron density at the resonance and where the notations and conventions introduced in Ref. 13 are followed. The retarded correlation component includes a commutator [.,.] and defines the frequency shift[13] and vibration decay[26] due to the electron–vibration (phonon) interaction. Here I evaluate both components (5), (6) out of equilibrium to establish the current-induced excitation level, Eq. (1).

The spontaneous vibration emission rate R_{sp} is to lowest order in the dimensionless electron–vibration coupling strength g,[13] given by the $<$ correlation component, Eq. (6). The rate is proportional to J_{RT} but limited by the availability of phase space:[27]

$$\begin{aligned}\frac{R_{sp}[E_{orb}(\Phi_{gate});\Omega_i]}{gJ_{RT}} &= \frac{[-\Omega^2\Pi_<^0(\Omega_i)/2]}{J_{RT}} \\ &= \frac{\Theta(\mu_L-\mu_R-\Omega_i)\Omega_i^2}{4(\Omega_i^2+4\Gamma^2)} \\ &\quad\times[\Delta P_{occ}(E_{orb};\Omega_i)+\Delta P_{log}(E_{orb};\Omega_i)].\end{aligned} \tag{7}$$

A significant variation and structure arises in the vibration emission (7) when $\Omega_i \gg \Gamma$, a condition relevant for the local molecular modes of the NRTH. The spontaneous vibration emission is then dominated by the simple phase-space measure

$$\begin{aligned}\Delta P_{occ}(E_{orb};\Omega_i) &= [P_{occ}^{\mu_L}(E_{orb}) - P_{occ}^{\mu_R}(E_{orb}-\Omega_i)] \\ &\quad + [P_{occ}^{\mu_L}(E_{orb}+\Omega_i) - P_{occ}^{\mu_R}(E_{orb})],\end{aligned} \tag{8}$$

while the logarithmic correction term ΔP_{log} can be ignored.[28] The phase-space measure (8) is specified by the nonequilibrium contributions (4) at the resonance level and at the vibration satellites $E_{orb} \pm \Omega$.

The net vibration absorption at $\Omega_i \gg \Gamma$ is given by[29]

$$\begin{aligned}\frac{R_{ab}[E_{orb}(\Phi_{gate});\Omega_i]}{gJ_{RT}} &= \frac{\Omega^2[-\mathrm{Im}\,\Pi_r^0(\Omega_i)]}{J_{RT}} \\ &\approx \frac{\Gamma\Omega_i^2}{4(\Omega_i^2+4\Gamma^2)}(\Gamma_R^{-1}[P_{occ}^{\mu_L}(E_{orb}-\Omega_i) - P_{occ}^{\mu_L}(E_{orb}+\Omega_i)] \\ &\quad + \Gamma_L^{-1}[P_{occ}^{\mu_R}(E_{orb}-\Omega_i) - P_{occ}^{\mu_R}(E_{orb}+\Omega_i)]).\end{aligned} \tag{9}$$

This rate is defined by a phase-space measure which, in contrast to Eq. (8), involves differences of contributions, Eq. (4), evaluated at the *same* chemical potential (at μ_L or μ_R). Thus it is possible to achieve an important independent control of $R_{sp}[E_{orb}(\Phi_{gate});\Omega_i]$ and $R_{ab}[E_{orb}(\Phi_{gate});\Omega_i]$.

The Pauli exclusion principle explains the phase-space limitations on the current-induced spontaneous and net absorption, Eqs. (8) and (9). The four right-most panels, *A*, C_0, C_1, and *B*, in Fig. 3 illustrate the set of different transport conditions (all with $J \sim J_{RT}$) which characterize the gate-control regimes identified in the left set of panels.

The presence of downward arrows r_{sp} identifies conditions when the current flow can stimulate a spontaneous vibration emission, as specified by the phase-space measure, Eq. (8). In region *A* (*B*) this emission arises when an electron tunnels into E_{orb} (into $E_{orb}+\Omega_{i=0,1}$) but leaves at energy $E_{orb}-\Omega_{i=0,1}$ (at E_{orb}). For an applied bias which satisfies $2\Omega_1 > eV_{bias} > \Omega_1$ (panel C_1) neither type-*A* nor type-*B* vibration-emission processes are possible for local mode Ω_1. However, both types of spontaneous emission processes remain possible for a vibrational mode at $\Omega_0 < eV_{bias}/2$ (panel C_0).

The presence of upward arrows r_{ab} instead identifies conditions for a net current-induced absorption $R_{ab} \neq 0$. In section *A* (*B*) a net absorption arises, when the electron enters at E_{orb} (at $E_{orb}-\Omega_{i=0,1}$) but leaves at $E_{orb}+\Omega_{0,1}$ (at E_{orb}). Tuning E_{orb} to the central region *C* causes an enhanced absorption for mode Ω_1, as both type-*A* and type-*B* absorption processes become possible (panel C_1). However, for the lower mode at $\Omega_0 < eV_{bias}/2$, I find an effective cancellation (panel C_0) as the energies E_{orb} and $E_{orb} \pm \Omega_0$ all carry a partial electron occupation and thus produce a vanishing net absorption rate, $R_{ab} \to 0$.

Frequency-selective molecular-vibration stimulation

The lower-left panel in Fig. 3 documents how an optimization of current-induced molecular excitation is possible. The panel contrasts the calculated gate-variation of the increase in the molecular excitation level, Eq. (1), $\delta N_{vib}(\Omega_0)$ and $\delta N_{vib}(\Omega_1)$, and details methods to enhance the current stimulation of mode Ω_0 at the expense of mode $\Omega_1 > \Omega_0$. Such selective excitation is possible even when $eV_{bias} > \Omega_1 \gg \Gamma$, and arises when $2\Omega_1 > eV_{bias} > 2\Omega_0$ and E_{orb} is tuned to region $C(E_{orb} \approx (\mu_L + \mu_R)/2)$. These nonequilibrium transport conditions simultaneously minimize $R_{st}(\Omega_1)$ towards zero and maximize the ratio $R_{st}(\Omega_0)/R_{ab}(\Omega_0)$ to extinguish $\delta N_{vib}(\Omega_1)$ and dramatically enhance the lower-frequency current stimulation $\delta N_{vib}(\Omega_0)$.

The molecular-dynamics source and probe

The lower-left panel in Fig. 3 also details the suggested operation as a molecular-excitation source. The panel documents a crisp electrostatic gate control for the current stimulation $\delta N_{vib}(\Omega_1)$ which arises through an adjustment of the resonant-level energy position $E_{orb}(\Phi_{gate})$.[11] This implicit gate control permits a switch between enabling and disabling the current stimulation (1). Such operation can produce a frequency-selective molecular-vibration source and even a strong nonequilibrium burst $\delta N_{vib}(\Omega_0) \gg 0$ of high-energy nanostructure vibrations.

Nanoscale molecular-dynamics probing is then possible with simultaneous Raman measurements of the anti-Stokes signal at Ω_0, because the anti-Stokes strength is directly sensitive[17] to the excess molecular-excitation burst $\delta N_{vib}(\Omega_0) \gg 0$. Such Raman measurements can, through Eq. (1), determine the decay $1/\tau_i$ that characterize these nanostructure molecular excitations and thus probe mechanisms[16,18,19] which help determine the intrinsic nanoscale molecular dynamics. The suggested *in situ* molecular-dynamics probe could implement an important strong test of our theoretical descriptions for both the nanostructure atomic configurations[10,11,30] and for the current-induced structural dynamics.[4,12–14]

In summary, I have suggested a novel *in situ* probe of the nanoscale molecular dynamics of organic-molecule and fullerene-tube heterostructures. General nonequilibrium Green function results for the current coupling to local nanostructure excitations were presented to document a frequency-selective electrostatic control and optimal operation as a necessary current-excitation source. Raman measurements of the anti-Stokes signal can then permit an *in situ* probe of the local nanostructure molecular dynamics at nonequilibrium conditions.

I thank R. Shekhter, B. I. Lundqvist, M. Persson, and M. Jonson for valuable discussions. Financial support from the Swedish Foundation for Strategic Research (SSF), through the Materials Consortium No. 9, is gratefully acknowledged.

*E-mail: hyldgaar@fy.chalmers.se

[1] S. Iijima, P. M. Ajayan, and T. Ichihashi, Phys. Rev. Lett. **69**, 3100 (1992); C. Dekker, Phys. Today **52**(5), 22 (1999).
[2] See, e.g., C. Zhou, M. R. Deshpande, M. A. Reed, L. Jones II, and J. M. Tour, Appl. Phys. Lett. **71**, 611 (1997); L. Jones II, D. L. Pearson, J. S. Schumm, and J. M. Tour, Pure Appl. Chem. **68**, 145 (1996); J. M. Tour, Chem. Rev. **96**, 537 (1996).
[3] J. Chen, M. A. Reed, A. M. Rawlett, and J. M. Tour, Science **286**, 1550 (1999).
[4] H. Park, J. Park, A. K. L. Lim, E. H. Anderson, A. P. Alivisatos, and P. L. McEuen, Nature (London) **407**, 57 (2000).
[5] S. J. Tans, A. R. M. Verschueren, and C. Dekker, Nature (London) **393**, 49 (1998).
[6] Z. Yao, H. W. C. Postma, L. Balents, and C. Dekker, Nature (London) **402**, 273 (1999); Article supplement in *Nature's* archive documents observation and wiring/measurement of also double-kink nanotube heterostructures.
[7] R. Saito, M. Fujita, G. Dresselhaus, and M. S. Dresselhaus, Phys. Rev. B **46**, 1804 (1992).
[8] C. T. White and J. W. Mintmire, Nature (London) **394**, 30 (1998).
[9] D. Orlikowski, M. B. Nardelli, J. Bernholc, and C. Roland, Phys. Rev. Lett. **83**, 4132 (1999).
[10] L. Chico, M. P. L. Sancho, and M. C. Múñoz, Phys. Rev. Lett. **81**, 1278 (1998).
[11] P. Hyldgaard and B. I. Lundqvist, Solid State Commun. **116**, 569 (2000).
[12] B. C. Stipe, M. A. Rezaei, W. Ho, S. Gao, M. Persson, and B. I. Lundqvist, Phys. Rev. Lett. **78**, 4410 (1997).
[13] P. Hyldgaard, S. Hershfield, J. H. Davies, and J. W. Wilkins, Annals of Physics **236**, 1 (1994); J. H. Davies, S. Hershfield, P. Hyldgaard, and J. W. Wilkins, Phys. Rev. B **47**, 4603 (1993).
[14] L. Y. Gorelik, A. Isacsson, M. V. Voinova, B. Kasemo, R. I. Shekhter, and M. Jonson, Phys. Rev. Lett. **80**, 4526 (1998).
[15] K. Kneipp, H. Kneipp, P. Corio, S. D. M. Brown, K. Shafer, J. Motz, L. T.

Perelman, E. B. Hanlon, A. Marucci, G. Dresselhaus, and M. S. Dresselhaus, Phys. Rev. Lett. **84**, 3470 (2000); K. Kneipp, Y. Wang, H. Kneipp, L. T. Perelman, I. Itzkan, R. R. Dasari, and M. S. Feld, *ibid.* **78**, 1667 (1997).
[16] V. Narayanamurti, Science **213**, 717 (1981).
[17] A. Yariv, *Quantum Electronics*, John Wiley & Sons, New York (1989), pp. 453–475; K. Kneipp, Y. Wang, H. Kneipp, I. Itzkan, R. R. Dasari, and M. S. Feld, Phys. Rev. Lett. **76**, 2444 (1996).
[18] S. G. Walkauskas, D. A. Broido, K. Kempa, and T. L. Reinecke, J. Appl. Phys. **85**, 2579 (1999); P. Hyldgaard and G. D. Mahan, *Thermal Conductivity* **23**, Technomic Publishing Company, Inc., Lancaster, Pennsylvania (1996), p. 172.
[19] P. Hyldgaard and G. D. Mahan, Phys. Rev. B **56**, 10754 (1997).
[20] M. Di Ventra, S. T. Pantelides, and N. D. Lang, Appl. Phys. Lett. **76**, 3448 (2000).
[21] M. A. Reed, W. R. Frensley, R. J. Matyi, J. N. Randall, and A. C. Seabaugh, Appl. Phys. Lett. **54**, 1034 (1989).
[22] S. Hershfield, J. H. Davies, and J. W. Wilkins, Phys. Rev. Lett. **67**, 3720 (1991); D. C. Langreth, in *1975 NATO Advanced Study Institute on Linear and Nonlinear Electron Transport in Solids*, Antwerp, 1975, Vol. B17, Plenum, New York (1976), p. 3.
[23] Our results apply to linear order in the current and describe the stimulation of local high-energy nanostructure vibrations. Cases where the tunneling rate coincides with standing-wave resonances requires a treatment of nonlinear excitation effect also; see, e.g., Ref. 12.
[24] R. Tsu and L. Esaki, Appl. Phys. Lett. **22**, 562 (1973); M. Büttiker, Phys. Rev. Lett. **57**, 1761 (1986).
[25] J. W. Wilkins, S. Hershfield, J. H. Davies, P. Hyldgaard, and C. J. Stanton, Phys. Scr. T **42**, 115 (1992); S. Hershfield, Phys. Rev. B **46**, 7061 (1992); P. Hyldgaard and S. Hershfield (unpublished).
[26] B. Hellsing and M. Persson, Phys. Scr. **29**, 360 (1984).
[27] The rate R_{sp} is just the excitation increase, $\delta N_{ph}=\delta\langle b^+ b\rangle$, as one enables the current–vibration coupling, $g>0$. I introduce $A_0(\omega)\equiv(2\tau_i)/[1+\tau^2(\omega-\Omega_i)^2]$ as the unperturbed vibration spectral function and find, to lowest order in g, the current stimulation $2\delta N_{ph}\approx g\Omega_i^2\int\Pi^0_<(\omega)A_0(\omega)d\omega$. The result Eq. (7) applies for $\tau_i^{-1}\ll\Gamma$.
[28] The logarithmic correction to the phase-space measure is given by $\Delta P_{log}(E_{orb};\Omega_i)=(\Gamma/\pi\Omega_i)\Sigma_{\alpha=1,2}\ln(\Delta_\alpha^2+\Gamma^2)-(\Gamma/\pi\Omega_i)\Sigma_{x=L,R}\ln[(\mu_X-E_{orb})^2+\Gamma^2]$, where $\Delta_{1(2)}=(\mu_{L(R)}-E_{orb}-(+)\Omega_i)$; The prefactor $(\Gamma/\pi\Omega_i)$ ensures a smooth behavior at general Γ/Ω_i and a vanishing one, $\Delta P_{log}\to 0$ at $\Gamma\ll\Omega_i$.
[29] A small logarithmic correction to R_{ab} is given through the full nonequilibrium determination of $\Pi^0_r(\omega)$.[13] I stress that $-\mathrm{Im}\,\Pi^0_r\geqslant 0$ and that single-resonance tunneling never produces coherent emission.
[30] See, e.g., J. M. Seminario, A. G. Zacarias, and J. M. Tour, J. Amer. Chem. Soc. **120**, 3970 (1998); A. Rubio, D. Sánchez-Portal, E. Artacho, P. Ordejón, and J. M. Soler, Phys. Rev. Lett. **82**, 3520 (1999).

This article was published in English in the original Russian journal. Reproduced here with stylistic changes by AIP.

ULTRALOW-TEMPERATURE TECHNIQUE

Automated unit for physical research on quantum crystals at millikelvin temperatures

A. N. Ganshin, V. N. Grigor'ev, V. A. Maĭdanoy, G. A. Mikhaĭlov,† V. A. Mikheev, N. F. Omelaenko, A. A. Penzev, V. N. Repin, E. Ya. Rudavskiĭ,* A. S. Rybalko, Yu. A. Tokar',† and V. A. Shilin

B. Verkin Institute for Low Temperature Physics and Engineering, National Academy of Sciences of Ukraine, pr. Lenina 47, 61103 Kharkov, Ukraine
(Submitted February 13, 2001)
Fiz. Nizk. Temp. **27**, 799–810 (July 2001)

A cryogenic unit designed for physical research on quantum crystals at ultralow temperatures is described. The unit includes a dilution refrigerator with a hybrid ^{3}He circulation system, an antivibration protection system, and a system of automated control and data acquisition and processing. The construction of the basic units, the thermometry system, the algorithms for measurements, and the software for conducting research on quantum crystals by the method of precision pressure measurements are described. The unit may be used for performing a wide range of tasks in research on various condensed systems at millikelvin temperatures.
 [DOI: 10.1063/1.1388426]

INTRODUCTION

Dilution refrigerators are now the most widely used ultralow-temperature apparatus in laboratory practice. Proposed in Ref. 1, this method of cooling, based on the use of the heat of mixing of two helium isotopes, provides a high cooling capacity and the capability of reaching ultralow temperatures and maintaining them for arbitrarily long times.

This method was first implemented successfully in 1966[2] in a refrigerator scheme with an external cycle of ^{3}He circulation that has become the most commonly used in cryogenics laboratories. A typical drawback of this type of refrigerator is the need for cumbersome evacuation lines in the circulation system and also the need for special measures to keep the cryostat free of oil or mercury vapor from the pumps. Furthermore, the boiling of the working liquid in the pumps causes additional vibrations, which are undesirable when the dilution refrigerator is used in nuclear demagnetization cryostats. These drawbacks are eliminated in refrigerators with a cryogenic ^{3}He circulation cycle using condensation or adsorption pumps. Different versions of such refrigerators are described in Refs. 3–8.

The primary advantage of a cryogenic circulation cycle lies in the use of ''sterile'' pumping, which reduces the chance of blockage of the capillaries and throttle by various impurities that could enter the ^{3}He circulation system. At the same time, implementation of a cryogenic cycle requires either an additional ^{3}He system (if condensation pumps are used) or reliably operating cryogenic valves (if the circulation is effected by adsorption pumps). The cyclic regeneration of adsorption pumps in refrigerators with adsorption pumping also leads to a greater expenditure of liquid helium.

It therefore looked promising to design a refrigerator that would combine the advantages of both a cryogenic cycle and external circulation of ^{3}He. In the this paper we discuss the design and present the basic characteristics of an ^{3}He–^{4}He dilution refrigerator which, depending on the experimental conditions, can employ either an external ^{3}He cycle or a cryogenic cycle. The dilution refrigerator described is a component of a cryogenic unit for physical research at ultralow temperatures. It is planned that this refrigerator will be supplemented by a nuclear demagnetization stage, and we have therefore taken special measures to protect against possible vibrations and rf noise. The unit is equipped with a system of automated data acquisition and processing, and the automation system is designed with provisions for the use of some manually controlled devices.

The unit was put into service for conducting experimental research on quantum crystals—in particular, ^{3}He–^{4}He solid solutions—by means of precision measurements of the pressure in the sample. Therefore the instrumentation part, the algorithms, and the software are described in terms of particular examples of physical problems that have been addressed in those studies. It should be noted, however, that the unit described can be used to perform a wide range of tasks arising in the study of various condensed systems at ultralow temperatures.

1. SYSTEM OF PROTECTION FROM VIBRATIONS AND ELECTROMAGNETIC RADIATION

To reduce vibrations the apparatus is mounted in a special annex constructed with large concrete blocks and not connected to the foundation or walls of the main building. The main element of vibration protection[9] is a one-and-a-half metric ton platform to which the cryostat is secured. The platform and cryostat are suspended on eight hemp ropes 6 m long to channel-iron beams beneath the ceiling. The load on the platform is chosen so that the resonance frequency of vertical vibrations

$$f_{\text{vert}}=\frac{1}{2}\pi\sqrt{K/M} \tag{1}$$

does not coincide with any of the main sources of vibrations. Here K is the stiffness of the rope and M is the mass of the platform. Special measurements showed that f_{vert} is 6.5 Hz, in agreement with the calculation by formula (1).[9] Of course, this frequency can be lowered by increasing the mass of the platform.

The surface velocity of horizontal vibrations is given by the formula for an ideal pendulum,

$$f_{\text{hor}}=\frac{1}{2}\sqrt{g/L}, \tag{2}$$

where L is the length of the rope, and g is the acceleration of gravity. The measured value $f_{\text{hor}}=0.25$ Hz, in good agreement with the value obtained by a calculation using formula (2).

The amplitudes of the vibrations of the platform were measured using an accelerometer[10] for two positions of the platform — suspended on ropes, and arrested (resting on special supports). The main sources of vibrations at frequencies above 10 Hz were the compressors of the liquefying room, located ~ 100 m away. It was found that the amplitude of the vibrations of the platform in the suspended state were reduced by a factor of 40–50 in comparison with the arrested platform and amounted to 0.01 μm far from resonance and ≈0.2 μm close to resonance. To reduce the vibrations transmitted along the pumping lines, the latter were made with metal sleeves and sylphon bellows isolators.

The need for rf shielding of the device is due to the proximity of a television/radio transmitter. To reduce the rf noise, which would affect the lowest attainable temperature of the refrigerator and the readings of the resistance thermometers used in the device, the laboratory room was shielded by copper sheets 0.3 mm thick. When the room was completely shielded the attenuation of the rf signal at 100 kHz (30-μm skin layer) reached 120 dB.

2. DILUTION REFRIGERATOR WITH A HYBRID CIRCULATION SYSTEM

Figure 1 shows a diagram of the main units and elements of the dilution refrigerator. A nitrogen-free helium cryostat *1* with an inner diameter of 210 mm and a length of the inner vessel 2.4 m had multilayer superinsulation, which provided economy of liquid helium consumption without additional nitrogen cooling.[11] 1 K pot 8 was pumped down by an NVPR-16 forevacuum pump with a capacity of 16 liter/s, and the throttle placed on the inlet tube *6* of the 1 K pot, had a resistance to flow of $2.2\times10^{-10}\,\text{cm}^{-3}$. To prevent its blockage by mechanical impurities in the liquid helium, a filter containing pressed copper powder was placed on the end of inlet tube. The working temperature of the thermal bath is ordinarily 1.2–1.4 K.

The low-temperature part of the dilution refrigerator includes a still *12*, a mixing chamber *19*, and a system of heat exchangers *15* and *17*. The circulating ^{3}He is preliminarily cooled in a copper capillary (inner diameter 1.2 mm, outer diameter 2 mm) helically wound on the shields of the neck of the cryostat and then condensed in a capillary *10* placed inside the 1 K pot. After this the ^{3}He is collected in a collector *9* intended for stabilizing the operation of the refrigerator when the ^{3}He circulation is effected by means of adsorption pumps *2*.

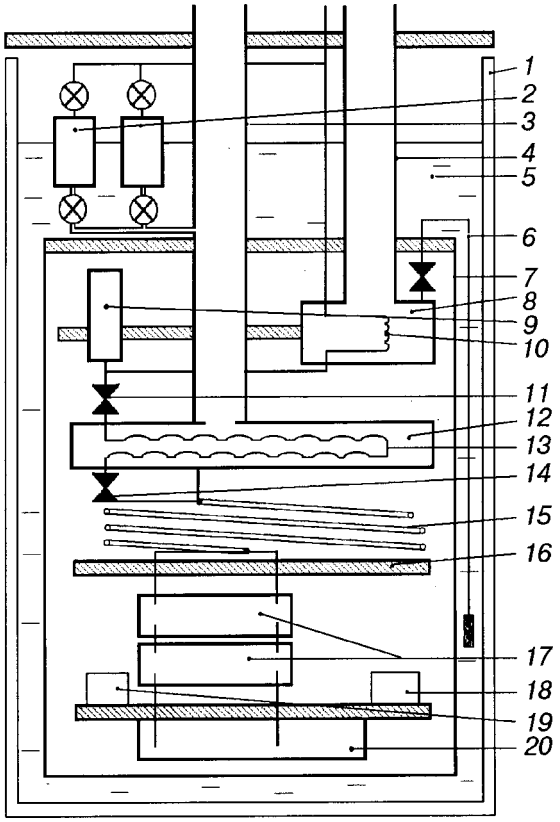

FIG. 1. Diagram of the construction of the dilution refrigerator: *1*—nitrogen-free helium cryostat; *2*—adsorption pumps; *3*—evacuation tube of the still; *4*—evacuation tube of the 1 K pot; *5*—liquid ^{4}He; *6*—filling capillary for the 1 K pot, with a throttle and filter at the end; *7*—vacuum can; *8*—1 K pot; *9*—receptacle; *10*— condenser of the solution; *11*—main throttle; *12*—still; *13*—heat exchanger of the still; *14*—secondary throttle; *15*—continuous-flow heat exchanger; *16*—intermediate plate placed between the continuous-flow and discrete heat exchangers; *17*—discrete heat exchangers; *18*—experimental cell; *19*—melting curve thermometer; *20*—mixing chamber.

The cross section of an absorption pump is illustrated in Fig. 2. For reliable cooling of the adsorbent a plug consisting of alternating copper trays *2* and copper grids *3* is attached to the copper tube *1* with hard solder. The gaps between the trays and grids are filled with the synthetic adsorbent SKM-4. The thickness of a tray with the adsorbent is 3 mm, and the repetition period is 5 mm. The pump is placed in an external vacuum can *4*, and for regeneration of the pump a heater *6* and special drainage tubes are used, analogous to those described in Ref. 7. In this construction the plate holding the adsorbent is in good thermal contact with the liquid helium, and the rate of removal of the heat of absorption provides a circulation of 7×10^{-4} mole/s.

The low-temperature valves of the evacuation line are analogous to the valves used in Ref. 7, except that the return valves are located directly in the liquid helium. The cross section of the return valves is $\sim1^2$ mm.

On leaving the receptacle, the liquid ^{3}He, after passing through the main throttle (*11* in Fig. 1) with a flow resistance of $2\times10^{-11}\,\text{cm}^{-3}$, enters the heat exchanger *13* of the still,

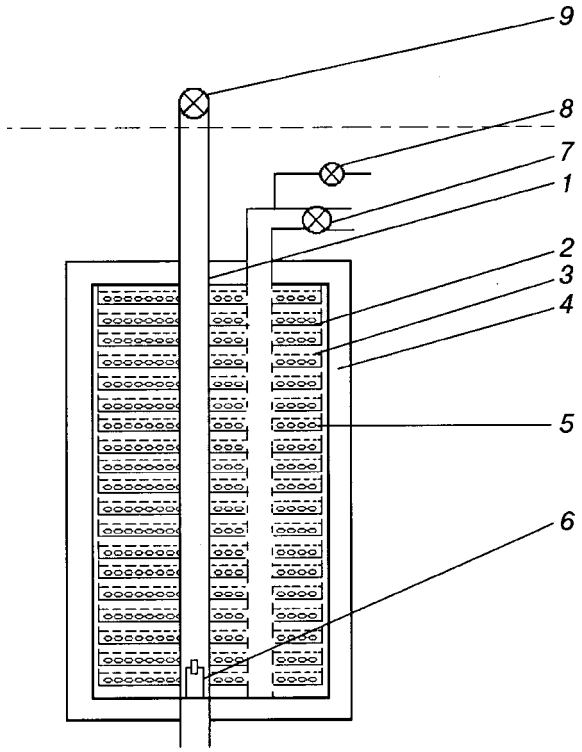

FIG. 2. Diagram of the construction of the adsorption pump: *1*—copper tube containing liquid helium; *2*—tray for adsorbent; *3*—copper grid; *4*—vacuum can; *5*—adsorbent; *6*—heater; *7*—valve for actuation of adsorption pumps; *8*—regeneration valve; *9*—drainage valve.

where its temperature is lowered to 0.7–0.8 K.

The still, with a volume of 240 cm^3, is made of copper. A polished diaphragm 4 mm in diameter is used for suppression of the superfluid film. The return flow from the still, after passing through the secondary throttle *14*, with a flow resistance of $1.8\times10^{-10}\,cm^{-3}$, enters a continuous-flow heat exchanger *15* of the ''coil in tube'' type and a system of discrete heat exchangers *17*. The continuous-flow heat exchanger is a capillary with a diameter of 2 mm and a wall thickness of 0.2 mm, twisted into a coil around a wire 2 mm in diameter and inserted into a tube having a diameter of 6 mm and a wall thickness of 0.3 mm. The dilute phase of the phase-separated ^{3}He–^{4}He liquid solution flows in the space between the tubes, and the concentrated liquid flows in the inner tube. The length of this heat exchanger is 1 m.

Eight discrete heat exchangers *17* were made at the University of Lancaster (U.K.).[12,13] A layer of silver powder with a particle size of 700 Å was baked onto both sides of the 30×75 mm by 0.1 mm thick silver plate of the heat exchanger. The surface area of each side of the plate was $\sim7\ m^2$. Stainless steel tubes for the inlet and outlet of the dilute and concentrated phases were joined to the tops of the heat exchanger with silver solder. The partition between the phases was attached to the tops with POS-61 ''soft'' solder. The diameters of the channels of the heat exchangers varied from 3 to 5 mm on the side with the concentrated phase and from 5 to 12 mm on the side with the dilute phase.

Between the continuous-flow and discrete heat exchangers is a plate *16* with a heat exchanger attached to it. This heat exchanger is a mixture of equal parts copper powder with a particle size of 25 μm and an ultradisperse silver

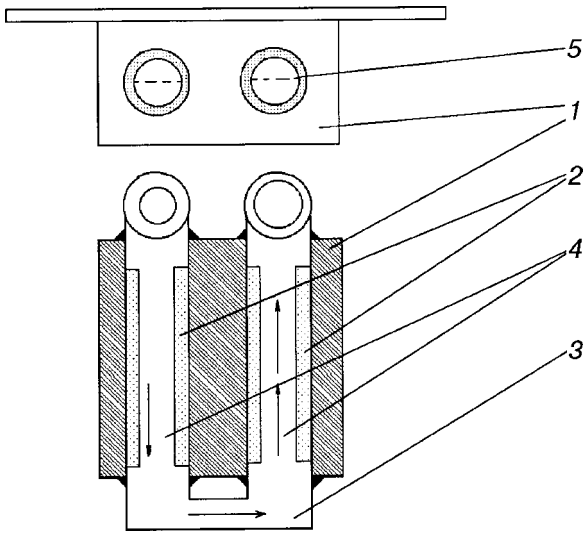

FIG. 3. Diagram of the construction of the mixing chamber: *1*—body of chamber; *2*—heat exchanger of the mixing chamber; *3*—connecting tube; *4*—valves for the liquid flow; *5*—position of the phase separation line.

powder with a particle size of 700 Å, pressed at a pressure of 2.3 kbar. The filling factor is 50% and the area of the heat exchanger is $\sim20\ m^2$.

After passing through the heat exchangers the flow enters the mixing chamber *20*, which was turned from a solid piece of oxygen-free copper together with the working flange, which is mounted to the plate *16* on three stainless steel tubes. The diameter of the flange is 131 mm, which provides enough space to accommodate the measurement cells and various types of thermometric apparatus. The mixing chamber and flange are coated with a layer of silver to improve the thermal contact. The mixing chamber is of the counterflow heat-exchanger type (Fig. 3) and is made of a copper block *1* through which two parallel passages, 22 mm in diameter and 90 mm long, have been bored. A mixture of a copper powder with a particle diameter of 5–10 μm and a silver powder with a particle size of 700 Å was pressed onto the walls of the passages to a thickness of 5 mm. The pressed powders (pressing pressure 2.3 kbar) served as the heat exchanger *2* of the mixing chamber. The passages are connected together on one end by a cross tube *3* and are connected on the other end to the lowermost discrete heat exchanger *17* (in Fig. 1).

Thus the flow of liquid ^{3}He enters the mixing chamber from the heat exchanger *17* and passes through the special channels *4*. It is very important to optimize the inner diameter of the channels in order to decrease the viscous heating. In accordance with Ref. 14, the inner diameter of the channel was chosen equal to 12 mm. The volume of the mixing chamber is 64 cm^3, and the surface area of its heat exchanger is $\approx400\ m^2$. The mixing chamber is mounted in such a way that the phase separation line in the steady-state mode is parallel to the axis of the channels. For the mounting of measuring devices the flange of the mixing chamber is equipped with conical and threaded connectors.

In addition to the adsorption pumping system the refrigerator has provisions for circulation of ^{3}He by means of a mechanical pump, which can substantially reduce the expenditure of helium in the preliminary cooling stage and also

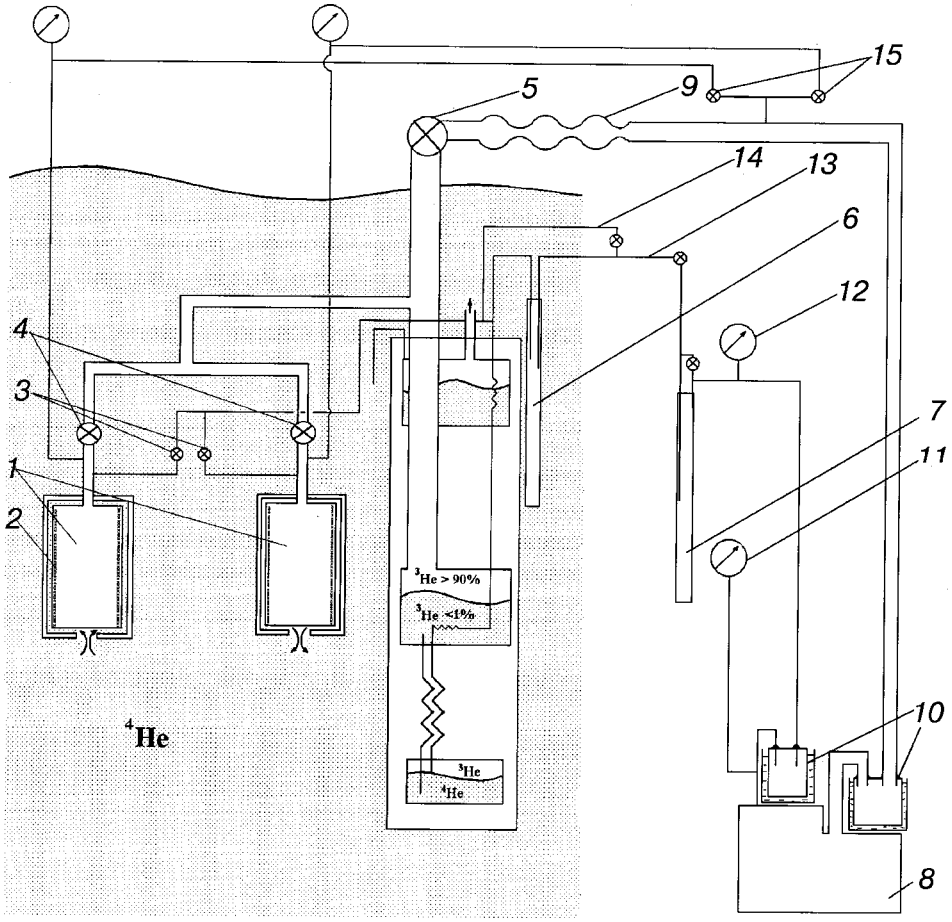

FIG. 4. Block diagram of the circulation of ^{3}He in the dilution refrigerator: *1*—adsorption pumps; *2*—heater of adsorbent; *3*—regeneration valves; *4*—low-temperature valves for actuating the adsorption pumps; *5*—valves for pumping out the still by the mechanical pump; *6*—helium trap; *7*—nitrogen trap; *8*—mechanical pump; *9*—sylphon evacuation hose; *10*—nitrogen traps; *11,12*—manometers; *13*—main condensation line; *14*—standby condensation line; *15*—return valves of adsorption pumps.

permits conducting prolonged experiments that do not require very low temperatures (temperatures down to $\sim 25-30$ mK). The adsorption pumps are ordinarily turned on when it is necessary to go to lower temperatures. Figure 4 shows a diagram of the circulation of ^{3}He by this hybrid scheme. As can be seen in the figure, when the circulation of ^{3}He is effected by the mechanical pump the flow of the gaseous ^{3}He to be condensed is purified before entering the cryostat by means of a nitrogen trap *7* placed at the output of the mechanical pump *8* and a helium trap *6* located inside the helium Dewar. A manometer *11* is used to monitor the pressure at the outlet of the pump to detect possible blockage of the oil trap *10*. The apparatus is also provided with a standby condensation line *14*, which is opened by a valve if the main line *13* becomes blocked. In the case of cryogenic pumping of ^{3}He from the mixing chamber the circulation is effected by the alternately operating pumps *1*, which are controlled by low-temperature valves *3* and *4*. This apparatus has provisions for the return of ^{3}He from the adsorption pumps *1*, when in the regeneration mode, to the condensation line *13* through the use of a mechanical sliding-vane rotary pump *8*. In that case the low-temperature valves *3* are permanently closed, and the return of ^{3}He directly to the evacuation lines *9* of the mechanical pump is effected through the valves *15*, which are at room temperature. In this situation valve *5* is closed. Thus the adsorption pump in the regeneration mode is continually pumped out by a mechanical pump.

This combination of cryogenic pumping and regeneration with evacuation by a mechanical pump has the following advantages:

— the requirements on the main cryogenic valves *4* are substantially reduced, since the pressure in the adsorption pump does not increase appreciably at the time of regeneration;

— the adsorption pump is almost completely cleansed of impurities without leaving behind an appreciable amount of ^{3}He after the regeneration process is completed;

— the heating regime of the adsorption pumps is more economical, since it is unnecessary to raise the pressure in the pump very much.

The minimum temperature that would be attained on cooling with an unfilled cell (without heat leakage along the filling capillary) was 4.2 mK. Originally the circulation was effected by a mechanical pump, and after the temperature reached 25–30 mK the adsorption pumps were turned on. In working with external pumping, when the experiment does not call for temperatures below 20 mK, the refrigerator is quite economical. For example, at a ''cruising'' circulation of 10^{-4} mole/s the expenditure of liquid helium is 7 liter/day.

3. EXPERIMENTAL UNIT FOR STUDYING SOLID HELIUM BY MEANS OF PRECISION PRESSURE MEASUREMENTS

The operation of the automated cryogenic unit can be examined for the example of the study of kinetic processes in solid mixtures of the quantum crystals ^{3}He–^{4}He in the millikelvin temperature range. The measurement cell *18* containing the sample is mounted on the plate of the mixing

chamber *20* (see Fig. 1) by means of a conical thermal contact. This plate also holds the main thermometers (see Sec. 4) and a heater.

The construction of the measurement cell is described in detail in Ref. 16. The geometry of the cell has been chosen so as to ensure the rapid establishment of thermal equilibrium in the crystal under study and to reduce to a minimum the inhomogeneities arising in the process of crystallization. The experiments are done at constant volume, and the change in pressure in the crystal due to various processes occurring in the system under study is recorded. The change in pressure is measured by a capacitance bridge with a resolution of ± 1 Pa.

The method of precision measurement of the pressure of a quantum crystal is very informative and convenient for performing the following physical tasks:

— studying the kinetics of growth and the dissolution of ^{3}He inclusions in a ^{4}He matrix or of ^{4}He inclusions in a ^{3}He matrix;

— construction of the equilibrium phase diagram;

— determination of the coefficient of interdiffusion;

— determination of the exchange interaction in solid helium.

4. THERMOMETRY SYSTEM

The main thermometer for measurement of ultralow temperatures is the melting curve thermometer (MCT), the working principle of which is based on the change in the melting pressure of ^{3}He. The ratio of the melting pressure to the melting temperature of pure ^{3}He is universal and has now been standardized to a high degree of accuracy. Thermometry based on the properties of the melting curve of ^{3}He became possible after the development of precision membrane pressure sensors[17–19] and is the most widely used method in the millikelvin temperature range. In the present study we have used the standard construction of the MCT,[19] which was calibrated at a temperature ≈ 1.3 K according to a standard manometer.

The indications of the capacitive sensor of the MCT were recorded by an E8-4 or E7-8 digital capacitance meter. The calibration curve obtained is well reproducible for each of the samples. The dependence of the pressure P on the capacitance C was approximated by the formula

$$P = P_1 - P_2/C, \tag{3}$$

where P_1 and P_2 are fitting coefficients, and the relation between the pressure and temperature, according to Refs. 20 and 21, was taken in the form

$$P = \sum_{n=-3}^{9} a_n T_n, \tag{4}$$

where

$$a_{-3} = -7.2175164 \times 10^{-13}, \quad a_{-2} = 2.9055958 \times 10^{-9},$$

$$a_{-1} = -5.044198 \times 10^{-6}, \quad a_0 = 3.4461924,$$

$$a_1 = -4.4127628, \quad a_2 = 1.5401113 \times 10^{1},$$

$$a_3 = -3.5780818 \times 10^{1}, \quad a_4 = 7.1567462 \times 10^{1},$$

$$a_5 = -1.0429605 \times 10^{2}, \quad a_6 = 1.0524591 \times 10^{2},$$

$$a_7 = -6.9301578 \times 10^{1}, \quad a_8 = 2.6659433 \times 10^{1},$$

$$a_9 = -4.5298212.$$

This formula, obtained at the metrological institute of the Physikalisch Technische Bundesanstalt in Berlin, Germany, approximates the melting curve of ^{3}He in the temperature range from 1 mK to 1 K.

The average sensitivity of the capacitance bridge used is 0.8 pF/atm. In the measurements by the automatic digital ac current bridge E8-4, with a sensitivity of 0.01 pF, the temperature resolution was 0.3 mK, which is entirely adequate for making measurements. The high-purity ^{3}He ($>99.99\%$) used for thermometry was obtained by the distillation of commercial-grade ^{3}He (99.75% pure) by the standard technique of purification by rectification.

In each cooling cycle a tie-in was made to the minimum of the melting curve of ^{3}He. The pressure measurements near the minimum on the melting curve of ^{3}He, were made by a General Radio (GR) 1615-A manual bridge, which permitted improving the pressure resolution to 12.5 Pa. It was found that the calibration curves before and after the experiment agreed to within 0.01%; however, the cyclic temperature change from room to helium temperature noticeably shifts the calibration curve, and it is therefore necessary to do the calibration over again for each experiment.

In these experiments we also used resistance thermometers: two Matsushita carbon thermometers with nominal resistances of 55 and 105 Ω, a gallium arsenide semiconductor thermometer with a nominal resistance of 0.6 Ω, and a ruthenium oxide thermometer with a nominal resistance of 1000 Ω. (The nominal resistances of the thermometers are indicated at room temperature.) These thermometers are placed at different points in the refrigerator and permit monitoring of the temperature distribution in it at any time. The resistance of the thermometers was measured by a four-lead scheme on a Cryobridge R441 ac current bridge at a dissipated power of 10^{-10}–10^{-12} W and also by a specially developed ac current bridge[22] at a dissipated power of the order of 10^{-15} W.

5. AUTOMATED SYSTEM FOR CONTROL AND DATA ACQUISITION AND PROCESSING

The automation system of the cryogenic unit for research on solid ^{3}He–^{4}He mixtures at ultralow temperatures is constructed on the basis of two computers and a CAMAC bus–module system. It includes a combination of hardware and software for performing experiments by different procedures. Figure 5 shows a block diagram of the automated control system of the refrigerator, in which one can discern the following main blocks:

— a two-computer complex;

— the CAMAC bus–module system;

— the experimental apparatus;

— the instrumentation unit.

The two-computer complex consists of two computers of the IBM PC type, computer *1* and computer *2*, which, through a CAMAC bus–module system, operates in a dialog mode with the instrumentation part of the refrigerator and performs data acquisition from the various channels, stores and monitors the data, and carries out preliminary data pro-

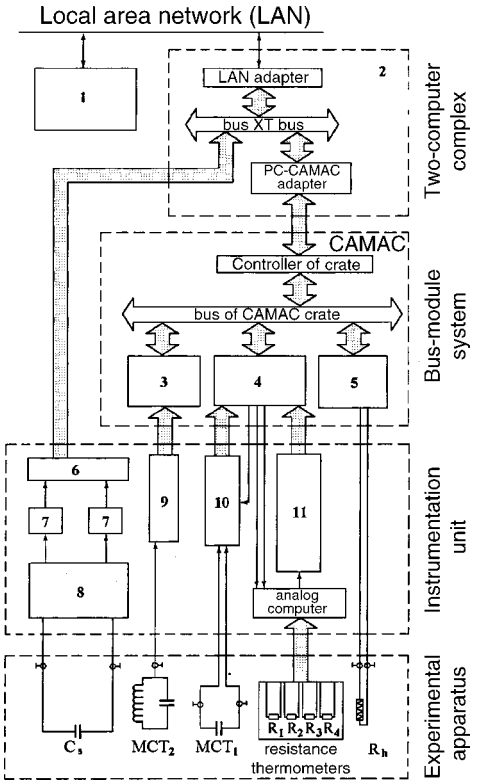

FIG. 5. Block diagram of the automated control system of the cryogenic unit: *1,2*—two-computer complex; *3*—input register; *4*—control unit; *5*—digital-to-analog converter; *6*—two-channel analog-to-digital converter (MS QUICK); *7*—scalers; *8*—Gr 1615-A capacitance bridge; *9*—Ch3-34A frequency meter; *10—L, C, R* meter of the E7-8 type; *11*—bridge for resistance measurement.

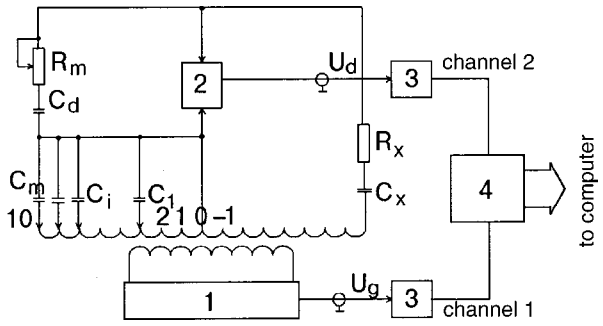

FIG. 6. Block diagram of the automated system for capacitance measurement: *1*—reference generator; *2*—null indicator; *3*—amplifier; *4*—analog-to-digital converter.

cessing and provides real-time visualization of the data on a monitor screen. As the information is accumulated, this computer transfers it to computer *1*, which receives the data through a local area network, performs the final data processing and visualization of the results on the monitor, and produces an archive of experimental data on the processing results.

The CAMAC bus–module system performs the function of interfacing with the object of study, since computer *2* was not designed for automation of experiments, and some of the instrumentation does not have standard interfaces. The interface functions are implemented by standard units: an input register *3*, a digital-to-analog converter *5*, and an original control unit *4*. The CAMAC bus interfaces with the bus of computer *2* through the controller of the crate and a specially designed adapter.

The experimentation unit contains the following set of primary sensors to permit tracking various parameters characterizing the state of the sample and refrigerator:

— a capacitive pressure sensor C_s used for measurement of the pressure of the investigated crystal *in situ*;

— capacitive transducers of the crystallization thermometers MCT_1 and MCT_2, intended for measurement of the temperature at various points of the dilution refrigerator;

— a block of resistance thermometers for measuring the temperature at various points in the refrigerator;

— a wire resistance R_h which is a control element of the temperature stabilization.

The instrumentation unit includes the following main devices:

— a GR 1615-A bridge for capacitance measurement;

— A Ch3-34A frequency meter;

— *L, C, R* meter of the E7-8 type

— an original precision digital bridge for resistance measurement.[22]

The input register *3* accepts data from the Ch3-34A frequency meter (*9*). The control unit *4* performs the triggering of the E7-8 meter (*10*) and the acquisition of data from it, controls the operation of an analog commutator, and also accepts data from the resistance bridge *11*. The eight-channel analog commutator is based on reed relays which do not introduce any errors into the measurement of the electrical resistance and provide fast action of the commutator. The control unit *4* is a multifunction device to which one can connect additional digital voltmeters of the ShCh-300, ShCh-302, and ShCh-304 types.

The analog-to-digital converter *5* provides for smooth control of the heater R_h. Special mention should be made of the two-channel 8-bit analog-to-digital converter *6* with a 32-kilobyte memory in each channel and a maximum measurement frequency of 50 MHz. This converter performs data acquisition in two channels from the GR 1615-A capacitance bridge and has an output directly to the bus of computer *2*. Precision scalers *7* are provided for ensuring the most complete use of the scale of the analog-to-digital converter *6*.

6. AUTOMATION OF THE MANUAL CAPACITANCE BRIDGE

Let us now discuss the automation of the precision system for capacitance measurement, consisting of a GR 1615-A capacitance bridge, a GR 1311-A sinusoidal signal generator, and a GR 1232-A null detector[21] (Fig. 6). As we see from the figure, the system uses a transformer bridge. The capacitance C_x to be measured is connected with an active resistance R_x to one arm of this bridge, and a set of standard capacitances C_{m1}, C_{m2},…,C_{mm} is present in the reference arm, together with a resistance box R_m with an additional capacitance C_d. An ac signal at frequency $w = 5$ kHz is applied to the reference generator *1* across the transformer bridge, from which it is taken off by a phase detector *2*. The latter is equipped with a filter that passes only the generator frequency. The imbalance voltage of the bridge from detector *2* and the reference signal after scaling by units

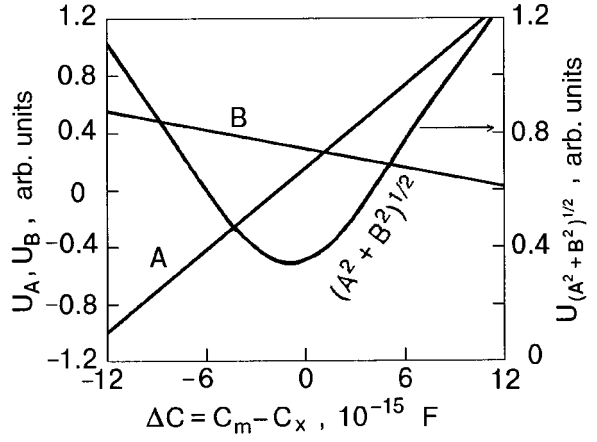

FIG. 7. Voltage across the null indicator of the capacitance bridge versus the imbalance of the capacitance. A is the real part of the imbalance voltage, and B is the imaginary part; $(A^2+B^2)^{1/2}$ is the voltage amplitude.

3 are fed to the analog-to-digital converter *4*. This converter is a programmable MSQUICK card, which simultaneously measures the voltage at the output of the generator in channel *1* and of the null detector in channel *2* and and enters them in a data file in the computer.

The automation of the manual bridge is based on the principle that after the preliminary calibration the value of the capacitance to be measured is calculated from the imbalance voltage of the bridge. An analysis (Fig. 7) of the imbalance voltage on the null detector, which is used as an amplifier, as a function of the imbalance of the capacitance showed that it is more advantageous to use phase instead of amplitude detection. Phase detection gives a unique relation between the measured values of the real A and imaginary B parts of the voltage of the null indicator of the bridge and the imbalance of the capacitance $C_m - C_x$ and of the dissipative factor $D_m - D_x$. For amplitude detection, as can be seen in Fig. 7 (the curve $(A^2+B^2)^{1/2}$), each value of the voltage U corresponds to two values of ΔC. Furthermore, in amplitude detection additional systematic error can arise due to the change in resistance of the cables.

A calculation are linear electrical circuits gives the following expression for the ratio of the voltage U_d after the detector to the generator voltage U_g:

$$U_d/U_g = A + iB = (k + i\varphi)\frac{C_m - C_x + i(C_m D_x - C_x D_m)}{C_k + C_x + i(C_k D_x + C_x D_m)}, \tag{5}$$

where $C_k = 1592$ pF is the total capacitance of the box, and $k + i\varphi$ is the gain of the null detector determined in the calibration. For fixed values of C_x and D_x the values of the capacitance of the box are changed in discrete steps: $C_{m1} = C_m + \Delta C_m$, which, in turn, leads to a discrete change in the quantities A and B. From this we determined the gain components

$$k = (A_1 - A)\frac{C_k - C_m}{\Delta C_m} + A;$$
$$\varphi = (B_1 - B)\frac{C_k - C_m}{\Delta C_m} + B, \tag{6}$$

where $A_1 + iB_1$ is the imbalance at the new value C_{m1}. If the gain is known, then by measuring the active and reactive components of the imbalance of the bridge in the course of an experiment, one can easily calculate the capacitance C_x and dissipative factor D_x to be measured:

$$\frac{1}{C_x} + iwR_x = (1 + iD_m)\frac{k + i\varphi - (A + iB)}{C_m(k + i\varphi) - C_k(A + iB)}, \tag{7}$$

$$D_x = wC_xR_x. \tag{8}$$

The bridge automation system described is quite simple and reliable and can be used for automating other bridges of the transformer type.

7. SOFTWARE FOR STUDYING THE KINETIC PROCESSES IN ^{3}He–^{4}He SOLID SOLUTIONS

The software for precision measurement of the pressure at constant volume and for reading the thermometers consists of a main program and a set of subprograms. All of the programs are written in the language Turbo Pascal 6.0 in the MS-DOS environment with the use of Assembler language plug-ins which permitted a substantial improvement in the execution time of the program. The subprograms are written as procedures and are linked to the main program. This structure makes it possible to use in one subprogram procedures described in other subprograms. In addition, one can always link new subprograms to the main program.

Pressure measurement

In the subprogram for pressure measurement are provisions for the analog-to-digital converter *4* (Fig. 5) to store parts of the sinusoid of the measurement and reference signals fed from the output of the scalers *3*. These signals are processed by the least-squares method on computer *2*, compared in phase and amplitude, and used to calculate the capacitance to be measured according to Eqs. (7) and (8). The result is stored in a file, and the procedure is repeated.

Before the program is started the GR 1615-A bridge is balanced in respect to the dissipative factor D_m and the gain of the null detector is chosen such that a change in capacitance by ΔC_m will correspond to the largest possible voltage (60% scaling limit). Upon the startup of the program the readiness of the CAMAC is determined and then, in a dialog mode, the parameters of the reference capacitances C_m, ΔC_m, and D_m and the averaging time of the measured quantities (the default is 1 min) are specified. Then a determination of the gain (calibration) is made and the real-time measurements begin. The averaging of the measured values of the pressure is done according to a quadratic dependence with monitoring of the overshoots. The program for automation of the capacitance bridge had to solve the following problems: Distinguish between the change in capacitance when the balancing knob is turned from a change in the capacitance to be measured. If it is a change in C_m a recalibration of the gain of the null detector is done. This makes it possible, having established a high sensitivity at the startup of the program, to measure the change in pressure more precisely by a stepwise change in C_m. Unfortunately, this method cannot be used to measure fast processes ($\sim$5 min)

occurring with a large change in pressure (e.g., upon a sharp heating of a separated solution to the one-phase region), because the recalibration time is ≈ 1 min.

Thanks to a systematic processing of the data obtained, it became possible to improve the accuracy of the pressure measurements from ± 8 to ± 1 Pa.

Temperature measurements

The subprogram for temperature measurements consists of two parts. The first is intended for measurement of the temperature according to the MCT and controls the triggering and readout of the E7-8 meter. The second part of the subprogram corresponds to commutation and measurement of the resistance thermometers with allowance for the balancing time of the special ac current bridge. The algorithm for reading the resistance thermometers can be written as follows:

— switch to the first resistance (reset);
— balance the resistance bridge (10–12 s);
— measure the resistance;
— switch to the second resistance;
— balance the resistance bridge;
— measure the second resistance, etc.

The switching occurs for all the resistances connected to the analog commutator, and after the measurement of the last resistance a reset is done.

Both of these parts of the subprogram operate simultaneously, and a measurement of the temperature of the MCT is made every 0.2 s.

Temperature stabilization

To implement the discrete temperature changes necessary for studying the temperature dependence of the kinetic coefficients at phase transitions, a heater-control subprogram is used. The input of a digital-to-analog converter is fed a digital signal given by the formula

$$n=\left[k1\cdot dR[1]+k2\sum_{i=1}^{7} dR[i]+k3(dR[1]-dR[2])\right]^{1/2}(R^*/R)^2, \tag{9}$$

where $k1$, $k2$, and $k3$ are the coefficients in front of the proportional, integral, and differential terms of the temperature stabilization, respectively; $dR[1,\ldots,7]$ is an array of differences of the measured resistance R and the reference resistance R_0 ($dR[1]$ corresponds to the last measurement, $dR[2]$ to the preceding one, etc.); R^* is the value of the resistance at which the coefficients $k1$, $k2$, and $k3$ had been chosen to provide the most effective temperature stabilization at that temperature. The factor R^*/R appears to the second power because it is assumed that the main role is played by the cooling capacity of the refrigerator, which is proportional to T^2.

Modes of operation

The main program, which unifies the subprograms for the pressure and temperature measurements, temperature stabilization, etc. can operate the unit in different modes and perform the measurement functions differently depending on the experimental tasks.

In the graphical mode the kinetics of the change in pressure of the sample and the temperature of the crystallization thermometer are displayed on the monitor screen. This mode is very convenient in operation and permits direct visual monitoring of the physical processes, so that, if necessary, one can rapidly correct the experimental conditions. The choice of the scale and digitization of the axes is made automatically.

In the digital mode the monitor also displays the values of the gain of the null detector, the reference capacitance, the imbalance of the bridge, and the readings of the crystallization thermometer and resistance thermometers.

In the nonaveraging mode each point is written to a file of results (the interval between measurements is around 0.2 s). This mode makes it possible to study fast processes with characteristic times of from 1 s to 2 min. In particular, the dissolution of solid inclusions of ^{3}He in a ^{4}He, matrix upon sharp warming of the sample was studied, and an anomalously fast mass transfer, of a threshold character, was discovered.[24]

In the temperature-stabilization mode no switching to different resistance thermometers is done, and it is not necessary to wait for balancing of the resistance bridge. The power of the heater is calculated from the difference between the reference value of the resistance and the actual resistance at each cycle of measurements (every 0.2 s).

The advantages of temperature stabilization with the aid of a computer are:

— convenience in operation (for a temperature measurement it is sufficient to specify only the reference value of the resistance);

— direct readings of the resistance thermometer are obtained (unlike the case when the reference value is established manually on the measurement bridge);

— the possibility of varying the heating power as a function of the temperature of the sample, which makes it possible to take into account the low-temperature behavior of the heat capacity of substances and the temperature dependence of the cooling capacity of the refrigerator;

— the implementation of special regulated modes of heating of the objects under study (for example, a linear change of the temperature with time).

CONCLUSION

The cryogenic unit described here makes it possible to realize various modes of operation that can be used in a wide range of physical studies at ultralow temperatures. When the refrigerator is operated with circulation by means of a mechanical pump a very economical mode (in terms of the use of liquid helium) is realized which permits doin research down to 20 mK. The use of two alternately operating adsorption pumps offers the possibility of lowering the limiting temperature to ~ 5 mK. For further lowering of the temperature it is planned to add a nuclear demagnetization stage.

The use of a flexible automation system makes it possible to easily alter the architecture of the system, to imple-

ment new algorithms of measurement, and to create new software.

The authors are grateful to Profs. G. R. Pickett and I. E. Miller (University of Lancaster, England) for providing the discrete heat exchangers and to the staff of the metrological institute of the Physikalisch Technische Bundesanstalt (Berlin, Germany) for technical support.

†Deceased.
*E-mail: rudavskii@ilt.kharkov.ua

[1] H. London, G. R. Clarke, and E. Mendoza, Phys. Rev. **128**, 1992 (1962).
[2] B. S. Neganov, N. S. Borisov, and M. Yu. Liburg, Zh. Éksp. Teor. Fiz. **50**, 49 (1966) [*sic*].
[3] V. S. Édel'man, Prib. Tekh. Éksp. **No. 4**, 229 (1991).
[4] V. A. Mikheev, V. A. Maidanov, and N. P. Mikhin, Cryogenics **24**, 190 (1984).
[5] P. R. Rocch, K. E. Gray, and B. D. Dunlap, in *Proc. LT-17*, Kyoto, Japan (1987), Vol. 2, p. 1727.
[6] R. H. Solmenin, J. M. Kyynaragnen, M. R. Berlund, and J. P. Pekola, J. Low Temp. Phys. **76**, 83 (1989).
[7] V. A. Maidanov, N. P. Mikhin, N. F. Omelaenko, E. Ya. Rudavskii, A. S. Rybalko, V. K. Chagovets, V. A. Mikheev, P. Mohandas, B. P. Cown, and J. Sounders, Fiz. Nizk. Temp. **20**, 672 (1994) [Low Temp. Phys. **20**, 527 (1994)].
[8] V. E. Sivokon', V. V. Dotsenko, A. A. Pogorelov, and V. A. Sobolev, Fiz. Nizk. Temp. **19**, 144 (1993) [Low Temp. Phys. **19**, 312 (1993)].
[9] A. S. Rybalko, V. A. Mikheev, B. I. Kolesnik, and V. I. Belobord'ko, Fiz. Nizk. Temp. **19**, 720 (1993) [Low Temp. Phys. **19**, 518 (1993)].
[10] G. A. Mikhailov, Prib. Tekh. Éksp. **No. 6**, 221 (1985).
[11] V. A. Goncharov, V. N. Lukashov, N. I. Pershin, and É. Ya. Rudavskiĭ, Inventor's Certificate No. 947593 (USSR), International Classification NF25D3/10; publ. July 30, 1982.
[12] Yu. M. Bunkov, A. M. Guenault, D. J. Hayward, D. A. Jackson, C. J. Kennedy, T. R. Nichols, I. E. Miller, G. R. Pickett, and M. G. Ward, J. Low Temp. Phys. **83**, 257 (1991).
[13] V. Keith and M. G. Ward, Cryogenics **24**, 249 (1994).
[14] J. C. Wheatley, R. E. Rapp, and R. T. Jonson, J. Low Temp. Phys. **4**, 1 (1971).
[15] A. S. Rybalko and M. B. Sterin, Fiz. Nizk. Temp. **22**, 1095 (1996) [Low Temp. Phys. **22**, 837 (1996)].
[16] A. N. Ganshin, V. A. Maidanov, N. F. Omelaenko, A. A. Penzev, E. Ya. Rudavskii, and A. S. Rybalko, Fiz. Nizk. Temp. **24**, 815 (1998) [Low Temp. Phys. **24**, 611 (1998)].
[17] G. C. Straty and E. D. Adams, Rev. Sci. Instrum. **40**, 1393 (1969).
[18] R. A. Scribner and E. D. Adams, Rev. Sci. Instrum. **40**, 287 (1970).
[19] E. D. Adams, Rev. Sci. Instrum. **64**, 601 (1993).
[20] G. Schuster, A. Hoffmann, and D. Hechtfisher, Doc. CCC/96-25 Bureau Intern. des Poids et Mesures, Comit Consulativ de Thermometrie, svres, France, Vol. 19 (1996), p. 25.
[21] G. Schuster, A. Hoffmann, and D. Hechtfisher, Comite Consultatif de Thermometrie, ''Toward an international temperature scale from 0.65 K to 1 mK,'' Leiden (1998), p. 7.
[22] G. A. Mikhailov, *Fourteenth International Cryogenic Engineering Conference and International Cryogenic Materials Conference*, Kiev (1992), p. 130.
[23] *Type 1615-A Capacitance Bridge, Type 1620-A Capacitance Measuring Assembly*, General Radio Company, Massachusetts, USA (1963).
[24] A. N. Gan'shin, V. A. Maidanov, N. F. Omelaenko, A. A. Penzev, E. Ya. Rudavskii, and A. S. Rybalko, Fiz. Nizk. Temp. **24**, 1117 (1998) [Low Temp. Phys. **24**, 840 (1998)].

Translated by Steve Torstveit

OBITUARY

In memoriam: Boris Georgievich Lazarev (1906–2001)

Fiz. Nizk. Temp. **27**, 811 (July 2001)
[DOI: 10.1063/1.1388427]

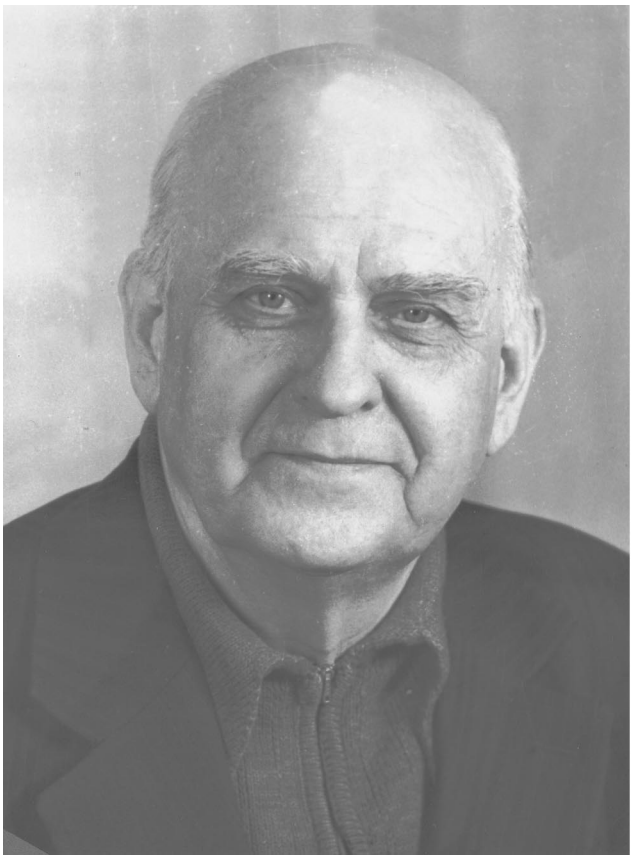

We are mourning the loss of the patriarch of low-temperature physics, Academician Boris Georgievich Lazarev of the National Academy of Sciences of Ukraine. Grief for his loss is shared by many cryogenic centers that have been founded in different cities across the enormous expanse of the Soviet Union. It would be hard to find any scientists in them who were not in some way influenced by his groundbreaking works on the electronic structure of metals, superconductivity, and the properties of liquid helium. He was the one who furnished the cryogenic equipment for the laboratories in Kiev, St. Petersburg, Ekaterinburg, Donetsk, Tbilisi, and Sukhumi, inspired their staffs with enthusiasm, and introduced them to the physics of subtle properties of matter. In turn, his fellow scientists and proteges, Academicians B. I. Verkin and A. A. Galkin of the Ukrainian Academy of Sciences, developed this branch of science and enriched it with new fields of study in institutes that they founded which have become the leading academic institutes of Ukraine. In addition to his gifts as a researcher, it fell to Prof. Lazarev to take on the mission of passing on to succeeding generations of physicists the spirit and traditions of that romantic time of the pioneers of science, who gave it their unselfish devotion. Now it is our duty to keep that epoch from disappearing without a trace.

Prof. Lazarev was the senior member of the editorial board of this journal, a wise and always interested advisor, an optimist and a great lover of life. It seemed that he was around long before us and would live on after us. His memory will always remain in our hearts and in the history of physics in our country.

Editorial Board

